# Design of Biomaterials

# for Soft Tissue Adhesion

**Edward Jonathan Cozens**

Submitted in partial fulfilment of the requirements of the Degree of Doctor of Philosophy

September 2019

# Declaration

I, Edward J. Cozens, confirm that the research included within this thesis is my own work or that where it has been carried out in collaboration with, or supported by others, that this is duly acknowledged below and my contribution indicated. Previously published material is also acknowledged below.

I attest that I have exercised reasonable care to ensure that the work is original, and does not to the best of my knowledge break any UK law, infringe any third party's copyright or other Intellectual Property Right, or contain any confidential material.

I accept that the College has the right to use plagiarism detection software to check the electronic version of the thesis.

I confirm that this thesis has not been previously submitted for the award of a degree by this or any other university.



Signature: Date: 26/09/19

Details of collaboration and publications:

Preparation of cell monolayers and collection of fluorescence microscopy images was performed by Dexu Kong. All analysis of the data was performed by me.

Parts of Chapter 3 and 4 have been submitted for publishing.

# Acknowledgements

Firstly I would like to thank my supervisor, Professor Julien Gautrot, for his invaluable support and guidance throughout my project. I am very grateful to have had the opportunity to work with him and to be a part of his research group.

I would also like to thank all of the members of the Gautrot group, particularly Danyang Li, Dexu Kong and Will Megone for their help and guidance with experiments. The technical support staff at Queen Mary University must also be acknowledged; in particular I'd like to thank Chris Mole, Dr. Alice Williams, Shafir Iqbal and Russell Bailey for their technical support, which made this research possible.

I extend my thanks to GlaxoSmithKline for their collaboration and support on this project, particularly Dr. Nima Roohpour for his technical expertise. Furthermore, I am very grateful for the opportunity to attend and present at the World Congress on Biomechanics and the European Society for Biomaterials, which was made possible through funding from Queen Mary University and the Institute of Materials, Minerals and Mining (IOM3). I would also like to acknowledge the EPSRC (grant EP/M507532/1) for making this research possible.

Finally, I am extremely grateful for love and support from my family, and I would like to thank my Wife and Father for helping with the proofreading of my thesis. I also wish to extend particular gratitude to my Wife, for all her support throughout my PhD studies.

# Abstract

The design of polymeric biomaterials for soft tissue adhesion is of great interest in applications such as skin adhesives for surgical applications, hydrogels for tissue regeneration and mucoadhesives for dental adhesion; in these applications careful regulation of the interactions between the material and soft tissue is vital. In order to promote adhesion to soft tissues, a greater understanding of the relationship between polymer chemistry and adhesion mechanisms at different length scales is required. This work investigated the adhesion of protein resistant and weak polyelectrolyte brushes to epithelial cell monolayers (primary keratinocytes and HaCaT cells), soft tissues (porcine epicardium and keratinized gingiva) and a range of substrates with defined surface chemistry (self-assembled monolayers (SAMs)). Testing was carried out via colloidal probe-based atomic force microscopy (AFM). Poly(acrylic acid) (PAA) hydrogels were developed through different functionalisation (conjugation with a primary amine or bromoalkane) and crosslinking strategies (chemical or physical) and their adhesion to soft tissues was investigated via tensile and lap shear testing. Nanoscale adhesion assays reveal the complex balance of interactions (electrostatic, Van der Waals interactions and hydrogen bonding) that regulate the adhesion of weak polyelectrolyte brushes. In turn, studies on cell monolayers highlighted the importance of the glycocalyx in regulating non-specific adhesions. Alongside these studies, macroscale tests further confirmed the effect of tissue biochemistry on adhesion, with thiyl-bonded gels displaying particularly strong adhesion. Overall, this work clearly demonstrates the complex nature of soft tissue adhesion involving non-specific interactions and covalent bonding, which are further regulated by the mechanical properties of the bulk biomaterial, the soft tissue

and their interface. It is hoped that this multi-scale insight into the adhesion of polymers to cells/tissues will further advance the understanding of soft tissue adhesion, enabling the more effective and rational design of a novel generation of bioadhesives.

# Nomenclature

| | |
|---|---|
| 3-BMPBA | 3-(bromomethyl)phenylboronic acid |
| AFM | Atomic force microscopy |
| aJ | Attojoule |
| APTES | (3-aminopropyl)triethoxysilane |
| ATR-FTIR | Fourier transform infrared–attenuated total reflectance spectroscopy |
| ATRP | Atom transfer radical polymerization |
| Bipy | 2,2'-bipyridyl |
| CMC | Carboxymethylcellulose |
| CPM | Colloidal probe microscopy |
| DAPI | 4',6-diamidino-2-phenylindole dihydrochloride |
| DCC | Dicyclohexylcarbodiimide |
| DCM | Dichloromethane |
| DLS | Dynamic light scattering |
| DMAEMA | 2-(dimethylamino)ethyl methacrylate |
| DMAP | 4-dimethylaminopyridine |
| DMEM | Dulbecco's modified eagle medium |
| DMF | Dimethylformamide |
| DMSO | Dimethyl sulfoxide |
| DMTMM | 4-(4,6-dimethoxy-1,3,5-triazin-2-yl)-4-methylmorpholinium chloride |
| DOPA | Dihydroxyphenylalanine |

| | |
|---|---|
| DTT | Dithiothreitol |
| ECM | Extracellular matrix |
| EDC | Ethyl(dimethylaminopropyl) carbodiimide |
| EDTA | Ethylenediaminetetraacetic acid |
| EGF | Human recombinant epidermal growth factor |
| $Et_3N$ | Triethylamine |
| FIB | Focused ion beam |
| fJ | Femtojoule |
| HA | Hyaluronic acid |
| HCl | Hydrochloric acid |
| $^1H$ NMR | Hydrogen nuclear magnetic resonance |
| HPK | Human primary keratinocytes |
| I-2959 | Irgacure 2959 |
| KSFM | Keratinocyte serum free medium |
| LCST | Lower critical solution temperature |
| $Me_4$Cyclam | 1,4,8,11-tetraaza-1,4,8,11-tetramethylcyclotetradecane |
| MeOH | Methanol |
| MUDA | 11-mercaptoundecanoic acid |
| $Na_2CO_3$ | Sodium carbonate |
| NaCl | Sodium chloride |
| NaOH | Sodium hydroxide |
| NHS | *N*-hydroxysuccinimide |
| Ni-NTA | Nickel-nitrilotriacetic acid |
| OEGMA | Oligo(ethylene glycol methyl ether methacrylate) |

| | |
|---|---|
| PAA | Poly(acrylic acid) |
| PAA-BA | Boronic acid-functionalised PAA hydrogels |
| PAA-BP | PAA-pentene hydrogels |
| PAA-Cys | PAA-cysteamine hydrogels |
| PAA-Tyr | PAA-tyramine hydrogels |
| PBS | Phosphate buffered saline |
| PDEA | Poly(2-(diethylamino)ethyl methacrylate) |
| PDMAEMA | Poly(dimethylaminoethyl methacrylate) |
| PDMS | Polydimethylsiloxane |
| PEG | Poly(ethylene glycol) |
| PEGDT | Poly(ethylene glycol) dithiol |
| PET | Polyethylene terephthalate |
| PFA | Formaldehyde solution (4% in PBS) |
| PhMe | Toluene |
| PK | Primary keratinocytes |
| PLL | Poly(L-lysine) |
| PMDETA | *N,N,N',N'',N''*-pentamethyldiethylenetriamine |
| PMMA | Poly(methyl methacrylate) |
| POEGMA | Poly(olgioethylene glycol methacrylate) |
| PtBA | Poly(tert-butyl acrylate) |
| QAPTES | Quartenized (3-aminopropyl)triethoxysilane |
| SAG | Salivary agglutinin |
| SAMs | Self-assembled-monolayers |
| SEM | Scanning electron microscope |

| | |
|---|---|
| SI-ATRP | Surface-initiated atom transfer radical polymerization |
| tBA | Tert-butyl acrylate |
| TEA | Triethanolamine |
| TFA | Trifluoroacetic acid |
| UV | Ultraviolet |
| VC | *N*-vinylcaprolactam |
| WGA | Wheat germ agglutinin |
| XPS | X-ray photoelectron spectroscopy |

# Table of Contents

# List of Figures and Tables

# CHAPTER 1

## Introduction

## 1.1 Chapter Overview

Soft tissue adhesion is a complex process involving non-specific interactions, interpenetration of polymer networks and soft tissue interfaces, and molecular coupling; these are regulated by the mechanical properties of the bulk biomaterial, the soft tissue and their interface.[1,2] Bioadhesives have a growing number of applications in areas such as skin adhesives for surgical applications,[3–5] hydrogels for epicardial placement and stem cell delivery,[6] soft tissue adhesion for tissue regeneration[7,8] and mucoadhesives for dental adhesion.[9,10] In all of these applications, and notably those such as tissue engineering scaffolds and drug delivery systems,[7,8,11–13] careful regulation of interactions between polymeric biomaterials and soft tissues is vital.

This chapter aims to introduce some of the underlying themes and concepts that will be relied upon within this thesis. Initially, the concept of supramolecular chemistry is discussed, with a focus on the non-specific interactions that will be explored later on in this chapter. Next, hydrogels are introduced with a discussion on their unique properties and applications, including a specific look at poly(acrylic acid) (PAA) hydrogels. Following this, some of the complex design requirements of bioadhesives are reviewed. Finally, the structure of the gingiva and the epicardium are discussed with a view to identifying some of the potential molecules to which polymer interactions could occur. This chapter will then be tied together with an overview of the aims of this project and thesis.

## 1.2 Supramolecular Chemistry

Living systems utilise both strong and weak chemical interactions. Covalent bonds, which involve the sharing of electron pairs between atoms, are naturally suited for static connections. Their formation and breakage will often require enzymatic assistance and stored chemical energy. Once a covalent bond is formed it is extremely strong (several 100 kJ/mol[14]) and can withstand the onslaught of thermal agitation. On the other hand, noncovalent bonds, which are significantly weaker (<4 kJ/mol for Van der Waals interactions and a few kJ/mol to tens of kJ/mol for ionic and hydrogen bonds[14]), are more suitable for connections that need to be formed and broken rapidly.[14,15] Several of these intermolecular bonds can be combined to form a stable and strong intermolecular connection. These interactions of multiple individually weak noncovalent bonds underlie many of the intermolecular interactions found in nature.[15] Table 1.1 gives a comparison of some of the typical bond strengths and lengths for covalent and noncovalent interactions.

**Table 1.1.** Typical bond length and energies characteristic of covalent and noncovalent molecular interactions. Data taken from Berg *et al.*[14]

| Nature of Molecular Interaction | Typical Bond Length / Å | Typical Bond Energy / $kJmol^{-1}$ |
|---|---|---|
| Covalent bond | 1.5 | 400 |
| Electrostatic interaction | 3 | 6 |
| Hydrogen bond | 2.4 -3.5 | 4-13 |
| Van der Waals interaction | N/A | 2 – 4 |

The field of supramolecular chemistry involves investigating new molecular systems in which components are held together reversibly by these weaker intermolecular forces. It refers to the domain of chemistry beyond that of the molecule and it focusses on

combining individual covalently bonded molecular building blocks through intermolecular forces in order to create functional architectures. Complementarity is one of the key concepts of this field; it is described as the relationship between two structures which both follow the 'lock and key' principle, where the arrangement of binding sites in the host (lock) is complementary to the guest (key), both sterically and electronically. The most elegant examples of complementary molecular systems are found in nature; such systems provide a very high standard for supramolecular chemists to attempt to match.[16]

There are a number of noncovalent interactions that supramolecular chemists study and take advantage of. These interactions include electrostatics, hydrogen bonding, π-π stacking interactions, Van der Waals forces, hydrophobic forces and metal coordination. Electrostatic interactions, such as ionic bonding, are based on Coulombic attraction between opposite charges. These interactions are high strength, making them ideal for applications requiring strong binding. Hydrogen bonds are weaker than ionic bonding, but they have a directional nature and high precision with which the individual components can be built into molecular systems. A hydrogen bond arises between molecules that have a hydrogen atom bound to a small, highly electronegative atom with lone electron pairs. The use of hydrogen bonds has facilitated the construction of a variety of complex structures.[16] Van der Waals forces are defined as the residual attractive or repulsive force between atomic groups or molecules after covalent and electrostatic interactions have been accounted for.[17] These are even weaker than hydrogen bonding and are also of a very general nature, meaning it is often hard to design receptors to specifically take full advantage of them.[16] Hydrophobic interactions, on the other hand, are viewed as the spontaneous tendency of nonpolar groups to

adhere in water in order to minimize their contact with water molecules.[18] When supramolecular chemists design a new system, it is quite common for them to combine many of these interactions discussed in order to maximize the selectivity and tunability of the interacting system.[16]

The principles of supramolecular chemistry are particularly useful in the field of tissue engineering. Synthetic polymers are increasingly being used as tissue engineering scaffold materials. However, these materials often lack biological recognition which is necessary for cellular adhesion and integration of the implant within the healing tissue. Through the biofunctionalisation of materials, they can be made to better emulate the properties of the native ECM, and thus will be more effective as bioactive tissue engineering scaffolds.[19] In the native ECM, cell attachment is a prerequisite for a number of important cell-function processes, such as cell proliferation and migration. Therefore, to mimic these interactions in synthetic hydrogels, a variety of ECM protein-derived cell-adhesive peptides can be incorporated into the hydrogel scaffolds.[20] For example, Gupta *et al.* modified the surface of polyethylene terephthalate (PET) for the immobilization of collagen biomolecules in order to promote the growth of human smooth muscle cells on *in vitro* grafted films. The PET surfaces were grafted with PAA by plasma processing, and then the collagen was bound to the surface through ionic interactions between the negatively charged PAA and the positively charged protonated amines of the collagen.[21]

## 1.3 An Introduction to Hydrogels

Hydrogels are a water-swollen three-dimensional network composed of hydrophilic polymers which are held together either through physical intramolecular and intermolecular attractions, or through covalent bonding. Due to the high hydrophilicity

of hydrogels, they are able to readily swell through the absorption of large amounts of water or biological fluids. As such, hydrogels better resemble natural soft tissues than any other type of polymeric biomaterial and are accordingly of great interest within the field of bioengineering.[22] Interest for hydrogels within biomedical applications dates back around 60 years when Wichterle *et al.* developed and investigated a poly(2-hydroxyethyl methacrylate)-based hydrogel for use within contact lenses.[23] Since then, and especially within the last two decades, research in the field of hydrogels has expanded significantly. Their use now covers a wide range of applications, which notably include drug delivery,[24–26] wound healing[3,27–29] and tissue engineering.[5,6,8,30,31] In recent years, hydrogel scaffolds have generated significant interest within the field of tissue engineering due to their unique compositional and structural similarities to the natural ECM.[22]

Hydrogels are characterized by their high hydrophilicity, as a result of hydrophilic moieties (including carboxyl, amide, amino and hydroxyl groups) arranged along the polymer backbone.[22] This ability to swell under physiological conditions makes hydrogels ideal for applications such as drug delivery and tissue engineering. The insoluble cross-linked structure allows effective immobilization of biomolecules, as well as high permeability for oxygen, nutrients, and other water-soluble metabolites, making them attractive scaffolds for use in cell encapsulation and delivery. Moreover, the use of hydrogels enables the control of structural and mechanical properties and the ability to provide molecularly tailored bioactivity.[20]

Hydrogels can be classified in several ways, as summarised in Figure 1.1.[32] In the past decade there has been extensive investigation into a category of hyrogels called “smart hydrogels”. These can exhibit unusual and often reversible changes in their swelling

behaviour, network structure and mechanical properties in response to various environmental stimuli such as temperature, pH or ionic strength. Hydrogels can be broadly classified into natural, synthetic or semi-synthetic according to the origin of the polymer backbone. Natural polymers include polypeptides, polynucleotides and different polysaccharides, which are from a variety of natural origins. For example, the polysaccharide chitosan can be obtained from shellfish exoskeletons. Advantages of natural polymer-based hydrogels include their intrinsic characteristics of biological recognition. Disadvantages include problems associated with purification, immunogenicity, and pathogen transmission. Hydrogels based on synthetic polymers ovecome some of these limitations whilst also allowing greater control over material properties such as the matrix architecture and chemical composition.[20,22]

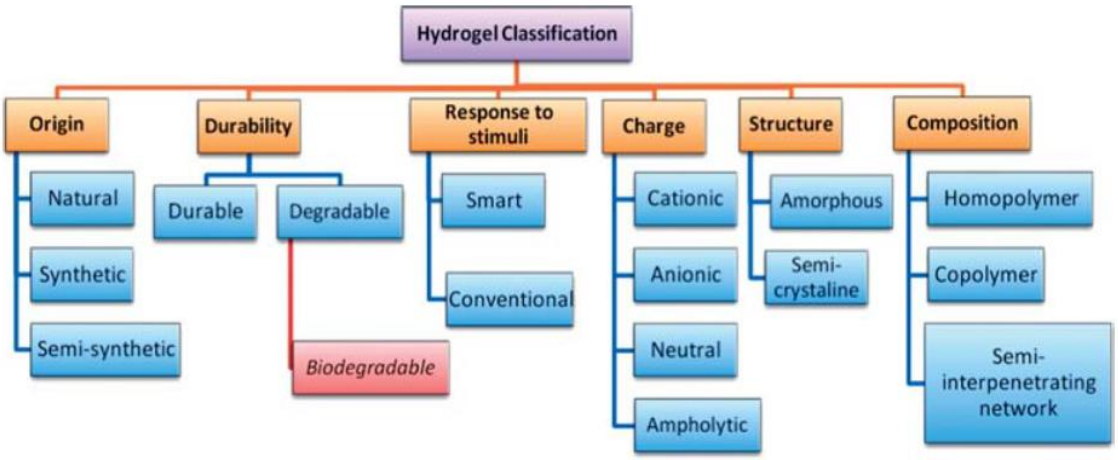


**Figure 1.1.** Diagram illustrating some of the common classifications of hydrogels. Figure taken from El-Sherbiny *et al.*[32]

Hydrogels have been developed for use in a variety of different soft tissue engineering applications. For example, they have been used as carriers for cell transplantation, due

to their ability to offer immunoisolation whilst still allowing nutritional and waste products to diffuse into their matrix.[22] Cruise *et al.* incorporated islets of Langerhans cells into poly(ethylene glycol) diacrylate-based hydrogels, achieving good immunoisolation of the cells both *in vitro* and *in vivo*.[33] Hydrogels have also had important applications as scaffolds due to the ability to tailor their mechanical characteristics to mimic those of the natural ECM. These scaffolds can effectively be used to provide structural integrity and bulk for morphogenic guidance and cellular organisation. Another notable application has been in their use as a barrier to prevent restenosis or thrombosis and subsequently enhance the healing response following tissue injury post-operation. In these applications, the hydrogel is applied as a thin film intravascularly in order to reduce the intimal thickening and thrombosis.[22,34] Finally, one of the most common applications of hydrogels within soft tissue engineering is as localised drug depots. This is attributed to their highly hydrophilic nature, biocompatibility and the ability to control the drug delivery kinetics through interactions with bio-molecular stimuli.[22] In addition to potential clinical applications, *in vitro* tissue engineering can provide an important tool for studying early human development and organogenesis.[35]

## 1.4 Poly(Acrylic Acid) Hydrogels

PAA is a highly ionic, hydrophilic polymer with a structure containing anionic groups.[36] Hydrogel networks of PAA have the ability to absorb many times their weight in water, and are consequently part of a class of materials called super absorbents. The ability to swell so extensively is facilitated by the carboxylic acid groups on the polymer backbone, which strongly associate with water molecules. These groups are readily ionisable and

upon ionisation polymer chains extend due to increased repulsion between carboxylic acid groups.[37] Consequently, PAA is a stimuli responsive gel that will reversibly swell/ deswell according to surrounding conditions, such as pH and ionic strength.[36] The high density of carboxyl groups within PAA enables the formation of intermolecular interactions, such as hydrogen bonds, electrostatic interactions, and dipole-dipole interactions, with other surfaces and molecules.[38] Furthermore, PAA has superior cytocompatibility and good thin film formation properties. All of these factors confer PAA great potential to be deployed in emerging fields such as tissue engineering, protein immobilisation, biosensors and biomedical devices.[36]

Owing to their excellent bioadhesion and strong anionic charge, PAA hydrogels are very common mucoadhesives, which are often used in topical and oral drug delivery.[25,26,39] These polymers are often known under trade names such as Carbopol, Carbomer, Polycarbophil and Noveon, and they typically comprise PAA cross-linked with various vinyl cross-linkers.[40] Due to the fact that PAA has pH-responsive behaviour with a varying swelling ratio depending on the pH environment, it has established applications in the area of pH-sensitive site-specific drug release. As an example, Huang *et al.* used a ketoprofen-loaded PAA hydrogel derivative, which upon delivery into the gastrointestinal tract, swells-up and releases the encapsulated drug. The high-water solubility of PAA has limited its applications in drug delivery to some extent, due to dissolution of the material before the drug can be released. As a result, PAA is often crosslinked with organic cross-linkers to form copolymers and interpenetrating networks.[38]

A further application of PAA hydrogels is in surface coatings and surface modifications for biomedical devices. Giglio *et al.* synthesised a PAA coating on titanium substrates as

a means of enhancing the biocompatibility of the surface. The intention was to produce a versatile surface coating for titanium-based orthopaedic implants that acts as both an effective anti-corrosion barrier and an effective bioactive surface.[41] Furthermore, Lee *et al.* combined graft polymerization with photolithography in order to produce well-defined PAA micropatterned surface layers on the surface of a PEG protein-repellent hydrogel. This was to enable covalent immobilisation of proteins, such as collagen, to the surface areas containing the PAA layer.[42]

Another area in which PAA hydrogels are commonly used, is in microdevice and sensor applications. One such application has been a miniature optical pH sensor, in which, using a novel 3D stereolithography-based micropatterning technology, Yin *et al.* patterned the PAA hydrogel into periodic micropads along an optical fibre.[36] With this device, changes in pH result in a distinctive swelling change, and a subsequent change in optical signal which can be measured.[36]

## 1.5 Bioadhesives for Soft Tissue Adhesion

Bioadhesives are commonly used for wound management and hemostasis, and are increasingly emerging in other applications such as tissue engineering and regeneration.[1] Soft tissue adhesion is a very complex process which involves non-specific interactions, interpenetration of polymer networks and soft tissue interfaces, and molecular coupling.[1,2] Typically, after bringing a polymer into contact with a soft tissue, initial physical entanglement is followed by secondary bonding. This secondary bonding can be in the form of either covalent bonds or multiple weak non-covalent bonds, such as hydrogen bonds, electrostatic interactions and Van der Waals

interactions.[15,43] Figure 1.2 gives examples of some of the common chemical and physical interactions that can form between hydrogels/bioadhesives and soft tissues.[3]

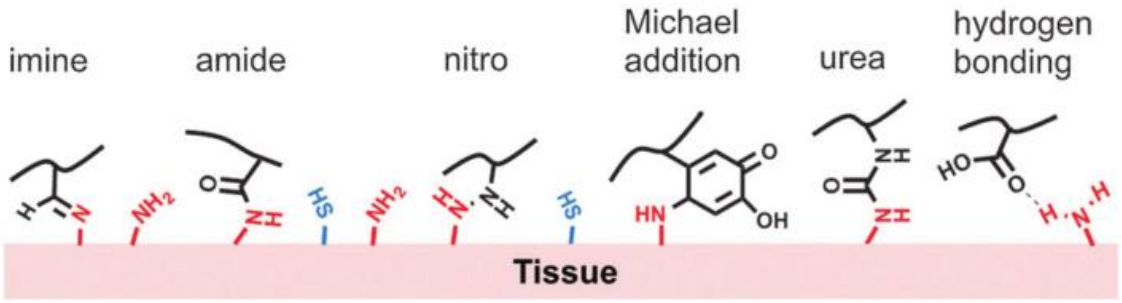


**Figure 1.2.** Examples of chemical/physical linkages formed between hydrogels/bioadhesives and surrounding tissues. Figure taken from Ghobril *et al.*[3]

Tissue adhesion is further complicated by the secretion of biomacromolecules from cells constituting the corresponding soft tissues. For example, salivary glands in the oral mucosa secrete mucins, a variety of antimicrobial substances, salts, water, and intestinal proteins that modulate mucosal adhesion. Hence, mucoadhesives must adhere to the moist surface of the oral mucosa whilst resisting the flushing action of the saliva and competition with associated biomacromolecules.[44,45] In applications as mucoadhesives, polymers such as carboxymethyl cellulose (CMC) and PAA have been shown to be particularly effective, due to the presence of hydrogen-bonding functional groups.[26,46] Overall, the mechanisms of mucoadhesion are still poorly understood and numerous theories have been proposed to try and explain these mechanisms.[25,26,39]

There are many essential requirements that a bioadhesive must fulfil. One such requirement that poses a considerable clinical challenge is achieving sufficient adhesion to a soft tissue whilst minimising tissue damage. Chemical-based adhesives typically

induce a significant inflammatory response.[47] For example, cyanoacrylate adheres strongly to tissues through an exothermic crosslinking reaction. However, this process releases toxic degradation products such as formaldehyde.[48] Biocompatible adhesives that covalently bond to specific tissues can attain strong levels of adhesion, although these require the presence of surface biomolecules with specific functional groups; as such, the chemistry of these adhesives must be tailored for specific tissue types. Furthermore, adhesives that rely on chemical bonding can be easily fouled in the presence of blood, limiting their use in surgical settings.[47]

Within the human body the mechanical properties of soft tissues vary greatly. Consequently, the mechanical compatibility between soft tissues and bioadhesives is an important consideration.[49] For example, in the application of hydrogels as scaffolds for cardiac tissue engineering,[6,30,31,50] cardiac muscle and blood vessels have distinct elastomeric properties that must be matched for optimum coupling with the tissues.[50,51] The mechanical characteristics of the scaffolds can also have a significant effect on either attached or encapsulated cells. Changes in the isometric tension and stresses within the scaffold are known to result in cells experiencing changes in gene expression as well as morphological alterations.[22]

A further design requirement that should be considered for bioadhesives in the context of tissue sealants is the method of its application to the desired area. It should have appropriate flow characteristics so it can be applied precisely to the desired area, and have the ability to rapidly solidify and bond under physiological conditions. Furthermore, tissue adhesives should maintain the required mechanical properties throughout the healing process and should degrade at an appropriate rate with minimal toxicity.[1,3]

## 1.6 Structure of the Keratinized Gingiva

The oral mucosa is the mucous membrane that lines the inside of the mouth. It can be subdivided further to give the masticatory mucosa, which is found in places including the hard palate and attached gingiva. The oral mucosa consists of stratified squamous epithelium, whereas the area containing the masticatory mucosa consists specifically of keratinized stratified squamous epithelium; these areas are therefore often referred to as the keratinized oral mucosa.[52] The difference between keratinized and non-keratinized surfaces is that the non-keratinized must be kept moist by bodily secretions to prevent them from drying out, whereas keratinized epithelia are protected from abrasion by keratin, a tough resistant protein which contributes greatly to the barrier properties of the epithelium.[53,54]

Epithelial cells can be shaped and arranged in a number of ways within a particular surface layer, forming different types of epithelium layers throughout an organism.[55,56] Squamous epithelial cells have the appearance of thin flat plates which fit closely together in tissues providing a smooth, low-friction surface over which fluids can easily move. Stratified epithelium differs from simple epithelium in that it is multi-layered. Only one layer of the stratified epithelium is in contact with the basement membrane and the other layers adhere to one another to maintain structural integrity. They are found in areas where body linings have to withstand mechanical or chemical degradation, so that layers can be continually stripped off and replaced without exposing the basement membrane.[54,57]

The layers found in the keratinized oral mucosa, from the deepest to the most superficial include: the lamina propria, basement membrane, stratum basale (basal layer), stratum

spinosum (prickle layer), stratum granulosum (granular layer), and the stratum corneum (keratinized layer).[58] This arrangement of structural layers within the masticatory mucosa is illustrated in Figure 1.3. The stratum corneum contains fully cornified keratinocytes that are constantly shed off and replaced. Cornification is the process whereby these living keratinocytes are transformed into dead corneocytes with no nuclei and no organelles. The purpose of this stratum corneum layer is to form a barrier to protect underlying tissues from infection, dehydration, chemicals and mechanical stress. Desquamation, which is the process of cell shedding from the surface of the stratum corneum, balances proliferating keratinocytes that form in the stratum basale.[44,59]

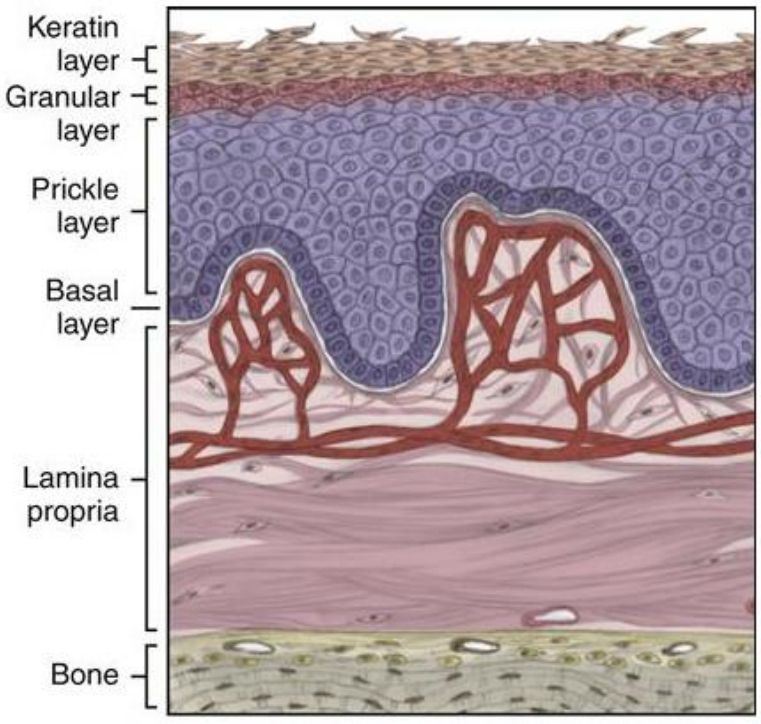


**Figure 1.3.** Illustration of general histological features of the masticatory mucosa. Figure taken from Marieb *et al*.[57]

Differentiating keratinocytes accumulate proteins in the form of keratohyalin granules. One of these proteins is profilaggrin, a high molecular weight histidine-rich highly phosphorylated protein. Towards the end of the differentiation programme for a keratinocyte, profilaggrin is dephosphorylated and proteolytically cleaved into a number of filaggrin units. Filaggrin binds to keratin fibres, causing them to aggregate into dense bundles of keratin that lie parallel to the plane of the epithelium. After the aggregation of the keratin, filaggrin is then broken down into its component amino acids. In addition to these amino acids, the cornified cells also contain a significant amount of lactate, which is a product of anaerobic glycolysis. The presence of the high quantities of lactate and amino acids in these corneocytes results in an extremely high osmolarity, which subsequently removes all of the free water from the intercellular spaces of the stratum corneum. Furthermore, prior to the collapse of the cytoskeleton in cornification, the degradation of the internal organelles results in the release of ionic calcium that had been sequestered by the membrane system.[60]

The keratinized tissue of the oral mucosa is very similar in structure to the skin. There are some differences observed in the morphology of each tissue and also some differences in the behaviour of the keratinocytes from these two sites. One significant difference is that, compared with skin wounds, oral mucosal wounds heal faster, with less inflammation, and with minimal to no scar formation. Turabelidze *et al.* demonstrated that these differences were reflected by differences in the gene expression profiles between oral and skin keratinocytes.[61] Further differences between the skin and oral mucosa include the requirement that the oral mucosa must have a continually moist surface and also that it has an absence of structures such as hair follicles, sebaceous gland and sweat glands.[44,61]

The oral mucosa is formed from many cell types which are attached to each other as well as to the extracellular matrix by junctional complexes. These contact points are highly specialised structures accommodating a number of different interactions that have a profound effect on cellular biology. For example, they mediate the adhesion of cells to one another and also help in forming communication channels that allow the passage of signals and metabolites between cells. They are responsible for a number of features of the cells within epithelium tissues, including their shape, position, differentiation, metabolism, proliferation, and morphogenesis. Within the oral mucosa, the proteins responsible for these interactions are well characterised and are known collectively as cell adhesion molecules (CAM); they include integrins, cadherins, catenins and lamins.[62]

Desmosomes are a type of junctional complex that are specialised for cell-to-cell adhesion. They serve as anchoring sites for intermediate filaments and assist in forming a structural framework. Consequently, they are partly responsible for giving tissues their resistance to tensile deformation. Desmogleins 1 and 3, which are component glycoproteins of desmosomes, are found exclusively in the oral epithelium. These can be observed throughout the stratum granulosum all the way to the stratum basale. These proteins are a member of the cadherin family of cell adhesion molecules. Integrins also have a unique role in cell adhesion and are involved in coupling the ECM to the intracellular cytoskeleton network. Integrins are responsible for intracellular cell signalling and are activated through ligand binding or via intracellular processes. Focal adhesions are the sites where integrin mediated adhesion links the ECM to the cytoskeleton of interacting cells. Focal adhesions are multi-protein structures where

multiple interactions occur. Some of the adhesion molecules that may be found here include focal adhesion kinase, talin, paxillin, calpain and vinculin.[62,63]

The oral mucosa contains minor salivary glands concentrated in the submucosa and connected to the mucosal surface via small ducts. The salivary glands maintain a controlled oral environment with a moist surface containing mucins, a variety of antimicrobial substances, salts, water, epidermal growth factor and intestinal proteins. Continual secretions of saliva cover the oral cavity with a salivary film that maintains a slightly acidic pH within the oral environment.[44,45] This salivary coating has been estimated to be around 70 to 100 μm thick.[45] Mucins are a family of high molecular weight glycosylated proteins contained within this salivary layer. More specifically, this layer contains a mucin named MG1, which binds to the oral mucosa and has many functions, including maintaining hydration, providing lubrication, concentrating protective molecules and limiting the attachment of microorganisms. In addition, histatins, which are small histidine rich polypeptides with antifungal activity, are found in saliva. Agglutinin, or salivary agglutinin (SAG), is one of the more abundant antimicrobial substances present in the human saliva. SAG is a glycosylated protein whose function is to aggregate bacteria and viruses in order to promote their clearance from the oral cavity.[44,45,64]

## 1.7 Structure of the Epicardium

The heart and proximal portions of the major vessels are contained within a sac called the pericardium (see Figure 1.4). The pericardium provides mechanical protection to the heart and protection from infection.[65] The parietal pericardium comprises a fibrous sac

with a serosal lining of mesothelial cells on the inside. Adjacent to this is the visceral pericardium, otherwise known as the epicardium. This is a continuous layer of mesothelial cells which surrounds the entire outermost surface of the heart, under which the myocardium lies. The void between these two surfaces, known as the pericardial cavity, contains serous fluid which lubricates the surface of the heart.[65,66]

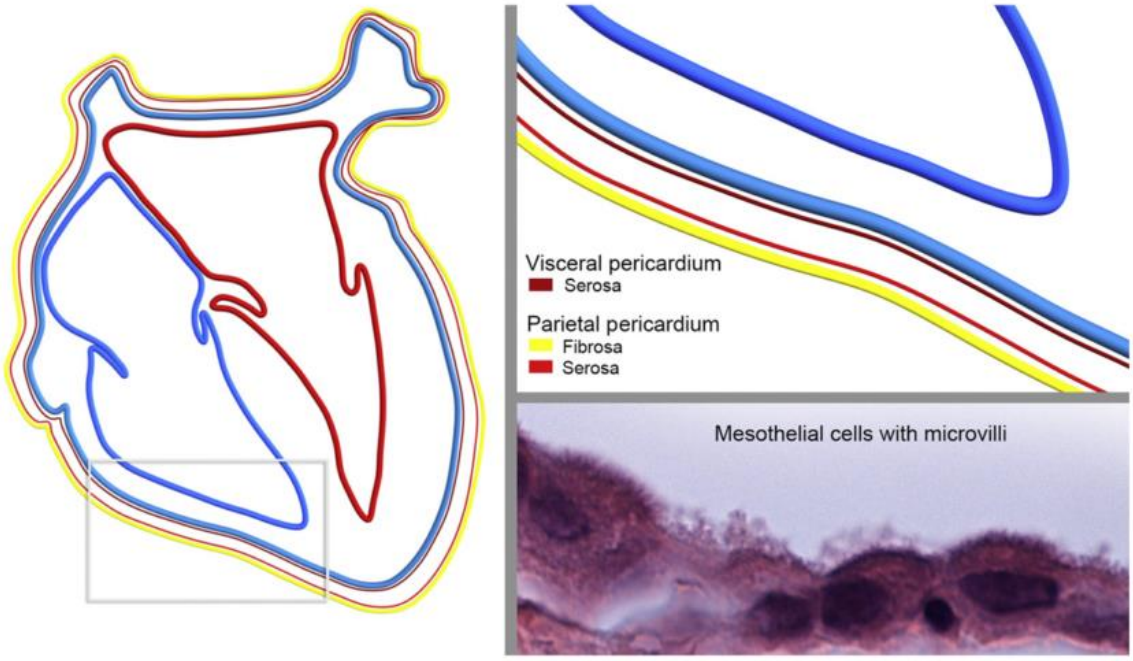


**Figure 1.4.** Parietal vs. visceral pericardium. The pericardium has a parietal and a visceral component. The parietal pericardium is composed of two layers: a serosal lining (thin red line) and a fibrous sac (thicker yellow line). The visceral pericardium (or epicardium) is shown as a thin brown line overlying the myocardium in blue. The serosal lining of the parietal and visceral pericardium is a continuous layer of mesothelial cells and the space between the two opposing layers is the pericardial cavity. The light micrograph shows a high magnification close up of mesothelial cells with distinct microvilli facing the pericardial cavity. These microvilli increase the surface area for production and reabsorption of normal pericardial fluid (×800, H&E). Figure taken from Rodriguez *et al*.[65]

Figure 1.5 shows an optical microscope image (x 200) displaying a cross section of the epicardium and underlying layers. The uppermost layer is the serosal component

comprised of mesothelial cells. Below this is a thin layer of fibrous tissue, comprised of elastic lamellae, that separates the mesothelial cells from the cardiac myocytes below. In areas of the heart with adipose tissue, such as the interventricular and atrioventricular grooves or around the coronary vessels, the elastic lamellae occupies are more substantial area between the mesothelial cells and myocardium. Blood vessels, lymphatic vessels and nerves that supply the heart are all found in the subepicardial layers.[65]

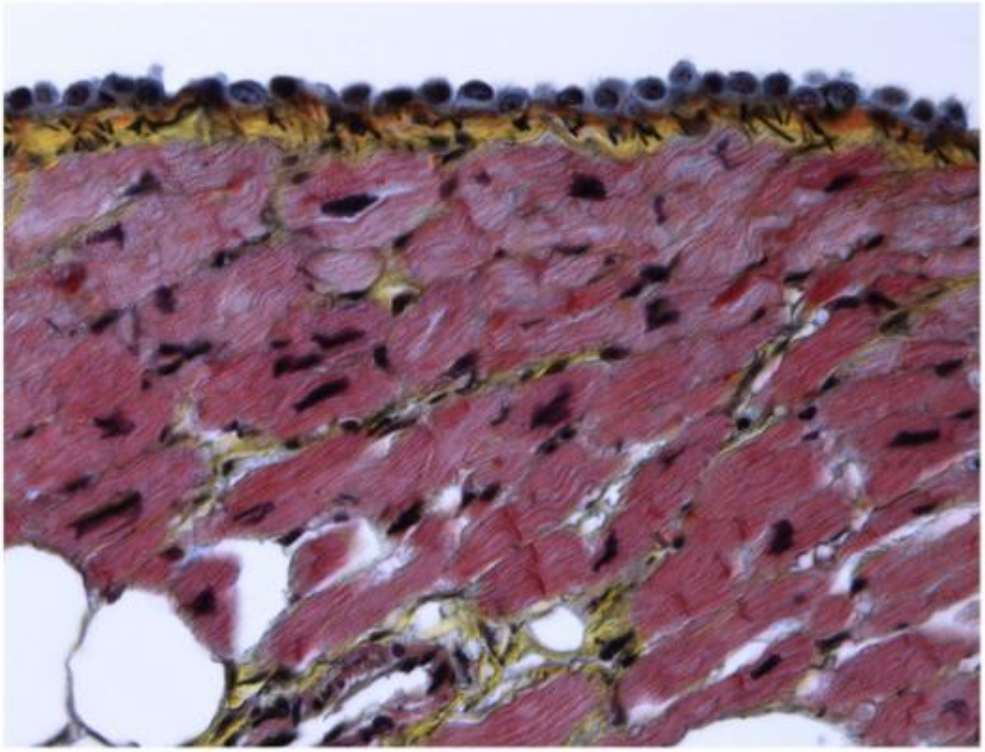

**Figure 1.5.** Microscope image of the human visceral pericardium, or epicardium (x 200). This image comprises mesothelial cells (grey blue cytoplasm), fibrous tissue (yellow), cardiac myocytes (red sarcoplasm) and elastic lamellae (black lines). Figure taken from Rodriguez *et al*.[65]

## 1.8 Summary and Project Overview

The two main objectives of this project are as follows:

1) To synthesise PAA-based biomaterials which effectively bond to soft tissue, specifically the oral mucosa and epicardium.
2) To correlate the bonding performance to the chemical design of the PAA derivatives through the characterisation and quantification of molecular binding events and macroscopic adhesion properties.

The gingiva was selected as one of the soft tissue types to study within the project as it was a line of research that was of interest to my industrial PhD sponsors, GlakoSmithKline. The epicardium was selected as it is a membrane to which adhesion is particularly relevant for epicardial placement strategies, an area of interest within my PhD supervisor's research group. Furthermore, it was also thought that these two soft tissue types would make for an interesting comparison due to their contrasting mechanical properties.

With regards to the organisation of this thesis, Chapter 2 will present the investigation of different strategies for the functionalisation of PAA. These strategies will include the functionalisation of carboxyl groups with amine moieties and bromoalkenes, as well as the use of thiol-ene chemistry to further functionalise these materials. The ultimate aim is to produce materials functionalised with either an alkene, boronic acid, hydroxyl or thiol-end group. The exploration of these different functionalisation strategies will enable the generation of hydrogels, through the formation of crosslinks (physical and chemical) between functional groups on the polymer backbone. The synthesis and characterisation of these PAA hydrogels will be the focus of Chapter 5.

Chapter 3 will focus on the chemistry associated with the generation of polymer brush layers. Within Chapter 4, these polymer brushes will then be utilised through colloidal probe force microscopy, in order to investigate the nanoscale interactions between polymers and cells/tissues. Chapter 5 will then investigate the adhesive interactions between the synthesised PAA hydrogels and cells/tissues through macroscale testing methods. Overall, this thesis is organised such that Chapter 4 collates the work on the characterisation of material properties at the nano/microscale, and Chapter 5 collates the work on characterisation at the macroscale.

# CHAPTER 2

## Functionalisation Strategies for Poly(Acrylic Acid)

# 2.1 Introduction

The aim of this to chapter is to investigate the functionalisation of poly(acrylic acid) (PAA) with a variety of different moieties; these include either an alkene, boronic acid, hydroxyl or thiol-end group. Initially, a literature review and discussion of the advantages and disadvantages of some of the common functionalisation routes was undertaken. Next, amine conjugation via Steglich esterification and DMTMM was experimentally investigated. Functionalisation via conjugation with a bromine moiety was then explored followed by functionalisation via thiol-ene chemistry. In each case, functionalisation was quantified by $^{1}$H NMR and additional characterisation was obtained by FTIR.

One of the purposes of this work is to enable the synthesis of materials that can form gels that crosslink via physical bonds, or through visible light or UV initiation. In addition, the formation of hydrogels with good bioadhesion to cells and tissues is of interest. The formation and characterisation of these gels and bioadhesives, from functionalised PAA, will be investigated in depth in Chapter 5.

## 2.1.1 Functionalisation with Amine Moieties

The presence of carboxyl groups in PAA enables direct binding to amines through a couple of very well-known methods; these methods include EDC/NHS conjugation and Steglich esterification, and these will both be discussed in the next few paragraphs. These well characterised methods enable PAA to be conjugated with amine derivatized molecules such as aminophenyl boronic acids. Ethyl(dimethylaminopropyl) carbodiimide (EDC) and *N*-Hydroxysuccinimide (NHS) reactions work through the

activation of the carboxyl group to directly react with the primary amine via a covalent amide bond. It is a very well-known method in areas such as peptide synthesis and various other biomolecular conjugations. Some of the merits of this approach include: the mild reaction conditions, high conversion efficiency, little influence on bioactivity of target molecules, clean reaction products, and solubility in water for aqueous coupling.[67]

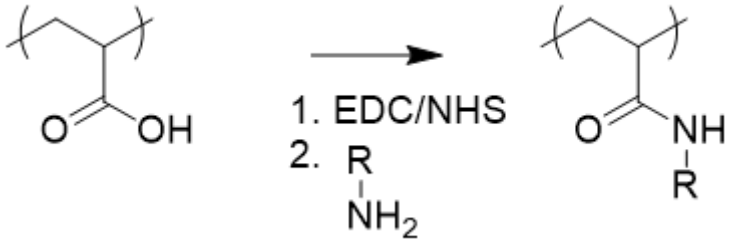


**Figure 2.1.** Synthetic strategy for the conjugation of PAA to an amine. EDC/NHS coupling activates the carboxylic acid (1) in preparation for direct conjugation to primary amines (-$RNH_2$) via amide bonds (2).

Figure 2.1 shows a simple representation of EDC/NHS coupling for the functionalisation of PAA. EDC works through reacting with the carboxylic acid groups to form an active but unstable O-acylisourea intermediate. This intermediate is easily displaced by nucleophilic attack from the primary amine. If this occurs, the primary amine forms an amide bond with the original carboxyl group and an EDC by-product will be released as a soluble urea derivative. NHS, or the water soluble sulfo-NHS, are often included in EDC coupling in order to improve the efficiency of the reaction. This works due to the fact that EDC couples NHS to the carboxyl groups, forming an active NHS ester that is considerably more stable than the O-acylisourea intermediate. The primary amine will

again displace this intermediate, forming an amide bond with the original carboxyl group.[67–69]

The EDC/NHS reaction is most efficient in slightly acidic conditions. However, effective conjugation will still be possible at physiological pH.[68] A molar ratio of EDC to NHS of 1:2 is widely used in these reactions as this has been determined as the optimum ratio for activation of the carboxyl groups.[67] If these optimal conditions are not met then there may be increased hydrolysis of the reactive intermediate. This is an unwanted side-reaction that can limit the reactions occuring between the primary amine and the reactive intermediate.[69] There are many examples from the literature for the functionalisation of free PAA through EDC/NHS coupling.[67,70] In addition to PAA, other carboxylic acid terminated polymers, such as hyaluronic acid (HA),[71] have been functionalised through this approach.

The activation of carboxyl groups with EDC/NHS is a standard and very well-established method for amine ligation. Recent papers have focussed on the use of 4-(4,6-dimethoxy-1,3,5-triazin-2-yl)-4-methylmorpholinium chloride (DMTMM) as an alternative to EDC/NHS coupling for ligation of amines to Hyaluronan.[72–74] Systematic comparisons between the two methods suggest that DMTMM is overall more efficient; it does not require such accurate control over the pH in order to be effective[74] and DMTMM is stable and soluble in water for significantly greater periods of time.[75,76] In addition, studies by Thompson *et al.*[77] and Pelet *et al.*[78] have used DMTMM reactions for the derivatization of PAA with high levels of success. As a result, DMTMM-mediated ligation is a new promising tool for the synthesis of polymer derivatives for biomedical and pharmaceutical applications. DMTMM-mediated conjugation proceeds through

aromatic substitution by the carboxyl groups, forming an intermediate that is reactive towards amines (Figure 2.2).[74,77]

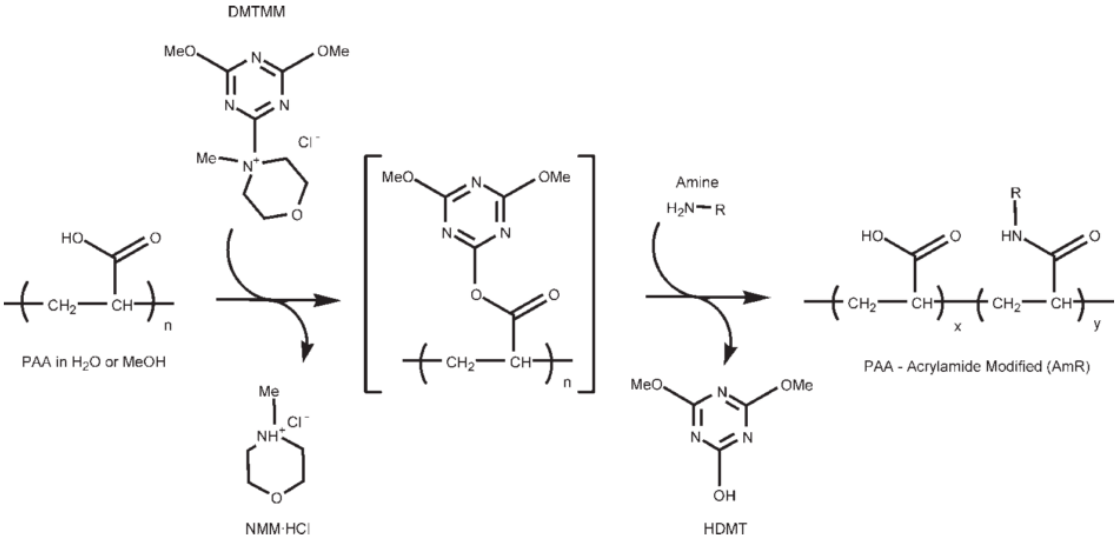


**Figure 2.2.** Conjugation of PAA with an amine via DMTMM-mediated ligation. Figure taken from Thompson *et al.*[77]

Steglich esterification is another method for conjugating a carboxyl group to a primary amine. It utilises the chemical dicyclohexylcarbodiimide (DCC) as the coupling reagent and 4-dimethylaminopyridine (DMAP) as the catalyst. DCC achieves conjugation of the carboxyl group and amine in a similar manner as EDC. However, one major difference is the fact that DCC is not aqueous-soluble.[77] DMAP is used in the reaction to increase the final yield of amine conjugation. This is achieved as DMAP prevents a side-reaction which would otherwise cause the O-acylisourea intermediate to convert to N-acylurea, and this product would be unable to further react with the primary amine.[79] An undesirable by-product of the DCC reaction is the formation of the urea compound dicyclohexylurea.

This can often present difficulties as it is mostly insoluble and is difficult to completely remove from the sample.[80]

In general, functionalisation of a polymer through EDC coupling compared with DCC has several disadvantages. Firstly, EDC is significantly more expensive than DCC. Furthermore, the O-acylurea intermediate is optimally formed at pH 4-5 and at this pH range many amines are protonated and unreactive.[77] However, in the case of PAA functionalisation through DCC/DMAP coupling, solubility is one of the main concerns. PAA is best dissolved in aqueous or hydrophilic media and amines that are often used for conjugation tend to be water soluble. As such, very few papers reporting the functionalisation of PAA through DCC/DMAP could be found.[81,82]

### 2.1.2 Functionalisation via Thiol-Ene Chemistry

The introduction of an alkene into the structure of a material allows the use of the well-established thiol-ene reactions. The thiol-ene reaction, otherwise known as alkene hydrothiolation, is an organic reaction between a thiol and an alkene to form an alkyl sulfide. Due to the reaction's high yield, high rate, stereoselectivity and thermodynamic driving force, the reaction is defined as a click chemistry reaction.[83,84] In addition, due to the high efficiency and orthogonality of the reaction, thiol-ene chemistry is increasingly being used in polymer functionalisation, as well as in macromolecular synthesis; examples include the generation of protein patterns,[85] or the design of dynamic micropatterned substrates which allow spatial and temporal control over cell adhesion and migration.[86]

Further advantages for the use of thiol-ene chemistry in polymer synthesis include: tolerance to many different reaction conditions, clearly defined reaction pathways, and simple synthetic strategies from a range of easily obtainable starting materials.[87] Furthermore, oxygen and water inhibition are typically known to prevent conventional radical reactions, but in most cases these will not be an issue in thiol−ene reactions.[88] Thiol-ene reactions have been utilised in many different applications; Chen *et al.* demonstrated the controlled binding and release of thiol-functionalised PAA from substrates for applications in drug delivery and marine antifouling.[89] Moreover, Gargari *et al.* investigated the interaction between methacrylate-functionalised nanoparticles and thiol-terminated PAA, for use in sensor and indicator applications.[90]

Thiol-ene reactions are known to proceed through two different mechanisms: free radical additions (Figure 2.3) and catalyzed Michael additions. The free radical additions are often more advantageous due to the fact that the step growth and chain growth processes can be effectively used to form homogenous polymer networks. In addition, these reactions can be initiated by light, heat, or radical initiators.[83,84] This ability of the reaction to be readily photo initiated allows precise spatial and temporal control over where the reaction can occur.[91] Some of the conditions that determine the efficiency of thiol-ene reactions include the pH of the environment, the $pK_a$ or charge of the thiols to be coupled, and the local structure of the alkene. Thiol-ene coupling to polymers generally works best in the acidic to neutral pH. In basic conditions polymers are inactivated due to the formation of a thiolate ion that prevents the thiol from being able to receive a radical.[85,88] In contrast, Michael additions typically require activated alkenes (substituted with an electron accepting group), which may restrict their synthetic accessibility or stability. Furthermore, they are typically less specific than thiol-ene

radical couplings as amines can also sustain Michael additions. Advantages of Michael additions include their ability to proceed at neutral pH relatively easily and the fact that additional reagents are not required (only the thiol and alkene).[85,88]

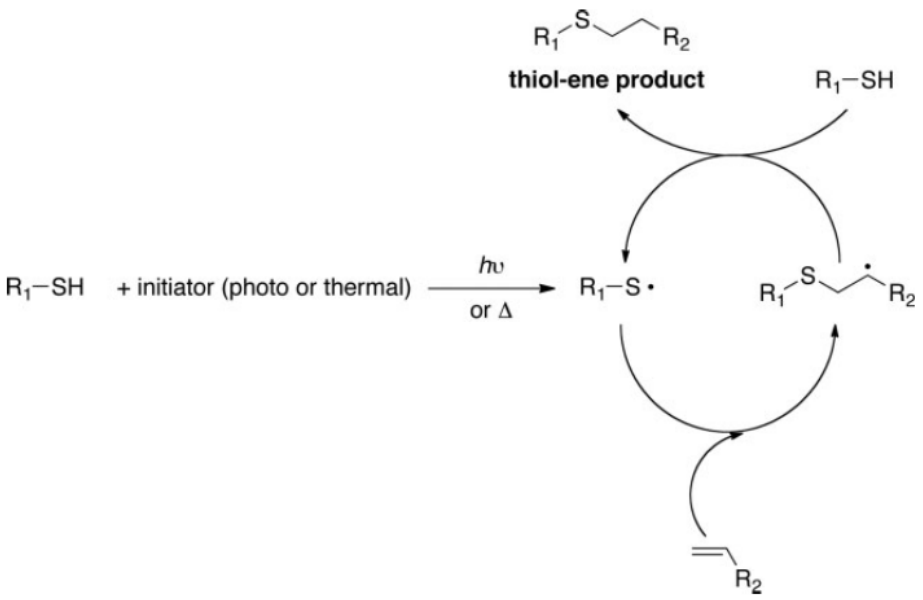


**Figure 2.3.** Mechanism of free-radical thiol-ene coupling. Figure taken from Kade *et al.*[87]

## 2.1.3 Characterisation Methods

Two characterisation methods which will be relied upon heavily in this chapter are Nuclear magnetic resonance (NMR) and Fourier transform infrared spectroscopy (FTIR). NMR is a method in which nuclei are placed within a weak oscillating magnetic field causing them to respond by producing an electromagnetic signal with a frequency that is characteristic of the magnetic field at the nucleus. An instrument consists of three main parts: a high strength magnet producing a uniform magnetic field, a stable oscillator creating a high-frequency alternating magnetic field, and an electronic device to detect the absorption of energy of radio-frequency radiation by the sample.[92,93]

When an isolated atom is placed in a magnetic field the electrons will precess about the direction of the field. In accordance with the laws of electromagnetic induction these currents induce a magnetic field in the opposite direction. As a result, an external field acts upon the nucleus, which is reduced relative to what would have acted in the absence of the electron shell. The shift in the resonance signal of the nuclei, as a result of the electronic environment, is called the chemical shift. The chemical shift is measured in relative units of parts per million (ppm) of the applied field. It is affected significantly by external factors, notably the nature of the solvent and the concentration of the solution. The most common solvent used is carbon tetrachloride since it contains no protons and therefore will not produce any peaks across the whole range of the spectrum. Other solvents can be used if the hydrogen atoms are replaced by their isotope, deuterium.[92,93]

NMR is utilised in numerous applications. It is extensively used in medical diagnosis in the form of magnetic resonance imaging (MRI). Chemists can study the peaks of nuclear magnetic resonance spectra to unambiguously determine the structure of known and novel compounds. As such, it is usually required within scientific journals to confirm the identity of novel synthesised compounds.[94] Furthermore, it is commonly used within the food industry to prove the authenticity of ingredients and to ensure local and international certification standards are met.[95] NMR is also used in the petroleum industry to identify potential sources of petroleum and natural gas. The equipment can be lowered into a drilled borehole to identify features such as rock porosity and identify pore fluids (water, oil and gas).[96]

FTIR is a technique which is used to obtain an infrared spectrum of emission or absorption for a solid, liquid or gas. A commonly used mode is attenuated total

reflectance (ATR) which enables functional groups present across a sample depth of approximately 1 mm to be identified. During analysis, an infrared ray arrives at a crystal which is placed in contact with the sample. Total internal reflection within the crystal gives rise to an evanescent wave which penetrates through the sample at each reflection. Curves of absorbance versus wavelength are obtained with absorption peaks characteristic of the functional groups present at the membrane surface.[97] FTIR-ATR is a non-destructive testing method which is regularly used accross organic chemistry. One application is in the characterisation of modified surfaces where spectral bands characteristic of the new functional groups can be identified.[98] Additionally, this method can be used to analyse the adsorption of macromolecules at a membrane surface and to determine whether the conformation of these adsorbed molecules has been modified.[97,99]

The use of NMR and FTIR for investigating organic compounds are both similar techniques which supplement each other significantly. Some differences include, that while NMR records magnetic nuclei (mainly for protons), FTIR records bonds between atoms. Since a molecule contains comparatively few magnetic nuclei, NMR spectra are usually simpler to interpret. A further important difference to note is the fact that high-resolution NMR is only possible with the use of liquid samples of low viscosity, whereas FTIR can be used with solid samples.[92]

## 2.2 Materials and Methods

Figure 2.4 summarises the different materials generated in Chapter 2 and the different functionalisation methods used to synthesise them. These methods include amine conjugation via Steglich esterification and DMTMM, as well as functionalisation with a bromine moiety via nucleophilic substitution. Further functionalisations were also obtained via thiol-ene reactions with alkene terminated PAA, and these are also discussed within this Chapter.

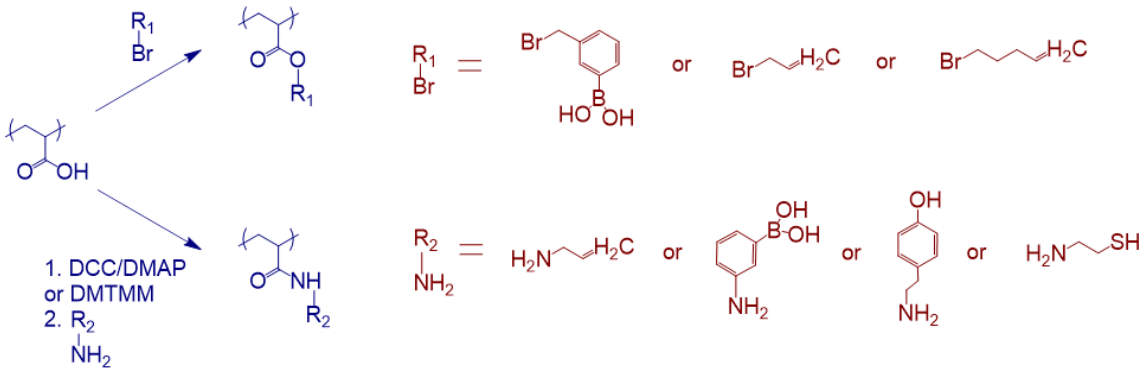


**Figure 2.4.** The different strategies used for the functionalisation of PAA.

### 2.2.1 Chemicals and Materials

Poly(acrylic acid) (PAA, $M_W$ = 450000), poly(acrylic acid, sodium salt) solution (PAA, $M_W$ = 15000, 35 wt. % in $H_2O$), allylamine (98%), 3-aminophenylboronic acid hydrochloride (98%), tyramine hydrochloride (≥98%), allyl bromide (99%), 3-(bromomethyl)phenylboronic acid (90%), 5-bromo-1-pentene (95%), *N*-acetyl-L-cysteine (≥99%), 4-mercaptophenylboronic acid (90%), cystamine dihydrochloride (≥98%), DL-dithiothreitol (≥98%), methanol (99.9%), diethyl ether (99%), 2-hydroxy-4'-

(2-hydroxyethoxy)-2-methylpropiophenone (Irgacure 2959, 98%), deuterium oxide ($D_2O$, 99.9 atom % D), deuterium chloride solution (DCl, 35 wt. % in $D_2O$, ≥99 atom % D), sodium deuteroxide (NaOD, 40 wt. % in $D_2O$, 99 atom % D), anhydrous dimethylformamide (99.8%), dimethyl sulfoxide-$d_6$ (DMSO-$d_6$, 99.9 atom % D), *N,N'*-dicyclohexylcarbodiimide (DCC, 99%) and 4-(dimethylamino)pyridine (DMAP, ≥99%) were purchased from Sigma-Aldrich and used as received. Cellulose ester dialysis membranes ($M_W$ = 3.5-5 kDa) were purchased from Spectrum Laboratories Inc. 4-(4,6-dimethoxy-1,3,5-triazin-2-yl)-4-methylmorpholinium chloride (DMTMM, >98%) was purchased from Tokyo Chemical Industry UK Ltd. Dimethylformamide (DMF, ≥99.9%) was purchased from VWR Chemicals. Chloroform-D ($CDCl_3$, 99.8%) was purchased from Cambridge Isotope Laboratories Inc.

## 2.2.2 Instrumentation

The UV light source used was an Omnicure series 1500 lamp. An ILT 1400-A radiometer photometer from International Light Technologies Inc. was used to measure UV light intensities. Fourier Transform Infrared–Attenuated Total Reflectance Spectroscopy (ATR-FTIR) was carried out using a Bruker Tensor 27 with an MCT detector (liquid $N_2$ cooled). Spectra were acquired at a resolution of 4 $cm^{-1}$ with a total of 256 scans per run. Nitrogen was run through the system during measurements in order to limit the effects of environmental fluctuations. $^1H$ NMR spectra were obtained using Bruker's 400 MHz spectrometers (Bruker AV 400 and AVIII 400) and data was analysed using Bruker's IconNMR software.

### 2.2.3 Functionalisation via Steglich Esterification

Steglich esterification was one of the routes investigated for the conjugation of primary amines to the carboxyl groups of PAA. For functionalisation of PAA (450000 g/mol) with allylamine, PAA (125 mg, 1.74 mmol) was initially dissolved in anhydrous DMF (3 mL) under a positive argon pressure, followed by the addition of DCC (360 mg, 1.74 mmol) and DMAP (210 mg, 1.74 mmol). Once these were mixed, allylamine (49.2 mg, 864 µmol) was added and the solution was left overnight at room temperature under a positive argon pressure. These conditions equate to molar equivalences of 0.5:1:1 for amine: DCC/DMAP:PAA. Next, the solution was precipitated in diethyl ether three times, each time from DMF, and the polymer was collected under vacuum filtration and left under reduced pressure to fully dry.

For functionalisation of PAA (450000 g/mol) with boronic acid, a protocol very similar to that of allylamine was used. Briefly, PAA (125 mg, 1.74 mmol), DCC (360 mg, 1.74 mmol) and DMAP (210 mg, 1.74 mmol) were dissolved in anhydrous DMF (3 mL) under a positive argon pressure. Following this step, 3-aminophenylboronic acid (150 mg, 864 µmol) was added and the solution was left overnight at room temperature under a positive argon pressure. The solution was precipitated in diethyl ether three times, each time from DMF, and then collected under vacuum filtration and left under reduced pressure to fully dry. The molar equivalences used in this case were 0.5:1:1 for amine:DCC/DMAP:PAA. However, under these conditions the resulting polymer did not re-dissolve for NMR analysis. The amine to polymer equivalence was reduced as low as 0.05:1, but the polymer was still not dissolvable. As such, the polymer structure was confirmed though FTIR spectroscopy alone.

## 2.2.4 Functionalisation using DMTMM Conjugation

The conjugation of PAA with an amine was obtained using a DMTMM conjugation procedure adapted from the literature.[72,73] For functionalisation of PAA (450000 g/mol) with tyramine, PAA (1.5 g, 20.8 mmol) was initially dissolved in deionized water (30 mL). The pH of the solution was adjusted to pH 5.5 using 2 M NaOH following which DMTMM (2.857 g, 10.4 mmol) was added and left to dissolve. Tyramine hydrochloride (1.429 g, 8.26 mmol) was dissolved separately in deionized water (20 mL) and the pH of this solution was adjusted to pH 5.5 using 50 mM NaOH. This solution was then added dropwise to the polymer solution, which was then left at 37˚C for 24 hours. The conditions used equate to molar equivalences of 0.4:0.5:1 for tyramine:DMTMM:PAA.

The cooled reaction mixture was then precipitated in acetone three times, re-dissolving the resulting material in deionised water each time, and the polymer was left for several days to dry under reduced pressure. After drying, the polymer was re-dissolved in deionized water (25 mL) and then dialyzed in a solution of 150 mM NaCl for two days, whilst changing the dialysis solution at least 3 times a day. Next, the polymer was dialyzed in deionized water for a further two days, whilst again changing the dialysis solution at least three times a day. Following dialysis the resulting polymer was frozen in liquid nitrogen and freeze dried for one to two days until fully dry.

For functionalisation of PAA (450000 g/mol) with cysteamine, PAA (300 mg, 4.17 mmol) was initially dissolved in deionized water (6 mL). The pH of the solution was adjusted to pH 5.5 using 5 M NaOH, following which DMTMM (572 mg, 2.07 mmol) was added and left to dissolve. Cystamine dihydrochloride (466 mg, 2.07 mmol) was dissolved separately in deionized water (4 mL) and the pH of the resulting solution was adjusted

to pH 5.5 using 50 mM NaOH. This solution was then added dropwise to the polymer solution and left at 37˚C overnight.

After being left overnight, the pH of the polymer solution was changed to pH 9 using a solution of 5 M NaOH. DTT (424 mg, 2.75 mmol) was dissolved separately in deionized water (5 mL) and the pH of this solution was adjusted to pH 9 using a solution of 500 mM NaOH. This DTT solution was then added dropwise to the polymer solution, which was then left overnight at room temperature. These conditions equate to molar equivalences of 0.5:0.5:1 for cystamine:DMTMM:PAA. Next, the reaction mixture was precipitated in acetone three times, from deionized water, and the polymer was then dried under reduced pressure.

### 2.2.5 Functionalisation with Bromoalkanes

The procedure for the functionalisation of PAA with a bromoalkane, via nucleophilic substitution, was adapted from protocols in the literature that investigated the functionalisation of carboxymethylcellulose (CMC)[100] and poly(dimethylaminoethyl methacrylate) (PDMAEMA).[88] For functionalisation of PAA (450000 g/mol) with allyl bromide, NaOH (104 mg, 2.6 mmol) was initially dissolved in deionized water (2 mL). PAA (250 mg, 3.47 mmol) was then added and the solution was heated to 70˚C. Allyl bromide (75 µL, 86.8 µmol) was dissolved in DMF (0.5 mL) separately and this solution was added dropwise to the polymer solution. The solution was then left overnight at 70˚C. The cooled reaction mixture was precipitated in acetone:diethyl ether (3:1), re-dissolved in deionized water and then precipitated in acetone twice, from deionized water. The polymer was then left for several days to dry under reduced pressure. Molar equivalences of 0.75:0.25:1 for base:alkene:polymer were used in this case. When

higher ratios of alkenes were used, the resulting functionalised polymer would become insoluble following the drying stage.

For functionalisation of PAA (450000 g/mol) with bromo pentene, NaOH (104 mg, 2.6 mmol) was initially dissolved in deionized water (2.63 mL). PAA (250 mg, 3.47 mmol) was then added, following which the solution was heated to 70˚C. 5-bromo-1-pentene (130 mg, 872 µmol) was dissolved in DMF (0.5 mL) separately and this solution was added dropwise to the polymer solution and then left overnight at 70˚C. These conditions equate to molar equivalences of 0.75:0.25:1 for base:alkene:polymer. The cooled reaction mixture was precipitated in acetone:diethyl ether (3:1), re-dissolved in deionized water and then precipitated in acetone twice, from deionized water. The polymer was then left for several days to dry under reduced pressure.

PAA (15000 g/mol) was also functionalised with bromo pentene. Poly(acrylic acid, sodium salt) solution (8.571 mL, 41.7 mmol) was mixed with deionized water (9.429 mL) and then heated to 50˚C. 5-bromo-1-pentene (1.557 g, 10.45 mmol) was separately dissolved in DMF (3 mL) and then added to the polymer solution dropwise. The mixture was then left overnight at 90˚C. These concentrations equate to molar equivalences of 0.25:1 for alkene:polymer. The cooled reaction mixture was precipitated in acetone three times, from deionized water. The polymer was then left for several days to dry under reduced pressure.

For functionalisation of PAA (450000 g/mol) with boronic acid moieties, PAA (3 g, 41.7 mmol) was initially dissolved in a solution of NaOH (1.25 g, 31.25 mmol) and deionised water (31.54 mL), which was then heated to 70˚C. 3-(bromomethyl)phenylboronic acid (2.241 g, 10.43 mmol) was separately dissolved in DMF (6 mL) and then added to the polymer solution dropwise. These conditions equate to molar equivalences of

0.25:0.75:1 for conjugate:base:polymer. The mixture was left at 70˚C overnight. The cooled reaction mixture was precipitated in acetone:diethyl ether (3:1), re-dissolved in deionized water and then precipitated in acetone twice, from deionized water. The polymer was then left for several days to dry under reduced pressure.

### 2.2.6 Functionalisation via Thiol-Ene Chemistry

In order to investigate the parameters impacting thiol-ene chemistry, PAA (450000 g/mol) functionalised with 5-bromo-1-pentene at a level of 5.2% (as quantified via NMR; see Figure 2.14 in the Results and Discussion) was used. First, the polymer was dissolved in $D_2O$ at an alkene concentration of 45 mM. Next, *N*-acetyl-L-cysteine was added at the required concentration and left to dissolve. NMR was used to confirm that the thiol:alkene peak ratio was at the desired level prior to UV initiation; if necessary minor adjustments in the concentrations were made. A stock solution of Irgacure 2959 was prepared in methanol (250 mg/mL). 5 mol% of photoinitiator, relative to the alkene content, was added to the polymer solutions from the stock solution and the pH values were adjusted with the addition of either NaOD or DCl. The lowest pH value investigated was pH 4, as below this the polymer began to precipitate. Samples were then placed in NMR tubes and irradiated with UV (17 mW/cm$^2$, 350−500 nm, power 5.10 J/cm$^2$) for 5 minutes. $^1$H NMR was carried out and reaction conversions were calculated through either the consumption of the alkene peaks or the formation of the thioether product peaks. For each pH value, three NMR repeats were aquired.

For conjugation of PAA (450000 g/mol) to boronic acid, PAA functionalised with allyl bromide was used as the starting material. PAA was functionalised with the alkene at a level of 12.5%, as quantified via NMR (see Figure 2.12 in the Results and Discussion). The

polymer was initially dissolved in deionized water (4 mL) at a concentration of 3% (w/v). 4-mercaptophenylboronic acid (thiol:ene, 1:1) was dissolved separately in DMF (0.75 mL) and then added to the polymer solution. NMR was used to confirm that the thiol:alkene ratio was at the desired level prior to UV initiation; if necessary minor adjustments in the concentrations were made. 5 mol% of the photoinitiator (Irgacure 2959), relative to the alkene content, was added to the polymer solution from the stock solution (250 mg/mL MeOH). The pH was adjusted to pH 6.5 before the sample was irradiated with UV (17 mW/cm$^2$, 350−500 nm, power 5.10 J/cm$^2$) for 5 minutes. Following this, the polymer was precipitated in acetone:diethyl ether (3:1) three times, from deionised water. The polymer was then left for several days to dry under reduced pressure and NMR was carried out on the product.

## 2.3 Results and Discussion

### 2.3.1 Functionalisation with Amine Moieties

Initial functionalisation of PAA focussed on conjugation of primary amines via activation of the carboxyl group. Steglich esterification was used to conjugate 3-aminophenylboronic acid (Figure 2.5). However, due to solubility issues of the resulting product in aqueous solutions, characterisation was only carried out via FTIR. As a result the level of functionalisation could not be quantified. It is thought that the solubility of the final product was perhaps limited by the formation of the reaction by-product dicyclohexylurea and difficulties associated with fully removing this from the final product, as well as potential crosslinks between chains (such as anhydride bonds, although these should hydrolyse with time). In comparison to our work, Levy *et al.* obtained successful functionalisation of PAA with aminophenylboronic acid, except this was through an EDC/NHS-mediated approach.[70]

From the FTIR spectra of PAA (Figure 2.5A), the broad O-H stretch can be seen between approximately 2400 and 3700 $cm^{-1}$. The C-H and C-O stretching bands can be seen at 2970 and 1260 $cm^{-1}$, respectively. The two O-H bending bands can be observed at 800 and 1440 $cm^{-1}$, and the strong C=O stretch is at 1700 $cm^{-1}$.[101,102] The presence of bands for the B-O vibration and the $BO_2$ deformation at 1330 and 700 $cm^{-1}$ respectively confirm the successful conjugation of 3-aminophenylboronic acid with PAA (Figure 2.5B).[103] Furthermore, the additional bands for the C=O stretch associated with the amide (amide bands I and II) can be seen between 1500 and 1700 $cm^{-1}$, for functionalised PAA.[104,105]

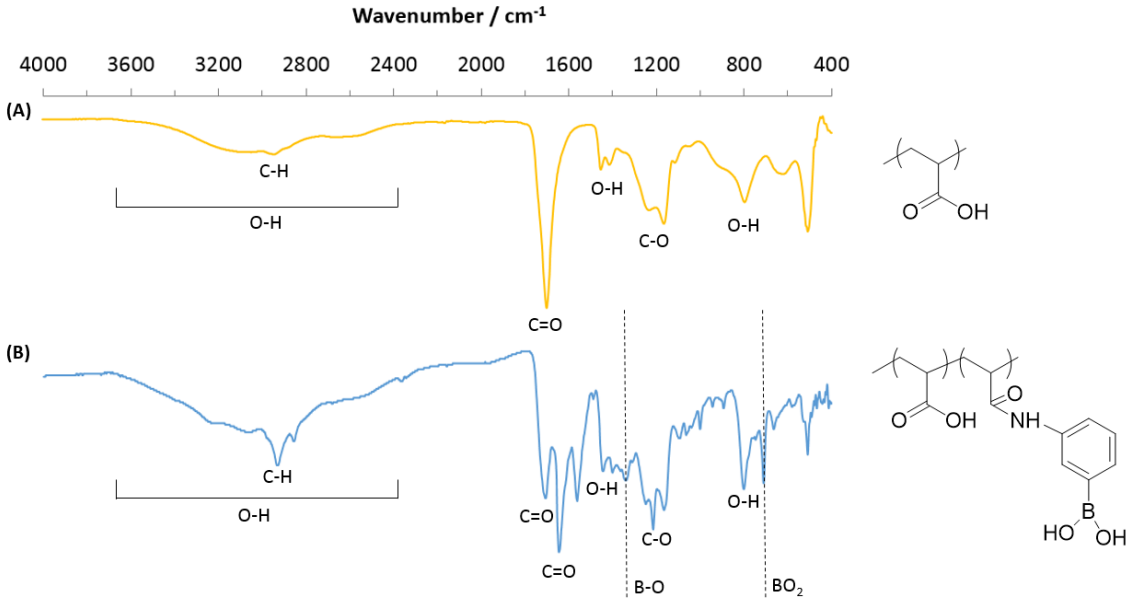


**Figure 2.5.** FTIR spectra of PAA (A) and PAA functionalised with 3-aminophenylboronic acid (B).

PAA was also functionalised with allylamine through a similar DCC/DMAP approach. Figure 2.6 shows the $^{1}$H NMR spectra obtained for the polymer and alkene starting materials, as well as the spectra for the product of the two. Figure 2.6A shows the presence of the peaks for the three protons from the PAA polymer backbone and Figure 2.6C illustrates the presence of the alkene peaks within the final polymer product. Using the ratio of the alkene to polymer backbone peaks, a functionalisation level of 35% was calculated. The FTIR spectra of the product (Figure 2.7) further illustrates the successful conjugation of the alkene through the =C-H bending bands at approximately 950 cm$^{-1}$. In addition, the amide I and II bands are clearly present (between 1500 and 1700 cm$^{-1}$), although their relative intensities (and possibly their exact positions) are shifted compared with the aminophenylboronic acid functionalised polymer (Figure 2.5B). This difference is presumably because the amide is no longer next to an aromatic group, affecting delocalisation of the free doublet of electrons on the nitrogen and the planarity of the amide.

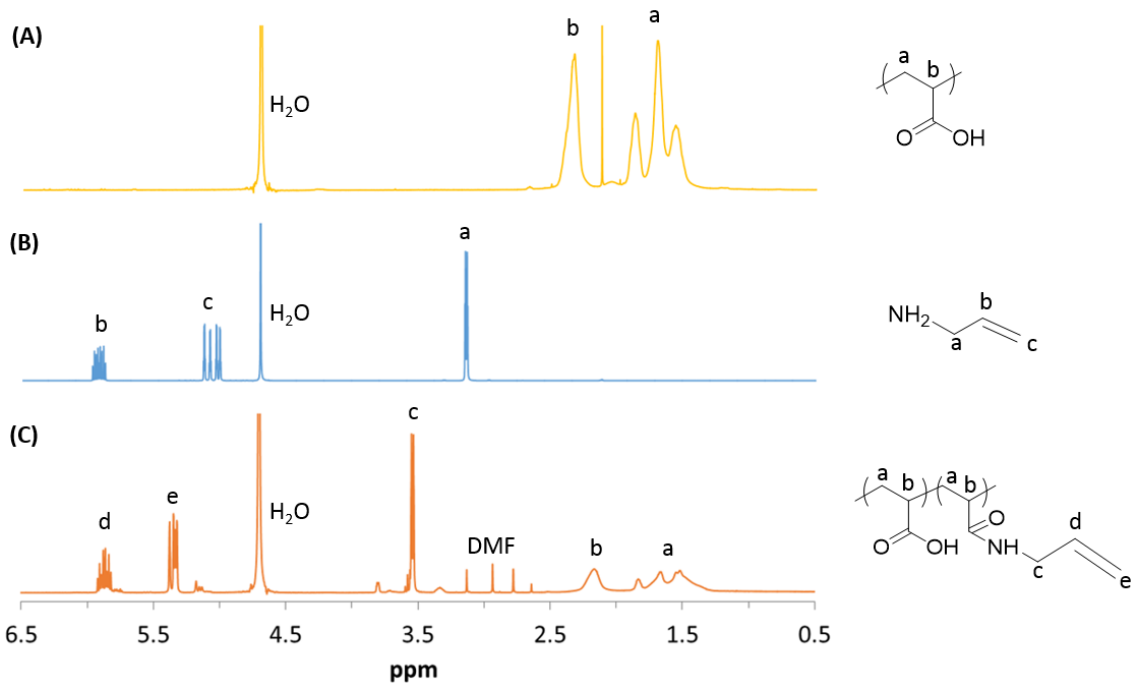


**Figure 2.6.** $^{1}$H NMR spectroscopy of poly(acrylic acid) (A), allylamine (B) and the functionalised product of the two (C), all in $D_2O$.

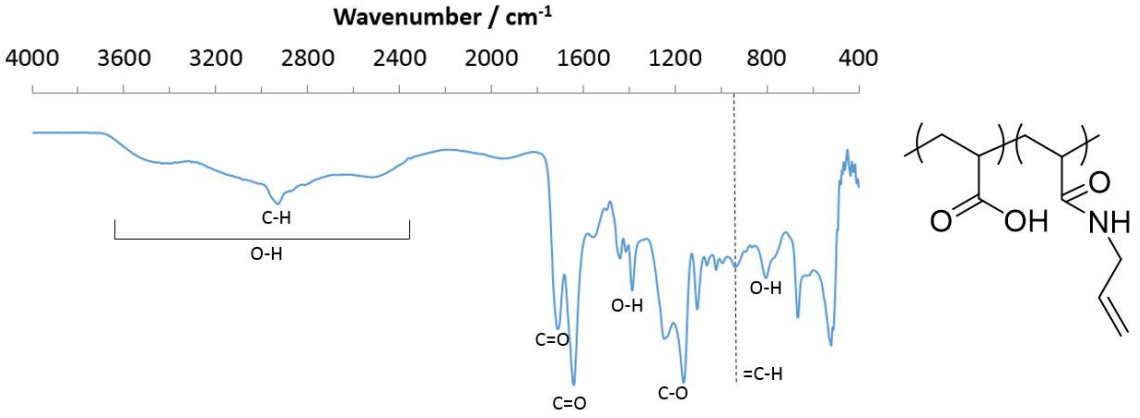


**Figure 2.7.** FTIR spectra of PAA functionalised with allylamine.

Next, functionalisation via DMTMM conjugation was investigated. DMTMM was selected as the route for functionalisation of PAA due to the fact that tyramine is highly unstable at the pH range required for EDC/NHS ligation.[106] Figure 2.8 shows the NMR spectra for the product of PAA and tyramine. The functionalisation level is calculated

using the ratio of phenyl ring peaks (protons c-f; Figure 2.8A) to polymer backbone peaks and is calculated as 1.9%. Figure 2.9 gives the FTIR spectra for the product. In comparison to the PAA spectra (Figure 2.5A), the shift and modification of the carboxyl peak and the additional amide I and II bands (between 1500 and 1700 $cm^{-1}$), confirms the incorporation of the amine within the polymer.

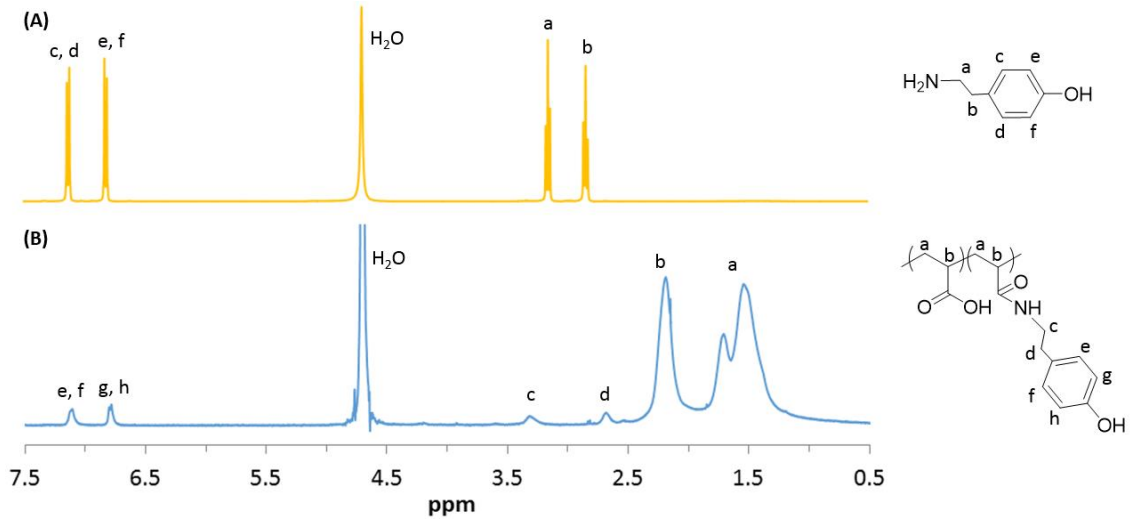


**Figure 2.8.** $^{1}H$ NMR spectroscopy of tyramine (A) and the functionalised product of poly(acrylic acid) and tyramine (B), both dissolved in $D_2O$.

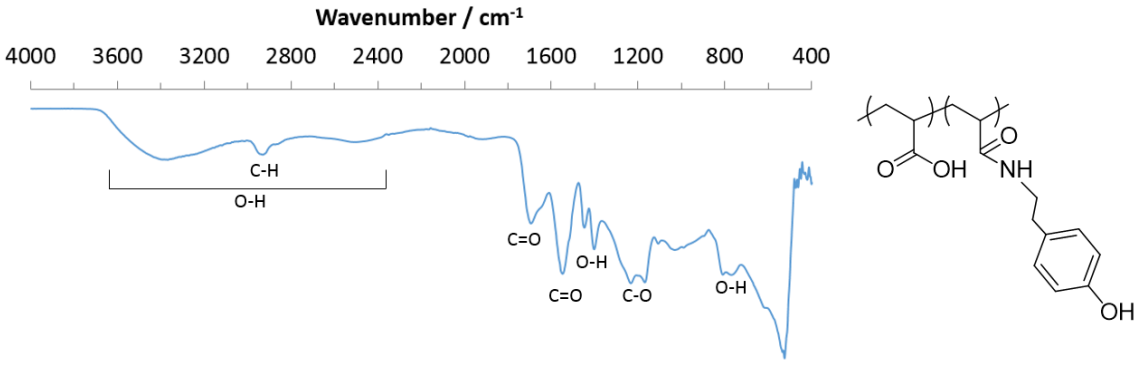


**Figure 2.9.** FTIR spectra of PAA functionalised with tyramine.

PAA was also functionalised with cysteamine via DMTMM conjugation. This was achieved through a two-step procedure involving initial functionalisation with cystamine followed by cleavage of the disulfide bond using dithiothreitol (DTT).[107,108] Figure 2.10 shows the NMR spectra for cystamine as well as the spectra for the functionalised product of cysteamine and PAA. The functionalisation level was calculated as 4.6% from the NMR spectra. FTIR spectra were obtained for the product (Figure 2.11); however, the S-H bond cannot be identified in the spectrum, presumably due to the fact that this band is known to be very weak in FTIR and also due to the low functionalisation level of the polymer.[105] The shift and modification of the carboxyl peak and the additional amide bands (between 1500 and 1700 $cm^{-1}$), relative to the PAA spectra (Figure 2.5A), again confirms the incorporation of the amine within the polymer.

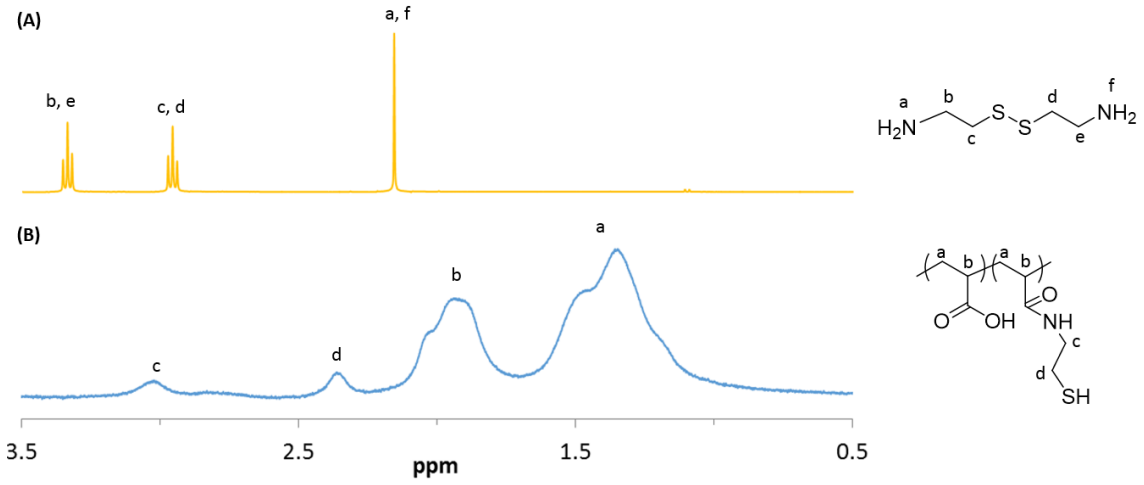


**Figure 2.10.** $^{1}H$ NMR spectroscopy of cystamine (A) and the functionalised product of poly(acrylic acid) and cysteamine (B), both dissolved in $D_2O$.

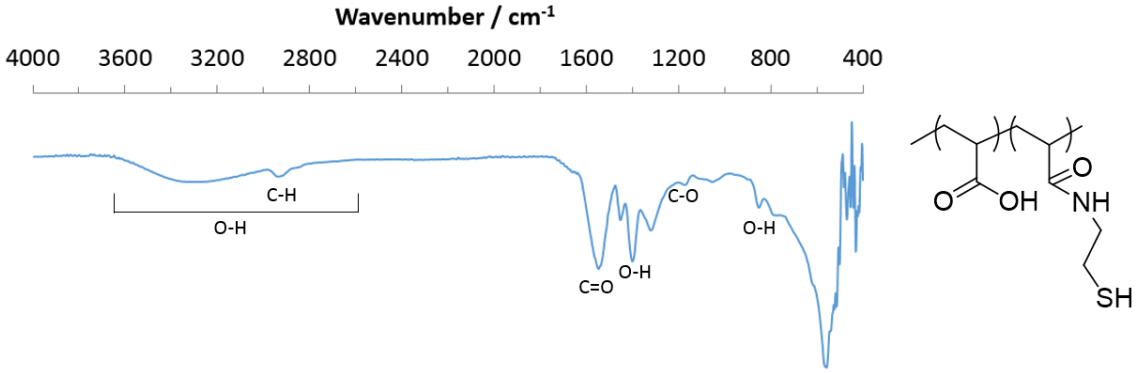


**Figure 2.11.** FTIR spectra of PAA functionalised with cysteamine.

## 2.3.2 Functionalisation with Bromoalkanes

PAA was initially functionalised with allyl bromide. $^{1}$H NMR confirmed the successful incorporation of the alkene (Figure 2.12) and a functionalised level of 12.5% was calculated from the ratio of the alkene to polymer backbone peaks. The FTIR spectra of the product (Figure 2.13) confirms the presence of the alkene through the =C-H bending band at approximately 950 cm$^{-1}$. In comparison with earlier FTIR spectra for the functionalisation of PAA with amine moieties, the C=O stretch is further split, forming separate peaks at 1657 and 1710 cm$^{-1}$. This additional peak at 1657 cm$^{-1}$ corresponds to the significant neutralisation of acids and the formation of sodium acrylate.[109] It was found that the allyl bromide functionalised PAA would degrade over time due to crosslinking of the polymer, making it insoluble in water. As a result, PAA was also functionalised with 5-bromo-1-pentene with the thought that the longer alkene chain length (and distance between the alkene and amide moiety) would reduce the reactivity of the alkene and chance of crosslinking.

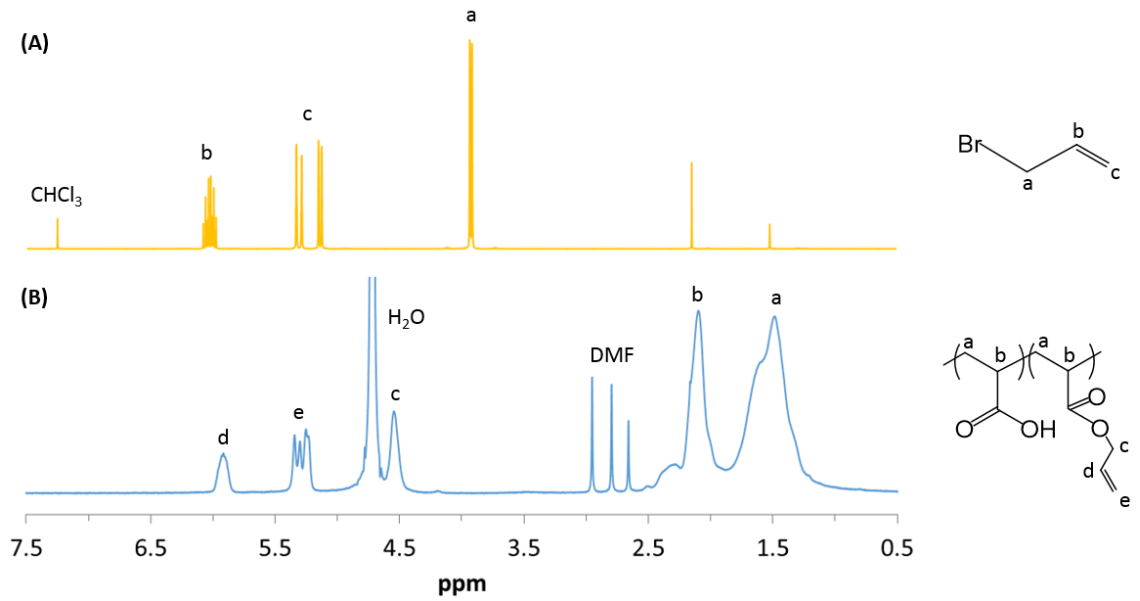


**Figure 2.12.** $^{1}$H NMR spectroscopy of allyl bromide in $CDCl_3$ (A) and the functionalised product of poly(acrylic acid) and allyl bromide in $D_2O$ (B).

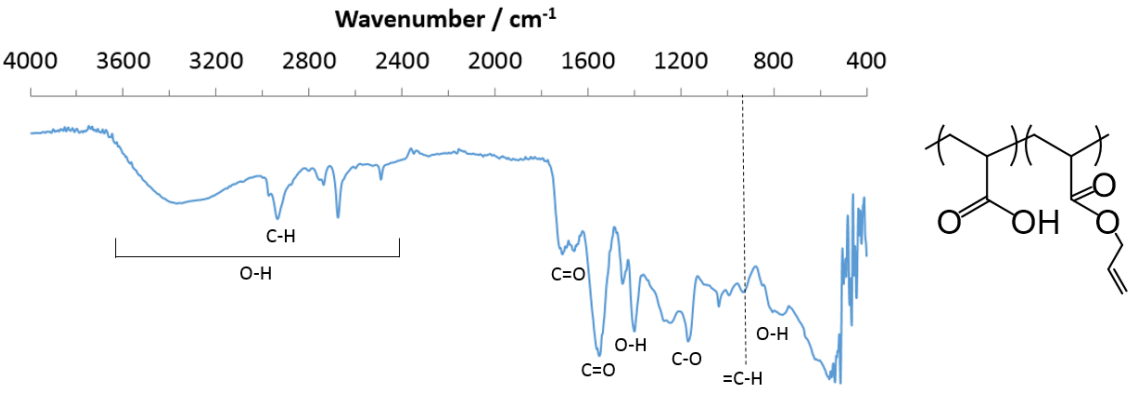


**Figure 2.13.** FTIR spectra of PAA functionalised with allyl bromide.

PAA with two different molecular weights (15000 g/mol and 450000 g/mol) was functionalised with 5-bromo-1-pentene. Figure 2.14 and Figure 2.15 show the $^{1}$H NMR spectra for functionalised 450000 g/mol and 15000 g/mol PAA, respectively. The functionalisation level is calculated by the ratio of alkene to polymer backbone peaks, taking into account the two concealed alkene peaks at approximately 2 ppm. The functionalisation levels were calculated as 5.2% and 12.9% for 450000 g/mol and 15000

g/mol PAA, respectively. In addition, the FTIR spectra (Figure 2.16; shown for 450000 g/mol PAA) confirm the presence of the alkene through the =C-H bending band at approximately 950 $cm^{-1}$. The C=O stretch (at approximately 1700 $cm^{-1}$) is again split as a result of the significant neutralisation of acids and the formation of sodium acrylate.

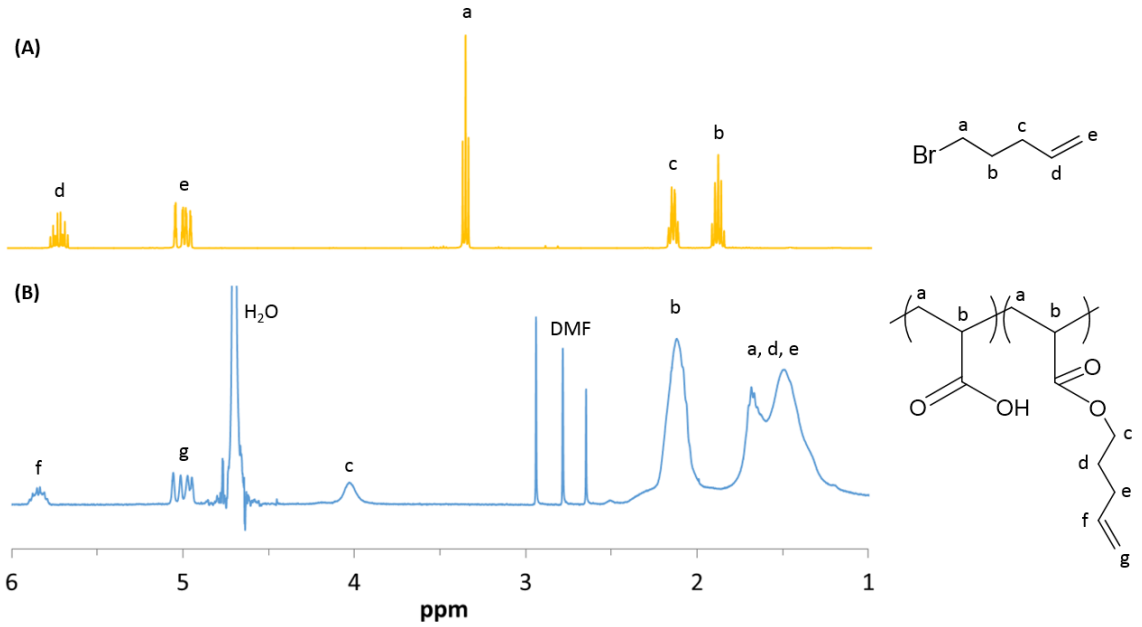


**Figure 2.14.** $^{1}$H NMR spectroscopy of 5-bromo-1-pentene in $CDCl_3$ (A) and the functionalised product of poly(acrylic acid) (450000 g/mol) and 5-bromo-1-pentene in $D_2O$ (B).

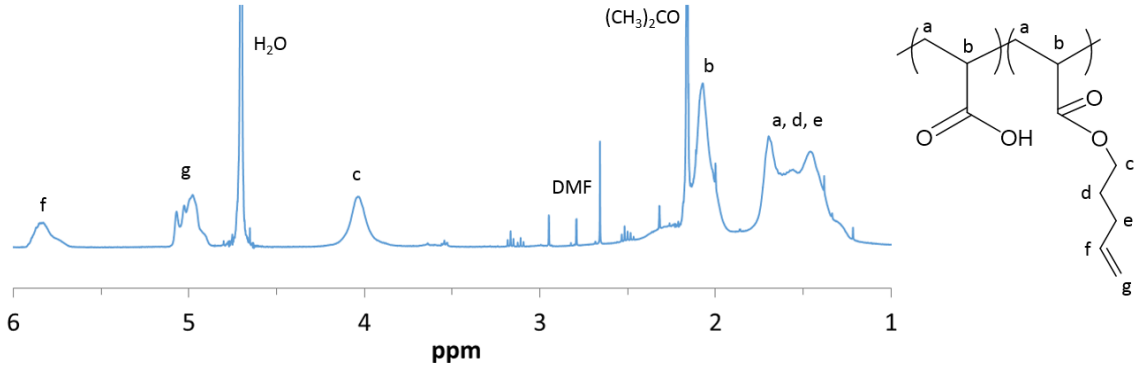


**Figure 2.15.** $^{1}$H NMR spectroscopy of the functionalised product of poly(acrylic acid) (15000 g/mol) and 5-bromo-1-pentene in $D_2O$.

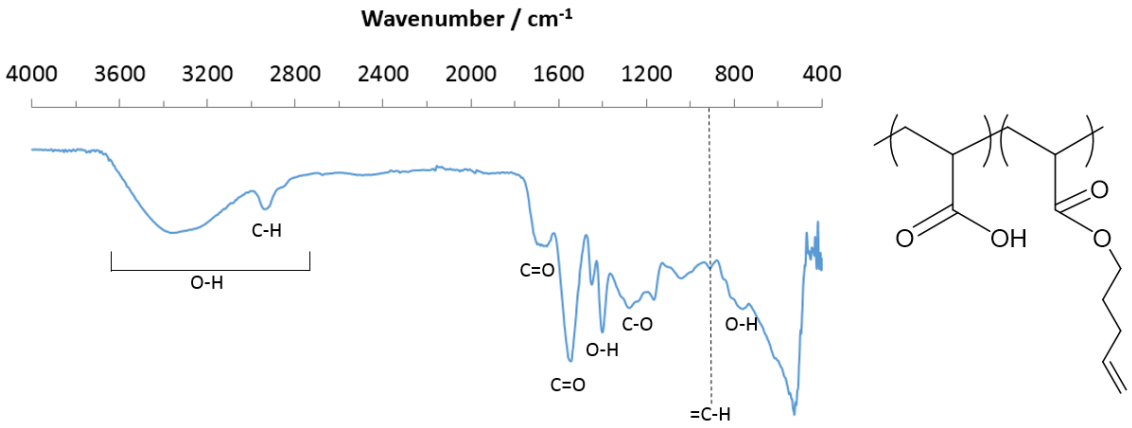


**Figure 2.16.** FTIR spectra of PAA (450000 g/mol $M_W$) functionalised with 5-bromo-1-pentene.

Figure 2.17 shows the $^1$H NMR spectra obtained for PAA functionalised with boronic acid. A functionalisation level of 18.1% was calculated using the ratio of phenyl ring peaks to polymer backbone peaks. From the FTIR spectra (Figure 2.18), the bands for the B-O vibration and the $BO_2$ deformation at 1330 and 700 cm$^{-1}$ respectively, confirm the presence of phenylboronic acid in the structure of the polymer.[103]

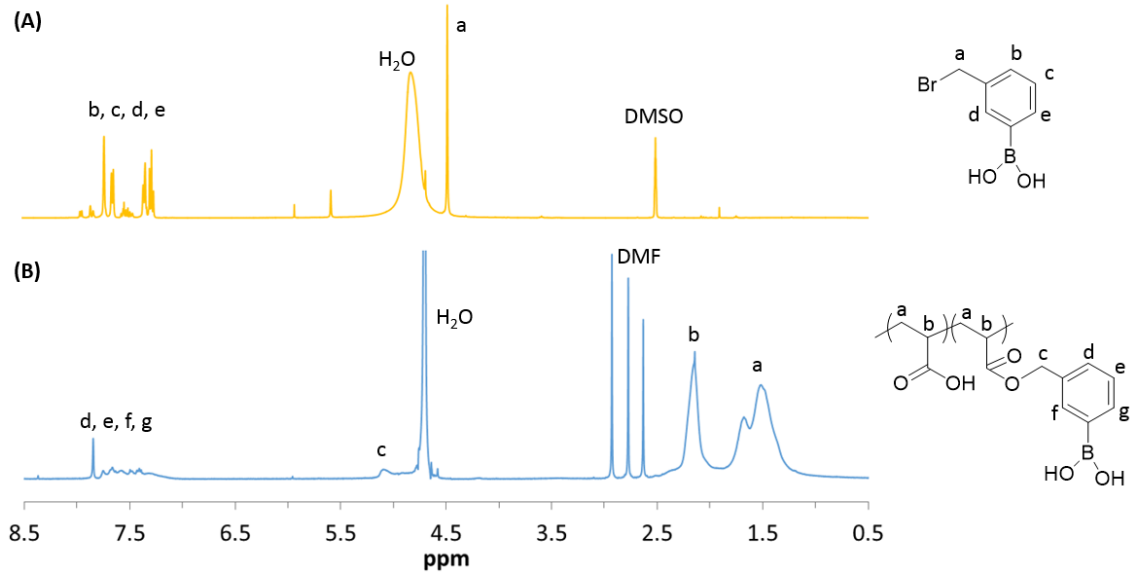


**Figure 2.17.** $^1$H NMR spectroscopy of 3-(bromomethyl)phenylboronic acid in DMSO-$d_6$ (A) and the functionalised product of poly(acrylic acid) and 3-(bromomethyl)phenylboronic acid in $D_2O$ (B).

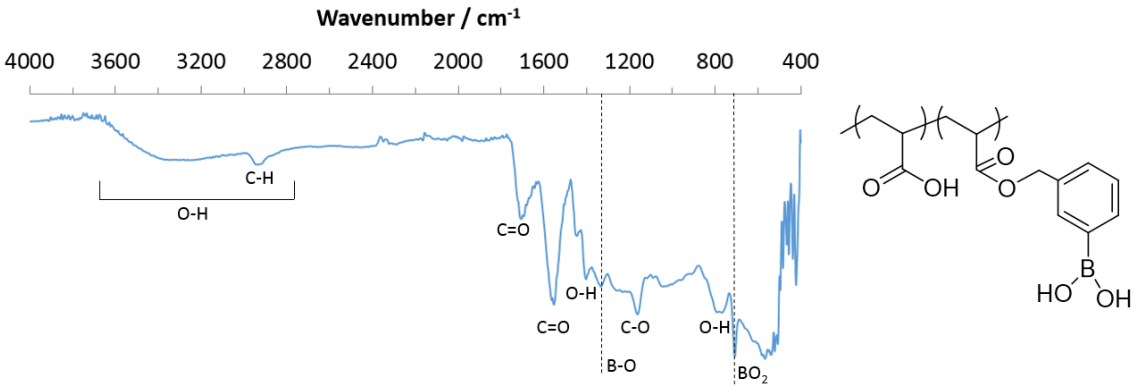


**Figure 2.18.** FTIR spectra of PAA functionalised with 3-(bromomethyl)phenylboronic acid.

## 2.3.3 Thiol-Ene Chemistry

The efficiency of thiol-ene reactions under different conditions was investigated first. Due to its low cost and relevance to peptide functionalisation, *N*-acetyl-L-cysteine was selected as the initial thiol to use for conjugation to alkene-functionalised PAA. Figure 2.19A shows the $^{1}$H NMR spectra for alkene-functionalised PAA in solution, alongside *N*-acetyl-L-cysteine, prior to UV initiation. At a thiol to alkene ratio of 2:1, and at pH 4, complete conversion of the alkene was observed under UV initiation (5 minutes at 17 mW/cm$^2$ with 5 mol% Irgacure 2959 relative to alkene, Figure 2.19B). This was confirmed through the complete absence of the terminal alkene peaks (‘f’ and ‘g’) and also by the presence of the thioether peak (‘g’), which had a matching integration with peak ‘c’ and was half that of peak ‘h’.

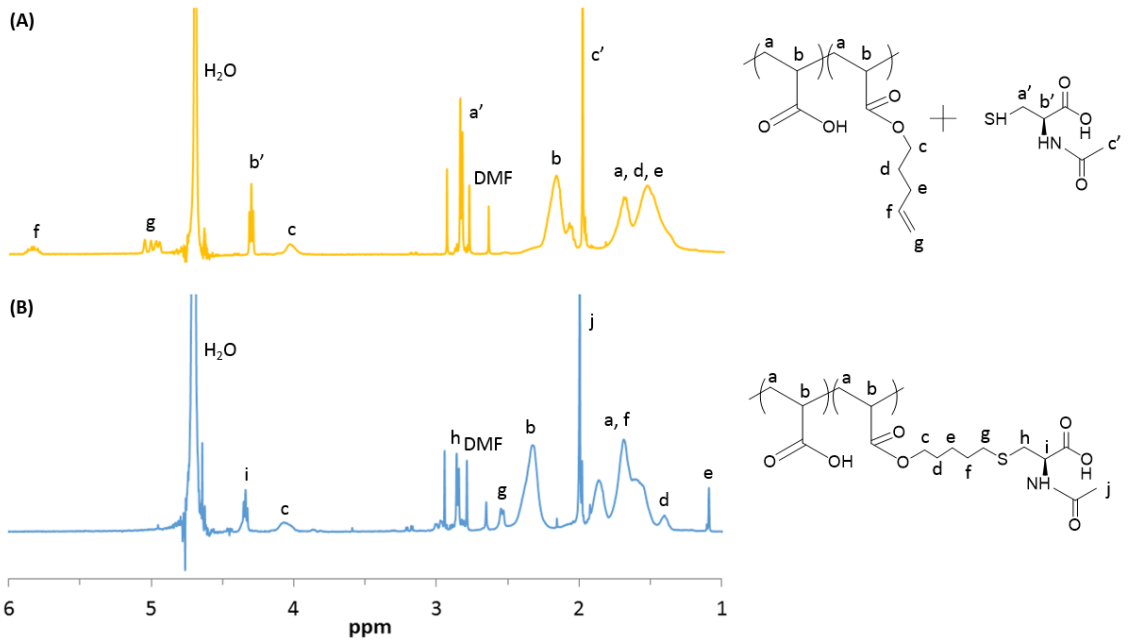


**Figure 2.19.** $^{1}$H NMR spectroscopy illustrating conjugation of thiols to alkene functionalised PAA via thiol-ene radical reactions. (A) Alkene functionalised PAA together with *N*-acetyl-L-cysteine in $D_2O$ (thiol:ene, 2:1). (B) The product of these two components following UV initiation (5 min at 17 mW/cm$^2$) with 5 mol% (relative to alkene) Irgacure 2959 (thiol:ene, 2:1). The reaction was done at pH 4 in $D_2O$ and these conditions illustrate 100% conversion of the alkene.

At a thiol to alkene ratio of 1:1, initial experiments revealed a surprisingly low reaction efficiency at neutral pH (26% at pH 7; Figure 2.20B). As a result, the effect of pH on thiol-ene reaction efficiency was further investigated (Figure 2.20). Here, reaction efficiencies were calculated through the reduction in the terminal alkene peak intensity relative to peak 'c' (see peak assignment in Figure 2.19). It was observed that the reaction efficiency increased at lower pH values, with a maximum alkene conversion of 60% occurring at pH 5 (Figure 2.20B). The reaction efficiencies were also calculated with regards to the formation of the thioether (ratio of formation of peak 'g' with respect to 'c'; Figure 2.21) and results were very similar to the efficiencies calculated from the terminal alkene intensities (Figure 2.20); this indicated that the alkenes were not themselves reacting and polymerising or undergoing radical addition from the initiator.

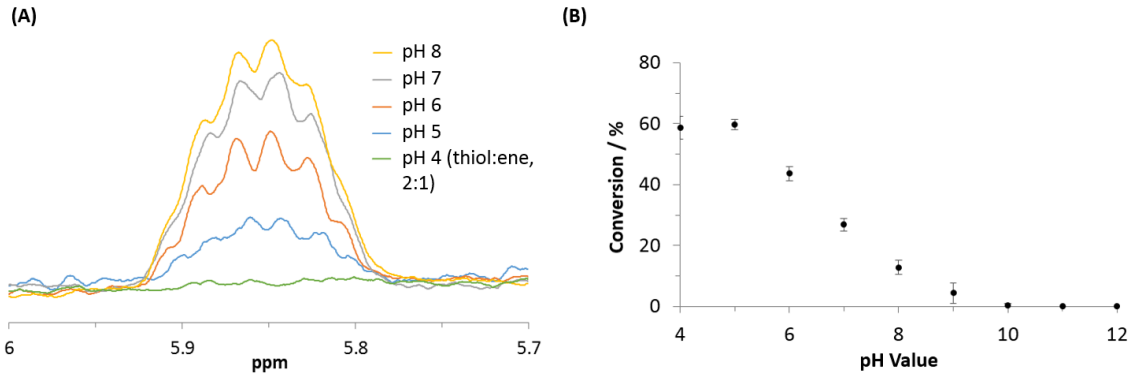


**Figure 2.20.** The effect of pH value on the reduction in the terminal alkene peak intensity, for the conjugation of *N*-acetyl-L-cysteine to 5-bromo-1-pentene functionalised PAA via thiol-ene radical reactions. (A) $^{1}$H NMR spectroscopy curves illustrating the reduction in the terminal alkene peak intensity (with NMR curves normalised about peak 'c'; see Figure 2.19) with pH. (B) Quantification of the conversion of alkene, via NMR, as a function of pH value. Reactions were initiated via UV initiation (5 min at 17 mW/cm$^2$) with 5 mol% (relative to alkene) Irgacure 2959. The thiol to alkene ratio was 1:1 unless otherwise indicated. Error bars show standard deviations for repeats across samples (sample size n = 3).

These high reaction efficiencies at low pH values were surprising given that thiol-ene reactions are typically most efficient at neutral pH, although this has been shown to depend on, to some extent, the p$K_a$ of the chosen thiol.[88] Indeed, Colak *et al.* showed that the reaction efficiency between pentenoic acid and *N*-acetyl-L-cysteine was most efficient in the range of pH 2 to 8 and only started to decrease significantly at values above this.[88] This contrasts with the results we obtained where the reaction efficiency starts to drop significantly at pH 5 or above (Figure 2.20 and Figure 2.21). This restriction of the thiol-ene reaction to more acidic conditions in the case of alkene-functionalised PAA is not fully understood, but it is thought to result from the high density of negatively charged carboxylates along the PAA backbone, which may result in a local pH higher than expected.

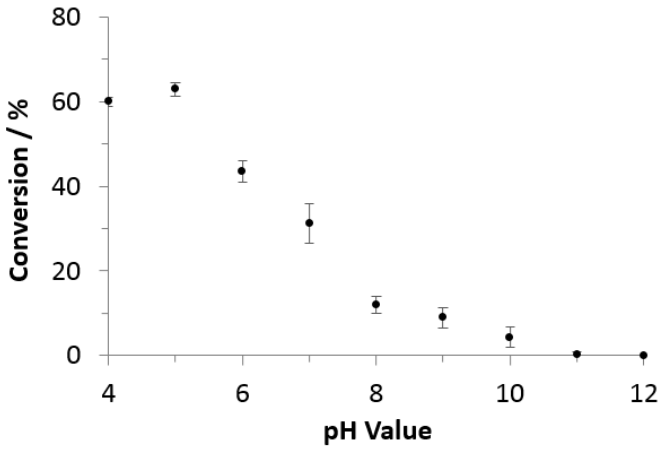


**Figure 2.21**. The effect of pH value on the conversion to thioether, for the conjugation of *N*-acetyl-L-cysteine to 5-bromo-1-pentene functionalised PAA via thiol-ene radical reactions. The thiol to alkene ratios were 1:1. Conversions were calculated with respect to the formation of the thioether (ratio of peaks 'c' and 'g'; see Figure 2.19). Error bars show standard deviations for repeats across samples (sample size n = 3).

Following the investigation of *N*-acetyl-L-cysteine conjugation, the functionalisation of PAA with boronic acid (4-Mercaptophenylboronic acid) via thiol-ene reactions was investigated. At pH 6.5 and a thiol:ene ratio of 1:1, a 33% alkene conversion was calculated from the ratio of peaks 'k' and 'c' (see Figure 2.22B). Given that PAA is functionalised with allyl bromide at a level of 12.5%, this represents a functionalisation level of 4.1% for boronic acid relative to PAA. From the results for *N*-acetyl-L-cysteine conjugation it is clear that thiol-ene coupling with boronic acid benzene thiol should increase at lower pH and increased thiol ratios, although this was not confirmed through experiments.

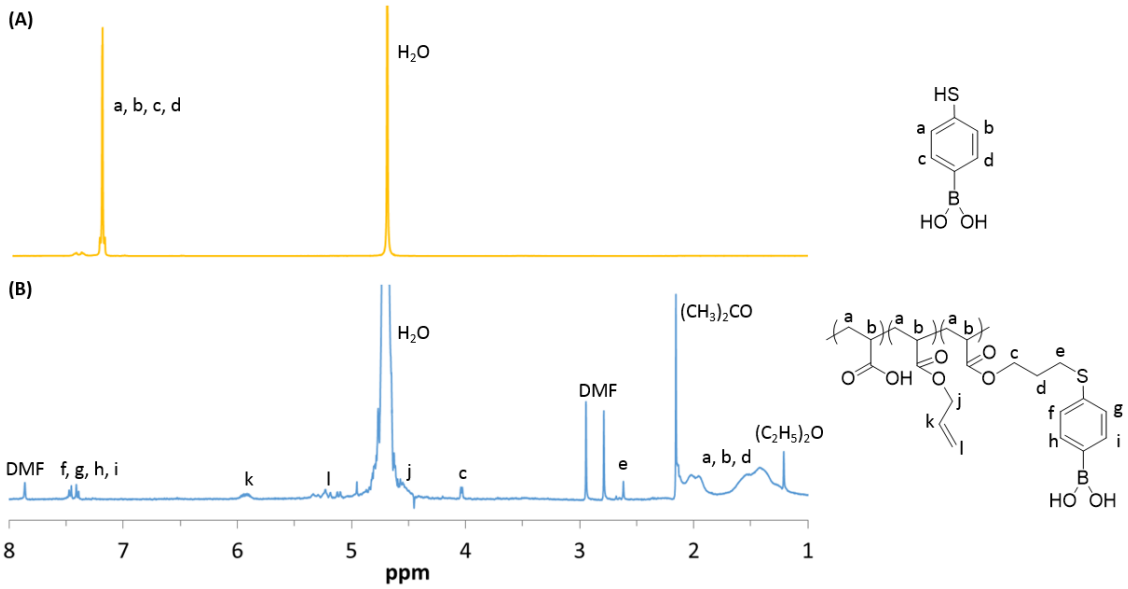


**Figure 2.22.** $^{1}$H NMR spectroscopy illustrating conjugation of boronic acid to alkene functionalised PAA via thiol-ene radical reactions. (A) 4-mercaptophenylboronic acid in $D_2O$. (B) The partially functionalised product of alkene functionalised PAA with thiol, following UV initiation (5 min at 17 mW/cm$^2$) with 5 mol% (relative to alkene) Irgacure 2959 (thiol:ene, 1:1). The reaction was done at pH 6.5 in $D_2O$ and the alkene conversion was calculated as 33%.

## 2.4 Summary

A number of functionalisation routes were investigated with the aim of producing PAA (450000 g/mol) derivatized with either an alkene, boronic acid, hydroxyl or thiol end-group. In all cases, the aim was to produce polymers at the highest possible functionalisation level via each synthesis route, and the $^{1}$H NMR spectra shown reflect these levels obtained. Typically, the functionalisation level was limited either by the solubility of the different components during the reaction or by gelation of the final product during the polymer purification steps.

Steglich esterification was used for amine-ligation with limited success. Although high alkene functionalisation was obtained (35%), functionalisation with boronic acid was limited by solubility of the final product in aqueous solutions; perhaps this was due to formation of the reaction by-product dicyclohexylurea and difficulties associated with fully removing this from the final product. Due to its good stability and solubility in water, as well as its proven high efficiency, DMTMM was next investigated as a method for amine conjugation. Through this route functionalisations with tyramine and cysteamine were obtained at comparatively low levels of 1.9% and 4.6%, respectively.

The reaction of PAA with bromoalkanes offered a very simple method for the functionalisation of PAA. Functionalisation with the alkenes, allyl bromide and 5-bromo-1-pentene, were at levels of 12.5% and 5.2%, respectively. Functionalisation with bromo-boronic acid was at 18.1%. A second molecular weight of PAA (15000 g/mol) was also investigated and a functionalisation level of 12.9% for 5-bromo-1-pentene conjugation was obtained.

The efficiency of thiol-ene reactions, for alkene-functionalised PAA, was investigated at a range of pH values. Surprisingly, compared to the results of others our polymers showed a shift in efficiency to slightly more acidic conditions. PAA was also functionalised with boronic acid benzene thiol at a level of 4.1% through thiol-ene chemistry. Through this route a maximum theoretical functionalisation level of 12.5% could have been obtained, given that a 100% efficiency of alkene to thiol conjugation was met for our polymer system. Given the higher functionalisation levels obtained through the (bromomethyl)phenylboronic acid route, alongside the much simpler reaction conditions, this was selected as the more effective route.

# CHAPTER 3

## Synthesis of Poly(Acrylic Acid) Brushes

## 3.1 Introduction

The aim of this part of the project was to produce well-defined brushes of poly(acrylic acid) on planar and spherical silica substrates, followed by their functionalisation with boronic acid. The introduction to this Chapter reviews the literature on some of the common methods for the production of polymer brushes and introduces some of the parameters affecting their growth. Some of the general applications of polymer brushes, including specific examples for PAA, are then explored. Following this, methods for the fabrication of PAA brushes are reviewed and compared and the impact of parameters, such as pH and ionic strength of the environment, on polyelectrolyte brush behaviour are discussed. The experimental sections presents the data for the generation and characterisation of polymer brushes on planar silicon substrates and silica nanoparticles. Following this, the work on the functionalisation of planar PAA brushes is presented.

Polymer brushes are a form of surface coating that enable control over the physico-chemical properties of an interface. They have applications in a number of areas, including, sample purification and analysis,[110–113] cell culture and tissue regeneration,[114,115] biosensing platforms[116–118] and antibacterial coatings.[119] PAA is a heavily studied polymer with many interesting applications arising from its high density of carboxyl groups. In polymer brush form, PAA brushes have been applied in numerous applications: the control of liquid and solute transport and separation through membranes;[120] controlling protein immobilisation on a surface;[121] immobilising enzymes on a surface;[122] promoting cellular adhesion or adsorption to a surface[123,124] and creating "smart"/ responsive surfaces.[125,126] The biofunctionalisation of PAA enables further control over the surface properties, allowing targeted bioadhesion and interactions. A further use of polymer brushes is in their application within colloidal

probe force microscopy. The functionalisation of an AFM tip with a polymer brush layer enables the interactions between polymer chains and various substrates to be probed at the nanoscale level. The use of polymer brushes in this respect will be investigated in detail in Chapter 4.

### 3.1.1 Physico-Chemical Properties of Polymer Brushes

Understanding and controlling interfaces is a vital attribute for a wide range of applications. Polymer brushes are a form of surface coatings which are particularly attractive as they allow the control of a number of important architectural features. Polymer brushes consist of polymer chains that are tethered at one of their ends to an underlying substrate.[127] At high grafting densities, steric repulsion leads to the extension and stretching of polymer chains and a brush-type conformation occurs.[128] The methods through which polymer brushes are fabricated enable architectural features such as grafting density, thickness of the coating, and the chemistry of polymer chains to be readily manipulated. This flexibility in design allows for the tuning of a number of interfacial properties such as hydrophilicity, the binding and absorption of molecules, and cell adhesion.[127] Polymer brush coatings are generally considered more controlled than other approaches for the formation of thin polymer films due to their good stability (improved bonding with the underlying substrate) and control over physico-chemical properties.[129]

The attachment of polymer chains to a surface generally occurs through either physisorption or chemical bonding of the chains to the interface. In the physisorption method, polymer coatings are rendered thermally and solvolytically unstable as a result of the physical nature by which the polymer chains are tethered to the surface.

Furthermore, this method allows poor control over the grafting density. The covalent grafting of chains to the surface, through either the "grafting to" or "grafting from" technique, can overcome these shortcomings.[129] However, "grafting to" coatings are still restricted to low grafting densities, due to the large entropic penalty associated with such processes. The different polymer brush synthesis strategies described are illustrated in Figure 3.1.

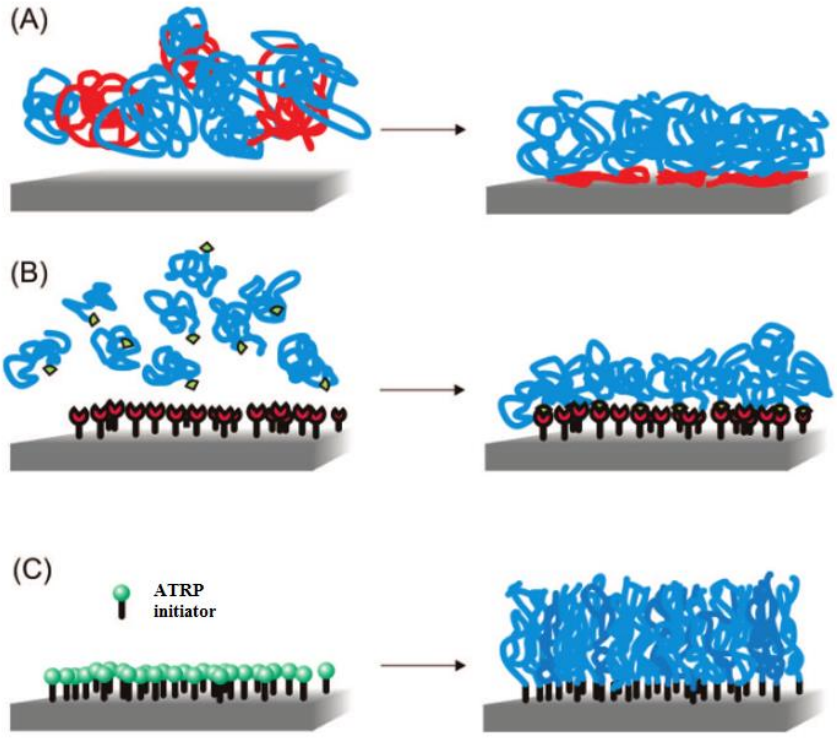


**Figure 3.1.** Illustration of the different strategies for the preparation of polymer brushes. (A) Physisorption of polymer chains via preferential adsorption of the red blocks to the surface. (B) Chemisorption via reaction of end-functionalised polymers with functional groups at the surface ("grafting to" approach). (C) Polymer brushes grown via surface-initiated polymerization ("grafting from" approach). Figure taken from Barbey *et al.*[128]

In the "grafting to" method, polymer chains containing a suitable end-functionalised group are reacted with a substrate. Polymer brush layers created this way possess

thermal and solvolytic stability. However, they also possess a low grafting density and film thickness. This results from the inability of large polymer chains to diffuse to the reactive sites of the substrate, as surrounding chains that are already bonded cause steric hindrance. A method which circumvents these disadvantages is the "grafting from" technique. In this method, a polymer brush layer is generated *in situ* from a surface immobilised initiator; this enables high grafting densities as the driving force of the grafting process is the polymerization reaction itself, typically associated with a large gain in free energy and able to overcome the associated entropic penalty. The "grafting from" technique requires the substrate surface to be modified to generate appropriate initiator functionality. This modification has been performed through methods such as Langmuir-Blodgett techniques or self-assembled monolayer (SAM) deposition. By varying the substrate material, initiator deposition technique and polymer synthesis method, numerous brush fabrication methods are enabled.[129]

Amongst the multitude of available polymerization techniques, radical-based strategies are most frequently used. Compared to other methods, radical-based polymerization strategies have several advantages; these include a high gain in free energy upon polymerization (ability to overcome the entropic penalty), compatibility with both aqueous and organic media, as well as a high tolerance toward a wide range of functional groups.[128] "Living" polymerization reactions are defined as polymerization processes in which termination or chain transfer of the polymer is eliminated or considerably reduced. These types of reactions have key features such as the control over brush molecular weight and architecture. However, they also suffer relatively low polydispersity. In addition, the ability to perform sequential polymerization steps can lead to both thicker homopolymer layers and diblock copolymer layers.[129] Consequently,

taking these facts into account, controlled radial polymerizations have been viewed as the most effective technique for grafting a polymer chain to a substrate, and, as such, have been extensively reviewed in the literature.[128,130–133] The most abundantly used controlled radical polymerization method, due to its extreme versatility and robustness, is known as surface-initiated atom transfer radical polymerization (SI-ATRP).[128]

There are four main components of SI-ATRP: the initiator, solvent, monomer and catalyst. The mechanism for SI-ATRP is illustrated in Figure 3.2 and utilises what is known as a reversible halogen atom abstraction step.[101] First, the initiators, which are often an alkyl halide, are fixed onto the substrate surface. Then, in the presence of a transition metal catalyst, usually a Cu(I)/ligand system, the initiators are activated to generate radicals.[130] This generation of a radical occurs through the conversion of the original lower oxidation state transition metal to a higher oxidation state metal complex. This occurs as a result of the single electron transfer step between the transition metal complex and halogen atoms on the dormant alkyl halide.[128] Next, the radical adds monomers forming the polymer chain. This growing radical can then be deactivated again to generate a dormant chain via the deactivation of the higher oxidation state metal back to a lower oxidation state. As both initiation and deactivation are fast, all chains begin growing at roughly the same time whilst maintaining a low concentration of active species. Consequently, this method provides excellent control over molecular weight.[101] Many parameters such as the ligand/transition metal ratio, temperature, ligand, solvent or initiator will all influence the ATRP performance and thus offer ways of fine-tuning the reaction.[128]

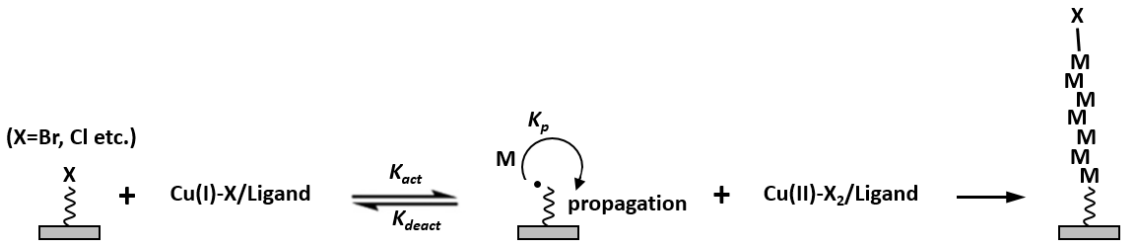


**Figure 3.2.** General equilibrium for the classic ATRP process. M is the monomer, $K_p$ is the propagation rate constant, and $K_{act}$ and $K_{deact}$ represent the rate constants of activation and deactivation, respectively. Figure adapted from Wu *et al.*[130]

Solvent effects (due to polarity) on radical reactions such as ATRP are generally moderate. However, it has been observed that the rate of ATRP is significantly accelerated in the presence of water. Values of the ATRP equilibrium constant in the presence of copper(I) bromide have been shown to vary by more than a factor of 80 in different organic solvents, with the highest in DMSO and the lowest in acetone.[134] Accordingly, the choice of the solvent and catalyst system remains important. Furthermore, the substrate material is another important consideration. ATRP is performed predominately on gold or silicon substrates due to their ease of characterisation. However, the field is constantly expanding to introduce brushes grown from other substrate types. For example, brushes have recently been fabricated on latex particles,[135] carbon nanotubes,[136] PDMS films[137] and a variety of other materials.[128] Advantages of ATRP on silicon substrates include the fact that silicon is inexpensive, molecularly flat, can form thermally stable linkages with organosilanes and also that the polymer chains are tethered via robust Si-C bonds.[128,129]

In summary, ATRP is an excellent technique to fabricate polymer brushes due to its chemical versatility, compatibility with a large range of monomers and functional groups, and ability to tolerate a relatively high degree of impurities. Furthermore, the

fact that most of the standard ATRP catalyst systems and surface initiators are easily available, either commercially or through simple fabrication procedures, makes it an attractive technique from an experimental point of view.[128] A limitation of ATRP is that the complete removal of the toxic transition metal catalyst following polymerization can be very challenging.[130] This raises potential concerns for the use of this method in preparing polymers for biomedical applications.[128] However, chemical extraction strategies can be applied, such as the use of ethylenediaminetetraacetic acid (EDTA). In addition, ATRP is sensitive to the presence of acids as they are thought to react with the catalyst, displacing the halogen atom from the higher oxidation state transition metal. This prevents ATRP of acid-based polymers as the deactivation step cannot occur.[101,138]

### 3.1.2 Applications of Polymer Brushes

Polymer brushes have numerous applications in a wide range of areas. Some of the more common applications include sample purification and analysis,[110–113] cell culture and tissue regeneration,[114,115] biosensing platforms[116–118] and antibacterial coatings.[119] Within the area of sample purification and analysis, applications are enabled by the swellability of brushes in appropriate solvents and also from their ability to deliver high binding capacity.[111] In addition, the chemical structure of these coatings can be easily manipulated with a diverse range of functional groups to allow for highly selective attachment to specific biomolecules.[129] These properties have led to the wide use of polymer brushes for improved chromatography and electrophoresis systems for protein separation and purification.[111–113] Due to the ubiquity of histidine-tagged proteins in protein synthesis and purification, the nickel-nitrilotriacetic acid (Ni-NTA) chromatography system is one such system that has been studied extensively.[127] Other

applications have included the use of poly[oligo(ethylene glycol) methyl methacrylate] coatings to decrease nonspecific binding and improve protein separation in capillary electrophoresis.[110] The process of nonspecific physisorption of a protein to a surface, which is seen in many simple surface coatings, is disadvantageous as it can result in unfolding or partial denaturing of the proteins upon absorption. Consequently, the fact that polymer brushes utilise chemisorption, which is non-harmful to protein structure, is a further reason polymer brushes are so advantageous for the selective and reversible capture of proteins.[139] In comparison with hydrogel coatings, polymer brushes differ in that there is no need for cross-links between polymer chains. As a result, protein access to functional groups is enhanced within polymer brush films.[111]

With regards to tissue regeneration applications, brushes can be used for controlling the interfaces between a material and surrounding cells or tissues. Polymer brushes enable material surfaces to be biofunctionalised with ECM molecules, growth factors and drugs without altering the bulk properties of the material. This allows the control of behaviours such as cell adhesion, proliferation, differentiation and matrix deposition.[127] As such, this biofunctionalisation makes the surfaces appear similar to biomembranes and thus provides an environment that enables attached biomolecules to maintain their bioactivity.[67] In order to obtain better integration of implants into surrounding tissues, polymer brushes have been biofunctionalised and used to coat titanium implants such as hip and knee joint replacements, dental implants and cardiac pacemakers.[114] Cell culture applications of polymer brushes have been enabled through the use of reversible cellular adhesion. This approach offers a scaffold-free technology which allows generation of epithelial cell sheets that can then be detached and harvested without the use of digestive enzymes.[115,127]

Applications in biosensing are enabled by the high density and multiple levels of proteins that can be bound to polymer brushes. This is in comparison to the much lower binding densities associated with self-assembled monolayers (SAMs).[123] In addition, the unique ultra-protein resistant properties of some brushes make these coatings particularly attractive for the label free detection of analytes from complex samples such as undiluted blood, plasma or saliva. Polymer-brush-based biosensing platforms include three main categories: (1) label-free detection systems, which use direct binding of the analyte to the brush;[118] (2) label-based systems, in which an analyte binds to the brush and detection occurs using a labelled molecule;[117] (3) mass-amplification systems, in which the surface-bound analyte is detected via the amplification of mass resulting from surface-initiated polymerization.[116,127]

The formation of biofilms on surfaces presents important challenges in a wide range of applications. For example, bacterial biofilms can cause problems in the healthcare industry through medical-device-associated infections, and biofouling from unwanted marine organisms can cause problems in the shipping industry through increased friction and biocorrosion on ships' hulls. Within the healthcare industry, implantable medical devices are known to be particularly susceptible to colonisation. Such bacterial communities are also mostly protected from the immune response and are much less susceptible to elimination by antibiotics. Both hydrophobic and hydrophilic polymer brushes have been shown to be effective surface modification methods to prevent biofilm formation from pathogenic bacteria. Rodriguez-Emmenegger *et al.* suggested that the prevention of biofilm formation by polymer brushes is a result of both the inhibition of the formation of a conditioning film and the decrease in the strength of direct adhesion observed.[127,140]

PAA is a heavily studied polymer with many useful applications resulting from its unique properties. These properties include its high density of hydrophilic carboxylic groups, good cytocompatibility, simple activation of carboxylic acid groups for functionalisation with a wide range of molecules, and readily ionisable groups enabling stimuli-responsive behaviour.[139] Some examples of the uses of PAA brushes include: controlling liquid and solute transport and separation through membranes,[120] controlling protein immobilisation on a surface,[121] immobilising enzymes on a surface,[122] promoting cellular adhesion or adsorption to a surface[123,124] and creating "smart"/responsive surfaces.[125,126]

One of the more common applications of PAA is the control of protein immobilisation to a surface. The high affinity of proteins for charged interfaces is a well-known phenomenon and the ability to supress this affinity would be of use in various biotechnological and biomedical applications. This is due to the implications protein adsorption can have in applications such as contact lens use, where biofilm formation should be prevented, and the biofouling of medical implants.[141] A unique salt effect is found in polyelectrolyte brushes such as PAA, which strongly binds to proteins at low ionic strength. However, when the ionic strength is increased to a few hundred mM the brush appears to be largely protein resistant. This salt-dependent protein affinity of a PAA brush, which has been observed in both planar and spherical brushes,[121] represents a unique effect that is independent of the sign of the protein's net charge.[142] The release of protein counterions is suggested as the dominant driving force for protein adsorption at the PAA surface at low ionic strengths. This binding force, resulting from a balance of electrostatic interactions and entropic contributions, then vanishes as the ionic strength of the solution is increased (resulting in particular in vanishing entropic contributions),

and protein molecules are then instead repelled from the interface by steric interactions.[141,143] Hence, by varying the ionic strength of a protein solution, a PAA brush can be "switched" between states of protein resistance and high protein affinity. Furthermore, it is worth noting that this "switching" of the protein affinity is over such a small range of concentrations that the structure and dynamics of the dissolved proteins are mostly left unaffected. Consequently, a PAA brush represents a particularly promising material coating for controlled protein immobilisation within biotechnological applications.[142]

### 3.1.3 Fabrication of Poly(Acrylic Acid) Brushes

One of the initial factors to contemplate for polymer brush synthesis (via the "grafting from" approach) is the choice of surface initiator. One surface initiator that has been used extensively over the last decade or so is 2-bromo-2-methyl-propionic acid 3-trichlorosilanyl-propyl ester. This has been used in a variety of applications to grow surface-initiated polymer brushes from both planar and spherical silicon substrates. Examples of its use include the generation of brushes using oligo(ethylene glycol)-based monomers,[144,145] methyl methacrylate monomers[146] and tert-butyl acrylate monomers,[147] amongst many others.

Methods for the formation of a monolayer of this initiator have been described in many papers. The procedure involves plasma oxidising of the silicon substrate and then placing it in a dish with the silane initiator, toluene and triethylamine, and leaving it overnight at room temperature. This process has been reported to give an ellipsometric thickness of the initiator monolayer of 0.6 to 0.9 nm.[145] The procedure for the synthesis of this

silane initiator was initially detailed by Husseman *et al.,*[148] and then minor adaptations of the procedure were detailed in later papers.[144,145] The procedure involves initially reacting propanol (propen-3-ol) with 2-bromo-2-methyl-propionyl bromide in the presence of trimethylamine to give an alkene terminated ester. Hydrosilylation of this chemical with trichlorosilane then gives the trichlorosilyl initiator derivative.[148] This can then be attached to the silicon substrate through the process detailed in Figure 3.3.

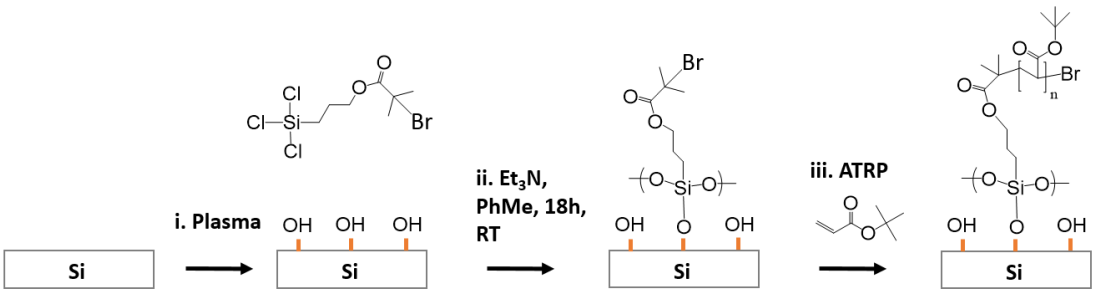


**Figure 3.3.** Schematic of the processes leading to ATRP of PtBA. Plasma treatment activates the silicon substrate (i) and the reaction of 2-bromo-2-methyl-propionic acid 3-trichlorosilanyl-propyl ester with triethylamine and toluene leads to the absorption reaction of the initiator (ii), following which SI-ATRP of tBA can proceed (iii).

Due to the fact that ATRP is sensitive to the presence of acids, PAA is difficult to directly polymerize. Upon direct ATRP of PAA we would expect to observe interactions between the carboxylic acid functionalities and the catalyst, resulting in the formation of metal carboxylates which would inhibit deactivation.[138] Accordingly, PAA brushes are usually fabricated through a two-step process. The protected monomer poly(tert-butyl acrylate) (PtBA), is first polymerized, followed by a deprotection step to generate PAA. There are a number of different methods reported within the literature through which these two steps can be carried out, and these will be compared next.

For ATRP of tBA, the nature of brushes produced depends strongly on four main variables: temperature, pressure, solvent, and catalyst/alkyl halide.[149] Methods in the literature report a variety of different systems for the production of PtBA brushes with respect to the variation of these four factors. Dai *et al.* suggest a procedure which uses a gold coated silicon wafer as the substrate, $Me_4$Cyclam as the ligand, CuBr as the catalyst and a DMF/anisole solvent mix. Polymerization was carried out at 50°C and 100 nm thicknesses were reported within just five minutes.[111] Wang *et al.* performed polymerization using a CuBr catalyst, silicone substrate, bipyridine ligand and methanol as the solvent. This reaction was performed at 40°C for twelve hours and it obtained a brush thickness of around 200 nm.[67] The last synthesis procedure of note was presented by Lego *et al.* and this used a CuBr/PMEDTA catalyst system, an acetone solvent and was performed on a silicon wafer. Brush thicknesses obtained were quite low, with approximately 20 nm growth in five hours, at a temperature of 60°C.[147]

Another useful paper, presented by Davis *et al.*, gives a detailed analysis of the effect that changing various parameters has on the molecular weight and polydispersity of the PtBA brushes produced. Factors that are varied include the ratios of monomer, initiator, ligand and catalyst, and also factors such as the temperature and time. They highlight the importance of introducing a small amount of copper(II) bromide into the initial polymerization mixture as a way of inducing more controlled polymerization, thereby lowering the molecular weights and polydispersity of the final brush.[101] This works through an effect called the persistent radical effect in which the copper(II) species ensures a fast deactivation process, thereby supressing termination.[130] Davis *et al.* also compared the use of PMEDTA and bipyridine as ligands and summarized that ATRP of tBA could occur under milder conditions, in terms of both lower catalyst concentrations

and lower temperatures, when PMDETA was used.[101] Indeed, Ma *et al.* also report faster polymerization rates when using PMDETA over bipyridine.[150]

For the deprotection of PtBA, there are again a variety of different procedures presented in the literature. Wu *et al.* used a method which involves placing the brush in a hydrochloric acid/dioxane bath for two to five hours. They report some cleavage of the polymer chains from the substrate, which is caused by the hydrolysis of the ester group of the initiator. However, as the reaction rate for tert-butyl hydrolysis is much faster than the rate of cleavage of polymer chains from the substrate, the conversion of PtBA can be completed before significant cleavage of polymer chains occurs.[126] Dai *et al.* present a hydrolysis method which involves placing the PtBA brush in a solution of methanesulfonic acid and dichloromethane for just fifteen minutes. However, there is very little data published that quantifies the efficiency of their procedure.[111] And lastly, Lego *et al.* present a method in which the PtBA brushes are immersed in a dichloromethane/trifluoroacetic acid solution overnight. They carried out a number of experiments to show that the initiator layer is stable under the hydrolysis conditions and that polymer chain cleavage due to initiator hydrolysis can be considered negligible.[102]

To summarise, the different methods presented for the ATRP of tBA vary with regards to growth rate of the brush, polydispersity of the polymer chains produced and ease of experimental set-up. In addition, the different hydrolysis procedures presented vary greatly with regards to initiator layer stability, proportion of tert-butyl groups removed, and the proportion of polymer chains cleaved from the surface. Consequently, due to the large variability in results from the different methods, the choice of an appropriate fabrication procedure should be carefully considered.

### 3.1.4 Behaviour of Polyelectrolyte Brushes

A polyelectrolyte brush is a brush that carries at least one ionisable group per repeat unit on its backbone. Depending on the nature of the electrostatic charges along the polymer backbone, two types of polyelectrolyte brushes can be distinguished: strong and weak. Strong ("quenched") polyelectrolytes have a fixed degree of dissociation and their properties do not depend on the pH of the solution. On the other hand, for a weak ("annealed") polyelectrolyte brush the degree of dissociation, and therefore properties, depends on the pH. Due to the relatively simple structure of PAA, it has been used as a model system for the investigation of the charge effect on the properties of polymer brushes. Consequently, there is a relatively large amount of literature published on the behaviour of PAA brushes with respect to various parameters such as pH, ionic strength and polymer grafting density.[126]

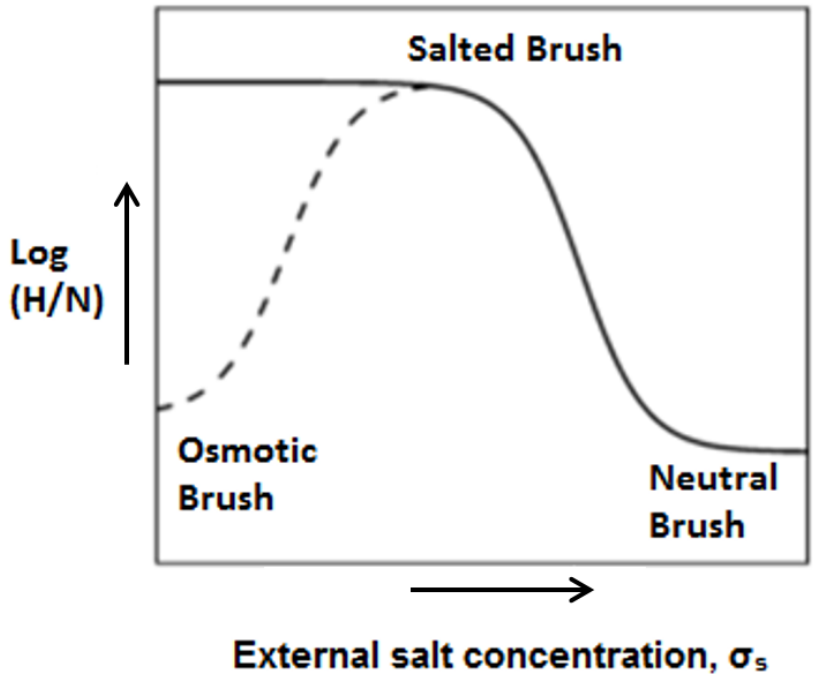


**Figure 3.4.** Dependence of the brush thickness (H), reduced by the number of polymer repeat units (N), on the the external salt concentration ($\sigma_s$). The solid line represents the behaviour of a strong polyelectrolyte brush and the dashed line represents a weak polyelectrolyte brush. Figure adapted from Wu *et al*.[126]

For a strong polyelectrolyte at high salt concentration, the salt concentration inside and outside the brush is about the same and the electrostatic interactions are largely screened. When the external salt concentration decreases, there is an imbalance in the ion concentration inside and outside the brush and electrostatic interactions within the brush cause polymer chain extensions. This brush expansion increases with decreasing salt concentration. However, at some point counterions will start to be expelled from the brush and a limiting brush thickness is reached which is independent of the external salt concentration. Figure 3.4 illustrates this behaviour for the strong polyelectrolyte brush (solid line) and illustrates the presence of three distinct regimes: osmotic, salted, and neutral brush regimes. For a weak polyelectrolyte brush (dashed line), the change in thickness with respect to external salt concentration follows a slightly different trend.

This difference occurs when the brush enters the osmotic brush regime at the lower salt concentrations. In this regime, a significant electrostatic potential develops between the brush and bulk solution, and the weak charge groups respond to the unfavourable conditions by discharging themselves. Because of the discharging process, a weak brush in the osmotic brush regime is less expanded than the strong brush. For the weak brush, the exact maximum thickness, which occurs at the transition point between the osmotic and salted brush regimes, will also depend on the grafting density and pH.[126]

PAA forms a weak polyelectrolyte brush. Indeed, Wu *et al.* show that for a wide range of pH values at a range of grafting densities, PAA will follow the general trends shown in Figure 3.4.[126,151] These results are in-line with theoretical predictions that have been presented in the past.[152] There have been a number of different models which have been introduced in an attempt to predict the complex behaviour of weak polyelectrolytes. As an example, Israels *et al.* used self-consistent mean-field theory to derive a model to predict how brush thicknesses may vary with respect to changes in the pH and salt concentration of the surrounding solution. However, oversimplifying assumptions led to poor estimations of brush thicknesses in a number of situations.[152] In addition, Gong *et al.* introduced a model based on molecular theories that predicts heights of brushes with regards to the interplay between factors such as the bulk pH, ionic strength and grafting density of the polymer brush. The predictions were generally in good agreement with experimental observations, except for one area in which the model broke down. Specifically, at very high pH values experimental observations were incorrectly predicted due to the phenomenon of counterion condensation.[153] A model by Hehmeyer *et al.* explicitly took into account this effect of counterion condensation

and experimental observations tested thus far seem to agree well with the predictions.[154]

Nap *et al.* also present an important molecular theory which looks at how the properties of weak polyelectrolyte brushes vary when grafted onto different substrate geometries such as planar, cylindrical and spherical surfaces. The role of surface geometry is becoming particularly important now that polymer coated nanoparticles and AFM tips of nanometer dimensions are increasingly being used. Polymer brushes are known to be highly inhomogeneous due to constraints imposed by the presence of the substrate and also because of interactions between neighbouring chains. Due to the intrinsic inhomogeneous densities within a polymer brush layer, the concentrations of ions and protons will vary as a function of the distance from the substrate. Correspondingly, the degree of dissociation within a polymer layer will also vary. Furthermore, if you tether these polymer chains to a substrate with a surface curvature the inhomogeneity of the brush will increase substantially due to variations in polymer density throughout the layer, and also because of subsequent interactions between these chains. Nap *et al.* show that the degree of dissociation within a polymer brush will increase with an increase in curvature of the surface that it is bound to. Furthermore, they found that the nature of interactions, such as the repulsive force between two surface grafted layers, will depend largely on the surface geometry of the underlying substrate. For example, the repulsion between polymer brush layers on cylindrical surfaces are much lower than the corresponding interactions between two planar films under the same conditions. This is due to the fact that in the case of the cylindrical surfaces the polymer chains have a greater ability to fold back towards the substrate.[151] These results have particular

relevance when studying the interactions between polymer brush-functionalised substrates of different shapes.

## 3.2 Materials and Methods

### 3.2.1 Chemicals and Materials

Tert-butyl acrylate (tBA, $M_n$ = 128.17, 98%), poly(acrylic acid) (PAA, $M_W$ = 450000), *N,N,N',N",N"*-pentamethyldiethylenetriamine (PMDETA, 99%), copper bromide (Cu(I)Br and Cu(II)Br2), trifluoroacetic acid (TFA, 99%), toluene (anhydrous, 99.8%), triethylamine (≥99.5%), Dulbecco's phosphate buffered saline (PBS), 3-(bromomethyl)phenylboronic acid (90%) and diethyl ether (99%) were purchased from Sigma-Aldrich and used as received. Cu(I)Br was kept under vacuum until use. The silane initiator (3-trimethoxysilyl)-propyl 2-bromo-2-methylpropionate was purchased from Gelest. Acetone (technical) was purchased from Thermofisher Scientific. Dichloromethane (DCM, ≥99.8%) was purchased from Honeywell. Dimethylformamide (DMF, ≥99.9%) was purchased from VWR Chemicals. Silica particles (unfunctionalised) were purchased from Bangs Laboratories (mean diameter of 300 nm). Silicon wafers (100 mm diameter, ⟨100⟩ orientation, polished on one side/reverse etched) were purchased from Compart Technology Ltd. All plasma treatment was carried out using a Henniker Plasma Vacuum System HPT-200. An SG2 – SevenGo pH meter (Mettler Toledo) was used for all pH measurements.

### 3.2.2 Polymer Brush Synthesis on Planar Silicon Substrates

Polymer brushes were synthesized via the "grafting from" method using atom transfer radical polymerization (ATRP). In order to deposit the silane initiator monolayer on the silicon substrates, samples of silicon wafer (1 x 1 cm) were initially plasma-oxidized (10 minutes, air). Following this they were immersed in a solution of silane initiator (3-

trimethoxysilyl)-propyl 2-bromo-2-methylpropionate (30 µL) and triethylamine (50 µL) in anhydrous toluene (30 mL) and incubated in this solution at room temperature overnight. Samples were then washed with ethanol and dried under a stream of nitrogen. The dry thickness of the silane initiator layer was near 2 nm, as measured using spectroscopic ellipsometry.

PAA brushes were fabricated through a two-step process: the protected monomer tert-butyl acrylate (tBA) was polymerized first, followed by deprotection to afford brushes of PAA. PtBA brushes were generated following a method adapted from Lego *et al*.[147] Prior to use, tBA was purified by passing through a column of basic alumina and freshly distilled under vacuum (78 mBar) at a temperature of 61-63˚C. Freshly purified and distilled tBA (30 mL, 205 mmol), PMDETA (122 µL, 584 µmol), $CuBr_2$ (3 mg, 13 µmol), and acetone (16 mL) were degassed via argon bubbling for 30 minutes. CuBr (65 mg, 453 µmol) was then very quickly added to this flask before degassing for a further 30 minutes. Initiator-coated silicon substrates were placed in reaction vessels which were subsequently degassed via three cycles of high vacuum/argon gas refilling and heated to 60˚C. The monomer solution was then transferred to these reaction vessels under inert atmosphere and polymerization was allowed to proceed at 60˚C. To stop polymerization, samples were immersed in acetone, rinsed with ethanol, deionised water, and dried under a stream of nitrogen. If necessary, silicon wafers were further cleaned through brief sonication in acetone. For the deprotection of PtBA brushes, samples were immersed overnight in a DCM/TFA solution (10:1 (v/v)) at room temperature. The samples were then washed well in ethanol, deionised water, and then dried under a stream of nitrogen.

### 3.2.3 Characterisation of Planar Polymer Brushes

Dry brush thicknesses were measured using an α-SE ellipsometer from J.A. Woolam Co., Inc., Ellipsometry Solutions. φ and *Δ* were measured at wavelengths between 400 and 900 nm and a fixed incidence angle of 70˚. For measurements of brush thicknesses when submerged in solution, substrates were placed in a sealed chamber fitted with quartz windows normal to the incident and reflected beam paths. Different solutions were then flowed through the chamber and their effect on the brush thickness was measured with the ellipsometer. Measurements were taken in triplicate and were taken once the brush thicknesses had maintained equilibrium. For data analysis, all coatings were treated using a Cauchy model built on top of a silicon/native oxide or gold substrate, depending on the system studied.[155] For dry measurements of PtBA and PAA brushes, refractive indices measured were 1.53 and 1.52, respectively (measured at λ = 632.8 nm). For measurements in solution, refractive indices varied between 1.38 in PBS and 1.41 in deionised water (depending on swelling and associated hydration).

Fourier transform infrared–attenuated total reflectance spectroscopy (ATR-FTIR) was carried out using a Bruker Tensor 27 with an MCT detector (liquid $N_2$ cooled). Spectra were acquired at a resolution of 4 $cm^{-1}$ with a total of 256 scans per run. Nitrogen was run through the system during measurements in order to limit the effects of environmental fluctuations. Contact angle measurements (using the sessile drop method) were taken using a Kruss DSA100 instrument using 3 µL droplets of deionised water. Measurements were carried out on three independent samples and for each sample an average reading was taken using measurements taken from three separate regions of the sample.

XPS was carried out on a Thermo Scientific K-Alpha X-ray XPS System using a monochromatic AlKα source. This was operated at 150 W under ultrahigh vacuum conditions ($10^{-9}$ mBar). As the surfaces were not electrically conductive, a built-in spectrometer charge neutralizing system was used, which compensates for sample charging during measurements by flooding the surface with low energy electrons (< 20 eV). To be able to compare data, the C1s hydrocarbon peak at 285.0 eV was used as an external standard for calibration of the binding energy (BE) scale. In order to identify the main peaks by their binding energies, survey spectra were collected from 1200 to 0 eV. In addition, high-resolution XPS spectra were acquired for O1s, C1s, and Si2p signals. An analyzer pass energy of 1 eV and 0.1 eV was used for the survey spectra and high-resolution spectra, respectively.

### 3.2.4 Synthesis of Polymer Brush-Coated Silica Nanoparticles

Silica beads were dispersed in deionised water for storage. To transfer them to a new solvent, beads were centrifuged at 5000 rpm for several minutes until the beads fully precipitated. The solvent was then carefully aspirated as much as possible using a syringe and the new solvent was added to the vial. The vial was then sonicated for 5 to 10 minutes until the suspension became cloudy. The sonication and centrifugation sequence was repeated three times to transfer the beads to the new solvent.

For grafting of the silane initiator the beads were transferred from water to ethanol and then to toluene using the aforementioned method. 50 mg of the beads were dispersed in a solution of anhydrous toluene (1 mL), triethylamine (50 µL) and silane initiator (10 µL) and left stirring overnight. The beads were then washed in toluene three times using

the sonication-centrifugation method and then transferred to acetone and left in 1 mL of the solvent in the fridge ready for the polymerization step.

The protocol for PtBA polymer brush synthesis from particles is a slight adaptation of the polymerization protocol used for planar silicon substrates. An extra 2 mL of acetone was initially added to the 1 mL silica dispersion and this was then degassed for 30 minutes with argon bubbling. Freshly purified and distilled tBA (3.0 mL, 21 mmol), acetone (1.6 mL), PMDETA (12 µL, 58 µmol) and $CuBr_2$ (0.3 mg, 1.34 µmol) were degassed for 30 minutes whilst mixing. The top was opened and CuBr (6.5 mg, 45.3 µmol) was quickly added to the monomer solution followed by a further 30 minutes of degassing. Next, 2.5 mL of this monomer mixture was extracted and added to the reaction vessel containing the 3 mL particle suspension. This resulted in a monomer/catalyst solution in which particles were suspended at identical concentration to the solutions used to grow brushes from planar silicon substrates, therefore enabling comparison of polymerisation rates. The syringe used to extract the monomer mixture was flushed with argon three times prior to use.

Polymerization was then carried out at 60˚C whilst stirring. Degassing was continued for a further 30 minutes and the reaction vessel was then covered with parafilm. To terminate polymerization, the reaction mixture was bubbled with oxygen for a couple of minutes. The $SiO_2$-polymer suspension was then centrifuged, washed in acetone three times and transferred into DCM/TFA (10:1 (v/v), 1 mL) and left stirring overnight at room temperature. The resulting PAA beads were washed in DCM three times and transferred into acetone for storage in the fridge.

The sizes and zeta potentials of functionalised silica particles were measured using a Malvern Zetasizer Nano ZS. For measurements, PtBA and PAA brushes were grown from

300 nm silica beads, then dispersed in ethanol or deionised water respectively, and then sonicated whilst shaking at regular intervals until a cloudy solution was obtained. Measurements of non-functionalised silica beads were carried out with beads dispersed in deionised water. Three independent repeats were obtained at room temperature for each sample and the average result was taken.

### 3.2.5 Functionalisation of Poly(Acrylic Acid) Brushes

In order to functionalise PAA brushes with boronic acid, PAA brushes were initially synthesised on silica using ATRP of PtBA, followed by treatment in DCM/TFA, as described previously. The functionalisation protocol was adapted from the procedure used for the functionalisation of free PAA (see Chapter 2). Initially, the base was dissolved in deionised water. 3-(bromomethyl)phenylboronic acid was separately dissolved in DMF and then added dropwise to the base/$H_2O$ solution. The solution was then heated to the required temperature and a PAA brush substrate (1 x 1 cm) was added to the solution and left for a set period of time. Substrates were washed using deionized water and ethanol and then dried under a stream of nitrogen. Thicknesses were measured on dried substrates via ellipsometry, before and after functionalisation. In addition, control substrates were used, with no bromotoluene-boronic acid in solution, in order to measure the effects of the reaction conditions on the brush thickness. PAA brushes of an initial thickness of approximately 30 nm were used in all cases. Thicknesses were systematically measured before and after functionalisation.

Next, functionalisation was attempted using $Na_2CO_3$ as the base instead of NaOH. This was to determine whether the selection of base used within experiments had a significant effect on brush functionalisation. Initially the protocol was developed on free

PAA (450000 g/mol) in order to be able to quantify the functionalisation level by NMR. PAA (200 mg, 2.78 mmol) was initially dissolved in a solution of $Na_2CO_3$ (221 mg, 2.08 mmol) and deionized water (1.6 mL), which was then heated to 50˚C. 3-(bromomethyl)phenylboronic acid (89.6 mg, 417 µmol) was separately dissolved in DMF (0.4 mL) and then added to the polymer solution dropwise. The mixture was then left at 50˚C overnight. The cooled reaction mixture was precipitated in diethyl ether followed by two precipitations in acetone, whilst re-dissolving in deionized water. The polymer was then left for several days to dry under reduced pressure. Molar equivalences of 0.15:0.75:1 for conjugate:base:polymer were used, leading to a functionalisation of 3.3%, as quantified via NMR. This functionalisation procedure was then adapted for use on brush samples. The procedure used was the same as mentioned in the previous paragraph, except for the replacement of the NaOH base with $Na_2CO_3$. All of the reaction concentrations are described in detail in Table 3.1 in section 3.3.3. $^1$H NMR spectra were obtained using Bruker's 400 MHz spectrometers (Bruker AV 400 and AVIII 400) and data was analysed using Bruker's IconNMR software.

## 3.3 Results and Discussion

### 3.3.1 Development of Polymer Brushes on Planar Silicon Substrates

Due to the fact that ATRP is sensitive to the presence of acids, PAA was generated through a two-step process. The method presented by Lego *et al.* was chosen for initial ATRP of PtBA brushes.[147] This procedure uses the copper(I) bromide/PMDETA complex, which is reported to be very active but is not suitable for aqueous ATRP due to very fast disproportionation.[133,156] Accordingly, the organic solvent acetone is used in this procedure and a slower brush growth is to be expected. For deprotection of PtBA, a protocol introduced by Lego *et al.* was also used. Although a number of other methods reviewed were faster for fully deprotecting the brush, this method was selected to selectively deprotect tert-butyl groups from the surface with minimal chain cleavage. Indeed, Lego *et al.* showed that during longer exposure times to the dilute trifluoroacetic acid, there is still negligible cleavage of both the polymer chains and initiator layer from the surface.[102] This is an important feature as other techniques reviewed all appear to suffer from some reduced surface coverage of the polymer layer during the time it takes for complete cleavage of the tert-butyl groups. Figure 3.5 schematically shows the procedure used for generation of PtBA brushes, their conversion upon mild treatment with dilute trifluoroacetic acid and also possible routes to their functionalisation.

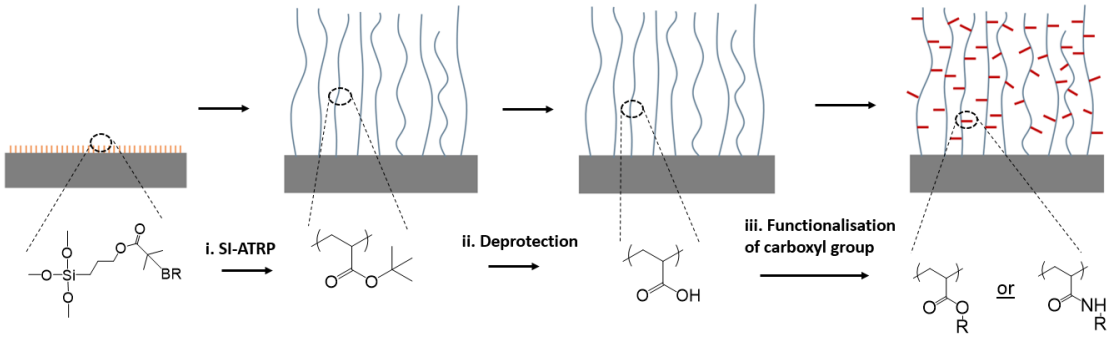


**Figure 3.5.** The process used to generate PtBA brushes via the "graft from" approach, their conversion upon mild treatment with dilute trifluoroacetic acid, and possible routes to generate functionalised PAA brushes.

The growth kinetics of the PtBA brushes (monitored via ellipsometry) was 3-4 fold faster than that previously reported in similar conditions, but appeared relatively linear (Figure 3.6A). However, Lego *et al.* had monitored brush growth via AFM, potentially underestimating thicknesses measured, due to the compression of the brush by the AFM tip.[128] In addition, the silane monolayers generated in the present study may display a higher density, resulting in higher brush densities and thickness growth profiles, although direct comparison is not possible. During experiments extra care was taken to remove any oxygen from the reaction vessels as otherwise the growth rate of the polymer was found to be severely inhibited.

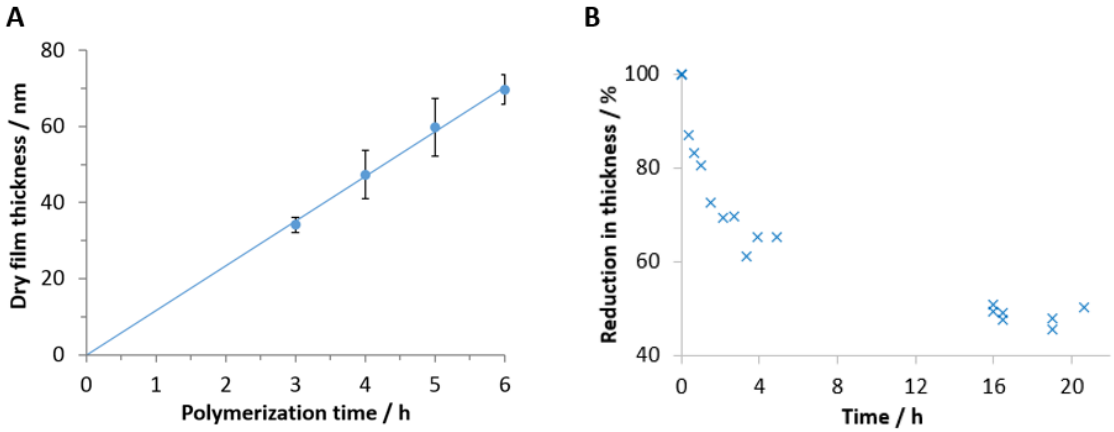


**Figure 3.6.** (A) Kinetics of the growth of PtBA polymer brushes from silicon substrates, monitored by ellipsometry. Error bars show standard errors for repeats across samples (sample size n = 3). (B) Reduction in dry ellipsometric thickness of PtBA brushes during the deprotection of t-butyl esters. PtBA brushes were immersed in a solution of dichloromethane/trifluoroacetic acid solution (10:1 v/v) at room temperature overnight. Thickness values are given as a percent of the original thickness.

The deprotection of PtBA brushes was subsequently monitored by ellipsometry (Figure 3.6B), indicating a rapid decrease in the dry thickness of the brush upon incubation in DCM/TFA solutions. This reduction in thickness was due to the loss of tert-butyl groups and the associated increasing hydrophilicity and chain relaxation. After overnight incubation in the DCM/TFA solution, the polymer thickness dropped to around 50% of its original value. This is in line with previous reports[102] and with the predicted reduction in molar mass of repeat units and associated dry film thickness (52%).[126] The FTIR spectra of PtBA brushes before and after deprotection confirmed the full conversion to PAA brushes (Figure 3.7), with the clear disappearance of the alkyl C-H stretch at 2976 $cm^{-1}$, the disappearance of the C-H bending of $C(CH_3)_3$ at 1367 $cm^{-1}$, and the shift (and broadening) of the carbonyl band from 1730 to 1712 $cm^{-1}$.[101,102,157]

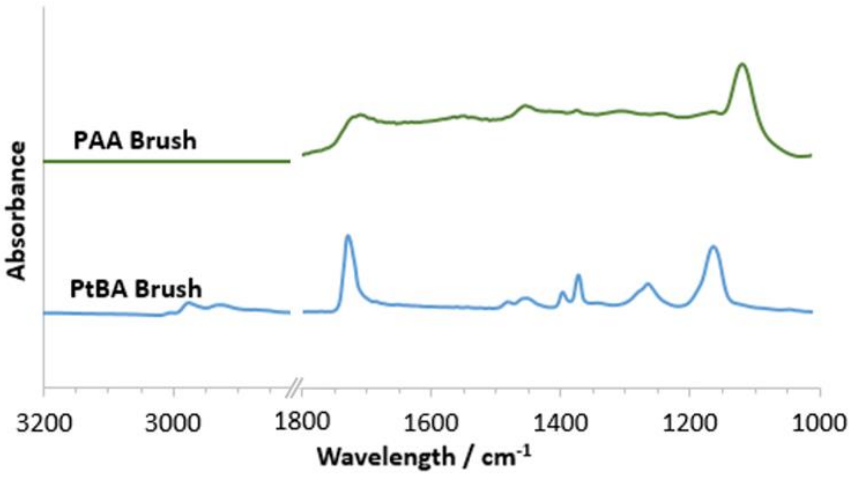


**Figure 3.7.** FTIR characterisation of PtBA brushes before and after deprotection. The full conversion of the brushes to PAA is represented by the clear disappearance of the tert-butyl bending bands at 2976 and 1367 $cm^{-1}$, and the shift (and broadening) of the carbonyl band from 1730 to 1712 $cm^{-1}$.

The conversion of PtBA is further confirmed by XPS spectra of the PtBA brushes before and after deprotection (Figure 3.8). The C1s range of the spectra was deconvoluted into three peaks corresponding to carbon atoms associated with C-C, C-O and C=O peaks. The peak associated with carbon atoms involved in C-O bonds was found to shift and broaden upon deprotection. In addition, the atomic percentages and corresponding binding energies of the C1s and O1s signals were extracted from the XPS survey spectra (Figure 3.8C), clearly indicating a reduction in the carbon content relative to oxygen following the deprotection of tBA groups. Both observations are in accordance with the expected change in the chemical structure of the brush, and in agreement with previously reported XPS characterisation data for these surfaces.[132,139,158]

A C1s Spectrum of PtBA

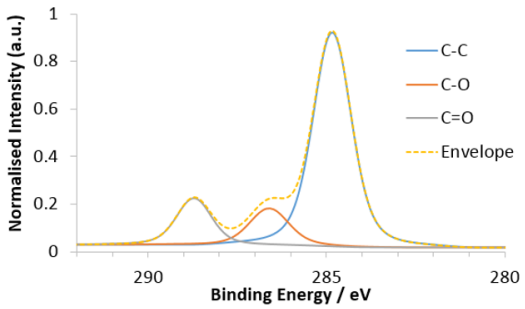


B C1s Spectrum of PAA

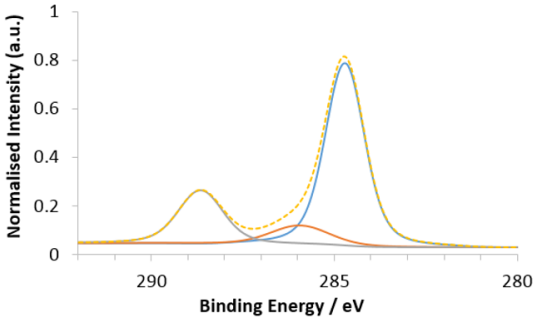


C Survey Scan Peaks

| Element and its orbital | Atomic % | | Binding Energy / eV | |
|---|---|---|---|---|
| | PtBA | PAA | PtBA | PAA |
| C1s | 79.56 | 68.37 | 285.51 | 285.48 |
| O1s | 20.44 | 31.63 | 533.02 | 532.96 |

**Figure 3.8.** XPS spectra for the characterisation of PtBA and PAA planar polymer brush surfaces. (A) High-resolution deconvoluted spectra for PtBA C1s signals. (B) High-resolution deconvoluted spectra for PAA C1s signals. (C) Atom composition (C1s and O1s) and corresponding binding energies of the main peaks measured for PtBA and PAA brushes.

The swelling of the corresponding brushes was characterised via *in situ* ellipsometry. The swelling ratio (Q), defined as the ratio between the wet (L) and dry (D) ellipsometric thicknesses (Q = L/D), was close to unity prior to deprotection of PtBA brushes (Figure 3.9A), as expected from the hydrophobicity of tert-butyl acrylate repeat units. In contrast, PAA brushes were characterised by high swellings in deionized water and 150 mM NaCl solutions; this is in agreement with the expected behaviour of weak polyelectrolytes in the osmotic regime, characterised by high proton dissociation at neutral pH, substantial electrostatic repulsion between repeat units and the associated stretching of polymer chains.[36,126,152]

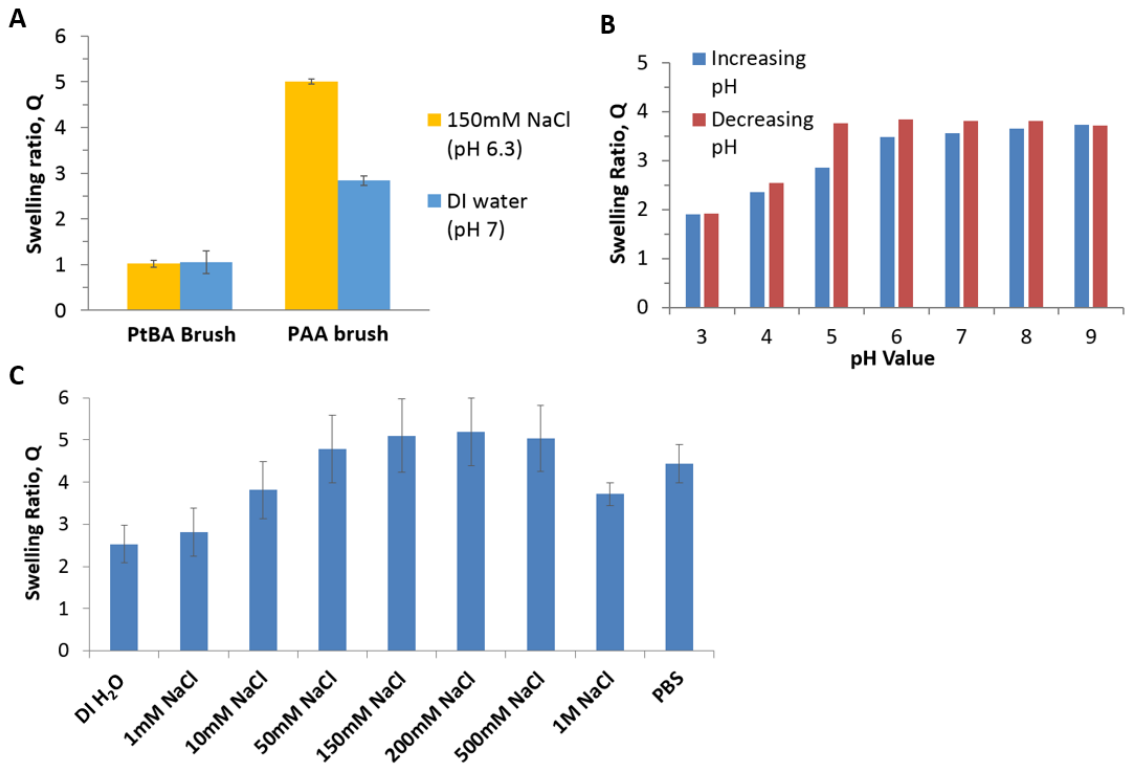


**Figure 3.9.** (A) Ellipsometric swelling ratio measured for PtBA and PAA brushes in deionised water (DI) and 150 mM NaCl aqueous solutions. (B) Ellipsometric swelling ratio of PAA brushes submerged in 150 mM NaCl at different pH values. Thickness measurements were initially taken sequentially from pH 3 upwards and then taken again when decreasing the pH. (C) Ellipsometric swelling ratio of PAA brushes (pH kept at 7.0 ± 0.4, except for PBS which had a pH of 7.4). Error bars show standard errors for repeats across samples (sample size n = 3).

The swelling ratio was further characterised at different pH values, with initial measurements taken sequentially from pH 3 upwards followed by measurements looking at the collapse of the brush with a decrease in pH (Figure 3.9B). The results show that as the pH rises the swelling increases due to the increasing dissociation of PAA brushes at higher pH values. At the tested ionic strength of 150 mM NaCl, the data for "increasing pH" shows that the increase in brush swelling stops at around pH 7 and above, in agreement with the results obtained by Currie *et al.* and associated with the brush reaching a maximum degree of dissociation.[159] The PAA brush also appears to display swelling hysteresis. When the brush is in a state of collapse, with the drop in pH,

the brush appears to maintain slightly higher thicknesses. These results compare with experiments performed by Willott *et al.* who demonstrated hysteresis in the swelling/collapse of a poly(2-(diethylamino)ethyl methacrylate) (PDEA) brush upon changes in pH. They attribute the hysteresis to the formation of a dense, more hydrophobic outer region of the polymer that forms upon deprotonation of the periphery of the brush. This barrier slows down the expulsion of solvent and counterions from the brush during collapse.[160] Furthermore, this hysteresis in the swelling/collapse of brushes was also identified by Mahentha *et al.* for poly(dimethylaminoethyl methacrylate) (PDMAEMA) brushes.[161]

The swelling ratio of PAA brushes was also characterised in PBS and in aqueous NaCl solutions at a range of ionic strengths (Figure 3.9C). The thickness was found to depend on the ionic strength in a non-monotonic fashion. Specifically, the swelling initially increased with the ionic strength, due to increasing proton dissociation and associated hydrophilicity. As the salt concentration increased further, the brush appeared to enter the neutral brush and salted brush regime and electrostatic interactions became largely screened, resulting in a decrease in brush thickness.[126,152] Finally, contact angle measurements were in agreement with the increase in hydrophilicity and brush swelling following the deprotection of PtBA brushes. Average contact angles shifted from 87.0 ± 1.1˚ to 37.4 ± 1.2˚ for PtBA and PAA brushes, respectively (Figure 3.10).

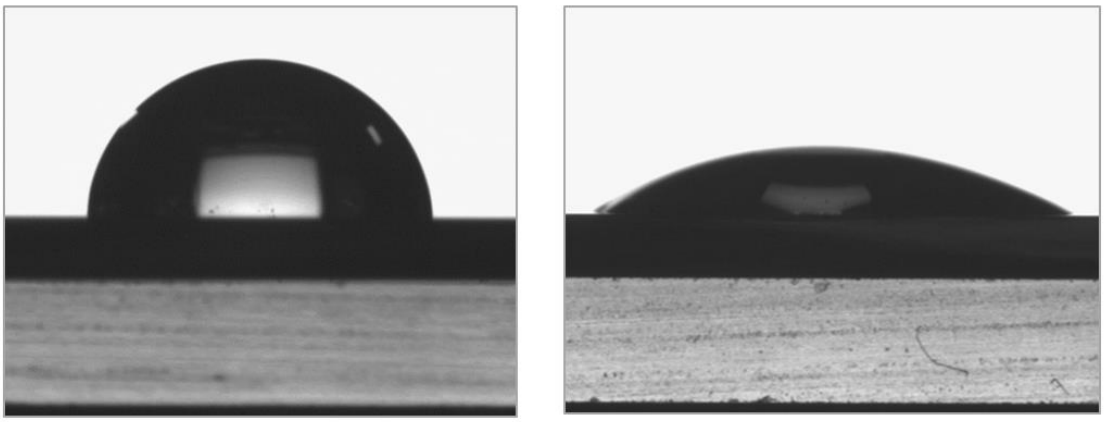

**Figure 3.10.** Contact angle images for PtBA brush (left) and PAA brush (right) on silica. PtBA brushes have a contact angle of 87.0 ± 1.1˚ and a 60 nm thickness. PAA brushes have a contact angle of 37.4 ± 1.2˚ and a 36 nm thickness. Thicknesses were quantified via ellipsometry.

All of this data obtained gives results consistent with the reported behaviour of PAA brushes. This, alongside the FTIR (Figure 3.7) and XPS (Figure 3.8) characterisation, confirms the formation of PAA brushes with controlled thickness and high grafting densities.

## 3.3.2 Development of Polymer Brush-Coated Silica Nanoparticles

The hydrodynamic diameter of nanoparticles coated with PtBA and PAA brushes was compared to that of uncoated nanoparticles (see Figure 3.11). The diameter of uncoated nanoparticles was found to be 320 ± 10 nm and increased to 390 ± 10 nm and 530 ± 10 nm for $SiO_2$-PtBA and $SiO_2$–PAA particles, respectively. This is in good agreement with the expected dry thickness of PtBA brushes (not swollen in ethanol), which were found to grow to 60 nm in 5 hours, from silicon substrates (Figure 3.6A). The significant increase in hydrodynamic diameter observed for PAA-coated nanoparticles is in agreement with their pronounced swelling in deionised water (the diameters measured

correspond to a swelling greater than 3) and the decrease in hydrophobicity associated with the deprotection of tBA groups. In addition, the ζ-potentials measured for $SiO_2$-PtBA and $SiO_2$–PAA particles were 23.1 ± 0.1 mV and -29.3 ± 0.1 mV, respectively, although these values are only qualitatively indicating the charge of the associated particles (PtBA particles did not re-suspend in aqueous solutions, therefore preventing direct comparison with PAA-coated particles). Hence, the charge reversal of the ζ-potential is consistent with a significant change in surface chemistry of these particles and the introduction of negatively charged carboxyl groups following the deprotection step.

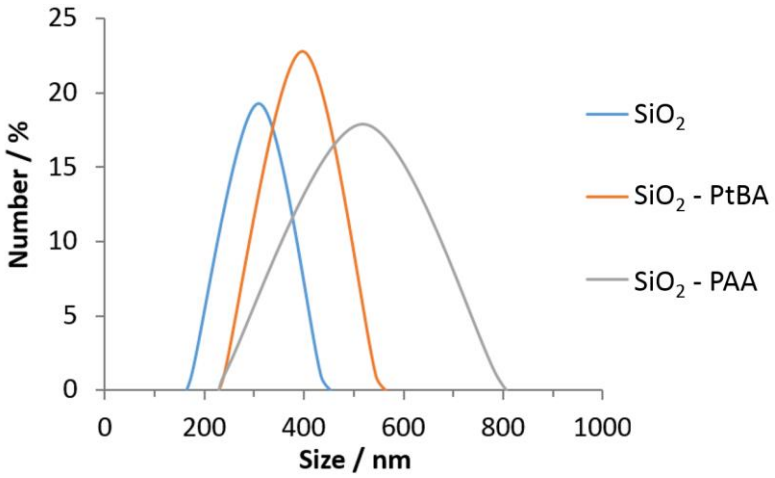


**Figure 3.11.** Dynamic light scattering data of functionalised and non-functionalised 300 nm silica microparticles. $SiO_2$ beads and PtBA functionalised beads were dispersed in ethanol and PAA in deionised water.

## 3.3.3 Functionalisation of Poly(Acrylic Acid) Brushes

Initial functionalisation attempts of PAA brushes focussed on adapting the established protocol that was used for the conjugation of bromotoluene-boronic acid to free PAA (see Chapter 2). The chemical quantities used are under 'condition A' in Table 3.1. Table

3.2 gives the ellipsometric thickness measurements obtained under 'condition A' at a variety of reaction temperatures and time lengths. Thickness readings for the control sample (with no boronic acid in solution) indicate that significant degradation of the PAA brush is occurring. This degradation even occurs at low temperatures (room temperature) and time frames as low as 1.5 hours.

**Table 3.1.** Different reaction conditions used for the functionalisation of PAA brushes with bromotoluene-boronic acid.

| **Solute/Solvent** | **Conditions** | | |
|---|---|---|---|
| | **A** | **B** | **C** |
| **NaOH** | 4.17 mg (30 mM) | | |
| **$Na_2CO_3$** | | 221 mg (520 mM) | 0.4 mg (1 mM) |
| **Deionized water** | 3.5 mL | 3.6 mL | 3.5 mL |
| **DMF** | 0.1 mL | 0.4 mL | 0.1 mL |
| **3-BMPBA** | 8.96 mg (12 mM) | 89.6 mg (105 mM) | 8.96 mg (12 mM) |

For the samples with boronic acid in solution there is still a reduction in the brush thickness, although to a much lesser extent. This suggests that there may be some conjugation of the boronic acid that is occurring and counteracting the degradation in brush thickness due to the reaction conditions. Lower reaction temperatures were investigated as it was thought that high temperatures may be contributing to the degradation of the polymer brush. However, even at room temperature, there was significant reduction in both the control and functionalised surface thicknesses. Across different tests there are often only small deviations in the reductions in thickness obtained, which may partly arise from small differences in the starting thicknesses of the PAA brushes.

**Table 3.2.** Changes in PAA brush thicknesses under different bromotoluene-boronic acid functionalisation conditions. Conditions used are detailed in Table 3.1.

| Condition | Temperature (˚C) | Time | % Reduction in Thickness | |
|---|---|---|---|---|
| | | | Control | Functionalised Sample |
| **A** | 70 | Overnight | 74% | 31% |
| | 50 | Overnight | 71% | 30% |
| | | 1.5 h | 71% | |
| | | 6 h | 73% | |
| | 25 | Overnight | 75% | 40% |
| **B** | 50 | Overnight | 70% | 65% |
| **C** | 50 | Overnight | 27% | -2.5% |

XPS spectra were obtained for the brush left at 70˚C overnight in order to determine if there was any conjugation of boronic acid within the brush (Table 3.3). When comparing the ratio of the atomic percentages to that of an unfunctionalised PAA brush there are small differences, presumably due to degradation of the brush structure under the reaction conditions. The brushes were also scanned for boron content; however, there was no peak detected. FTIR data was also obtained for the brushes, but due to the large reduction in the brush thicknesses under the reaction conditions minimal polymer remained and no meaningful peaks could be distinguished from the spectra.

**Table 3.3.** Atom composition (C1s, O1s and B1s) for different polymer brush chemistries, extracted from XPS spectra. PAA-BA refers to PAA brushes functionalised with bromotoluene-boronic acid.

| Brush Chemistry | Conditions | Element Atomic % | | |
|---|---|---|---|---|
| | | O1s | C1s | B1s |
| **PAA** | Non-functionalised | 31.63 | 68.37 | N/A |
| **PAA-BA** | Condition A, 70˚C | 39.70 | 60.30 | 0 |
| **PAA-BA** | Condition C, 50˚C | 31.49 | 68.51 | 0 |

As there was no indication of successful boronic acid conjugation and as significant degradation of the control samples was occurring a different approach was attempted. Conditions B and C (see Table 3.1) used sodium carbonate as the base instead of sodium hydroxide. The functionalisation procedure was initially developed on free PAA in order to quantify conjugation through NMR. Figure 3.12 shows the NMR spectra obtained, illustrating successful conjugation of boronic acid. A functionalisation level of 3.3% was calculated from the ratio of the integrals of the polymer backbone peaks ('a' and 'b') to those of the phenyl ring (peaks 'd'-'g'). From the ellipsometric data for Condition B (Table 3.2), a large reduction in the thickness of both the control and functionalised sample was still observed. As a result, functionalisation was investigated under Condition C, which used much lower concentrations of the solutes. Ellipsometric data under these conditions illustrated a much lower reduction in the thickness of the control and indicated a slight increase in the thickness of the functionalised sample (2.5%). Consequently, XPS spectra were obtained for this sample (Table 3.3); however, results again showed no detection of a boron peak.

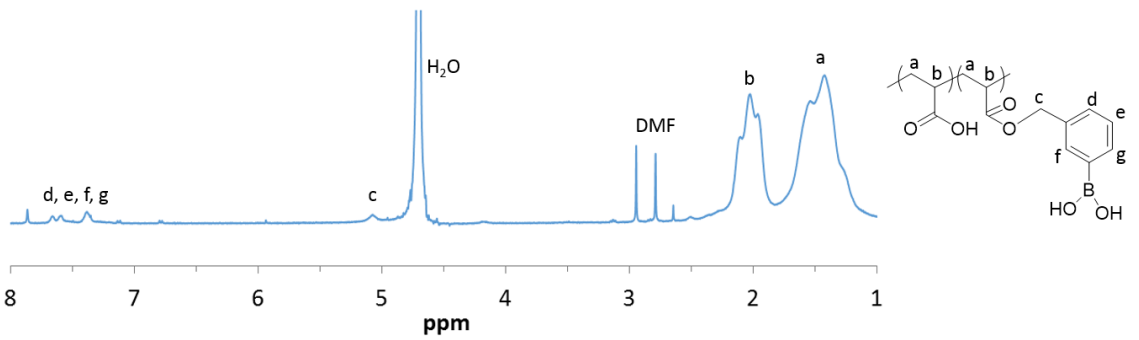


**Figure 3.12.** $^{1}H$ NMR spectroscopy of the functionalised product of free poly(acrylic acid) and 3-(bromomethyl)phenylboronic acid in $D_2O$. The reaction conditions were replicated from the protocol used to functionalise the brush, with $Na_2CO_3$ as the base.

Using the equation provided by Tan *et al.*, we are able to calculate the increase in brush thickness that would be expected following functionalisation.[85] This equation is given below and describes the relationship between several variables: the molar mass of the repeat unit ($M_0$), the molar mass of the fragment added ($M_x$), the starting thickness ($h_0$), the change in thickness ($\Delta h$) and the functionalisation level (f).

$$\Delta h = \frac{f h_0 M_x}{M_0}$$

Considering a 30 nm brush starting thickness and a functionalisation level of 3.3%, we would only expect to see a 2.95 nm increase in the brush thickness. This functionalisation level of 3.3% is the level obtained on free PAA (see Figure 3.12), and as such we may expect a reduced functionalisation level for the polymer brush due to the lower penetration of the boronic acid molecules throughout the brush structure. On the other hand, the large excess of reagents for polymer brush functionalisation may lead to an increase in functionalisation levels. Nonetheless, in these regions of low functionalisation, it is possible that the boronic acid content may in fact be too small to detect by characterisation techniques such as FTIR or XPS.

From the results obtained, significant reduction in the thickness of the control brush is occurring even at room temperature (see Table 3.2). When the concentration of the base is largely reduced (Condition C) there appears to be a drop in this reduction. As such, we expect the brush degradation results partly from a high concentration of base within solution. However, it could equally be affected by a combination of other factors such as DMF concentration and temperature. Indeed, when reviewing the literature a number of papers reported on the degradation of polymer brushes under various

conditions.[162–166] The exact mechanism for polymer chain scission is not known, but it is thought that the degradation is facilitated by solvent-induced stretching and also by hydrolysis of the ester or silane.[162,163,165] Borozenko *et al.* report that for PAA brushes covalently immobilized on glass, polymer degrafting occurs at pH ≥ 9 when 10 mM NaCl is added, whereas no cleavage occurs between pH 6.5 and 10.5 in the absence of NaCl.[162]. Furthermore, Menzel *et al.* investigated a number of polyelectrolyte brushes and found that solvent quality and temperature strongly affect their stability.[163] Moreover, other factors such as grafting density are shown to play an important role in brush stability. An increased number of chains per surface area results in greater chain stretching and a larger tensile stress on the chains.[164] All of these factors work in combination, increasing or decreasing the extension of polymer chains and their associated tension. Accordingly, it is thought that functionalisation techniques that are effective at lower temperatures and in "milder" conditions, such as DMTMM or EDC/NHS-mediated ligation, would be more appropriate for brush functionalisation. Indeed, there are several accounts of PAA brushes being successfully functionalised through EDC/NHS.[67,104,111]

## 3.4 Summary

To generate PAA brushes, we opted for the controlled growth of PtBA brushes, prior to their conversion upon mild treatment with dilute trifluoroacetic acid. PtBA brushes grew at a linear rate of approximately 12 nm per hour, as quantified via ellipsometry. Upon deprotection of PtBA, a reduction in thickness of around 50% was monitored as a result of the loss of tert-butyl groups and associated chain relaxation. The chemical structure of the resulting brush was confirmed through XPS and FTIR spectroscopy and the reduction in hydrophobicity, following deprotection, was confirmed through contact angle measurements. The swelling of the brushes, as measured via wet ellipsometry, was studied in solutions displaying various ionic strengths and pH. The identification of the osmotic, salted and neutral brush regimes confirmed the generation of a weak polyelectrolyte brush.

The protocols used for the generation of planar brushes were then adapted for use on 300 nm silica nanoparticles. The significant drop in $\zeta$-potential of the particles following conversion to PAA, and the dynamic light scattering data which confirmed brush thicknesses were in line with those on planar substrates, confirmed the successful generation of PAA brushes. Attempts were then made to functionalise planar PAA brushes with bromotoluene-boronic acid. The brush functionalisation was attempted under a number of different conditions. However, the absence of boronic acid in the brush structure was confirmed though XPS. It is believed that the “harsh” conditions required for PAA functionalisation with a bromo moiety were responsible. Through reviewing the literature, it is thought that brush degrafting is occurring through a mechanism of solvent-induced stretching facilitated by the high temperatures required for functionalisation, the solvents used, or the high concentrations of base. Accordingly,

functionalisation techniques that are effective at lower temperatures and in “milder conditions”, such as DMTMM or EDC/NHS-mediated ligation, may be more appropriate for PAA functionalisation. Originally, it was intended that brush functionalisation with boronic acid would allow the interaction of these moieties with cells/soft tissues to be probed within chapter 4. However, as this element of our experiments did not work as intended these investigations were not possible.

# CHAPTER 4

## Characterisation of Nanoscale Mechanical Properties of Brush-Cell/Tissue Interfaces

# 4.1 Introduction

The non-specific interactions between polymeric biomaterials and soft tissues play an important role in the performance of implants, tissue engineering scaffolds and drug delivery systems.[7,8,11–13] Physico-chemical interactions are particularly important in regulating the strength of bioadhesives, such as skin adhesives for surgical applications,[3–5] hydrogels for epicardial placement and stem cell delivery,[6] soft tissue adhesion for tissue regeneration[7,8] or mucoadhesives for dental adhesion.[9,10] Although a range of chemical functions and molecules have been introduced in biomaterials to promote covalent coupling and adhesion to soft tissues, the control and regulation of non-specific physico-chemical interactions with surrounding tissues post-implantation and delivery can play an important role and even dominate adhesion performance.[2] As an example, polymeric coatings introduced around nanomaterials for drug and gene delivery, or for imaging, can significantly impact their biodistribution and systemic persistence/clearance.[11,12,167] Typically, after bringing a polymer into contact with a soft tissue, initial physical entanglement will be followed by secondary bonding to strengthen adhesive interactions.[43] As is often the case in nature, these secondary bonds will be formed by multiple individually weak non-covalent bonds that combine to form a stable, highly specific, reversible and strong intermolecular connection. These intermolecular interactions typically involve a combination of hydrogen bonds, electrostatic interactions and Van der Waals interactions.[15] The design of interfaces with controlled chemistry and intermolecular interactions is particularly important in the modelling and understanding of biointerface adhesion.

In order to promote better adhesion to soft tissues, a greater understanding of the relationship between polymer chemistry and nanoscale adhesion mechanisms is

required. In this chapter the adhesion of three types of polymer brushes to cells and tissues is studied. Poly(acrylic acid) (PAA), poly(dimethylaminoethyl methacrylate) (PDMAEMA) and poly(olgioethylene glycol methacrylate) (POEGMA) were selected as three important types of polymer brushes with distinct physico-chemical properties (anionic, cationic and neutral hydrophilic polymers, respectively). These were grown from the surface of silica beads, and their adhesion to a variety of substrates was investigated via colloidal probe-based atomic force microscopy (AFM). Overall, although the non-specific adhesion of solid substrates, bacteria and proteins to polymer brushes has been widely studied, limited studies have focussed on non-specific adhesion to cells and tissues.

The three polymers were further selected based on their ease of fabrication, surface stability and their widespread use in the field of biomaterials. PAA is a highly hydrophilic polymer containing a high density of carboxylic acid groups with negative charges (at high pH). PAA has superior biocompatibility, good thin film formability and excellent water absorptivity, all of which give it great potential to be deployed in emerging fields of biomaterials.[36] PDMAEMA is a weak polybasic polymer with pH responsive properties[168] that has applications in gene delivery.[169,170] Finally, POEGMA is known for its excellent protein resistance arising from the high density of ethylene glycol moieties on the polymer backbone, its ability to grow at high grafting densities and its hydrophilicity.[171] As such, its applications include surface modifications and coatings that resist protein absorption and thus prevent bacterial adhesion and biofilm formation.[171–173]

Initially, the adhesion of these three brushes to a range of model monolayers presenting a range of chemistries (surface charge, hydrogen bonding and hydrophilicity) is

examined. Next, the impact of brush chemistry on adhesion to model cell monolayers is explored (epithelial cell sheets), and the impact of their glycocalyx on adhesion is investigated. Indeed, most epithelial cells are surrounded by a glycoprotein and glycolipid layer associated with their membrane known as the glycocalyx; this ranges from 7 nm in thickness for red blood cells up to several 100 nm in some cases.[174] Consequently, when an implanted material comes into contact with epithelial cell sheets, often lining the surface of tissues, the glycocalyx is the first point of contact and its interaction with the material is of significant importance. Finally, brush adhesion to tissues (gingival epithelium and epicardium) is explored and the impact of brush chemistry, as well as the tissue's mechanical properties, on adhesion is discussed. Within the introduction to this chapter, a couple of techniques (colloidal probe AFM and nanoindentation) will be reviewed, both of which will be relied upon heavily within the experimental section.

### 4.1.1 AFM Nanoindentation

AFM was originally developed as a topographic imaging technique. However, by quantifying the elastic properties of the cantilever the stiffness of the underlying substrate can also be determined.[175,176] As cantilevers can be purchased with a wide range of stiffness values this technique can easily be tuned for use on a variety of samples. In addition, this technique requires minimal sample preparation and it is a non-destructive testing method.

For the setup of an AFM system, an AFM cantilever is loaded onto a piezoelectric stage. This stage then moves the AFM tip into and out of contact with the surface of a sample

whilst the cantilever deflection is recorded via a laser aligned on the end of the tip (see Figure 4.3, section 4.2, for a diagram of the setup). The cantilever deflection (nA) is plotted against the total displacement of the piezoelectric stage (nm). In order to convert the cantilever deflection into a displacement, the cantilever is calibrated against a hard material such as a silcon wafer. By doing so, a calibration constant can be obtained which relates the recorded cantilever deflection to a set cantilever displacement. As the spring constant of the cantilever is known, the deflection can then be converted to a force using Hooke's law.

Although the setup for AFM nanoindentation is often trivial, the processing of data in order to produce meaningful information can often be more complex. Methods to obtain the stiffness and elastic modulus of hard elastic materials are often the best defined. One such method, which is very commonly used, is the Oliver-Pharr method.[177] This method was originally defined to be used with sharp indenters, such as a pyramidal Berkovich tip. However, it has since been extended for use with any axisymmetrical indenter geometry.[178] Its attractiveness stems largely from the fact that the technique does not require an image of the hardness impression, and mechanical properties can therefore be determined directly from load-displacement data. The method is built on the foundation developed by Sneddon[179] that defines the relationship between contact area of the tip, load and displacement. In the Oliver-Pharr method, the load-displacement data (from the unloading curve) is fit to a simple power-law expression:

$$P = \alpha(h-hf)^m$$

For this equation, 'P' is the indenter load and 'h' is elastic displacement. 'α', 'hf' and 'm' are fitting parameters from which the stiffness at peak load can be calculated. Oliver

and Pharr showed that this force-displacement relationship held for a number of different indenter geometries assuming that the contact is elastic. In the case of biological materials, it is highly likely that they will exhibit some time dependant mechanical response, and hence, this is a limitation that should be considered. Advanced models have been introduced which take into account viscoelastic behaviour;[180–182] however, these are significantly more complex to set up.

Another key parameter to consider with nanoindentation is the choice of indenter tip geometry. Using a broader tip, such as a spherical one, can significantly reduce plastic deformation compared with a sharper tip.[183] For some highly compliant materials the use of triangular tips may also present limitations due to issues associated with surface detection and data interpretation. Furthermore, tips with a larger radius enable the average mechanical properties of tissues to be determined, rather than the properties of individual tissue components such as elastic fibres.[184]

### 4.1.2 Nanoindentation of Soft Tissue

The mechanical properties of materials are controlled by their microstructure. In humans and mammals, a small number of ECM proteins control the mechanical behaviour of tissues. These proteins are generally thought to be much stiffer than the organ itself. When measuring the elastic stiffness of tissues, there is a general trend that as the structural scale of a tissue decreases the elastic stiffness of the tissue component increases (Figure 4.1). As such, new techniques such as nanoindentation using AFMs and ultra-high frequency acoustic imaging, significantly reduce the length scales at which mechanical information can be obtained, leading to new insight into how different tissue components influence mechanical properties.[185] Due to the high compliance of AFM

cantilevers, nanoindentation via this method offers a promising tool for the determination of the mechanical properties of highly compliant materials, such as soft tissues.[185] The mechanical behaviour of extremely compliant objects, such as cells, have also been investigated to a large extent using this tool.[186,187]

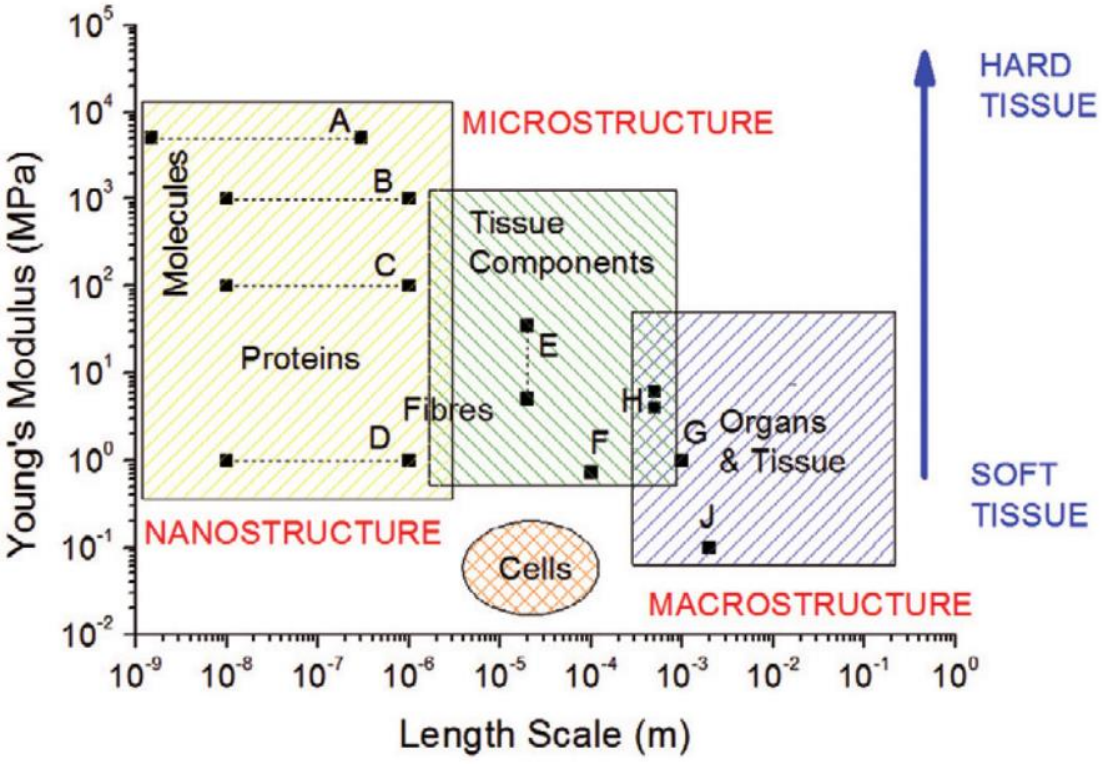


**Figure 4.1.** Elastic properties of soft tissues and their structural components at different length scales. Superimposed are measurements of the elastic moduli of aorta and ECM components at different length scales (A: single collagen fibrils, B: fibrillar collagen, C: fibrilin microfibrils, D: elastin, E: ferret aorta components, F: porcine aorta components, G: human radial artery, H: rat aorta, J: human aorta). Figure taken from Akhtar *et al*.[185]

The mechanical properties of cardiac muscle tissue have been extensively investigated via AFM nanoindentation.[188–195] A large proportion of these studies investigate the difference in mechanical properties between healthy and infarcted heart tissue.[188,189,194] Berry *et al.* investigated the elastic modulus of ligated and control rat tissue samples,

extracted from the left ventricular wall. They found that the baseline modulus for normal heart muscle was 18 ± 2 KPa, whereas infarcted animals had a threefold increase in elastic modulus (55 ± 15 KPa).[189] Similarly, Jacot *et al.* found that the elastic modulus of the epicardial surface, from the left ventricle of mice 30 days post myocardial infarction, was significantly higher in the ischemic region than in the non-ischemic region (56 ± 6 KPa vs. 21 ± 2 kPa, respectively).[194] Kossivas *et al.* found an elastic modulus of 14.7 ± 0.8 kPa for the epicardial muscle stiffness in sectioned, healthy murine left ventricular samples.[190] Soufivand *et al.* investigated the mechanical properties of cardiac myocytes from 13 to 15 days embryonic mouse hearts, finding elastic modulus values of either 48.08 ± 2.26 kPa or 55.67 ± 2.56 kPa, depending on which model they used.[192] Overall, from the papers reviewed for AFM nanoindentation of heart tissue, values for the elastic modulus of healthy heart muscle vary within the range of 15 to 100 KPa, with values depending on the specific region of tissue sectioned and the source used for animal samples (rats, mice or rabbits).[188–195]

The thickness of the oral mucosa can vary over a wide range depending on the location. In the canine mandible this has been shown to vary from 0.3 mm for the attached buccal mucosa to 6.7 mm in the maxillary tuberosity region.[196] The thickness is one of the main factors contributing to the mechanical response of the oral mucosa, and as such the elastic modulus of the tissue will vary significantly depending on location.[197] Although no papers could be found that explore the mechanical properties of the keratinized gingiva via nanoindentation, the elastic modulus, as determined via macroscale testing methods such as uniaxial tensile/compression tests, was found to be in the range of 0.06 to 8.89 MPa.[197–201] One of the more recent publications by Goktas *et al.* investigated the dynamic compressive properties (1 Hz; 15% strain) of the gingiva from the lower

mandible of pigs, finding an instantaneous and steady state elastic modulus of 7.81 ± 1.11 MPa and 0.86 ± 0.09 MPa, respectively, for the buccal attached gingiva.[201] It should be noted, however, that the 15% strain used within these studies is relatively high and we may expect some permanent deformation of the tissue samples to have occurred within this range. The Young's modulus value can depend heavily on the experimental method used, sometimes spanning orders of magnitude.[202] As such, it would not be surprising that modulus values obtained through nanoindentation would vary significantly from the values obtained through macroscale compression testing methods.

### 4.1.3 Colloidal Probe AFM

Complex processes regulate the adhesion of biomaterials to tissues and the magnitude of these interactions often define the overall performance of the implants. Colloidal probe AFM, sometimes referred to as colloidal probe microscopy (CPM), is a powerful tool which utilises an AFM cantilever with a spherical particle attached at the apex in order to study the nano-scale forces between a particle and substrate with defined physico-chemical properties. The most commonly used material for the microspheres is silica, as it has a low rms roughness, is commercially available in a variety of sizes, and its surfaces can be readily chemically modified.[203,204] Attachment of silica microspheres is typically done using micromanipulators in combination with an optical or electron microscope. The microsphere is then firmly bound using a small amount of epoxy resin. Alternatively, in cases where a microsphere material such as polystyrene or borosilicate glass is used sintering of the particle to the cantilever can be performed.[205]

One way in which the microspheres used in colloidal probe AFM can be modified is through functionalisation with a polymer brush coating. Polymer brushes offer a unique control of the chemistry of interfaces, enabling the formation of both very hydrophobic and hydrophilic polymer coatings, as well as polyelectrolytes. Furthermore, the morphology and mechanics of these interfaces can be regulated via the control of brush grafting density, thickness, swelling and conformation.[127,131] The wealth of monomers that can be incorporated in polymer brushes has enabled a wide range of properties for these coatings, including protein resistance,[206] thermoresponsiveness,[145,207] electrolyte responsiveness[208,209] and bacterial resistance.[119,210] Polymer brush techniques are generally considered better than other techniques for deposition of thin polymer films due to their good stability and the fact that high strength interactions with the underlying substrate can be obtained.[127–129] The combination of colloidal probe AFM with polymer brush-functionalised microspheres is a pivotal tool for investigating the nano-scale interactions between polymers and various substrates. The adhesive and anti-fouling properties of polymer brushes and their nanoscale mechanics have been characterised relatively extensively via this method. As an example, Rodriguez-Emmenegger *et al.* quantified the adhesion of Yersinia pseudotuberculosis to seven types of polymer brushes, all known for the excellent protein resistance.[119]

The use of CPM has enabled the characterisation of protein adhesion to polymer brushes,[211–213] as well as bacterial adhesion.[119] In these studies, neutral and zwitterionic brushes that are particularly well solvated were shown to effectively limit adhesion of unwanted biomacromolecules and components of the bacterial membranes such as lipopolysaccharides. In addition, CPM with silica colloidal probes was used to quantify adhesion and friction to hydrophobic and fluorophilic brushes; the brushes displaying

increasing degrees of fluorination displayed reduced adhesion and friction.[214] The conformation and swelling of polymer brushes also strongly affects adhesion strength and contact mechanics, therefore highlighting the impact of environmental factors on non-specific adhesion.[215] Such impact of the environment is also strikingly illustrated by the response of polyelectrolyte brushes to pH, electrolyte chemistry and ionic strength. Hence, the strength of adhesion of silica microparticles to poly(2-vinylpyridine) brushes is enhanced by phosphate and sulfate electrolytes, compared to chloride, and is reduced at higher ionic strength.[216]

## 4.2 Materials and Methods

### 4.2.1 Chemicals and Materials

2-(dimethylamino)ethyl methacrylate (DMAEMA, $M_n$ = 157.21, 98%), oligo(ethylene glycol methyl ether methacrylate) (OEGMA, $M_n$ = 300), poly (L-lysine) (PLL), 2,2'-bipyridyl (bipy, ≥99%), triethylamine (≥99.5%), copper chloride (Cu(I)Cl), copper bromide (Cu(II)Br2), toluene (anhydrous, 99.8%), iodomethane (99%), (3-aminopropyl)triethoxysilane (APTES, 99%), triethoxy(octyl)silane (97%), trichloro(1H,1H,2H,2H-perfluorooctyl)silane (97%), 11-mercaptoundecanoic acid (MUDA, 95%), 11-mercapto-1-undecanol (97%), Dulbecco's phosphate buffered saline (PBS), neuraminidase (from Clostridium Perfringens), heparinase III (from Flavobacterium Heparinum), wheat germ agglutinin (WGA, lectin from Triticum vulgaris, FITC conjugate), formaldehyde solution (4% in PBS) (PFA) and 4',6-diamidino-2-phenylindole dihydrochloride (DAPI) were purchased from Sigma-Aldrich and used as received. Cu(I)Cl was kept under vacuum until use. Versene solutions (0.2 g/L EDTA in PBS), keratinocyte serum free medium (KSFM), Dulbecco's modified eagle medium (DMEM), trypsin (0.25%), L-glutamine, penicillin-streptomycin, bovine pituitary extract (BPE), human recombinant epidermal growth factor (EGF) and goat anti-mouse IgG (H+L) secondary antibodies (conjugated to AlexaFluor 488) were purchased from Thermofisher Scientific. Fibronectin solution (from human plasma) and the anti-heparin/heparan sulfate antibody were purchased from Merck Millipore. Foetal bovine serum (FBS) was purchased from Labtech. Collagen I (type I) was purchased from Corning. Dichloromethane (DCM, ≥99.8%) was purchased from Honeywell. Dimethylformamide (DMF, ≥99.9%) was purchased from VWR Chemicals. AFM probes (ORC8-10) were purchased from Bruker. Silica particles (unfunctionalised) were

purchased from microParticles GmbH (mean diameter of 19.59 µm). SEMGLU was purchased from Kleindiek Nanotechnik GmbH, Germany. Silicon wafers (100 mm diameter, ⟨100⟩ orientation, polished on one side/reverse etched) were purchased from Compart Technology Ltd. All plasma treatment was carried out using a Henniker Plasma Vacuum System HPT-200. Human keratinocyte HaCaT cells and human primary epidermal keratinocytes were kindly provided by Dr. John Connelly, Blizard Institute, Barts and The London School of Medicine and Dentistry, Queen Mary University of London.

### 4.2.2 Synthesis of Polymer Brush-Coated Silica Microparticles

Polymer brushes were grown from silica microparticles (19.6 µm) via atom transfer radical polymerization (ATRP). The growth of poly(dimethylaminoethyl methacrylate) (PDMAEMA) and poly(oligoethyleneglycol methacrylate) (POEGMA) brushes from silica particles was directly adapted from protocols previously reported.[217,218] PDMAEMA brushes on planar silicon were synthesised following a similar protocol as PtBA brushes (see Chapter 3) except for a few differences: a monomer solution of DMAEMA (6.6 g, 42 mmol), bipy (320 mg, 2.05 mmol), $CuBr_2$ (18 mg, 81 µmol) and CuCl (84 mg, 849 µmol) in water/ethanol (4:1 (v/v), 15 mL) was used. The monomer was used as purchased without any need for initial purification, and polymerization was carried out at room temperature and was stopped by immersing samples in deionised water, rinsing with ethanol and drying under a stream of nitrogen.

The procedure for the synthesis of POEGMA brushes on planar silicon was identical to that of PDMAEMA brushes, except that a monomer solution of OEGMA (12.6 g, 42 mmol), biby (320 mg, 2.05 mmol), $CuBr_2$ (18 mg, 81 µmol) and CuCl (84 mg, 845 µmol)

in water/ethanol (4:1 (v/v), 15 mL) was used. Details on the synthesis and characterisation of PAA brushes can be found in Chapter 3. For PAA, PDMAEMA and POEGMA brushes polymerization times were adjusted accordingly to give dry ellipsometric thicknesses of 30 nm; these thicknesses equated to polymerization times of 5 hours, 20 minutes and 30 minutes, respectively. The swelling behaviour of PDMAEMA and POEGMA brushes was previously studied by ellipsometry and reported by our group as well as others.[207,219]

Details of the methods used for the synthesis of brushes on silica microparticles, such as the grafting of the silane initiator, can be found in Chapter 3. For growth of PDMAEMA polymer brushes on silica microparticles, 5 mL of the DMAEMA monomer solution (see above) was added to a 5 mL silica dispersion (50 mg $SiO_2$-silane beads in water/ethanol (4:1 (v/v)), degassed under argon for 30 minutes). Argon bubbling was continued and polymerization was allowed to proceed at room temperature. The reaction was stopped with oxygen bubbling and the beads were washed in water/ethanol (4:1 (v/v)). Synthesis of POEGMA polymer brushes was identical except that 5 mL of the OEGMA monomer solution (see above) was instead added to the silica bead dispersion.

### 4.2.3 Formation of Self-Assembled Monolayers (SAMs) on Silicon and Gold-Coated Substrates

Table 4.1 gathers the contact angle data for all SAMs generated on silicon and gold-coated substrates. Contact angle measurements were taken using a Kruss DSA100 instrument using 3 µL droplets of deionised water. The sessile drop method was used to measure angles. For formation of 3-aminopropyl triethoxysilane (APTES) SAMs, a

plasma-oxidized (10 minutes, air) silicon substrate was immersed in a solution of ethanol (1 mL) and 3-aminopropyl triethoxysilane (APTES) (10 µL) and left at room temperature for 30 minutes. The sample was then rinsed with ethanol and dried under a stream of nitrogen. Subsequently, the APTES-coated silicon substrate was immersed in a solution of 1 mM HCl for 5 minutes and then washed thoroughly with deionised water, ethanol, and then dried in a stream of nitrogen. Quartenized APTES (QAPTES) SAMs were prepared similarly to the APTES samples, except that, following APTES deposition, they were immersed in a solution of 5 mM NaOH for 5 minutes, followed by incubation overnight at room temperature in a solution of iodomethane (13.3 µL) in DMF (1.5 mL). The samples were then washed with ethanol and dried under nitrogen.

For triethoxy(octyl)silane SAMs, a plasma-oxidized silicon substrate was immersed in a solution of anhydrous toluene (1 mL), triethylamine (20 µL), and triethoxy(octyl)silane (20 µL) and left at room temperature overnight. The sample was then rinsed with ethanol and dried under a stream of nitrogen. With trichloro(1H,1H,2H,2H-perfluorooctyl)silane SAMs a solution of trichloro(1H,1H,2H,2H-perfluorooctyl)silane (30 µL) in anhydrous toluene (1 mL) was prepared. This solution was placed in a desiccator, in an open vial, adjacent to a plasma-oxidized (10 minutes, air) silicon substrate (but protected from splash by aluminium foil to avoid solution droplets contacting the substrate). The pressure was reduced using a vacuum pump until the toluene started evaporating (ebullition). The desiccator was closed and the vapour phase deposition was allowed to proceed overnight. The sample was then rinsed with ethanol and dried under a stream of nitrogen.

Gold-coated silicon substrates were prepared by initial cleaning of the silicon substrate in plasma (5 minutes, air), followed by the evaporation of a chromium layer (20 nm

followed by the evaporation of a gold layer (200 nm) using an Edwards Auto 500 evaporator). The resulting gold-coated silicon substrates were then plasma-oxidized (10 minutes, air) and then directly immersed in 5 mM thiol ethanolic solutions (hydroxyl and carboxylic acid SAMs were generated from 11-mercapto-1-undecanol and 11-mercaptoundecanoic acid (MUDA), respectively) at room temperature overnight. The substrates were then washed with ethanol and dried with nitrogen.

**Table 4.1.** Contact angle measurements of deionised water droplets (3 μL) deposited at the surface of SAMs, assembled on either gold or silicon substrates.

| Surface Functionalisation | Substrate Material | Contact Angle |
|---|---|---|
| Silanol | Silicon | 14.2 ± 5.4˚ |
| APTES | Silicon | 37.7 ± 5.2˚ |
| QAPTES | Silicon | 21.5 ± 2.1˚ |
| Octyl | Silicon | 96.3 ± 2.3˚ |
| Perfluorooctyl | Silicon | 103.7 ± 2.5˚ |
| Undecanethiol | Gold | 32.5 ± 4.9˚ |
| MUDA | Gold | 50.3 ± 1.5˚ |

## 4.2.4 Preparation of Colloidal Probe Force Microscope

Cantilevers were selected with a nominal spring constant of 0.38 N/m and this value was more accurately determined using the Sader calibration method.[220] Considering the proper alignment of beads with the longitudinal axis of a cantilever, recent work has shown that the spring constant of the cantilever is not significantly affected by colloidal attachment,[221] and it was therefore decided to measure the spring constant of cantilevers prior to bead attachment. A small volume of polymer brush functionalised-bead suspension was deposited onto a silicon wafer and the solvent was allowed to evaporate overnight; this resulted in a sparse arrangement of functionalised-beads at the silicon surface. In order to attach individual beads to the apex of an AFM cantilever,

a custom built AFM (Attocube GmbH, Germany) integrated within an SEM (Quanta 3D FEG, FEI, EU/USA) was used, as described in previous work.[146,222] An integrated focussed ion beam (FIB) was used to etch off a portion of the AFM tip to produce a blunted surface to which a bead can be attached. Figure 4.2A and B show the AFM tip before and after exposure to the FIB. Next, the AFM tip was translated to a droplet of vacuum compatible glue (SEMGLU). Removal of the tip from the glue resulted in the deposition of a small amount of glue at the apex of the tip, which was translated into contact with a single bead. This SEM system, combined with a high-resolution piezoelectric stage, allows the accurate positioning of the bead onto the apex of the tip, resulting in the accurate alignment of the bead with the longitudinal axis of the AFM cantilever. Focussing a high current electron beam of 1 nA or more for 5 minutes causes curing of the glue and subsequent firm attachment of the bead to the tip. Figure 4.2C shows the AFM tip in contact with the bead on the silicon surface and Figure 4.2D shows the resulting colloidal AFM tip after the curing of the adhesive. The use of tipless cantilevers was also investigated. However, using this method often resulted in the deposition of large amounts of glue on the cantilever surface, subsequently leading to encapsulation and fouling of the surface of the bead.

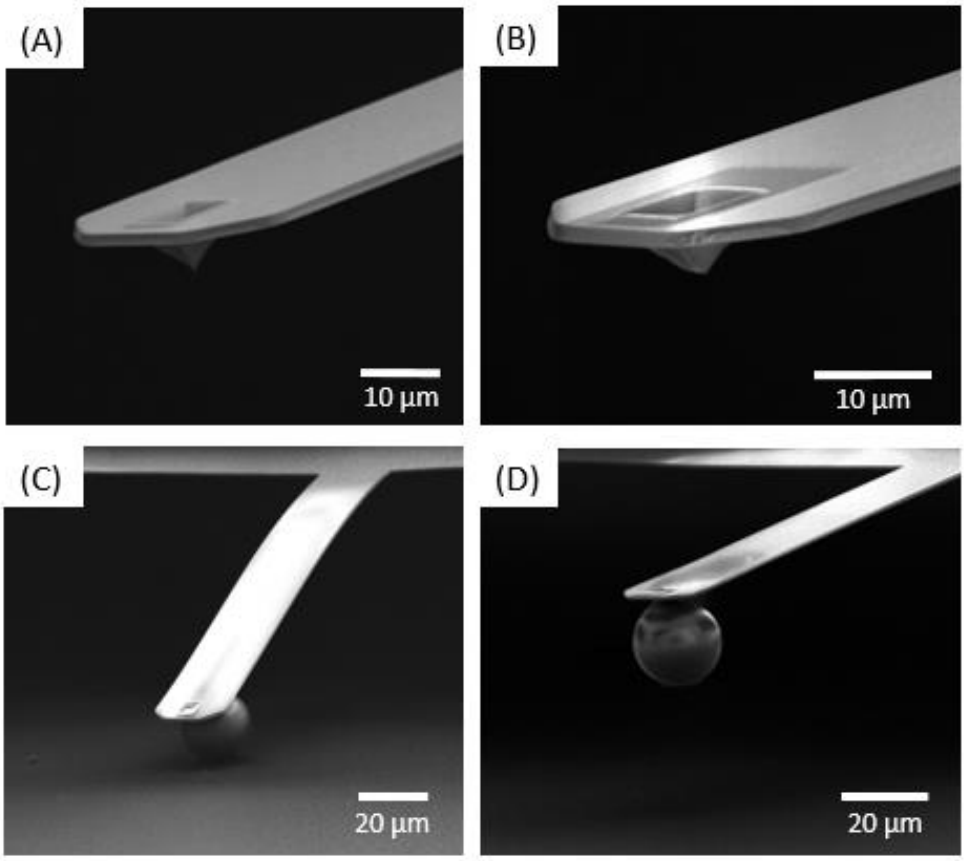


**Figure 4.2.** Sequence of steps used for the fabrication of colloidal probe cantilevers. (A) Rectangular cantilever with sharpened tip, as purchased from the manufacturer. (B) An integrated FIB was used to remove a portion from the end of the tip, providing a more effective surface for the placement of the bead. (C) The end of the tip was dipped into glue and then brought into contact with the surface of a bead that had been deposited on a silicon wafer. A high current (1-3 nA) was focussed at the glue for several minutes, resulting in curing of the adhesive and creation of a strong bond between the tip and bead. (D) The resulting colloidal AFM probe was then removed from the surface, ready for AFM measurements. All images were acquired using a Scanning Electron Microscope (Quanta 3D FEG, FEI, EU/USA).

### 4.2.5 Operational Set Up of Force Probe Microscope

Force measurements were acquired using an NT-MDT Ntegra AFM rig operated in conventional force mode. The cantilever was approached towards the substrate surface and retracted away from the surface at a constant speed (1 µm/s for all experiments) by the piezo electric stage. Silicon and gold substrates, glued to the bottom of a petri dish, were submerged in the corresponding solution and allowed to equilibrate for a

minimum of 15 minutes. AFM tips were washed in deionised water before and after any testing was carried out, or before the ionic concentration of the testing solution was changed. The pH of solutions was kept at 7.0 ± 0.4 during all testing (Mettler Toledo, SG2 – SevenGo pH Meter), except for experiments carried out in PBS, which displayed a pH of 7.4. For the characterisation of cell monolayers, confluent monolayers grown on glass coverslips (fixed with PFA) were carefully glued to the petri dish using Loctite Super Glue Precision. The glue was left to dry for a couple of minutes, during which time a small amount of PBS was pipetted onto the upper surface to ensure the cells remained hydrated. The cells were then submerged in PBS and left in the fridge until testing was carried out.

Soft tissue samples were cut to a surface area of approximately 20 $mm^2$, with a thickness of approximately 5 mm. These were blotted dry with tissue paper and then glued to a petri dish; the glue was left to set for a couple of minutes and then samples were submerged in PBS and left in the fridge until testing. In between tests on different samples AFM tips were submerged in deionised water and then submerged in a versene solution (0.48 mM) for 5 minutes, and again washed in deionised water for 2 minutes. For every sample and condition tested, a minimum of three independent samples were characterised with a minimum of two different functionalised colloidal probes. Each repeat involved probing at least three different areas of a substrate, and for each of these scanned areas 100 indentation curves were performed in a grid pattern with areas ranging from 20 to 60 $\mu m^2$.

Calibrations were carried out for each AFM tip on a hard, non-functionalised silicon substrate using a custom-built Matlab script for conversions. The parameters extracted are illustrated in Figure 4.3. The detachment force is the maximum negative force

reached on the cantilever. The detachment work is the total work required to fully detach the colloid from the substrate. The detachment length is defined as the distance between the lower surface of the colloidal probe and the substrate, taken at the maximum force value (the detachment force). For measurements on soft tissues, the Young's modulus was additionally characterised from the AFM curves. This parameter was quantified using a custom-built Matlab script based on the Oliver-Pharr method for nanoindentation.[177] For Young's modulus measurements, probes were fabricated in the same way as for the adhesion tests, except for the fact that silica beads were left unfunctionalised.

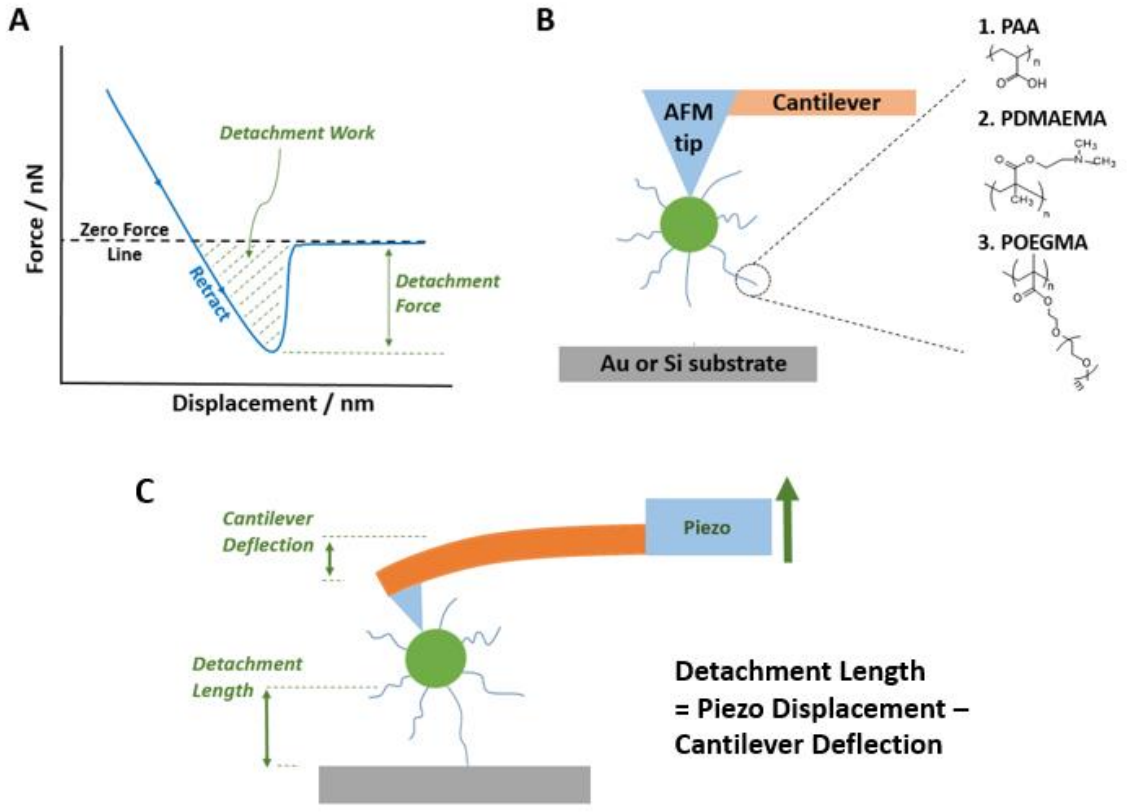


**Figure 4.3.** Quantitative analysis of colloidal probe adhesion profiles. (A) Extraction of detachment work and force from AFM retraction curves. (B) Illustration of colloidal AFM probes and the three polymers used to functionalise them. (C) Physical representation of the detachment length, taken from the retraction portion of the AFM curves.

### 4.2.6 Preparation of Cell Monolayers

Preparation of cell monolayers and collection of fluorescence microscopy images was performed by Dexu Kong, a colleague from my research group at Queen Mary University. All data analysis was performed by me. HaCaT cells (human keratinocyte cell line) were cultured in DMEM containing 10% foetal bovine serum, 1% L-glutamine (200 mM) and 1% penicillin-streptomycin (5,000 U/mL). HaCaT cells were harvested with trypsin and versene solutions in a ratio of 1/9, centrifuged, counted and re-suspended in DMEM at the desired density before seeding onto substrates, in a 24-well plate, at a density of 20,000 cells per well (13,000 cells per $cm^2$), and left to form a confluent monolayer for 24 hours in an incubator (37 °C and 5% $CO_2$). After three aspirations with PBS, confluent monolayer samples were fixed with 4% formaldehyde solution in PBS (PFA) for 10 minutes, washed with PBS and left in the fridge ready for AFM measurements.

Human primary keratinocytes (HPKs) isolated from neonatal foreskin were cultured on collagen I (type I, 20 μg/mL in PBS for 20 minutes) treated T75 flasks in keratinocyte serum free medium (KSFM), supplemented with bovine pituitary extract (BPE) and EGF (Human Recombinant). Keratinocytes were harvested with trypsin and versene solutions in a ratio of 1/9, centrifuged, counted and re-suspended in KSFM at the desired density before seeding onto substrates. Glass coverslips (13 mm) were sterilized by autoclave and put in 24 well-plates. Glass coverslips were first treated with poly(L-lysine) (PLL, final concentration: 100 μg/ mL) followed by treatment with fibronectin solution (final concentration: 10 μg/ mL). Cells were seeded at a density of 20,000 cells per well (13,000 cells per $cm^2$) and left to form a confluent monolayer for 24 hours in an incubator (37°C and 5% $CO_2$). After three aspirations with PBS, confluent monolayer

samples were fixed with 4% PFA for 10 minutes, washed with PBS and left in the fridge ready for AFM measurements.

Neuraminidase was used to cleave the glycosidic linkages of neuraminic acids. Keratinocyte monolayers (cultured on coated glass coverslips) were treated with neuraminidase (1 U/mL) in KSFM medium for 1.5 hours in a 24 well-plate. Heparinase III was used to cleave 1-4 linkages between hexosamine and glucuronic acid residues in heparan sulphate. Keratinocyte monolayers (cultured on coated glass coverslips) were left in Heparinase III solutions (0.2 U/mL, in KSFM) for 1.5 hours in a 24 well-plate.

Wheat germ agglutinin (WGA, 10 µg/mL) and anti-heparin/heparan sulfate antibodies (10 µg/mL) were used to stain the glycocalyx on the cell membrane. Dapi solutions (stock concentration: 5 mM, 1:1000) were prepared by dissolving 5 mg 4',6-diamidino-2-phenylindole dihydrochloride in 1750 µL deionised water. Goat anti-mouse IgG (H+L) secondary antibodies conjugated to AlexaFluor 488 (1 µg/mL) were used for immunofluorescence staining. Fluorescence microscopy images were acquired with a Leica DMi8 fluorescence microscopy (CTR compact lamp; 63×1.30 NA, oil lens; DFC9000 GT camera). For each sample and condition three fluorescence microscopy images were taken. Quantification of the fluorescence intensities and profiles was then performed using ImageJ.

### 4.2.7 Preparation of Tissue Samples

Fresh soft tissue samples were obtained from C Humphreys & Sons Abattoir in Chelmsford, Essex. Both the epicardial and gingival samples were extracted from freshly slaughtered 6 to 7-month-old pigs. The animals were sacrificed and the relevant parts

were extracted at the abattoir; these were then delivered by courier to the lab on the same day as the slaughter. The samples were then washed and stored in PBS overnight at 5˚C. All AFM adhesion testing was then carried out within 48 hours from the initial sacrifice of the animals.

Gingival samples were extracted using a scalpel from the lingual side of the lower mandible. These samples were taken from the region of the keratinized attached gingiva which is the gingival portion that lies between the free gingival groove and the mucogingival junction (Figure 4.4B). If the dissection was initiated at the gingival margin, complete strips of tissue could be removed all the way down to the mucogingival junction with relative ease. Epicardial samples were extracted from the wall of the left and right ventricles. These samples were taken from the healthy areas of the myocardium away from any major adipose tissue deposits or prominent blood vessels (Figure 4.4C). For AFM testing, results were obtained across samples from at least two different animals for each condition tested. Figure 4.4A shows an example of loaded epicardial samples in the AFM.

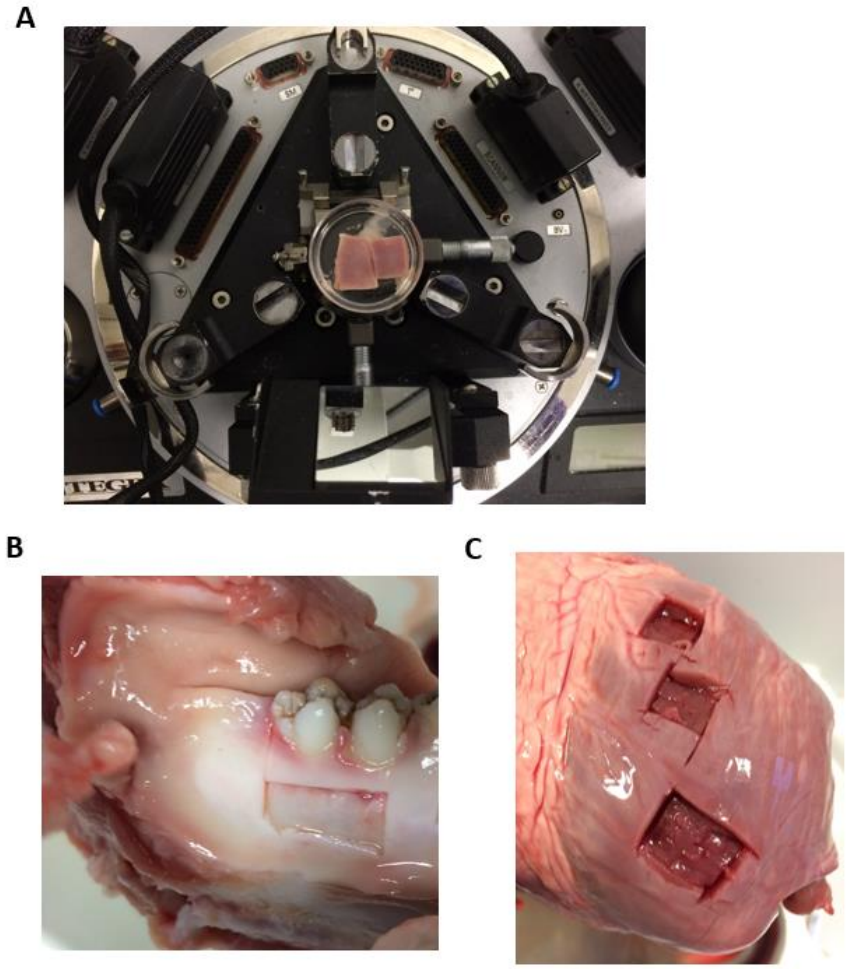


**Figure 4.4.** Dissection and preparation of porcine tissues for AFM. (A) Loading of epicardial samples in the AFM. Following dissection samples were glued in place within petri dishes and submerged in PBS. (B) Example of dissection location for keratinized gingiva samples. (C) Example of dissection locations for epicardial samples.

## 4.2.8 Statistics

A one-way ANOVA test with Tukey's post hoc analysis was used to determine statistical significance. In the case of the quantification of the glycocalyx, the analysis was carried out pairwise. For box and whisker diagrams the box represents the 1st, 2nd and 3rd quartiles, as standard, and the whiskers represent the standard deviations of data sets. Mean values for the data sets are also shown. In all other figure types (and for in-text referencing) standard errors are reported

## 4.3 Results and Discussion

### 4.3.1 Nanoindentation of Soft Tissues

In order to gain a better understanding of the mechanical properties of the epicardium and gingiva at the microscale, nanoindenation was performed (Figure 4.5). Because of the complexities associated with obtaining human oral soft tissues and due to the resemblance of porcine tissue to human tissue,[223] porcine tissue was used in this study. Measurements were based on the AFM lift curves obtained, using the Oliver-Pharr method to quantify corresponding moduli.[177] The gingiva was found to be significantly stiffer than the epicardium (Young's moduli of 1020 ± 130 and 20.7 ± 0.5 kPa, respectively; Figure 4.5A) as qualitatively seen in the difference in gradients between the representative lift curves of the two tissues (Figure 4.5B). The significantly higher moduli for the gingiva are expected as the attached gingiva is found in the area referred to as the masticatory mucosa, the region specifically containing keratinized stratified squamous epithelium. This area of the mucosa is subject to constant abrasion and as such the process of keratinization forms a stiff barrier which protects the underlying tissue from infection, dehydration, chemicals and mechanical stress.[54]

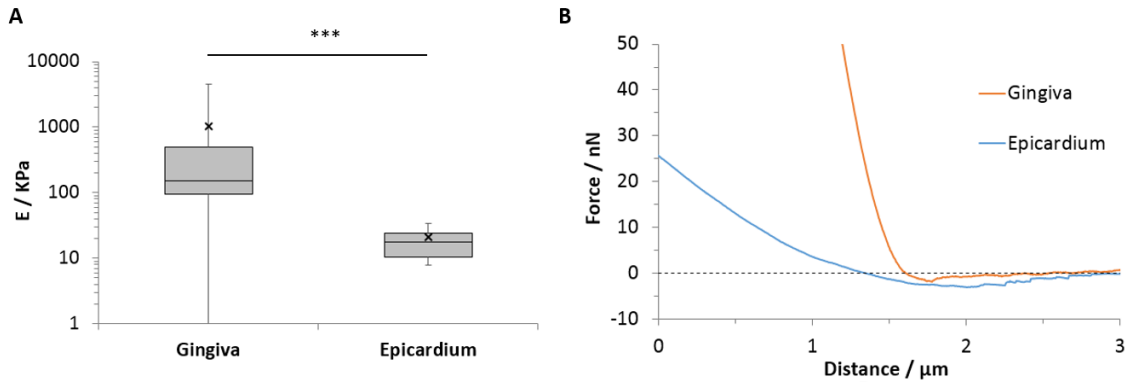


**Figure 4.5.** Stiffness values for porcine gingiva and epicardium, calculated from AFM curves using the Oliver-Pharr method for nanoindentation. (A) Young's modulus data obtained for tissues. Data is plotted as means, with box plots. ***, $p \leq 0.001$. (B) Representative lift curves for gingiva and epicardium.

The stiffness values obtained for the porcine epicardium compare closely with the range of values reported in the literature; values are typically in the range of 15 to 100 KPa for experiments undertaken on healthy cardiac muscle tissue (including the endocardium, myocardium and epicardium) of mice, rats or rabbits, via AFM nanoindentation.[188–195] More specifically, Kossivas *et al.* found a value of 14.7 KPa for the stiffness of epicardial samples extracted from the left ventricular region of the murine heart.[190] For the keratinized gingiva, a large standard deviation in the data is reported (see Figure 4.5A). Although samples were extracted from the same region of the gingiva each time (the attached gingiva from the lingual side of the lower mandible), significant variations in thickness and mechanical properties still exist both across a sample and also between the different sacrificed animals. These variations in thickness and mechanical properties are a well reported feature of the oral mucosa.[196,197]

### 4.3.2 Polymer Brush Adhesion to SAMs

Prior to studying polymer brush adhesion to cells and tissues, their adhesion to model substrates (self-assembled monolayers) presenting chemical moieties with a range of hydrophilicities, hydrogen bonding and charge was initially investigated. Figure 4.6 presents the detachment forces observed for the adhesion of PAA, PDMAEMA and POEGMA brushes to hydroxyl-terminated monolayers alongside the corresponding representative lift curves. Overall, similar adhesions were measured to both undecanethiol monolayers assembled to gold and silicon oxide interfaces. As the surface packing density for monolayers assembled on silica[208,224] and gold[225] substrates are reported to be in the region of 5 molecules/nm$^2$, the similarity of these adhesion profiles is justified. POEGMA displayed little adhesion to these interfaces, in good agreement with its neutral structure, lacking strong proton acceptor or donor functions. POEGMA brushes indeed typically display moderate hydrophilicity and excellent anti-fouling properties.[226,227]

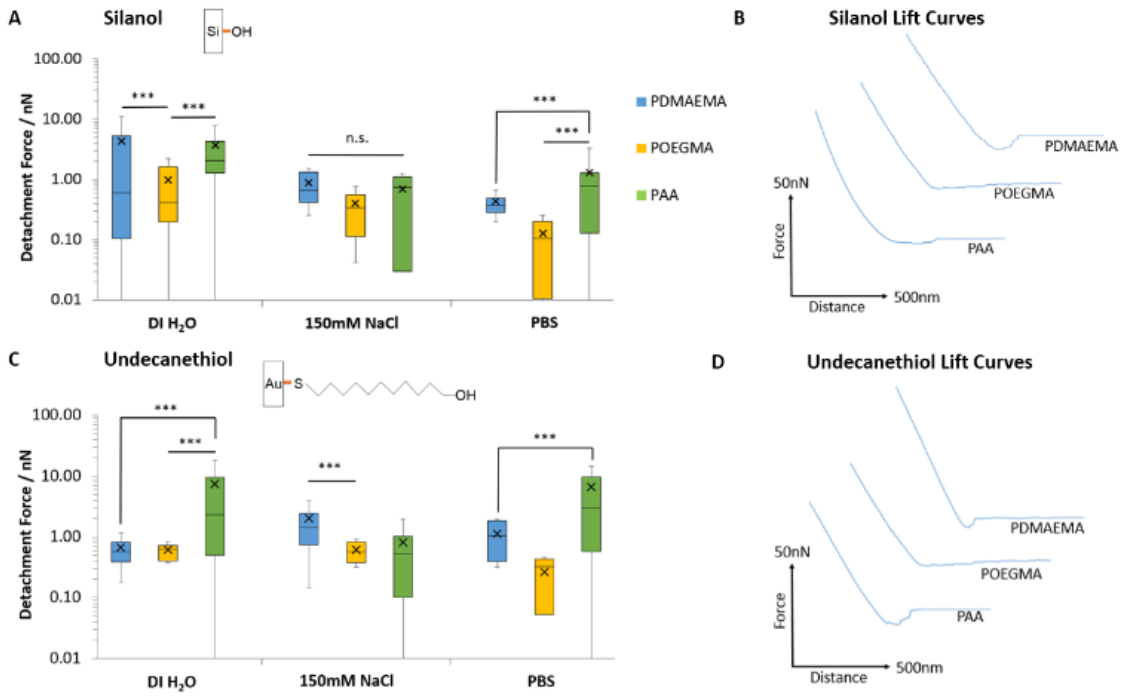


**Figure 4.6.** Detachment forces and corresponding representative lift curves for the adhesion of PAA, PDMAEMA and POEGMA brushes to hydroxyl-terminated monolayers. Representative curves are taken from adhesion experiments performed in deionised water. (A) Detachment forces to silicon oxide interfaces. (B) Representative lift curves for adhesion to silanol monolayers. (C) Detachment forces to undecanethiol monolayers assembled on gold-coated silicon substrates. (D) Representative lift curves for adhesion to undecanethiol monolayers. Data is plotted as means, with box plots. ***, $p \leq 0.001$. n.s., non-significant.

In contrast to POEGMA, PAA and PDMAEMA displayed moderate adhesions to both hydroxyl-terminated monolayers. At the near-neutral pH at which these measurements were carried out (the pH of deionised water and NaCl solutions was in the range of 7.0 ± 0.4, whereas that of PBS solutions was 7.4), PAA brushes are globally negatively charged (we found a ζ-potential of -29 mV)[228,229] and PDMAEMA brushes are positively charged (ζ-potential of 40mV),[217,230] whereas silica substrates are negatively charged (ζ-potential of -40 mV).[229,231] Hence, in the case of PDMAEMA brushes, electrostatic interactions should lead to increased adhesion. However, PAA and PDMAEMA brush adhesion (detachment force) to silanol and undecanethiol monolayers are typically

comparable and, in some cases, increased in the case of PAA (in deionised water and in PBS, in the case of undecanethiol monolayers; Figure 4.6A and C). In addition, higher ionic strength (150 mM NaCl) did not lead to substantial reduction in adhesion force, as would be predicted in the case of oppositely charged surfaces. These changes were qualitatively reflected in the corresponding detachment work (see Figure 4.7A and B). Therefore, weak adhesion of PAA and PDMAEMA brushes to moderately hydrophilic and moderately charged silanol and undecanethiol monolayers appeared to be dominated by weak hydrogen bonding.

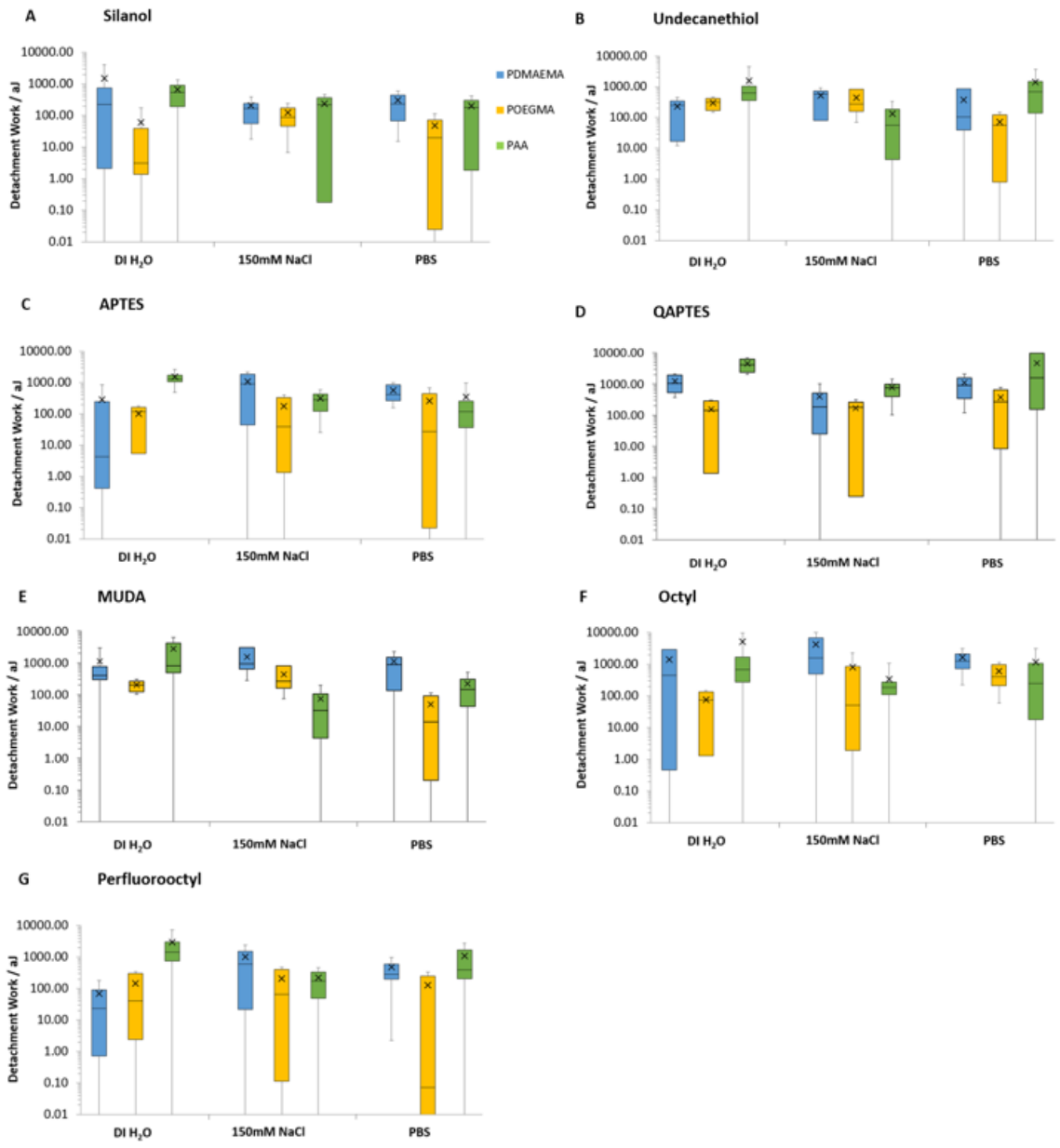


**Figure 4.7.** Detachment work measured for the adhesion of PAA, PDMAEMA and POEGMA brushes to hydroxyl-terminated, charged and hydrophobic monolayers. (A) Silanol monolayers. (B) Undecanethiol monolayers assembled on gold. (C) Ammonium (APTES) monolayers. (D) Quaternary ammonium (QAPTES) monolayers. (E) Undecanoic acid (MUDA) monolayers assembled on gold. (F) Octyl monolayers. (G) Perfluorooctyl monolayers.

In PBS solutions, adhesion forces measured for PDMAEMA and POEGMA brushes to hydroxyl-terminated monolayers remained comparable to those measured in 150 mM NaCl solutions. Indeed, PBS has a NaCl concentration of 137 mM, similar to that of the

NaCl solution used, and the pH of both solutions were relatively close (pH 7.4 and pH 7.0 ± 0.4, for PBS and NaCl, respectively). For PAA brushes, adhesion forces were increased in PBS compared with 150mM NaCl (forces increased from 0.69 to 1.29 nN and 0.82 to 6.60 nN for silanol and undecanethiol SAMs respectively). This phenomenon is associated with a reduction of the swelling of PAA brushes in PBS, compared to 150 mM NaCl, and may indicate the contribution of phosphate to hydrogen bonding at the surface.

Figure 4.9 presents the adhesion forces measured for the three different polymer brushes to charged model substrates (associated detachment work values are given in Figure 4.7). As expected, negatively charged PAA brushes strongly adhered to positively charged quaternary ammonium monolayers (QAPTES); this is further evidenced in Figure 4.8A where the jump-to-contact is indicative of a strong attractive interaction. In the corresponding representative lift curves (Figure 4.8B), it is also clear that interactions between PAA brushes and oppositely charged monolayers (APTES and QAPTES) are strong (adhesion forces > 10.16 nN in deionised water) and decrease at higher ionic strength (Figure 4.9D), as would be expected from the corresponding screening of coulombic forces. Indeed, at neutral pH we found $\zeta$-potentials of 13 mV[232,233] and 37 mV for APTES and QAPTES respectively, whereas $\omega$-mercaptoundecanoic acid (MUDA) displays a $\zeta$-potential of -40 mV.[234] This behaviour contrasts with the adhesion of poly(2-vinylpyridine), which displayed increased adhesion forces at higher ionic strength.[235,236] This was attributed to changes in brush conformation from the salted regime to the osmotic regime. We also note that the ionic strength range at which brush adhesion was maximised was above the range of ionic strength presently tested (matching that of physiological buffers such as PBS).

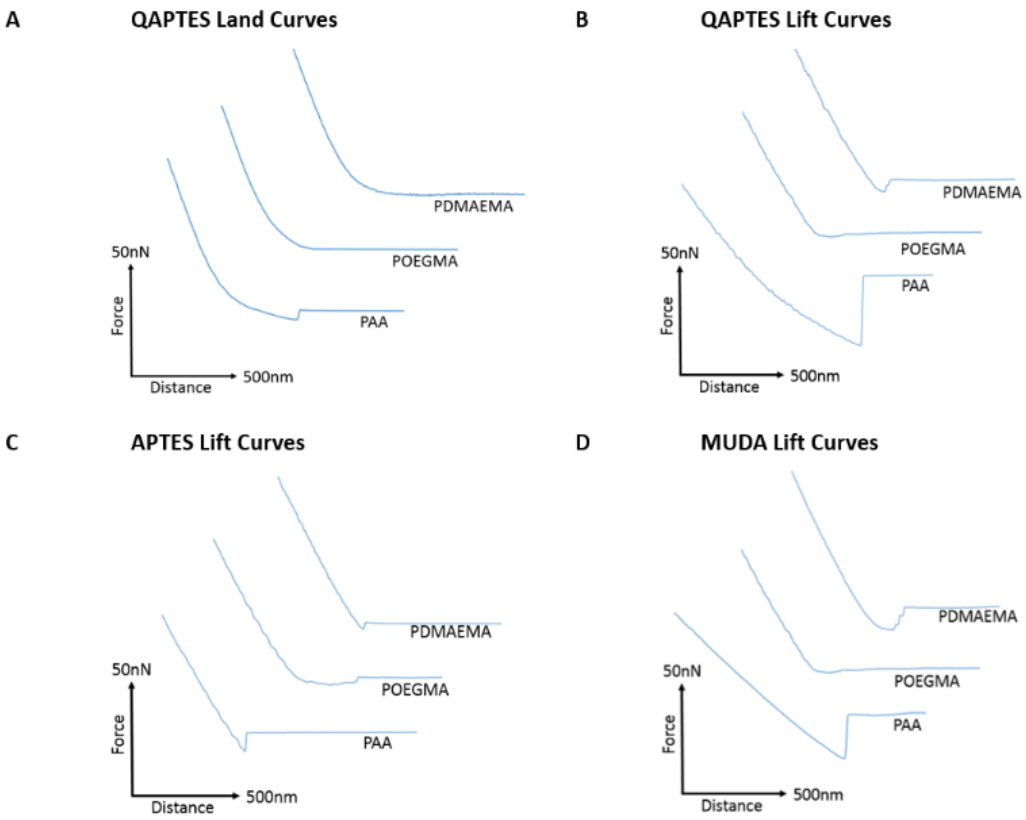


**Figure 4.8.** Representative lift and land curves for the adhesion of PAA, PDMAEMA and POEGMA brushes to charged monolayers. All curves are taken from adhesion experiments performed in deionised water. (A) Land curves representative of adhesion of brushes to QAPTES monolayers. (B) Lift curves representative of adhesion to quaternary ammonium (QAPTES) monolayers. (C) Lift curves representative of adhesion to ammonium (APTES) monolayers. (D) Lift curves representative of adhesion to undecanoic acid (MUDA) monolayers assembled on gold.

The neutral POEGMA, in contrast, displayed interactions below 3.45 nN, comparable to what was measured on neutral hydroxyl functionalised interfaces (detachment forces were reduced for hydroxyl SAMs in comparison to charged monolayers. However, from the detachment work (Figure 4.7), interactions are of a similar scale), in agreement with its neutral charge. The adhesive response of PDMAEMA to these three charged monolayers was more surprising as, although it adhered weakly to APTES surfaces (< 4.05 nN), its adhesion to MUDA was not as significantly increased (< 5.93 nN) as was observed in the case of PAA adhering to APTES interfaces. This indicates that other

interactions dominate the adhesive behaviour of PDMAEMA to the charged monolayers studied.

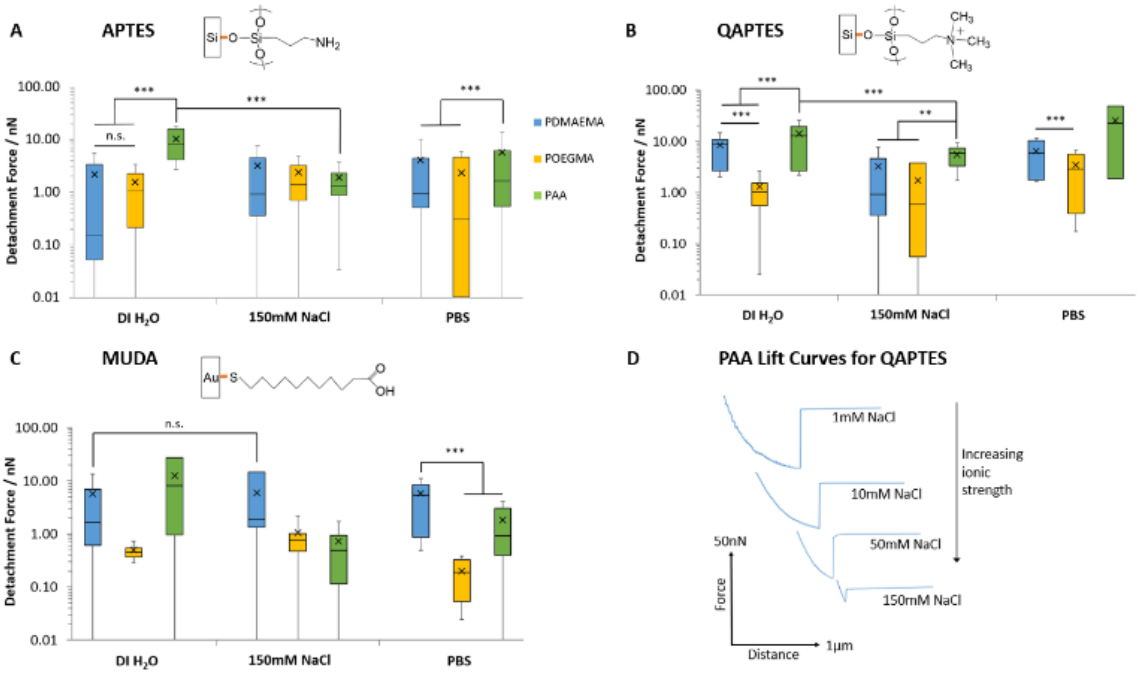


**Figure 4.9**. Detachment forces measured for the adhesion of PAA, PDMAEMA and POEGMA brushes to charged monolayers. (A) Detachment forces to ammonium (APTES) monolayers. (B) Detachment forces to quaternary ammonium (QAPTES) monolayers. (C) Detachment forces to undecanoic acid (MUDA) monolayers assembled on gold-coated silicon substrates. (D) Representative lift curves for adhesion of PAA to QAPTES monolayers in solutions of increasing ionic strengths. Data is plotted as means, with box plots. **, $p \leq 0.01$. ***, $p \leq 0.001$. n.s., non-significant.

In addition to electrostatic interactions, hydrogen bonding may significantly impact the adhesion strength of PAA and PDMAEMA brushes to charged monolayers, owing to their acid/base character. Indeed, in contrast to PAA brushes, which showed a marked decrease in interactions at increasing ionic strength, the adhesion of PDMAEMA brushes to MUDA monolayers remained unaffected by increasing ionic strength (150 mM NaCl vs. deionised water; Figure 4.9C). At neutral pH (and slightly below), PDMAEMA is only

partially charged and a substantial proportion of amine moieties are not protonated.[217,237] Similarly, APTES and MUDA monolayers and PAA brushes will only be partially deprotonated at the neutral pH of the solutions used in this study. Therefore, hydrogen bonding between polymer brushes and APTES and MUDA monolayers may significantly contribute to bonding and adhesion profiles. Furthermore, although hydrogen bonding is reported to be influenced by the ionic strength of the medium, predicting the impact of electrolytes on hydrogen bonding remains difficult. Hence, cations are known to alter the melting temperature of double stranded oligonucleotides, although this is via their combined impact on coulombic repulsion between phosphates and on hydrogen bonding between bases.[238] Electrolytes were shown to reinforce hydrogen bonding[239] and to perturb networks of intra-molecular hydrogen bonds of water molecules.[240] In addition, electrolytes such as phosphates are particularly prone to hydrogen bond and alter interactions with biomacromolecules.[241,242] The relatively high interactions of PAA and PDMAEMA to MUDA and APTES, respectively (Figure 4.8 and Figure 4.9), in particular in PBS solutions, may therefore be explained by hydrogen bonding between the corresponding interfaces, perhaps stabilised by phosphate ions.

Further to the evidence for strong hydrogen bonding between polymer brushes and monolayers, the adhesion behaviour of PDMAEMA brushes to QAPTES also implies some impact of hydrophobic interactions on adhesion strength (Figure 4.8B and Figure 4.9B). Indeed, QAPTES is highly positively charged and cannot directly be involved in hydrogen bonding with other molecules. Therefore, the high charge density of cationic PDMAEMA (at neutral pH) should result in repulsive forces. In contrast to this expected behaviour, we observed no evidence of repulsion in the corresponding landing traces (Figure 4.8A),

and relatively strong adhesions can be observed in the retraction traces (Figure 4.8B). Quaternary ammoniums such as those of QAPTES are known to display some level of hydrophobicity, enabling the solubility of salts in some organic solvents. In addition, PDMAEMA also shows significant hydrophobicity and a clear pH-responsive behaviour, as detailed above, especially close to its pKa and above.[217] Therefore, hydrophobic interactions between these two interfaces are likely to play an important role in determining adhesion profiles.

In order to probe further into the impact of hydrophobic forces in regulating adhesion of PAA, PDMAEMA and POEGMA brushes, we generated octyl and perfluorooctyl SAMs on silicon substrates (with contact angles of 96.3 ± 2.3˚and 103.7 ± 2.5˚, respectively). Significant adhesion was measured for PDMAEMA and PAA brushes, whilst POEGMA brushes displayed lower adhesions, but higher than what was reported for hydrophilic SAMs (Figure 4.10; detachment works follow similar trends, see Figure 4.7). In particular, PDMAEMA displayed strong adhesion to octyl SAMs (> 5.13 nN) and the perfluorooctyl SAMs (10.30 nN in 150 mM NaCl solutions). PAA displayed overall weaker adhesion to octyl SAMs, especially at high ionic strength, but relatively high adhesion to perfluorooctyl SAMs.

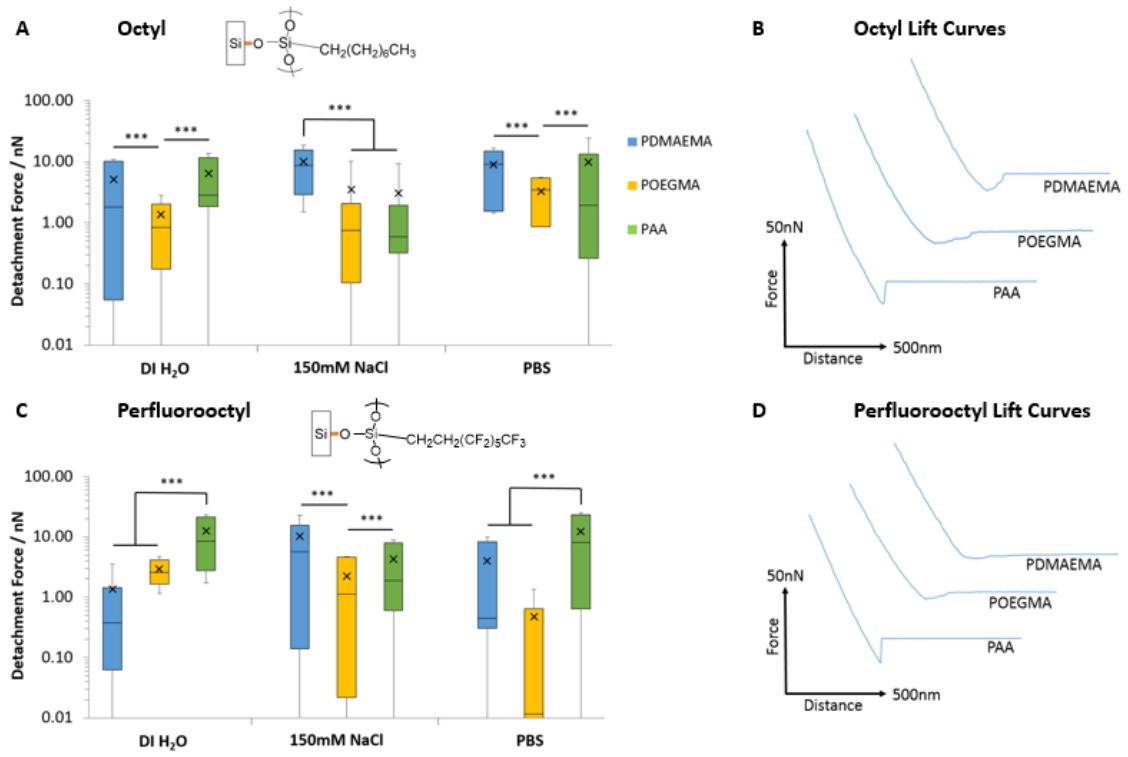


**Figure 4.10.** Detachment forces and corresponding representative lift curves for the adhesion of PAA, PDMAEMA and POEGMA brushes to hydrophobic monolayers. Representative curves are taken from adhesion experiments performed in deionised water. (A) Detachment forces to octyl monolayers. (B) Representative lift curves for adhesion to octyl monolayers. (C) Detachment forces to perfluorooctyl monolayers. (D) Representative lift curves for adhesion to perfluorooctyl monolayers. Data is plotted as means, with box plots. ***, $p \leq 0.001$.

The relatively strong adhesion of weak polyelectrolyte brushes to hydrophobic surfaces is likely due to their partial protonation/deprotonation at neutral pH and associated moderate hydrophobicity.[217,237] Hence, PDMAEMA brushes were found to adhere relatively strongly to PDMAEMA surfaces at neutral pH,[243] whereas little adhesion was observed between two symmetrical hydrophilic polymer brushes.[244] Similarly, polymer brushes displaying a lower critical solution temperature (LCST) were reported to strongly adhere (symmetrical interface bonding) above their LCST, but displayed weak interactions below their LCST.[245] Interestingly, the adhesion force of sparse (grafted to) PAA brushes was also reported to be significantly higher to alkyl monolayers than

corresponding hydroxyl and carboxylic acid-terminated SAMs,[246,247] although this was for single desorption events rather than the cumulative desorption forces associated with full detachment of the tip.

To account for such strong interactions between PAA brushes and hydrophobic SAMs, Friedsam *et al.* proposed that the structure of water close to these interfaces (and the lack of hydrogen bonding of interfacial water molecules, in contrast to the networks formed with hydroxyl and carboxylic acid terminated SAMs) led to easier displacement of water molecules closely associated with the hydrophobic SAMs, compared to hydrophilic SAMs. Indeed, the profiles of desorption of our PAA brushes displayed strong adhesion forces with a sharp detachment step in the case of alkyl SAMs (> 6.43 nN detachment force, > 2.78 fJ detachment work and < 22.3 nm detachment lengths; Figure 4.11), whereas detachment from hydrophilic silanol SAMs displayed an overall weak adhesion force, but a more gradual detachment profile and increased detachment length (3.69 nN detachment force, 0.48 fJ detachment work and 68.4 nm detachment length; Figure 4.11).

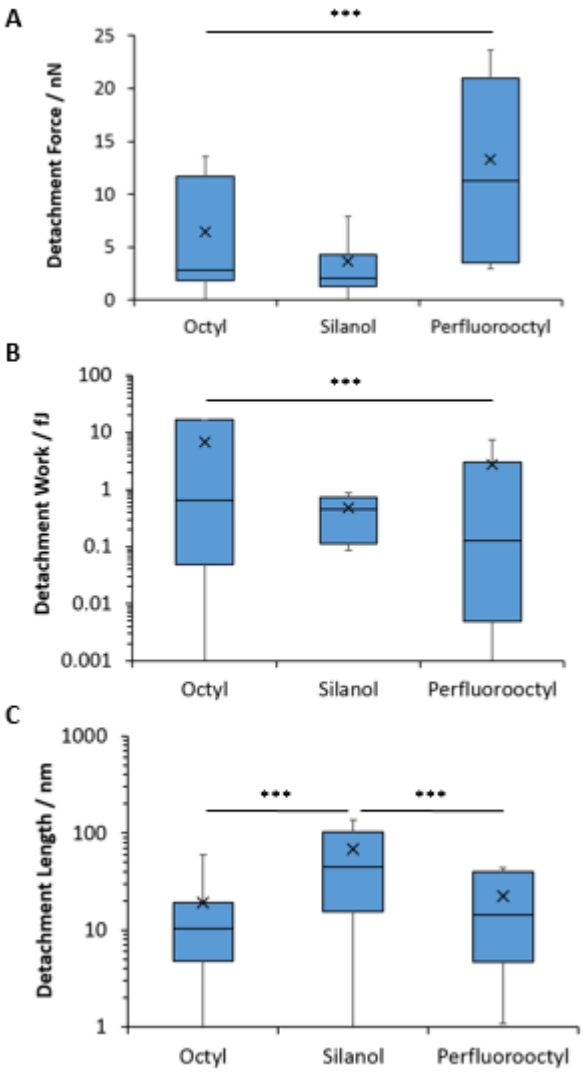


**Figure 4.11.** Detachment force (A), work (B) and length (C) measured for the adhesion of PAA brushes to hydrophobic (octyl and perfluorooctyl) and hydrophillic (silanol) monolayers submerged in deionised water. Data is plotted as means, with box plots. ***, $p \leq 0.001$.

Such difference in the structure of water at hydrophobic and hydrophilic SAMs is also supported by molecular dynamics studies that give evidence for the occurrence of 0.3 nm gaps between vicinal water and hydrophobic SAMs.[248] Similarly, such water structuring was found to impact the adhesion of moderately hydrophobic peptides presenting catechol residues (DOPA), which showed increased bonding forces to hydrophobic SAMs, despite increased hydrogen bonding to hydrophilic SAMs.[249] Hence, our results also support the occurrence of an aqueous interfacial layer that differentially

regulates adhesion of moderately hydrophobic polymer brushes to hydrophobic SAMs (Figure 4.12).

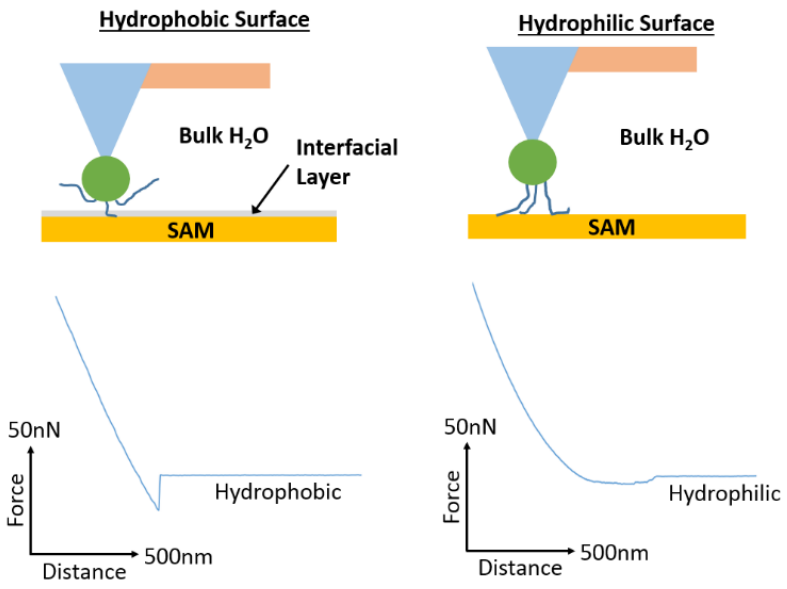


**Figure 4.12.** Proposed mechanism of adhesion of PAA brushes to hydrophobic and hydrophilic monolayers. Representative lift curves are taken from adhesion measurements for alkyl (octyl and perfluorooctyl) and hydrophilic (silanol) SAMs submerged in deionised water. The desorption profiles indicate strong adhesion forces, with a sharp detachment step in the case of alkyl SAMs but overall weak adhesion forces with a more gradual detachment profile for hydrophilic SAMs. These profiles support the occurrence of an aqueous interfacial layer that differentially regulates adhesion of moderately hydrophobic polymer brushes to hydrophobic SAMs.[246,247]

## 4.3.3 Polymer Brush Adhesion to Cell Monolayers

Having studied the impact of substrate chemistry in a set of monolayers with a range of hydrophobicity/hydrophilicity, charge and hydrogen bonding potential, we next turned our attention to the adhesion profile of weak polyelectrolyte brushes and POEGMA to epithelial cell sheets. These biointerfaces can be regarded as simplified systems to the understanding of tissue bonding due to the greater cellular homogeneity within cultured cell sheets, their planarity and relative rigidity (at the macroscale, owing to the rigidity

of the underlying substrate). We focussed on two epithelial models: HaCaT cells (a human epidermal cell line) and primary keratinocytes (stem cells responsible for the homeostasis of the interfollicular epidermis).[250]

Figure 4.13A and B present the adhesion profiles and quantification of adhesion forces of POEGMA, PDMAEMA and PAA brushes to cell sheets of keratinocytes and HaCaT cells. Due to the high density and the length of their oligo(ethylene glycol) side chains, POEGMA brushes are known for their excellent protein and bacterial resistance.[226,227] The exact detailed mechanism of their protein resistance remains only partially understood, but was proposed to result from their combined hydration shell and steric hindrance (and high chain densities), restricting the infiltration of biomacromolecules.[172,173] In agreement with these reports, POEGMA brushes were found to display very low adhesion to both HaCaT and primary keratinocyte monolayers, with adhesion forces below 0.29 nN (Figure 4.13A/B). Such adhesions are lower than those measured for POEGMA, in the case of hydrophobic or charged SAMs, indicating relatively hydrophilic and weakly charged cell membranes. This is in contrast with the moderate adhesion forces measured between POEGMA brushes and bacteria,[119] which typically display relatively charged and hydrophobic membranes (with lipopolysaccharides).[210]

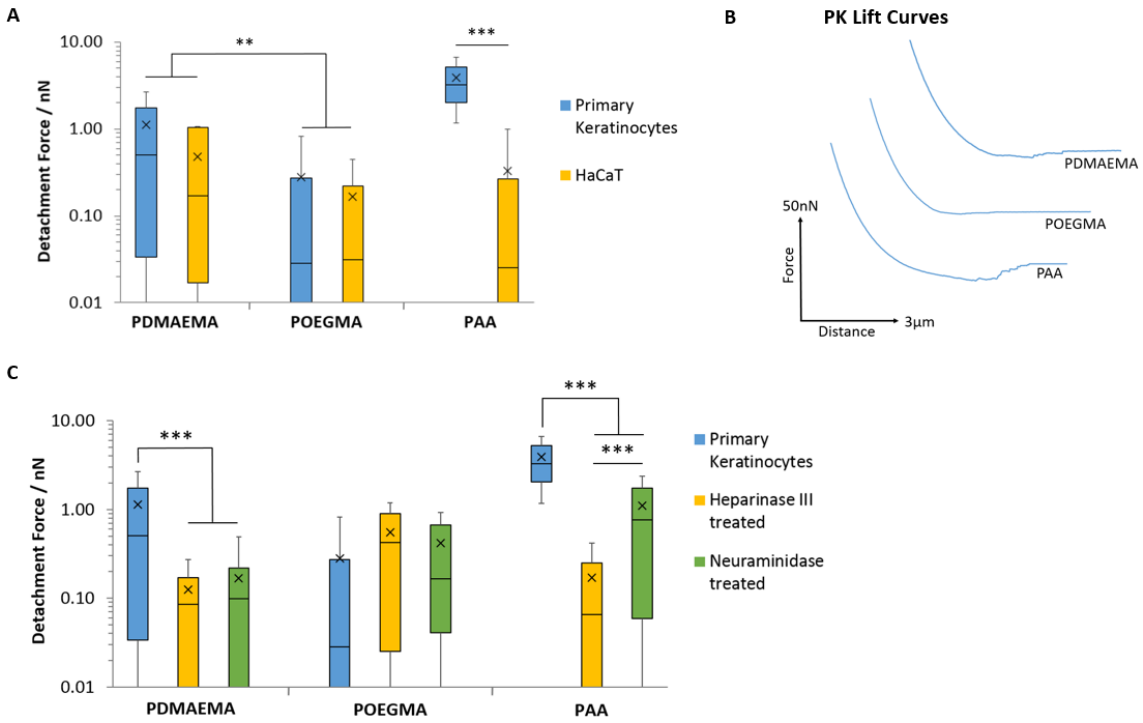


**Figure 4.13.** Characterisation of adhesive interactions between polymer brushes and cell monolayers. Testing was carried out on samples submerged in PBS. (A) Detachment forces between polymers and primary keratinocyte (PK) and HaCaT cell monolayers. (B) Representative AFM lift curves displaying the interaction between the polymers and primary keratinocyte cells. (C) Detachment forces between polymers and primary keratinocyte monolayers with and without enzymatic treatment. Data is plotted as means, with box plots. **, $p \leq 0.01$. ***, $p \leq 0.001$.

PDMAEMA displayed relatively weak interactions with both cell monolayers; this is associated with low adhesion forces and detachment work (< 1.14 nN and < 0.87 fJ, respectively; Figure 4.13A/B and Figure 4.14A). Although higher than interactions measured for POEGMA, such low adhesion is surprising considering the high positive ζ-potential of PDMEAMA brush-based colloids and their rapid uptake by cells, for example for gene delivery applications.[170,251,252] Hence, it is possible that the rapid fouling of cationic polymer brushes by proteins and components found in the medium results in the substantial modification of the PDMAEMA brush surface and associated decrease in

ζ-potential,[253] leading to a masking of short range hydrophobic interactions and hydrogen bonding.

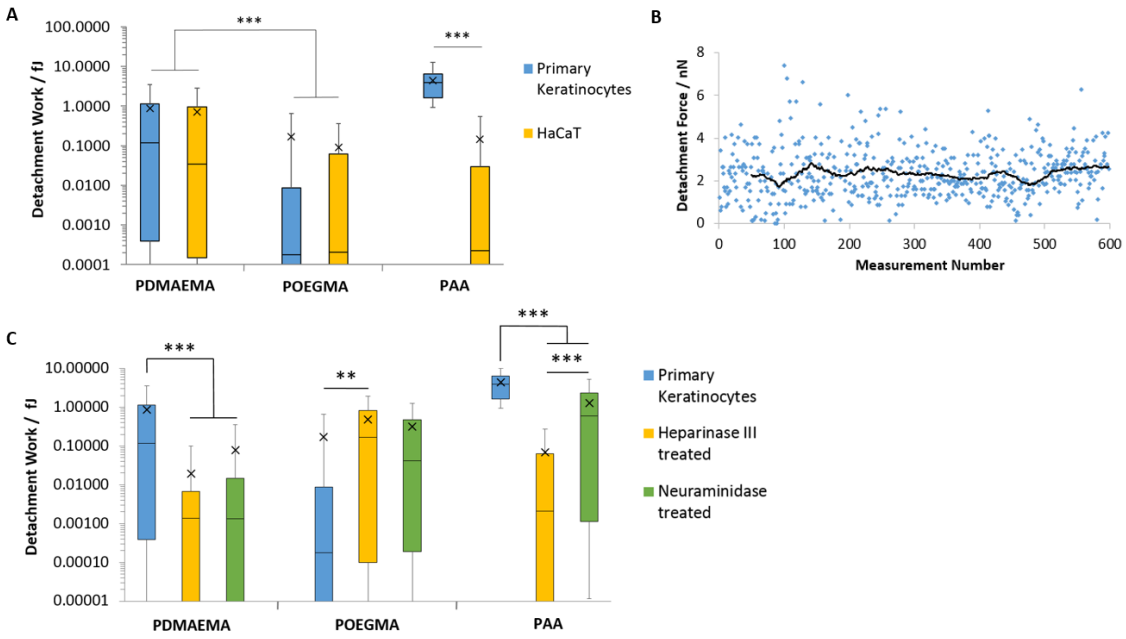


**Figure 4.14.** Characterisation of adhesive interactions between polymer brush functionalised colloidal AFM probes and cell monolayers. Testing was carried out on samples submerged in PBS. (A) Detachment work between polymers and primary keratinocyte (PK) and HaCaT cell monolayers. (B) Variation of PAA detachment force during repeated measurements on a primary keratinocyte cell sheet as a function of time. The black line illustrates a 50 point moving average of the data. (C) Detachment work between polymers and primary keratinocyte monolayers with and without enzymatic treatment. Data is plotted as means, with box plots. **, $p \leq 0.01$. ***, $p \leq 0.001$.

In contrast, PAA brushes displayed strong adhesions to primary keratinocytes (3.91 nN and 4.41 fJ, respectively; Figure 4.13A/B and Figure 4.14A). This behaviour was associated with substantially longer detachment lengths than those reported for SAMs (752 ± 17 nm, compared to lengths typically < 100 nm for SAMs), suggesting that the retraction of PAA-coated colloids is associated with substantial deformation of the cell membrane, contributing to the overall retraction profile. Strikingly, the adhesion of PAA

brushes to HaCaT cells was very low (0.33 nN). To test whether fouling occurred at the brush surface, repeated measurements (600 adhesion and retraction events) were carried out and plotted as a function of cycle number (Figure 4.14B). The scatter of the data as function of cycle number, compared to the overall average, clearly indicates no significant positive or negative deviations as a function of time. To account for the high adhesion of PAA brushes to primary keratinocytes, we proposed that the glycocalyx (a proteoglycan brush-like layer that coats the cell membrane)[254] of the epithelial cell sheets studied differed. Staining of the glycocalyx with wheat germ agglutinin (WGA) and specific immunostaining of the heparin component of the glycocalyx indeed revealed striking differences in the abundance and localisation of the glycocalyx in primary keratinocytes and HaCaT cells (Figure 4.15).

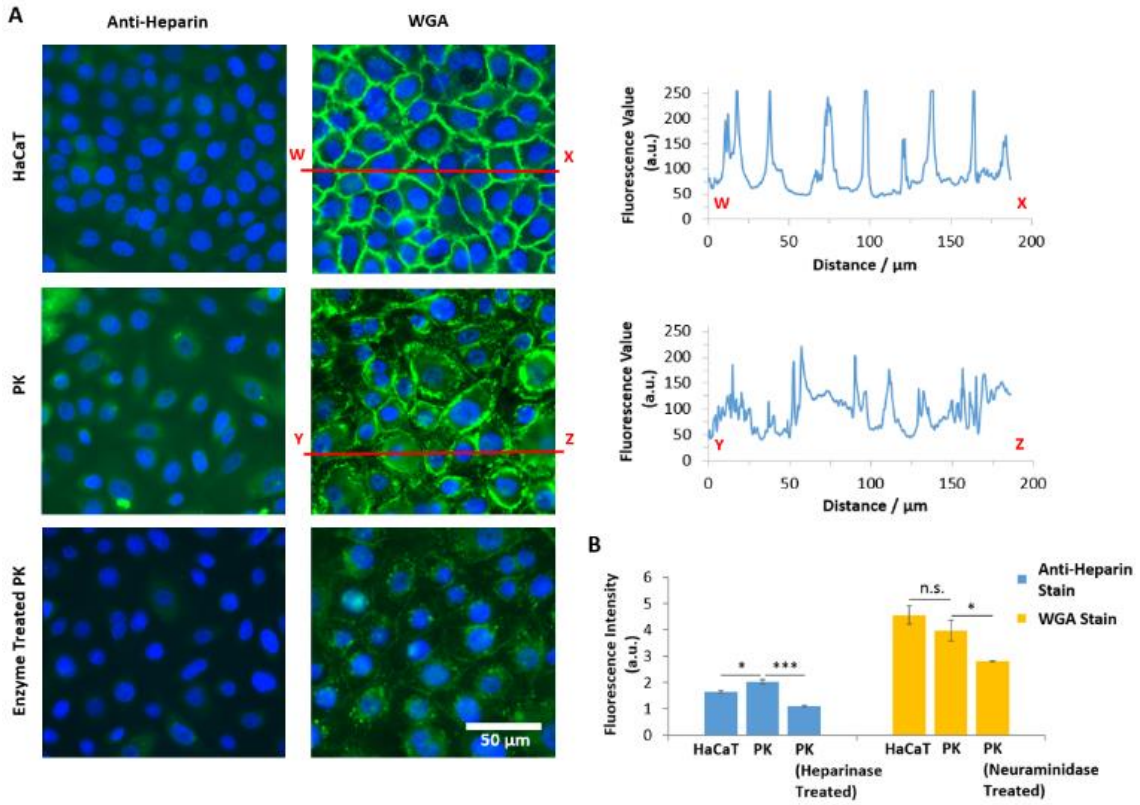


**Figure 4.15.** Quantification of the glycocalyx in primary keratinocytes (PK) and HaCaT cells through staining with wheat germ agglutinin (WGA) and specific immunostaining of the heparin component of the glycocalyx using anti-heparin. (A) Representative fluorescence images (Blue, DAPI; Green, anti-heparin or WGA) for HaCaT cells and primary keratinocytes. Primary keratinocytes were treated with Heparinase III and Neuraminidase and staining was carried out using anti-heparin and WGA, respectively. Cross-sections in the fluorescence values illustrate the differing localisation of the glycocalyx for HaCaT and primary keratinocyte cells. (B) Fluorescence intensity values for HaCaT cells, primary keratinocytes and enzyme treated primary keratinocytes, stained with either anti-heparin or WGA. Error bars show standard errors for repeats across samples (sample size n = 3). Data is plotted as means. *, $p \leq 0.05$. ***, $p \leq 0.001$. n.s., non-significant.

Heparin was found to be expressed at lower levels in HaCaT cells compared to primary keratinocytes (Figure 4.15A and B). In contrast, non-specific staining of the glycocalyx using WGA did not show the same trend; instead of a diffuse relatively homogenous staining, the glycocalyx was strongly localised at cell-cell junctions in the case of HaCaT monolayers (Figure 4.15A). With primary keratinocytes, the glycocalyx was spread more uniformly on the apical membrane, with little sequestration at cell junctions. This was

quantified by plotting the intensity profile of WGA sequestration in HaCaT cells and keratinocytes. This differential regulation of the localisation of the glycocalyx is proposed to result from the culture conditions: HaCaT cells were cultured in normal DMEM medium, which contains high levels of $Ca^{2+}$, enabling the formation of cell junctions, whereas keratinocytes were cultured in KSFM, a medium containing low levels of $Ca^{2+}$, in which conditions cadherin-mediated junctions are typically not stabilised.[255] Overall, these results indicate that the localisation and abundance of the glycocalyx in HaCaT cells and keratinocytes differs significantly, and this correlates with the changes in adhesion measured for polyelectrolyte brushes to the corresponding cell monolayers.

To further test the impact of the glycocalyx on colloidal probe adhesion to primary keratinocytes, we treated cell sheets with neuraminidase (broad spectrum enzyme cleaving the glycocalyx) and heparinase (enzyme specifically cleaving heparin components).[256] The efficiency of such cleavage was confirmed by staining and fluorescence microscopy (Figure 4.15B). Following such treatment, PAA brush adhesion was significantly reduced (Figure 4.13C and Figure 4.14C). In particular, heparinase treatment resulted in a reduction of adhesion forces to levels comparable to POEGMA adhesion on untreated cells. Neuraminidase treatment had a more modest impact, indicating that, although cleavage of heparin accounts for most of the adhesion strength of PAA brushes to cell membranes, full cleavage of the glycocalyx reveals buried domains and potentially directly exposes the phospholipid bilayer, accounting for the moderate adhesion measured. These observations are in good agreement with the work of Servais *et al.*, who reported that the adhesive force of pectin/CMC formulations to the mesothelium of several different tissues (investigated via uniaxial tensile strength tests

using a customized apparatus for load/displacement measurements) was reduced after treatment of these samples with neuraminidase; in some cases this was by as much as 50%.[257] The dependence of weak polyelectrolyte adhesion to cells, mediated by the glycocalyx, is therefore demonstrated across multiple length scales. Similarly, enzymatic cleavage of the glycocalyx components had a significant impact on the adhesion of PDMAEMA brushes, indicating that steric repulsion may also be responsible for the weak adhesion profile of these brushes to cell monolayers; this further suggests that fouling of the PDMAEMA surface is responsible for such low adhesion, despite the absence of medium or serum in the testing conditions. Surprisingly, the adhesion of POEGMA brushes slightly increased after enzymatic treatment of primary keratinocytes (to 0.55 and 0.42 nN after heparinase and neuraminidase treatment, respectively). This suggests that such enzymatic treatment leads to the exposure of residues, perhaps with higher hydrophobicity, as this was a particular type of interaction that promoted stronger adhesion of POEGMA brushes with SAMs.

### 4.3.4 Polymer Brush Adhesion to Soft Tissue Samples

We next studied the adhesion of polymer brushes to soft epithelial tissues: the gingiva (which structure and homeostasis is regulated by gingival keratinocytes) and the epicardium (a membrane to which adhesion is particularly relevant for epicardial placement strategies).[258,259] Figure 4.16 presents the detachment force and work measured during the adhesion of PDMAEMA, POEGMA and PAA brushes to porcine gingiva and epicardium samples. Overall, interactions of polymer brushes were stronger with the epicardium compared to the gingiva. As expected, adhesion between POEGMA brushes and both tissue types was minimal, consistent with the protein resistance of

this polymer brush. Adhesion forces and work of PAA and PDMAEMA brushes to gingival epithelium were increased compared to that of POEGMA but remained overall relatively weak (< 2.72 nN). In contrast, the adhesion of PAA and PDMAEMA brushes to the epicardium increased significantly (3.58 and 5.67 nN, respectively). Hence PDMAEMA was found to adhere relatively strongly to the epicardium, perhaps reflecting a higher coulombic attraction or hydrogen bonding with this tissue. The adhesion of PAA brushes to the epicardium was in line, although slightly lower than that measured to primary keratinocyte monolayers. These differences in adhesion to the epicardium and gingiva likely reflect differences in the composition of the cell surface, and in particular that of the glycocalyx in these two tissues.

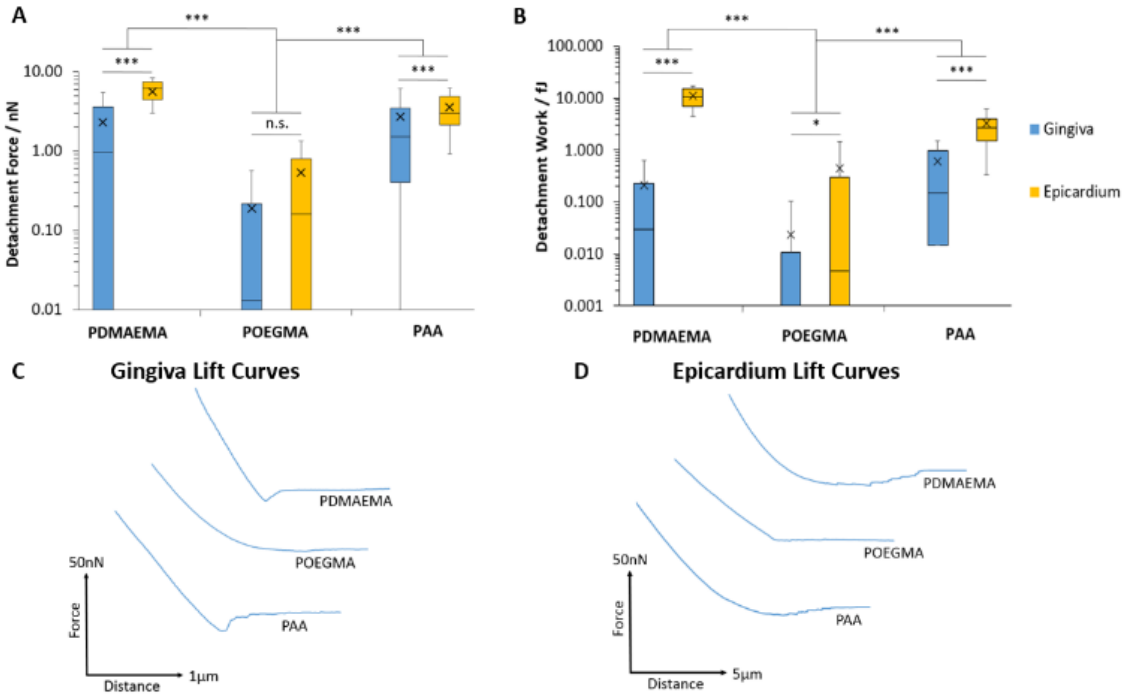


**Figure 4.16.** Characterisation of adhesive interactions between polymer brushes and porcine tissue samples. Testing was carried out on samples submerged in PBS. (A) Detachment force of epicardium and keratinized gingiva to polymers. (B) Detachment work between polymers and soft tissue samples. (C) Representative AFM lift curves between polymers and gingival samples. (D) Representative AFM lift curves between polymers and epicardium. Data is plotted as means, with box plots. *, $p \leq 0.05$. ***, $p \leq 0.001$. n.s., non-significant.

To the best of our knowledge, the epicardial glycocalyx has not yet been characterised. The parietal and visceral pericardium (epicardium) are known to be similar in structure, both comprising a serosal (mesothelial cell) component adjacent to a fibrous tissue layer.[65] The parietal pericardium has been shown to display a rich glycocalyx coating, in particular, rich in sialic acid residues.[260] Assuming there is similarity in the glycocalx structure of both of these layers, the higher level of sialic acid content at the surface of the epicardium could qualitatively account for the strong adhesion observed for PDMAEMA brushes to this tissue.

In the oral mucosa, the epithelium forms a keratinized layer in which the glycocalyx interpenetrates with the salivary film.[261] The presence of a glycocalyx layer on the surface of corneocytes has been evidenced via electron microscope,[262,263] but to the best of our knowledge the exact composition of this layer is yet to be determined. The salivary film, which is estimated to be 70-100 μm thick,[264] contains several molecules which include a large concentration of mucins[265] and a number of different types of bacterial species. These bacteria have been shown to adhere to each other, as well as to the surface of the oral epithelium via a network of their glycocalyx.[266,267] As such, there are a number of potential molecules that could contribute to polymeric adhesion to the keratinized gingiva; additional enzymatic studies will be required to identify the specific molecules present and the role that each plays in adhesion.

However, it should be noted that significant differences in tissue stiffness could account for at least some of the differences in adhesion measured between these two tissues. Indeed, the epicardium was found to be significantly softer than the gingival epithelium. This can be clearly seen in the large retraction lengths measured for the epicardium, especially for PDMAEMA brushes, compared to those measured for the gingiva and even cell monolayers (Figure 4.16C and D). Furthermore, from the nanoindentation results (Figure 4.5) the gingiva was significantly stiffer than the epicardium (1020 ± 130 and 20.7 ± 0.5 kPa, respectively), suggesting that the colloidal probe indentation may result in substantial conformal deformation of the epicardium, and therefore an associated increase in contact area. As such, our data suggests that tissue biochemistry and stiffness combine to regulate the strength of adhesion of soft polymeric interfaces.

## 4.4 Summary

Adhesion tests to SAMs reveal the complexity of weak polyelectrolyte brushes with adhesion arising from combinations of electrostatic, Van der Waals interactions and hydrogen bonding, resulting in particularly strong adhesion of PAA brushes to a wide range of surface chemistries. The response of such adhesive behaviour to electrolytes and changes in the Debye length are in turn equally complex, and are further modulated by the formation of hydrogen bonds with electrolytes (such as phosphates). POEGMA brushes generally displayed little adhesion to SAMs, in good agreement with its neutral structure, lacking strong proton acceptor or donor functions. Furthermore, POEGMA brushes are known for their excellent protein and bacterial resistance and accordingly were found to display very low adhesion to both HaCaT and primary keratinocyte monolayers. Comparatively, PDMAEMA and PAA brushes showed increased adhesion to these cell monolayers. Upon enzymatic treatment of primary keratinocytes with heparinise III and neuraminidase, both of which are known to disrupt the glycocalyx layer, adhesion of PDMAEMA and PAA was found to reduce significantly. These results highlight the importance of the glycocalyx in regulating non-specific adhesion between polymers and cells, particularly in the case of PAA brushes.

The identified factors which are responsible for adhesion to SAMs and cell monolayers further determine the response of polymer brush adhesion to more complex biological tissues. The mechanical properties of soft tissues was also found to have a contributing effect, as a result of the conformal contact of soft tissues to soft matter interfaces. Studies of the stiffness of soft tissues, via AFM-based nanoindentation, confirmed that the keratinized gingiva was significantly stiffer than the epicardium, in line with the differing functionalities of the two tissue types.

Our results demonstrate that simple considerations of electrostatic and hydrophobic interactions between polymer brushes, and even relatively simple interfaces (self-assembled monolayers), cannot fully account for adhesive profiles. In this context, in studies of brush adhesion to cells and tissues, the prediction of interactions is particularly difficult to establish; relatively elaborate models, such as molecular dynamics simulations based on atomistic and coarse grain models will be essential to capture the complex nature of polymer brush-interactions with biological samples, whether bacteria, eukaryotic cells or tissues. Our study also points to the need for an improved understanding and characterisation of the glycocalyx of the epithelium, or the surface chemistry of tissues, to which biomaterials bonding is required. Some studies have explored the structure and morphology of the glycocalyx in epithelial layers, but this is not systematic across all tissues, and often remains incomplete.

# CHAPTER 5

## Characterisation of Macroscale Mechanical Properties of Soft Hydrogel-Tissue Interfaces

# 5.1 Introduction

The central focus of this chapter is to study the interaction between PAA-based hydrogels and soft tissues at the macroscale. Hydrogels have applications in areas such as skin adhesives for surgical applications,[3–5] epicardial placement and stem cell delivery,[6] soft tissue adhesion for tissue regeneration,[7,8] and mucoadhesives for dental adhesion.[9,10] In all of these applications, an in-depth understanding of the interactions occurring between the hydrogel and soft tissue is required. PAA hydrogels have interesting properties such as stimuli responsive behaviour and high hydrophilicity, due to their high density of carboxyl groups.[36–38] As a result, PAA hydrogels have great potential to be deployed in areas such as mucoadhesives for drug delivery,[39,40] surface coatings for biomedical devices,[41,42] and microdevice and sensor applications.[36]

Four different polymer-gelation systems were studied within this Chapter, each of which present different types (chemistry) of crosslinks and crosslinking mechanisms. Two of these gels were formed through UV initiation using Irgacure 2959 as the photoinitiator, and another gel used visible light-mediated crosslinking with eosin Y as the photinitiator. The final gel utilised physical crosslinking alone through the interaction between boronic acid moieties and the polysaccharide mannan. The strength of adhesion between two materials will partly depend on the mechanical properties of the adhesive. Consequently, prior to adhesion tests, oscillatory rheometry was used to characterise the rheological behaviour of the different gels, including their gelation kinetics. Tensile testing was used to characterise the adhesion of the different gels to hydroxyl and methacrylate SAMs, as a means of studying adhesion to interfaces with defined chemistry. Finally, adhesion to soft tissues was studied through lap shear and tensile testing. The literature review for this chapter discusses some of the different crosslinking

mechanisms that can be used to generate hydrogels, followed by a discussion on methods for the characterisation of hydrogels and some of the complications associated with these.

### 5.1.1 Crosslinking of Hydrogels

Hydrogels can either be classed as chemical gels, where the crosslinks are permanent covalent bonds, or physical gels, where the crosslinks are non-permanent and a result of either physical entanglement of the network or some secondary bonding such as ionic bonding.[268] PAA is often supplied in powder form which can then be dissolved in aqueous solution. This powdered PAA can then be made into a physical or chemical gel depending upon the preparation method. In physical gels, secondary hydrogen bonds will crosslink polymer chains to form a gel network. PAA gels will also form physically entangled structures, in which polymer chains are physically trapped, resulting in non-covalent crosslinks. Adding ionic salts to the gel will also assist in the crosslinking of PAA through the introduction of ionic bonding between carboxyl groups. Calcium is a commonly used ionic binder that can be dissolved into the gel solution in the form of calcium chloride. Ionic cross-linkers can also, in some instances, be used to give a tuneable stiffness of the gel, as has been reported for alginate gels.[269] The crosslinking of a gel has a huge influence on its mechanical properties and consequently it is an important factor to consider.[268,270]

Hydrogels can be chemically crosslinked using a photoinitiator in the presence of UV or visible light.[71,73,271,272] This typically requires radical reactive groups on the polymer backbone, such as alkenes and thiols (for thiol-ene coupling).[88,273] Eosin Y is one such photoinitiator, which is FDA-approved, highly water soluble and excited by visible light

(450 – 550 nm).[274] The excitation of eosin Y by visible light exposure results in hydrogen abstraction from a sulfhydryl group to create a thiyl radical. These thiyl radicals then initiate a rapid and orthogonal thiol-ene gelation reaction. Using this approach, a co-monomer and co-initiator are often required in order to generate sufficient radicals to achieve high functional group conversion.[274,275]

Irgaure 2959 (I-2959) is another photoinitiator that is regularly used for UV-crosslinking of hydrogels. I-2959 cannot be used for visible-light-mediated crosslinking as a result of its near zero molar absorptivity at wavelengths greater than 400 nm.[275] There are limitations associated with the clinical translation of UV crosslinkable hydrogels due to biosafety concerns associated with the use of UV light. UV light can generate reactive oxygen species which may lead to DNA damage, accelerated tissue ageing or cancer.[274] As an example, Federovich *et al.* demonstrated that the combination of both UV light and the photoinitiator I-2959 resulted in adverse effects on the viability of stem cells embedded within hydrogels.[276] As such, gels that can crosslink under wavelengths closer to the visible light or even infrared radiation (IR) range would be beneficial within biomedical applications. Accordingly, the development of hydrogels that utilise visible light, in combination with safer photoinitiators, such as eosin Y, is of great interest.[274]

Boronic acids have generated a lot of interest in biomedical applications due to their ability to form reversible covalent bonds with a number of biologically important molecules; these include molecules with a diol functionality, which include saccharides such as glucose and a wide range of polysaccharides.[277] The reversible covalent interaction of boronic acids with diols has proven sufficiently strong that it enables binding of saccharides at mM or sub-mM levels.[278] Due to this ability to bind saccharides at low concentrations, along with the wide range of molecules boronic acid can bind to,

boronic acids have been widely exploited in various biosensor applications.[277] Compared to other synthetic receptors that can bind to saccharides, boronic acids have demonstrated good flexibility in giving functional materials due to their high affinity and high selectivity for a variety of different molecules encountered within the body.[278,279]

When boronic acids react with diols they form boronate esters. These boronate esters undergo hydrolysis in acidic conditions, and as such are pH-sensitive. Consequently, boronic acid cross-linked polymers have been extensively studied as stimuli-responsive hydrogels.[277,280] For example, Heleg-Shabtai *et al.* demonstrated the use of Gossypol-cross-linked boronic acid-modified hydrogels as a functional matrix for the controlled release of an anticancer drug.[280] In addition, due to the reversibility of the covalent bonding between boronic acids and diols, hydrogels cross-linked with boronic acid have demonstrated self-healing properties at neutral and acidic pH.[281]

### 5.1.2 The Characterisation of Hydrogels

There are a few prominent factors that make both the measurement and interpretation of the mechanical data from hydrogels a significant challenge for researchers. Firstly, since hydrogels are multi-phase materials with a solid and a liquid solvent phase, they exhibit neither the behaviour of solids nor that of liquids. Consequently, simple treatments established for solid polymers will not give the level of insight required to fully understand the mechanical response of hydrogels; a more sophisticated analysis is therefore required.[282] In addition, hydrogels generally have poor mechanical properties due to the fact that a substantial fraction of the hydrogel material is water, and also due to the random alignment of fibres within hydrogels.[283] As such, hydrogels have a

relatively small elastic modulus, in the order of kPa, whereas most mechanical testing equipment classically used for the characterisation of polymers is optimised for the range of MPa to GPa.[282]

It can also be difficult to 'grip' and manipulate hydrogels for use within the various mechanical testing equipment that is available on the market. The basic mechanical testing techniques that are used for polymeric materials are also often used for the characterisation of hydrogels. Similarly to most polymers, hydrogels exhibit time-dependent mechanical behaviour due to the viscoelasticity of the polymer network. However, for hydrogels there is an additional time dependent deformation mechanism due to fluid flow. Consequently, time is an especially important factor in the planning and execution of the mechanical characterisation of hydrogels.[282]

Six of the most common mechanical characterisation methods for hydrogels are shown in Figure 5.1. These include unconfined tension and compression tests, confined tension tests, local indentation tests with a probe, and frequency based tests such as shear rheometry or dynamic mechanical analysis (DMA). In order to execute an effective tensile test, there must be good sample gripping. However, this can be difficult in the case of hydrogels which are hydrated and compliant. Tensile tests are typically done at a fixed rate until specimen failure occurs, and these tests may be repeated at a variety of strain rates due to the time-dependent nature of hydrogels. Hydrogels are difficult to 'machine' into a regular specimen geometry and as such probe-based tests such as indentation or nanoindentation are a popular choice for material characterisation Furthermore, these tests do not require 'gripping' of the materials in the way that other tests do.

Although there are a number of established techniques for the characterisation of mechanical properties of hydrogels, Oyen recently acknowledged that we are currently lacking a consensus within the scientific community on how to best execute these different characterisation techniques, as well as how to best analyse data from them.[282]

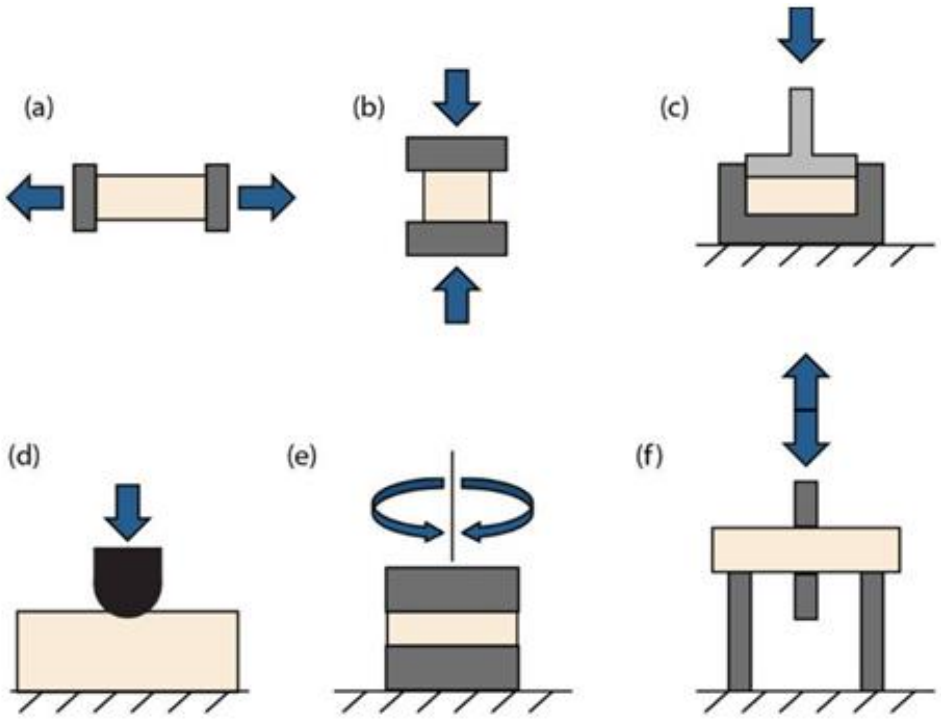


**Figure 5.1.** Schematic of common testing methods for the characterisation of the mechanical properties of hydrogels. (A) Tension. (B) Compression. (C) Confined compression. (D) Indentation. (E) Shear rheometry. (F) Dynamic mechanical analysis (DMA), illustrated here for three point bending. Figure taken from Oyen.[282]

For the characterisation of the adhesive properties of hydrogels to a surface, there are a few common methodologies that are used; these include tensile bond tests and lap shear tests, which measure adhesion strength (the maximum force per unit area). In addition, peel tests measure adhesion toughness (the energy required to advance separation per unit area).[49] The remainder of this chapter will utilise some of these

aforementioned characterisation methods in order to measure the mechanical properties of soft hydrogels and their bonding to tissues. For the characterisation of hydrogels, parallel plate shear rheometry was chosen, as this method enables the characterisation of the complex flow and deformation behaviour of materials before, during and after curing. For adhesion testing, tensile bond and lap shear tests were selected due to their ease of setup for our hydrogel/tissue bonding system.

## 5.2 Materials and Methods

### 5.2.1 Chemicals and Materials

Poly(acrylic acid) (PAA, $M_W$ = 450000), poly(acrylic acid, sodium salt) solution (PAA, $M_W$ = 15000, 35 wt.% in $H_2O$), 3-(bromomethyl)phenylboronic acid (90%), 5-bromo-1-pentene (95%), 2-hydroxy-4'-(2-hydroxyethoxy)-2-methylpropiophenone (Irgacure 2959, 98%), toluene (anhydrous, 99.8%), triethylamine (≥99.5%), Dulbecco's phosphate buffered saline (PBS), cystamine dihydrochloride (≥98%), tyramine hydrochloride (≥98%), methanol (MeOH, 99.9%), 3-(trimethoxysilyl)propyl methacrylate (98%), mannan from *Saccharomyces cerevisiae* (prepared by alkaline extraction), poly(ethylene glycol) dithiol (PEGDT, average Mn 1,000) and eosin Y (99%) were purchased from Sigma-Aldrich and used as received. 4-(4,6-dimethoxy-1,3,5-triazin-2-yl)-4-methylmorpholinium chloride (DMTMM, >98%) was purchased from Tokyo Chemical Industry UK Ltd. All Plasma treatment was carried out using a Henniker Plasma Vacuum System HPT-200. pH measurements were taken using a Mettler Toledo, SG2 – SevenGo pH meter.

### 5.2.2 Characterisation of Hydrogels by Oscillatory Rheology

The mechanical properties of gels were characterised by oscillatory rheology, using a TA Discovery HR-3 hybrid rheometer with a 20 mm standard Peltier plate geometry installed. Gels were characterised using time sweeps, frequency sweeps, amplitude sweeps and through stress relaxation profiles. Time sweeps were used to monitor the change in mechanics before, during and after curing of the gels; for these tests, oscillating frequencies of 1 Hz and oscillating displacements of $10^{-4}$ rad were used. The

frequency sweeps were performed from 0.1-100 Hz at an oscillating displacement of $10^{-4}$ rad. Amplitude sweeps were performed from $10^{-5}$ to $10^{-3}$ rad at an oscillating frequency of 1 Hz. For stress relaxation experiments, gels were subjected to a 2% strain (2 s strain rise time) and the subsequent drop in stress was monitored. All rheology experiments were repeated at least 3 times and representative curves are shown in all cases. Curing of the gels was obtained through application of the light source through the lower surface of the gels using a TA Instruments UV curing accessory; both UV and visible light could be applied using this light guide accessory. The UV light source used was an Omnicure series 1500 lamp. An ILT 1400-A radiometer photometer from International Light Technologies Inc. was used to measure UV light intensities. Visible light of controllable intensity was generated using an OSL2 fiber illuminator from Thorlabs.

The various protocols used for the functionalisation of poly(acrylic acid) are described in detail in Chapter 2. The chemical composition of the polymers and their functionalisation levels, as quantified via NMR, are also summarised within Chapter 2.

*PAA-tyramine hydrogels.* PAA was functionalised with tyramine at a functionalisation level of 1.9%. For the preparation of gels, tyramine functionalised PAA was initially dissolved in PBS. Following this, an eosin Y solution was prepared (50 mg/mL PBS) and added at 0.15% molar equivalence relative to the polymer. For all of the gels generated, they were prepared freshly before tests and the photoinitiator, or crosslinking agent, was added the evening before testing to allow for a more homogeneous mixing without the introduction of bubbles. Visible light curing was done at an intensity of 40 mW/cm$^2$. In order to obtain a good bond between the hydrogels and the upper and lower geometries of the rheometer, functionalised glass coverslips were used.[100] These were

glued in place using Loctite super glue and could subsequently be easily removed by immersion in acetone. Glass coverslips (20 mm) were plasma oxidized (10 minutes, air) and then placed in a solution of anhydrous toluene (30 mL), 3-(trimethoxysilyl)propyl methacrylate (30 µL) and triethylamine (50 µL), and left overnight. They were then washed with deionised water, followed by ethanol, and then dried under a stream of nitrogen. The complete scheme, from generation of the functionalised polymer through to the generation of gels, is shown in Figure 5.2. Throughout this chapter gels formed through this approach will be referred to by the notation PAA-Tyr.

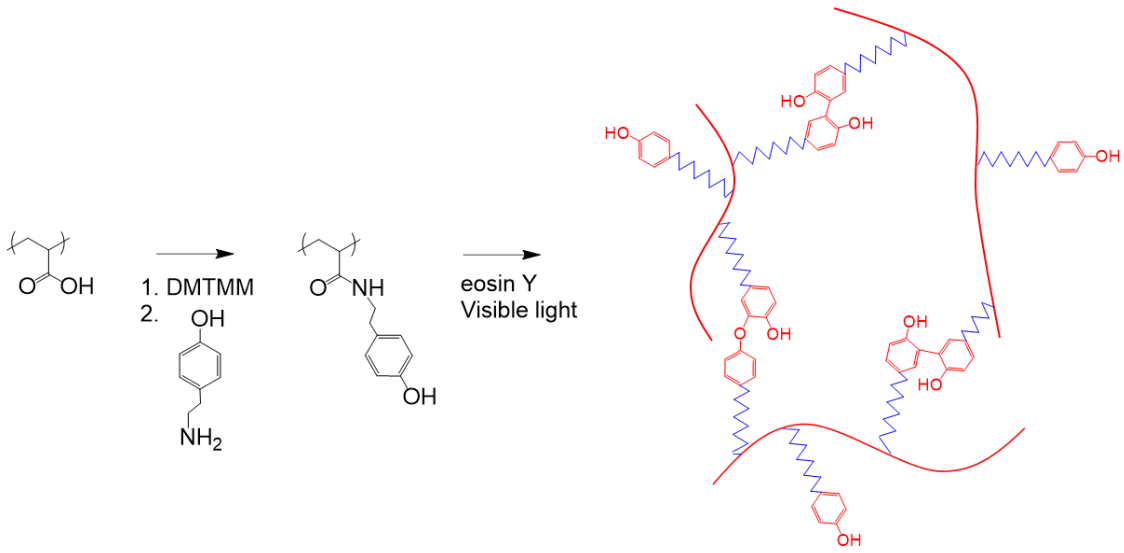


**Figure 5.2.** Generation of PAA-Tyramine gels (PAA-Tyr) through crosslinking of tyramine molecules under visible light-mediated initiation.

*Boronic acid-functionalised PAA hydrogels.* PAA was functionalised with boronic acid at a functionalisation level of 18.1%. Mannan was used to physically crosslink these gels and this was dissolved in PBS (250 mg/mL), before addition to the polymer solutions. For preparation of the gels the polymer was initially dissolved in PBS, and then once fully dissolved the mannan solution was added at a level of 10% molar equivalence relative

to boronic acid. As these gels were not cured through UV or visible light initiation, the light guide accessory was not used, and this allowed the use of a solvent trap geometry (40 mm Peltier solvent trap and evaporation blocker). This enabled characterisation of the properties of the gels without the stiffening effects due to sample drying. However, with the solvent trap, functionalised glass coverslips were not used. The scheme for the generation of these gels is shown in Figure 5.3 and these gels are referred to by the notation PAA-BA.

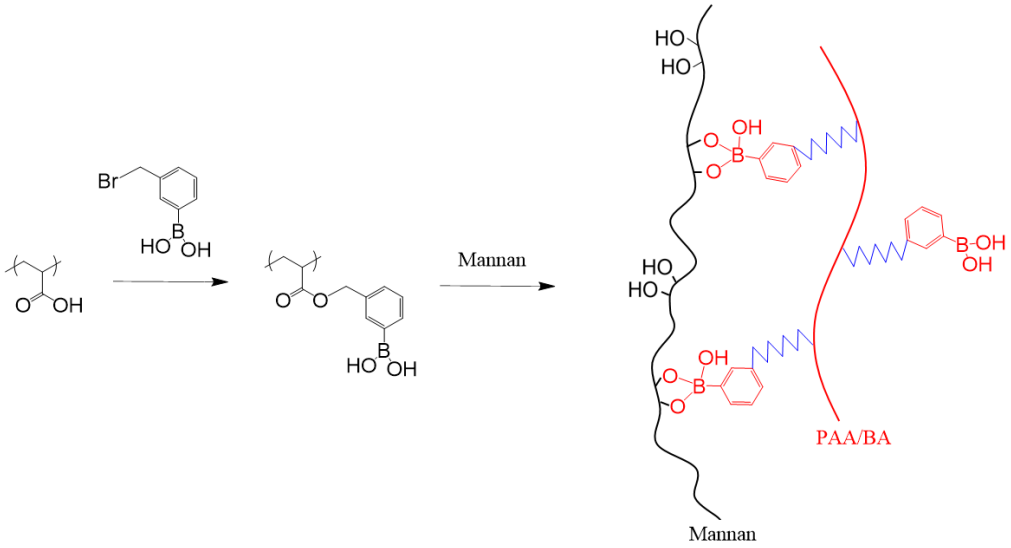


**Figure 5.3.** Generation of PAA-boronic acid gels (PAA-BA), physically crosslinked using the polysaccharide, mannan.

*PAA-pentene hydrogels.* PAA was functionalised with 5-bromo-1-pentene at a functionalisation level of 5.2% and 12.9% for PAA molecular weights of 450000 and 15000 g/mol, respectively. For preparation of gels the polymer was initially dissolved in PBS. PEGDT (225 mg/mL PBS) and Irgacure 2959 solutions (250 mg/mL MeOH) were prepared, and PEGDT was then added at a molar ratio of alkene:thiol of 2:1, followed by the addition of Irgacure 2959 at a molar ratio of 5% relative to the alkene level. pH values

of solutions were altered after the addition of PEGDT and were reduced with the addition of small volumes of 3 M HCl. For rheology of the gels, methacrylate coverslips were used, as described previously, and UV initiation was carried out at an intensity of 17 mW/cm$^2$ for 2 minutes. Table 5.1 in the results summarises the thiol equivalences and general conditions used for the different concentrations of gels that were generated. Figure 5.4 illustrates the procedures used to generate these gels; these will be referred to by the notation PAA-BP.

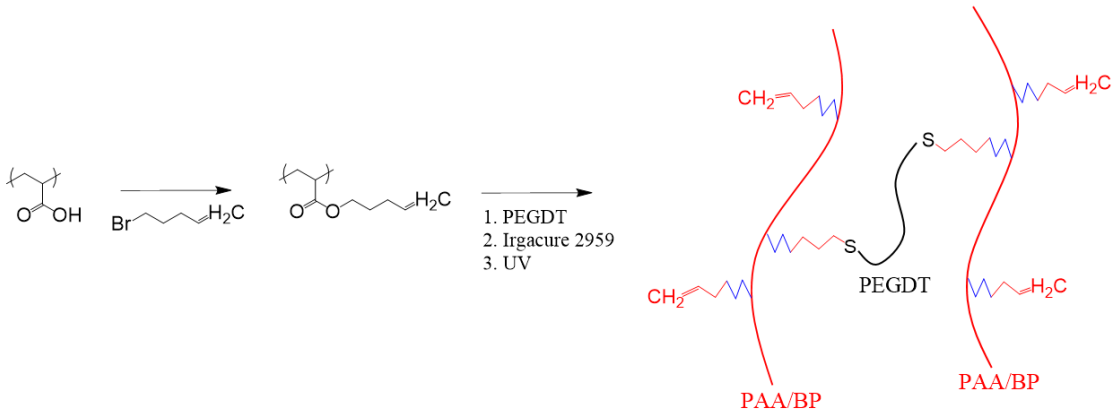


**Figure 5.4.** Generation of bromo-pentene-based gels (PAA-BP), crosslinked using thiol-ene reactions.

*PAA-cysteamine hydrogels.* PAA was functionalised with cysteamine at a level of 4.6%. The polymers were dissolved in PBS, followed by the addition of 30% molar ratio of Irgacure 2959 relative to the thiol content. Similarly to the PAA-BP gels, the photoinitiator was added in solution form (250 mg/mL MeOH). Gels were cured under UV light at an intensity of 17 mW/cm$^2$ and rheometry was carried out using methacrylate functionalised glass coverslips. The scheme for the synthesis of these gels is illustrated in Figure 5.5 and these gels will be referred to by the notation PAA-Cys.

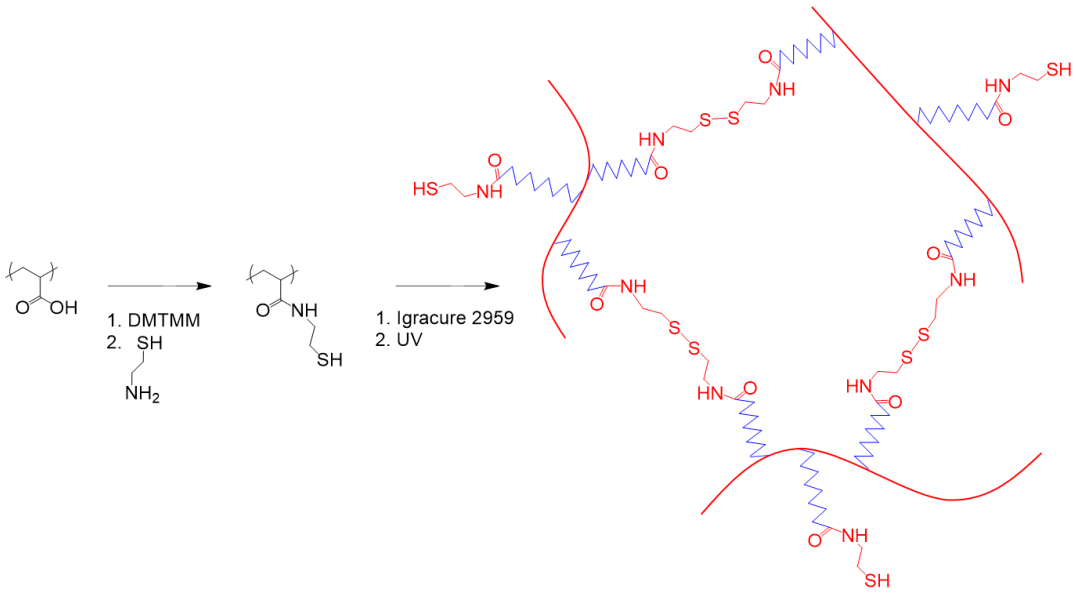


**Figure 5.5**. Generation of cysteamine-based-PAA gels (PAA-Cys), crosslinked under UV-mediated initiation.

## 5.2.3 Characterisation of the Adhesive Properties of Hydrogels

Tensile bond tests were carried out using a TA Discovery HR-3 hybrid rheometer in axial mode, moving at a constant linear rate of 2.5 mm/min and with an angular velocity of 0 rad/s. Testing utilised a 20 mm Peltier plate geometry and the gel was loaded in-between the upper and lower plates (similarly to oscillatory rheometry experiments) ensuring there was full gap coverage. Tests were ended when any material bridging the gap between the upper and lower Peltier plates had completely detached or failed. To keep material loading constant between tests and conditions, an approximate gap size of 300 µm was used. Adhesion tests to self-assembled monolayers (SAMs) were carried out using either plasma treated (10 minutes, air) or methacrylate functionalised (see section 5.2.2) glass cover slides glued to the lower and upper plates. Adhesion tests to soft tissue were carried out using a modified 20 mm Peltier plate geometry. A plasma treated (10 minutes, air) 20 mm glass slide was glued to the lower plate to still allow for

curing of photosensitive gels. To allow sufficient adhesion of the tissue samples to the upper plate, the tissue was bonded to the lid of a 40 mm plastic petri dish and this was then glued to the Peltier plate (see Figure 5.15 and Figure 5.17 in the results for images of the setup). Similarly to the oscillatory rheometry experiments, *in situ* light curing was applied using the light accessory guide. Sample curing was completed immediately before tensile bond testing was carried out.

Soft tissue samples were sourced and dissected, as described in Chapter 4, and were cut in to 15 x 15 mm samples. All testing was carried out within 48 hours from the initial sacrifice of the animals and samples were stored in PBS in the fridge prior to tests. In order to accurately account for variations in sample sizes, images were captured for each sample and the area was calculated using ImageJ. From the data obtained, two parameters were characterised: adhesion strength and energy density. Both of these were calculated using a custom-built Matlab script. Adhesion strength is defined as the maximum force divided by the initial contact area between the gel and substrate. Energy density is defined as the detachment work (the area under the force-extension curve) divided by the contact area between the gel and substrate.

Lap shear tests were performed using an Instron 5967 universal testing system with a 100 N static load cell and lap shear rig installed. During testing a constant extension speed of 10 mm/min was used. Similarly to the tensile bond tests, adhesion strength and energy density were both extracted from the data obtained. Furthermore, tissue dissection was carried out similarly to tensile bond tests and 15 x 15 mm sample sizes were again used (the areas of these were again more accurately determined using ImageJ). For loading of samples, tissue segments were initially glued to a PMMA slide that had been positioned flat on the bench. Approximately 150 µl of polymer solution

was pipetted over the tissue surface. A plasma treated (10 minutes, air) glass slide was then placed on top of the polymer solution/tissue with the hydroxyl-functionalised surface facing downwards. This setup allowed for the curing of gels with UV light (through the upper surface of the glass slide) before they were loaded into the Instron testing rig. Immediately after UV curing of gels, samples were very carefully loaded into the testing rig ready for tests. Testing was ended when there was no longer any contact between the upper and lower slides. Figure 5.19 and Figure 5.20 in the results show images of the lap shear setup used for experiments. A summary of the conditions used for the different gels in the adhesion studies is given in Table 5.2 in the results.

### 5.2.4 Statistics

A one-way ANOVA test with Tukey's post hoc analysis was used to determine statistical significance. For box and whisker diagrams the box represents the 1st, 2nd and 3rd quartiles, as standard, and the whiskers represent the full range of values for each data set. Mean values for the data sets are also shown. In all other figure types (and for in-text referencing) standard errors are reported.

## 5.3 Results and Discussion

### 5.3.1 Characterisation of Hydrogels by Oscillatory Rheology

The properties of several PAA-based gels were characterized via oscillatory rheology in order to compare the effectiveness of various crosslinking strategies. Initially, the properties of PAA-Tyr hydrogels (see scheme in Figure 5.2) were investigated (Figure 5.6). Figure 5.6A shows the gradual stiffening of the gels over extended time periods under the action of visible light. Variations in modulus values were observed initially due to sensitivity of the equipment at such low values (<<1 Pa). In order to ensure stiffening was a result of polymer crosslinking rather than sample drying, the evolution in storage modulus was measured for a period of time before and after the light source was switched on (Figure 5.6E). Although sample drying appears to have an effect on the polymer stiffness to a certain degree, there is also a clear increase in modulus values upon switching the light source on, indicating the formation of polymer crosslinks.

PAA-Tyr gels were found to have relatively weak mechanical properties. As an example, for the gels at a concentration of 10% (w/v) (Figure 5.6A-D), a storage modulus of 40 Pa was found after a 5 min curing time (Figure 5.6A). Even though these weak mechanical properties were identified, the frequency sweep (Figure 5.6B) and stress relaxation profile (Figure 5.6D) indicate the formation of a chemically crosslinked gel. Following the 2% strain rise (in the stress relaxation profile) the gel maintains its structure well, showing minimal relaxation, indicating the formation of covalent crosslinks.

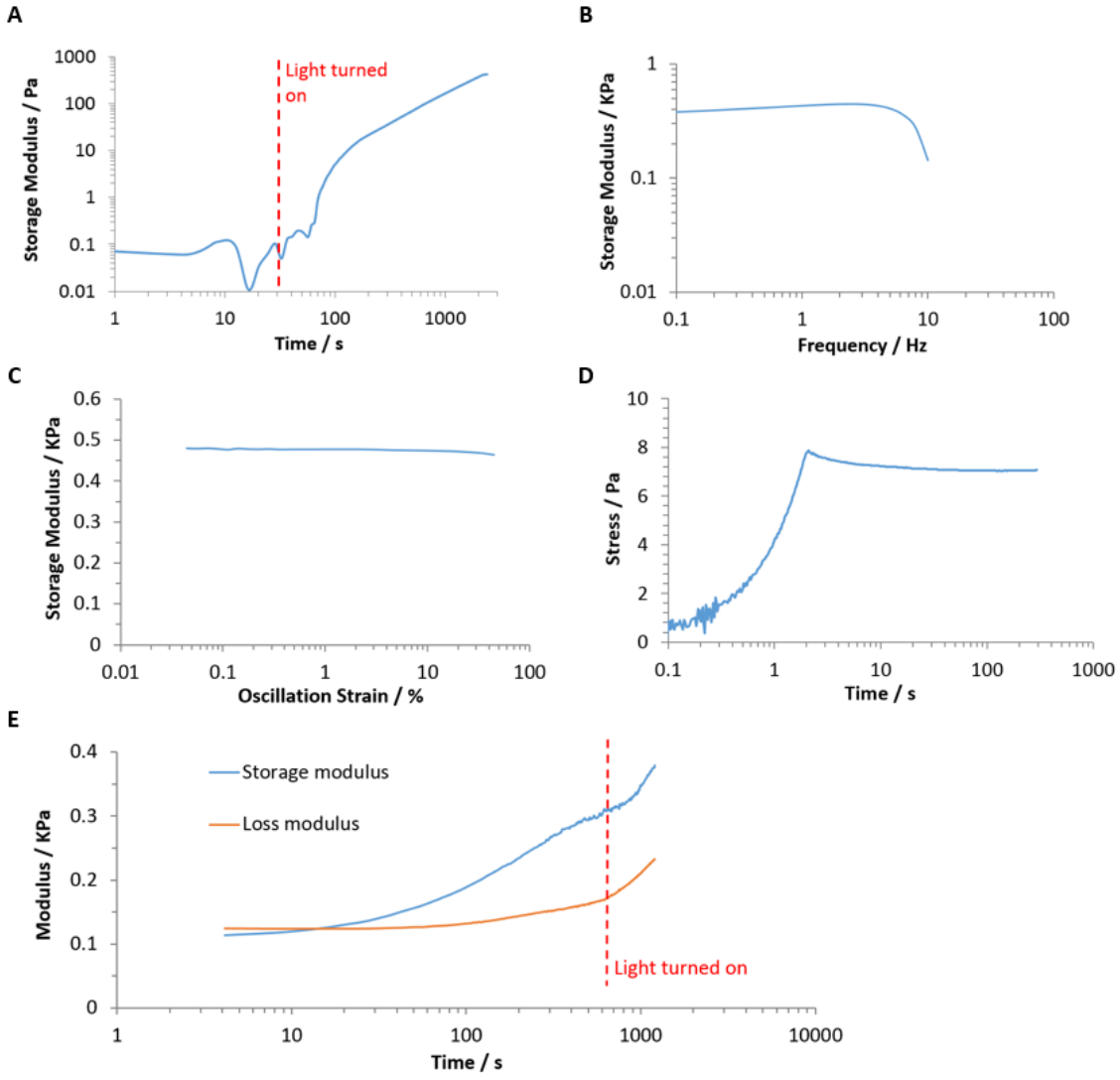


**Figure 5.6.** Characterisation of the shear mechanical properties of PAA-Tyr hydrogels via oscillatory rheometry. Gels were cured through visible light initiation with eosin Y (0.15% molar equivalence to polymer) at 40 mW/cm$^2$, and are functionalised at a level of 1.9%. (A) Evolution of storage modulus as a function of time (frequency of 1 Hz and 0.2% strain) at a concentration of 10% (w/v) in PBS. The light source was turned on at 30 s and off at 2500 s. (B) Frequency sweep (0.2% strain) of corresponding gel. (C) Strain sweep of corresponding gel (frequency of 1 Hz). (D) Stress relaxation of corresponding gel subjected to a rise in strain of 2% over the initial 2 s. (E) Evolution of storage modulus as a function of time (frequency of 1 Hz and 0.2% strain) at a concentration of 20% (w/v) in PBS. The light source was turned on at 625 s.

The weak mechanical properties identified for PAA-Tyr gels are presumably a result of the low functionalisation level of the polymer, in combination with the slow curing and low reaction efficiency for the gelation system. In order to further enhance radical

generation, the use of eosin Y can be coupled with a co-initiator and a co-monomer, leading to faster and greater functional group conversion.[274,275] As an example, Noshadi *et al.* generated visible light crosslinked gelatin-based hydrogels, using eosin Y as a photoinitiator, triethanolamine (TEA) as a co-initiator and *N*-vinylcaprolactam (VC) as a co-monomer. These gels had compressive moduli in the range of 5–56 kPa, depending on the concentrations of the co-initiator and co-monomer used.[274]

Next, the rheological properties of PAA-BA gels (see scheme in Figure 5.3) were characterised (Figure 5.7). A different geometry was used for PAA-BA gels due to the fact that the light guide accessory was not required; this allowed a solvent trap geometry to be used. In addition, for these experiments functionalised glass coverslips were not used, as silane methacrylate layers would not promote radical-based coupling of the gel to the glass. Figure 5.8A shows that for the case of PAA-BA gels, the lack of coverslips had no significant effect on the results obtained. Furthermore, the significant effect of sample drying and resulting increase in stiffness of the material is evident when not using the solvent trap geometry (Figure 5.8A/B). Compared to other polymers studied, PAA-BA gels appeared to suffer the effects of sample drying significantly. For comparison, PAA-BP thiol-ene gels, which are discussed later, showed minimal to no deviation in the storage modulus following sample curing (Figure 5.9A). This enhanced drying of PAA-BA gels is believed to be a result of their significantly low storage modulus values compared with the other gels studied, leading to a reduced ability of the gels to attract and encapsulate water molecules.

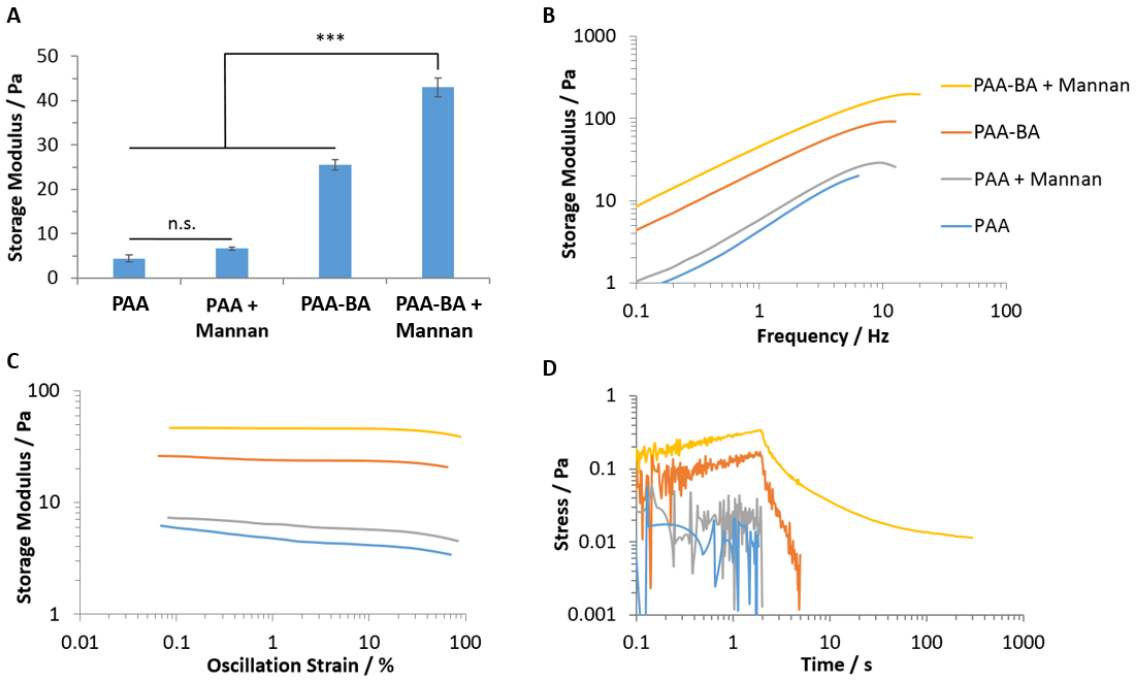


**Figure 5.7.** Oscillatory rheometry data for PAA gels, PAA gels with mannan, and PAA gels functionalised with boronic acid (PAA-BA), with and without the addition of mannan. Gels are all at a concentration of 15% (w/v) in PBS. Boronic acid functionalisation levels are at 18.1% and mannan is added at 10% molar equivalence (relative to boronic acid). (A) Storage modulus values of different gels. Values taken from frequency sweeps at 1 Hz (0.2% strain). Error bars show standard errors for repeats across samples (sample size n = 3). ***, $p \leq 0.001$. n.s., non-significant. (B) Frequency sweep (0.2% strain) of gels. (C) Corresponding strain sweeps (frequency of 1 Hz). (D) Stress relaxation of corresponding gels subjected to a rise in strain of 2% over the initial 2 s.

Figure 5.7A shows the comparison of storage modulus values (1 Hz, 0.2% strain) for PAA and boronic acid-functionalised PAA (PAA-BA), with and without the addition of mannan in solution (10% equivalence relative to boronic acid). The interaction between boronic acids and carbohydrates, through reversible covalent bonds, are well documented.[277] Furthermore, a number of papers have specifically studied the affinity of small sugars, such as mannan to boronic acid.[70,284]

When mannan is added to PAA-BA, a significant increase in the storage modulus is observed. In comparison, when mannan is added to PAA no significant increase in

storage modulus is recorded. This indicates that polymer crosslinking is primarily occurring as a result of interactions between boronic acid molecules on the polymer backbone and mannan. This was important to distinguish as hydrogen bonding between PAA carboxyl groups and mannan could themselves lead to physical crosslinking, negating the need for boronic acid functionalisation. Frequency and strain sweeps are also shown for the different polymers, with and without the addition of mannan (Figure 5.7B/C). Stress relaxation profiles indicate the greater elasticity of PAA-BA gels with the addition of mannan (Figure 5.7D). All other gels demonstrated rapid relaxation upon application of strain (2%), whereas the PAA-BA with mannan, retained its structure for a significantly greater period of time. The stress relaxation profile of the mannan-crosslinked gels, in comparison with PAA-Tyr gels (Figure 5.6D), indicated a substantially more pronounced viscous behaviour. Furthermore, the frequency sweeps and stress relaxation experiments (Figure 5.7B/D) indicate the strong viscoelastic profiles observed for these four gels tested.

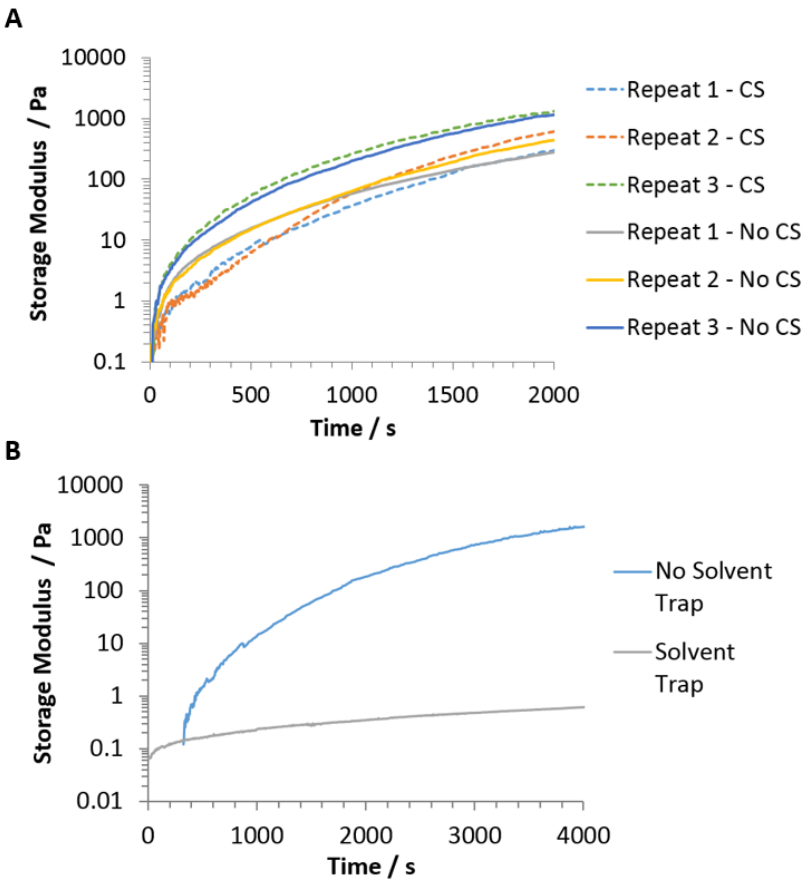


**Figure 5.8**. Oscillatory rheometry data for PAA-BA gels illustrating the effect of different parameters on the mechanical characterisation of the gels. (A) The evolution of modulus values with and without methacrylate functionalised coverslips (CS). Experiments were carried out on the 20 mm Peltier plate geometry. (B) Evolution of modulus values with a solvent trap (40 mm Peltier plate) and without (20 mm Peltier plate). Significant drying of gels was observed when not using a solvent trap, as illustrated by significant increases in modulus values. All tests were done at 10% (w/v) concentration in PBS and the evolution of storage modulus with time was observed at a frequency of 1 Hz and a 0.2 % strain.

Figure 5.9 shows the characterisation of the mechanical properties of PAA-BP hydrogels (see scheme in Figure 5.4) which have been synthesised from PAA at molecular weights of 15000 and 450000 g/mol (referred to as PAA 15K and 450K, respectively). The conditions used for these experiments are shown in Table 5.1. PAA 15K and 450K were functionalised with bromo-pentene at different levels (12.9% and 5.2%, respectively), and as the four conditions used (C1-C4) were dependent on the alkene concentration, the polymer concentrations used for PAA 15K and 450K, differed largely. Due to the high

polymer concentrations required for PAA 450K at C3 and C4 (30.9 and 38.7% (w/v), respectively), reliable results could not be obtained due to issues with sample loading.

**Table 5.1.** Conditions used for PAA-BP hydrogels. These gels were based on PAA at an $M_W$ of either 15000 or 450000 g/mol (15K or 450K, respectively), with corresponding functionalisation levels of 12.9% and 5.2%, respectively. In all cases the Irgacure 2959 concentration was 5% molar equivalence relative to the alkene.

| **Condition** | **Polymer** | **Concentration (mM)** | | **Weight (per mL solution)** | |
|---|---|---|---|---|---|
| | | **Alkene** | **Thiol** | **Polymer (mg)** | **Thiol (mg)** |
| C1 | 15K | 90 | 45 | 64 | 23 |
| C2 | 15K | 135 | 67.5 | 95 | 34 |
| C3 | 15K | 180 | 90 | 127 | 45 |
| C4 | 15K | 225 | 112.5 | 159 | 56 |
| C1 | 450K | 90 | 45 | 155 | 23 |
| C2 | 450K | 135 | 67.5 | 232 | 34 |

All PAA-BP gels showed significant and rapid stiffening upon application of the UV light (Figure 5.9A). The majority of PAA-BP gels showed excellent mechanical properties, maintaining their structure even at high frequency oscillations (in particular for the higher concentration gels and those formed from high molecular weight PAA, Figure 5.9B). In comparison, other gels (see Figure 5.6B, Figure 5.7B and Figure 5.11B) typically display reduced moduli at frequencies greater than 10 Hz, possibly due to more complex viscoelastic responses and the destabilisation of the waveform of the oscillatory deformation. In addition, stress relaxation experiments further illustrate the strong covalent crosslinking and resulting elastic response of PAA-BP gels (Figure 5.9D); these gels showed little structural relaxation upon application of strains over periods of time up to 300 s.

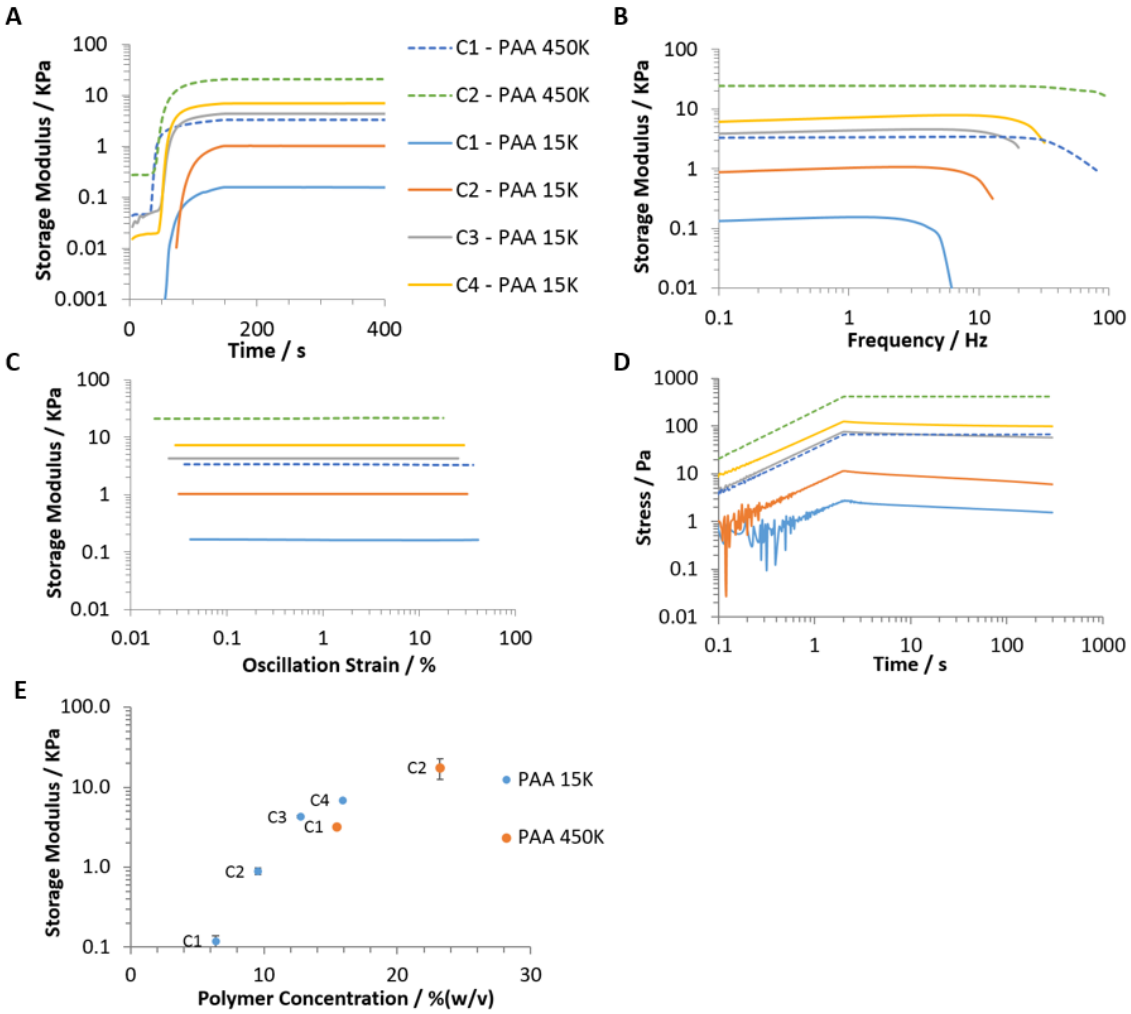


**Figure 5.9.** Characterisation of the shear mechanical properties of PAA-BP thiol-ene hydrogels by oscillatory rheometry. The thiol:alkene ratio was 1:2 and Table 5.1 gives the concentrations of thiol used for conditions C1 to C4. Gels were cured with PEGDT under UV initiation for 2 min (5% Irgacure 2959 relative to alkene) at 17 mW/ $cm^2$. For PAA at an $M_W$ of 450 KDa, there was an alkene functionalisation level of 5.2%, and for 15 KDa $M_W$ it was 12.9% (quantification by NMR). (A) Evolution of storage modulus as a function of time (frequency of 1 Hz and 0.2% strain). The light source was turned on at 30 s and off at 150 s. (B) Frequency sweeps (0.2% strain) of corresponding gels. (C) Strain sweeps of corresponding gels (frequency of 1 Hz). (D) Stress relaxation of corresponding gels subjected to a rise in strain of 2% over the initial 2 s. (E) Storage modulus values for different gels as a function of their concentration (% (w/v)) in PBS. Values taken from frequency sweeps at 1 Hz (0.2% strain). Error bars show standard errors for repeats across samples (sample size n = 3).

The mechanical properties of PAA-BP gels, synthesised at different pH values, was also investigated (Figure 5.10). The effect of pH on the efficiency of thiol-ene reactions was

previously investigated (see Figure 2.20 and Figure 2.21, Chapter 2). These experiments looked at the conjugation of *N*-acetyl-L-cysteine to bromo-pentene functionalised PAA (450K $M_W$) at thiol to alkene ratios of 1:1. From these experiments, the percent conjugation of thiol to alkene was found to be 60% and 27%, at pH 5 and 7, respectively (Figure 2.20). These significantly higher efficiencies observed at lower pH values contradict with the rheological results obtained. Given this two-fold increase in thiol conjugation observed at pH 5 over pH 7 (Figure 2.20, Chapter 2) we would expect that significantly more crosslinks would form for the PAA-BP gels at lower pH, and hence significantly stiffer gels would be formed. The fact that the reverse trend is observed is surprising (Figure 5.10).

One explanation for this anomaly may be in the curing times used. For rheology-based experiments, the curing times used were 2 minutes, whereas, for the experiments in Chapter 2 curing times of 5 minutes were used. It is proposed that at lower pH values, the rate of initiation and crosslinking of gels is reduced. Indeed, from Figure 5.10A it appears that at pH 5, the evolution of the storage modulus is delayed somewhat and the increase in modulus stops when the light is switched off, not reaching its maximum value. At pH 7 the storage modulus has almost reached a plateau at around 150 s, near 1029 Pa, when the UV source was switched off. The delayed gelation at low pH implies a retardation and potentially an inhibition in thiyl radical formation in these conditions, although this is not in agreement with our NMR data (see Figure 2.20 and Figure 2.21). It could be hypothesised that PAA chains start to precipitate at this pH and chains are unable to form extended interconnected networks, potentially resulting in nanogel local crosslinking instead. This hypothesis would be compatible with the higher extents of

reaction observed at low pH, via NMR. Methods such as dynamic light scattering (DLS) would have helped confirm this theory; however, these tests have not be performed.

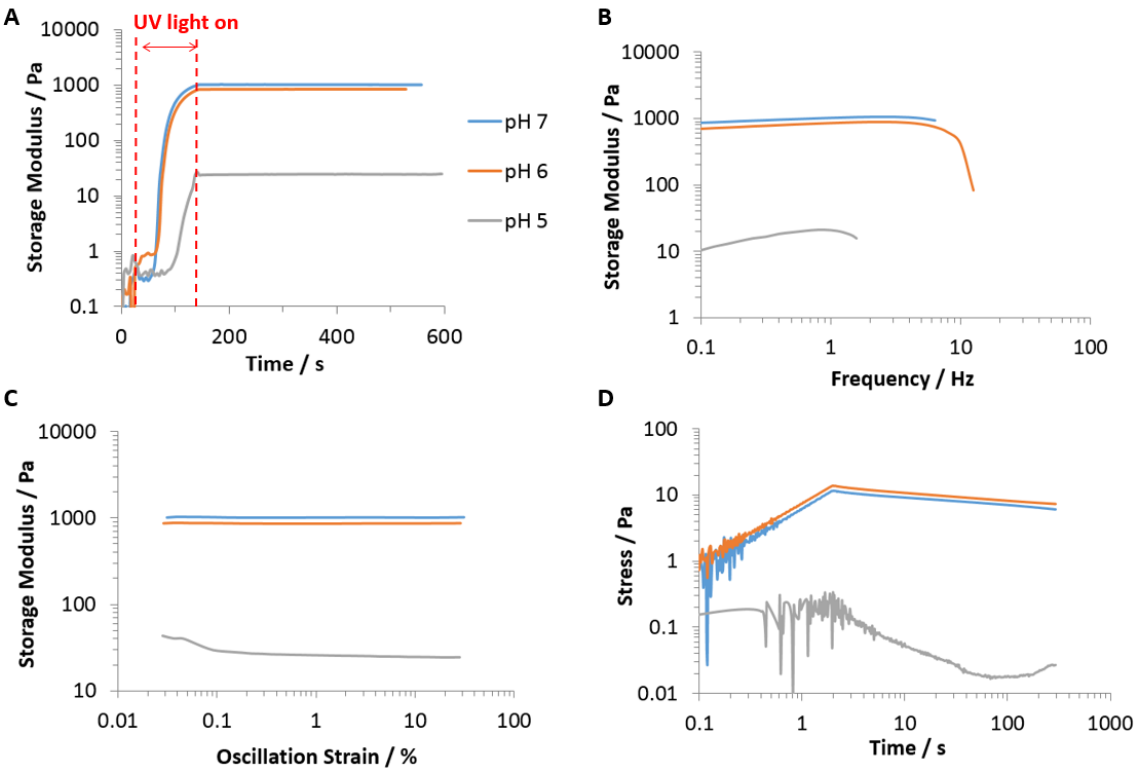


**Figure 5.10.** The effect of pH on the shear mechanical properties of PAA-BP thiol-ene hydrogels. Gels were all at an $M_w$ of 15000 g/mol and were all at condition C2 (see Table 5.1). Gels were cured for 2 min under UV light at 17 mW/cm$^2$. (A) Evolution of storage modulus as a function of time (frequency of 1 Hz and 0.2% strain). The light source was turned on at 20 s and off at 140 s, as indicated (B) Frequency sweeps (0.2% strain) of corresponding gels. (C) Strain sweeps of corresponding gels (frequency of 1 Hz). (D) Stress relaxation of corresponding gels subjected to a rise in strain of 2% over the initial 2 s.

Next, the mechanical properties of PAA-Cys gels (see scheme in Figure 5.5) were characterised (Figure 5.11). Prior to UV initiation this polymer already displayed a particularly high storage modulus value of approximately 600 Pa (see Figure 5.11A). Taking into account the low concentration of this polymer (10% (w/v)), these starting mechanical properties were significantly higher than those measured for other gelation

systems studied (see Figure 5.6A/E and Figure 5.9A). As an example, PAA-BP gels with a $M_W$ of 450K and at condition C2, only had an initial storage modulus value of 270 Pa (Figure 5.9A); given that this polymer is at a concentration of 23.2% (w/v), this is significantly lower in comparison. This significant level of crosslinking for PAA-Cys gels, by air oxidation alone, is a phenomenon that has been reported elsewhere for other similar gelation systems. Indeed, Shu *et al.* reported a disulfide crosslinking strategy to prepare hyaluronic acid (HA) hydrogels from thiol-modified HA.[107,108] Although both are formed through UV initiation with Irgacure 2959 as the photoinitiator, the rate of gelation is significantly faster for PAA-BP gels (Figure 5.9A) compared with PAA-Cys gels (Figure 5.11A).

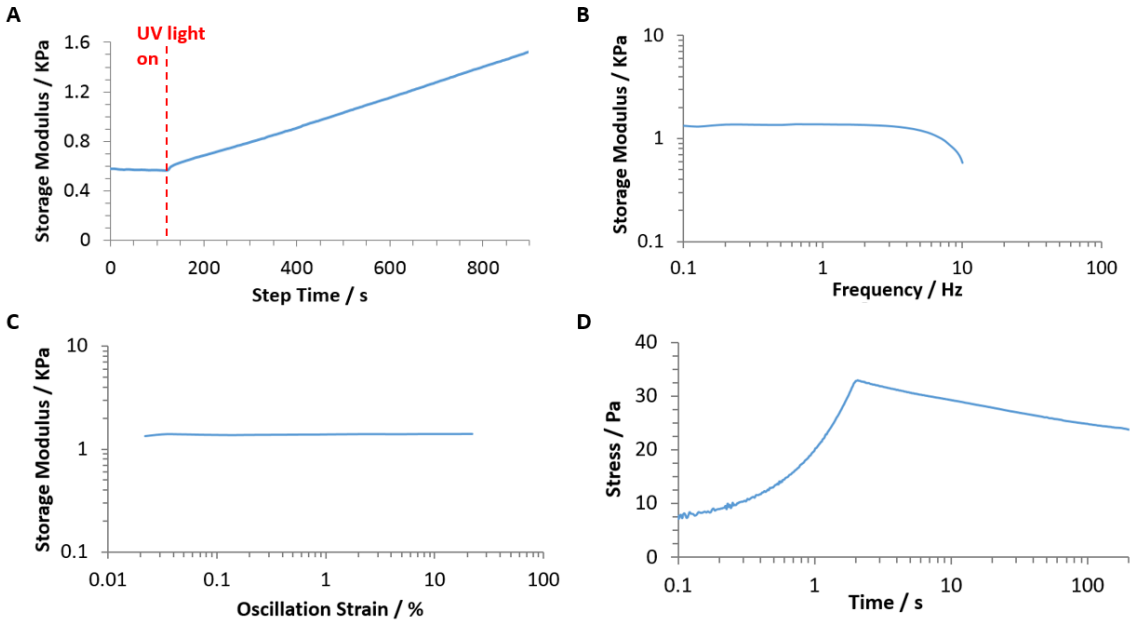


**Figure 5.11.** Characterisation of the shear mechanical properties of PAA-Cys hydrogels by oscillatory rheometry. Gels are at a concentration of 10% (w/v) in PBS and are cured under UV initiation for 15 min (30% molar ratio of Irgacure 2959 to thiol) at 17 mW/cm$^2$. The functionalisation level of cysteamine is 4.6%, as quantified via NMR. (A) Evolution of storage modulus as a function of time (frequency of 1 Hz and 0.2% strain). The UV source was left on for a total of 15 min starting at t = 120 s, as indicated. (B) Frequency sweep (0.2% strain) of corresponding gel. (C) Strain sweeps of corresponding gels (frequency of 1 Hz). (D) Stress relaxation of corresponding gel subjected to a rise in strain of 2% over the initial 2 s.

A summary of the rheological properties for the four gels, for which adhesion testing was carried out in the next chapter, is given in Figure 5.12. In addition, the gel concentrations and conditions used in these tests are summarised in Table 5.2. The storage moduli of the gels, taken from the frequency sweeps at 1 Hz (0.2% strain), are given in Figure 5.12A. As the gel mechanics are primarily determined by the polymer concentration, all polymers are kept at a concentration of 15% (w/v). The physically crosslinked PAA-BA gels represent the weakest of the gels, despite their high functionalisation level. Not surprisingly, the chemically crosslinked gels have a significantly higher storage modulus as a result of strong covalent crosslinking. The high stress relaxation of PAA-BA gels (Figure 5.12D) is indicative of the physical crosslinks that have formed, which break and deform under load, resulting in significant energy dissipation in this material. On the other hand, the other gels tested demonstrate a more elastic response due to their permanent covalent crosslinking.[268] As the excitation of eosin Y by visible light exposure results in a slower generation of radicals than UV-crosslinking, under the photoinitiator I-2959,[274,275] PAA-Tyr gels are unsurprisingly weaker than PAA-BP and PAA-Cys gels (470 Pa versus 3.20 KPa and 970 Pa, respectively; Figure 5.12A).

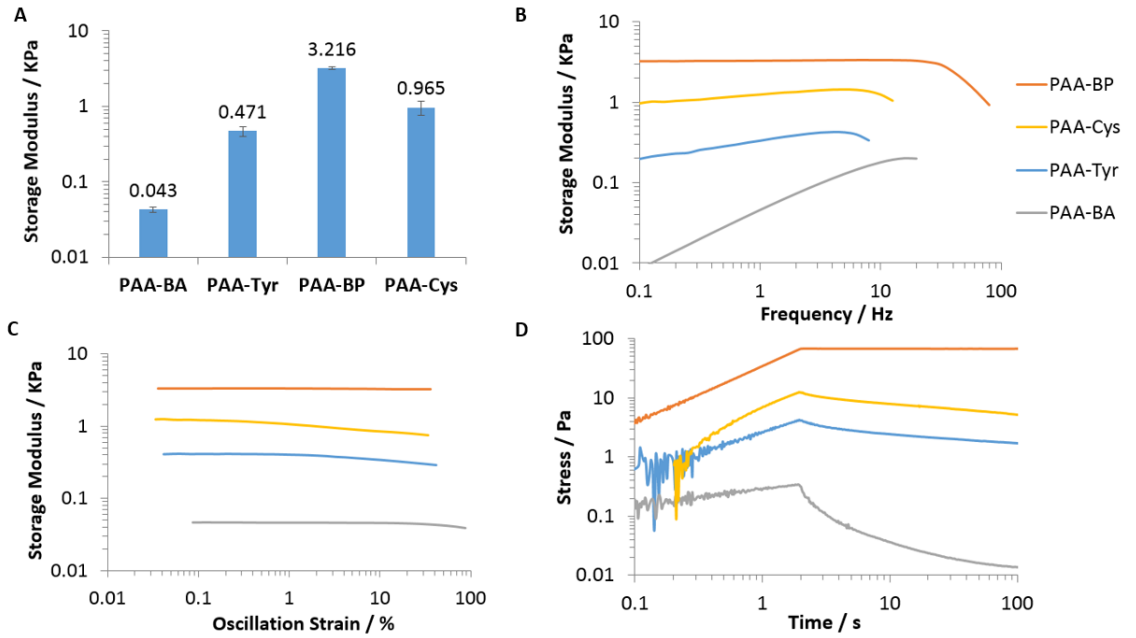


**Figure 5.12.** Characterisation of the shear mechanical properties, by oscillatory rheometry, of PAA-based gels under the conditions and concentrations used in adhesion tests (see Table 5.2). Gels are all at a concentration of 15% (w/v) in PBS. (A) Storage modulus values of gels. Values taken from frequency sweeps at 1 Hz (0.2% strain). Error bars show standard errors for repeats across samples (sample size n = 3). (B) Frequency sweeps (0.2% strain) of gels. (C) Strain sweeps (frequency of 1 Hz). (D) Stress relaxation of gels subjected to a rise in strain of 2% over the initial 2 s.

PAA-BA gels display an interesting feature in the frequency sweeps (Figure 5.12B). The three other gels tested display a relatively constant storage modulus across all frequencies tested, up until higher frequencies are reached. This is not the case for PAA-BA gels which display significantly higher stiffnesses at high frequencies compared with low frequencies (gels displayed a storage modulus of 46 Pa at 1 Hz, compared with 176 Pa at 10 Hz; Figure 5.12B). This behaviour is a result of the reversibility of the reaction between boronic acid and mannan, which creates a transient network that can restructure dynamically after mechanical disruption.[277] Indeed, this feature of boronic acid-crosslinked gels has been utilised in the synthesis of gels with self-healing properties.[285,286] At long time scales (at low frequencies), PAA-BA gels exhibit viscous

behaviour, as the gel network has sufficient time to reorganize and accordingly flow. At short timescales (at high frequencies), the gels exhibit a more elastic response, as the crosslinks do not completely dissociate and the network is therefore more rigid.[277] This frequency-dependent behaviour was also evident in other PAA gels (see Figure 5.7B), presumably due to the reversibility of hydrogen bonding occurring between carboxyl groups.

**Table 5.2.** Summary of the compositions and conditions used for the formation of the gels used in the adhesion tests. For all tests, the functionalised PAA polymer is dissolved in PBS and has an $M_W$ of 450000.

| Polymer | Functionalisation Level | Gel Concentration %(w/v) | Crosslinker Concentration | Photoinitiator Concentration | Crosslinking Mechanism |
|---|---|---|---|---|---|
| PAA-Tyr | 1.9% | 15% | N/A | eosin Y (0.15% equiv. to polymer) | 5 min visible light (40 mW/cm$^2$) |
| PAA-Cys | 4.5% | 15% | N/A | Irgacure 2959 (30% equiv. to thiol) | 10 min UV light (17 mW/cm$^2$ |
| PAA-BP | 5.2% | 15% | PEGDT (50% equiv. to alkene) | Irgacure 2959 (5% equiv. to alkene) | 2 min UV light (17 mW/cm$^2$) |
| PAA-BA | 18.1% | 15% | Mannan (10% equiv. to boronic acid) | N/A | Physical |

## 5.3.2 Adhesion of Hydrogels to SAMs

Figure 5.13 shows the data for the adhesion of the four different gels to hydroxyl and methacrylate-functionalised glass coverslips, as measured via tensile bond tests. A representative force-extension curve is also shown for each gel (Figure 5.13C). These curves provide important details on failure mechanisms that may not be highlighted from the adhesion strength or energy density values. An important observation from these curves is the apparent differences in starting loads measured for each gel. Before

running experiments, loads were zeroed, and so it is believed this difference comes from the contraction of gels during in situ curing. If the force profiles were normalised about the starting loads this would have removed a signification portion of the data recorded at higher extensions, and as such, the data was not adjusted in this way. This trend is also observed in later tensile bond tests performed on soft tissues (see Figure 5.14 and Figure 5.16).

From Figure 5.13 it can be observed that PAA-BP gels strongly adhere to both glass coverslips (adhesion strength > 66 KPa; Figure 5.13A). However, they fail rapidly at relatively low extension (Figure 5.13C), representing the profile of a stiff but brittle gel. PAA-BP gels failed adhesively at the glass interface. On the other hand, the other gels tested all displayed relatively elastic properties under load, with failure represented by a gradual decrease in force (Figure 5.13C). Hence, the adhesion strength of PAA-Cys to SAMs was significantly lower than that of PAA-BP (adhesion strength of PAA-Cys was < 13 KPa; Figure 5.13A). However, the energy densities measured for both gels were very similar (Figure 5.13B). Given that the gels have significantly different rheological properties (Figure 5.12), this similarity in the energy densities indicates the high toughness of PAA-Cys gels under deformation. PAA-Cys gels failed cohesively, with long fibres forming between the upper and lower substrates, leading to the large energy densities measured.

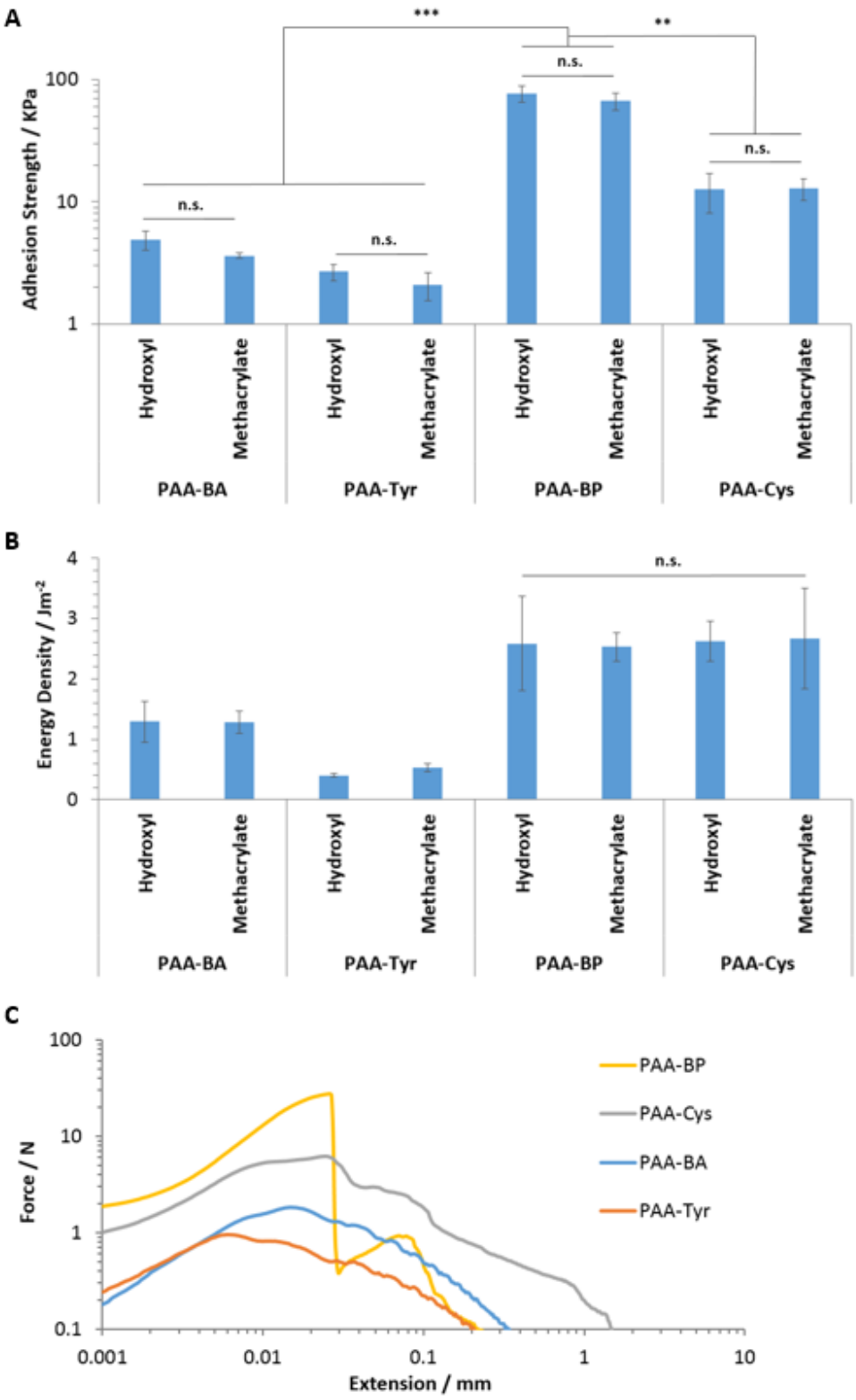


**Figure 5.13.** Tensile bond tests for adhesion of hydrogels to hydroxyl and methacrylate functionalised silicon substrates. (A) Adhesion strength of gels (maximum tensile force (N)/contact area ($m^2$)). (B) Energy density for gels (detachment work (J)/contact area ($m^2$)). (C) Force-extension for gels at a constant extension speed of 2.5 mm/min. Error bars show standard errors for repeats across samples (sample size $n \geq 3$).**, $p \leq 0.01$. ***, $p \leq 0.001$. n.s., non-significant.

Most covalently crosslinked hydrogels display relatively brittle properties with limited stretchability and toughness.[270] However, hydrogels formed through a synergy of physical and covalent crosslinks, have been shown to demonstrate significantly enhanced stretchability and toughness.[270,287] This behaviour can result from the introduction of energy dissipating mechanisms in the form of sacrificial physical bonds. Upon loading of a material, this network of physical bonds ruptures and dissipates energy, leaving the covalent bonding intact.[288,289] Furthermore, these physical bonds show the ability to re-form upon unloading of a sample, leading to the recovery of these energy dissipating mechanisms. As an example, Sun *et al.* synthesised hydrogels from a network of ionic and covalent crosslinks, leading to a gel which can be stretched to beyond 20 times its initial length.[270] Accordingly, the high toughness of PAA-Cys gels is proposed to result from its network of covalent crosslinks, coupled with hydrogen bonding from unreacted thiols.

The methacrylate SAMs contain an alkene end group, and so strong covalent bonding to the thiol containing PAA-BP and PAA-Cys gels following UV initiation would be expected. Indeed, several papers have reported the use of this thiol-ene based reaction between thiol-funtionalised PAA and 3-(Trimethoxysilyl)propyl methacrylate for various applications.[89,90] When comparing the adhesion of these gels to hydroxyl and methacrylate SAMs, there is no significant difference both in terms of the adhesion strength and energy density. These results suggest that the adhesion profiles observed are predominantly dependent on the bulk mechanical properties of the gels, rather than their adhesion to the underlying substrates.

PAA-BA and PAA-Tyr gels failed cohesively. Interestingly, although PAA-Tyr gels had a storage modulus over an order of magnitude greater than that of PAA-BA gels (Figure

5.12A), the adhesive properties of PAA-BA gels are greater, or at least comparable to those of PAA-Tyr (energy density > 1.28 $Jm^{-2}$ compared with an energy density < 0.53 $Jm^{-2}$ for PAA-Tyr gels; Figure 5.13B). This may be a result of the higher functionalisation levels for PAA-BA gels coupled with stronger interactions of these gels with the underlying substrates. PAA-BA gels showed increase adhesion with hydroxyl substrates compared with methacrylate (4.87 KPa and 3.62 KPa, respectively; Figure 5.13A), indicating the presence of strong hydrogen bonding as a mode of adhesion for these gels. A further factor that should be considered is the drying of PAA-BA gels during testing and the effect this may have on its mechanical properties. PAA-BA rheological characterisation was originally performed using a solvent trap geometry (Figure 5.7) and characterisation of the gel without this geometry indicated rapid drying of the gels and an associated increase in storage modulus values (Figure 5.8A/B). Adhesion tests did not use the solvent trap geometry and the effective stiffness of PAA-BA gels during these tests may therefore be higher than initially indicated (Figure 5.12). As such, the mechanical properties of PAA-BA gels may in fact be closer to those of PAA-Tyr. This said, time between sample loading and initiation of tests was kept as minimal as possible (around 1 to 2 minutes), particularly in the case of PAA-BA gels where no curing time was required. Therefore it is hoped that sample drying would not play a significant role in the adhesion profiles measured for PAA-BA gels.

### 5.3.3 Adhesion of Hydrogels to Soft Tissues

For the characterisation of the adhesion of hydrogels to porcine tissues, both lap shear and tensile bond tests were used. Both these methods are commonly used to quantify the adhesion strength between hydrogels and soft tissues, and there are numerous

accounts of their use within the literature.[24,28,71,257,290–292] Figure 5.14 and Figure 5.16 show tensile bond test data for adhesion of the different gels to epicardium and keratinized gingiva, respectively. Adhesion was investigated with a functionalised glass slide on the lower surface and the tissue sample on the upper, with the gel cured *in situ* between the two (see Figure 5.15 and Figure 5.17 for images of the experimental set up). As there was no significant difference found between the adhesion profiles of the gels to hydroxyl-functionalised slides or methacrylate-functionalised ones (Figure 5.13), hydroxyl functionalisation was used due to its simpler synthesis approach. Failure for PAA-BA and PAA-Tyr, to both the epicardium and gingiva, was cohesive. Following testing, both gels showed good wetting and surface coverage of the tissue surface (see Figure 5.15D and Figure 5.17C for images of PAA-BA and PAA-Tyr, respectively). This indicates both PAA-BA and PAA-Tyr gels displayed good bonding to the tissue surfaces, with failure determined by the weak bulk mechanical properties of the gels. Similarly to the SAM studies, PAA-BA and PAA-Tyr gels showed elastic deformation profiles (Figure 5.14B). Figure 5.15A and Figure 5.17A show the elastic deformation observed for PAA-BA during testing. In addition, similarly to the studies on SAMs, no significant difference in the adhesion strength was observed between PAA-BA and PAA-Tyr gels to both the epicardium and gingiva.

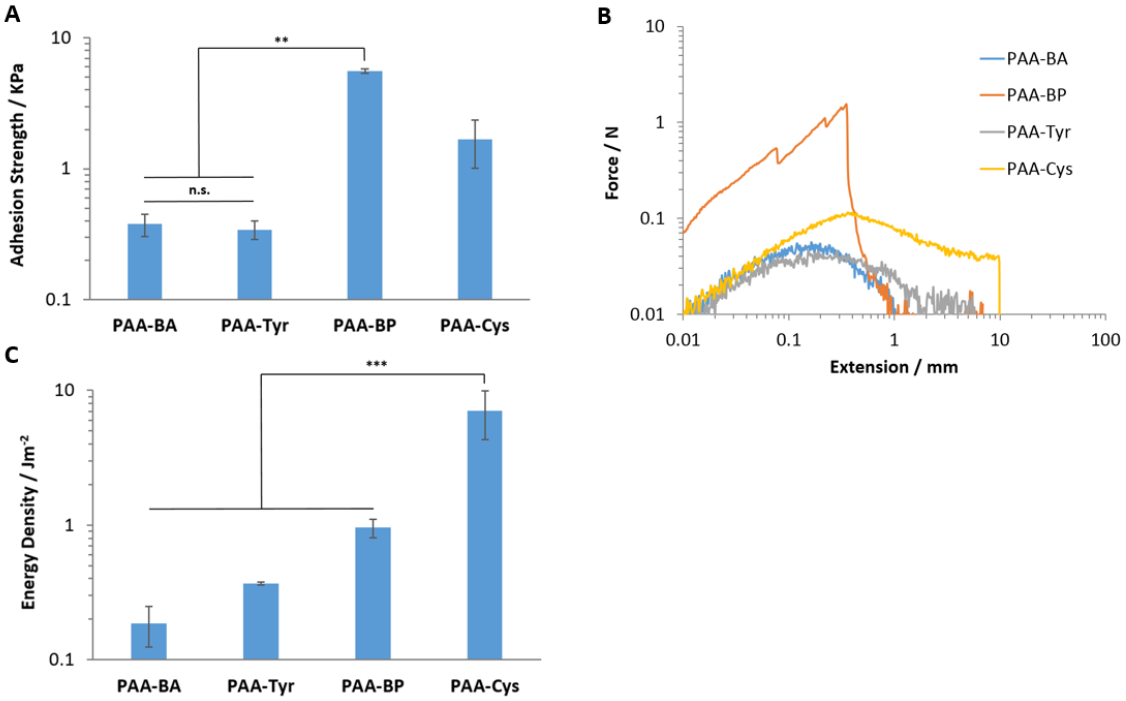


**Figure 5.14.** Tensile bond tests for adhesion of hydrogels to porcine epicardium. (A) Adhesion strength of gels (maximum tensile force (N)/contact area ($m^2$)). (B) Force-extension for gels at a constant extension speed of 2.5 mm/min. (C) Energy density for gels (detachment work (J)/contact area ($m^2$)). Error bars show standard errors for repeats across samples (sample size n ≥ 3). **, p ≤ 0.01. ***, p ≤ 0.001. n.s., non-significant.

For the UV-initiated gels, PAA-BP and PAA-Cys, failure for both was adhesive. For PAA-Cys gels, failure occurred at the epicardium and gingiva tissue interface. Similarly to the SAM studies, this gel displayed high elasticity and toughness with failure only occurring at relatively large extensions (Figure 5.14B and Figure 5.16B). Figure 5.15B and Figure 5.17B show images of the large deformation of this gel prior to failure, for epicardium and gingiva tissue samples, respectively. In addition, the large energy densities calculated for PAA-Cys to the epicardium and gingiva further highlight this behaviour (energy densities of 7.1 $Jm^{-2}$ and 12.8 $Jm^{-2}$ were calculated, respectively; Figure 5.14C and Figure 5.16C). As these gels extended so significantly with long fibres forming between the upper and lower substrates, the tests were ended early, prior to complete

failure of the sample; hence, there is a sudden drop in force at extensions of 10 mm, when testing was ended (Figure 5.14B and Figure 5.16B).

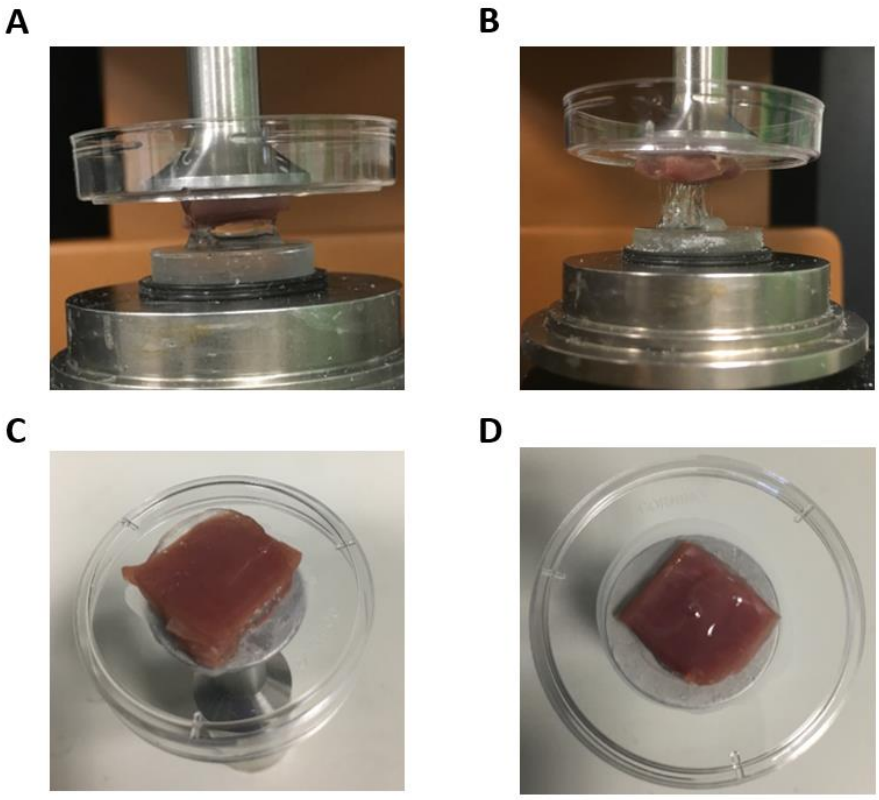


**Figure 5.15.** Images from tensile bond tests of gels to porcine epicardium. (A) Deformation observed for PAA-BA gel during testing. (B) Significant deformation observed for PAA-Cys gel during testing with the formation of long fibres between tissue and glass. (C) Complete deposition of PAA-BP gel on epicardium surface following adhesive failure of gel at glass interface. (D) Partial deposition of PAA-BA gel on epicardium surface following cohesive failure of gel. The gel can be seen to maintain near-complete wetting of the tissue surface.

In terms of energy density, PAA-Cys gels displayed significantly greater adhesion to tissue substrates than all other gels tested. This significant increase in energy density is thought to arise, in part, from the ability of these elastic gels to maintain conformal contact with the tissue surface. As the tissue surface is fairly rough, extension of gels will result in an application of a force to the tissue surface and a resulting disruption in the

surface morphology of the tissue. It is thought that the more elastic gels will be able to maintain conformal contact, and therefore will remain bonded to the tissue surface for a greater length of time during testing.

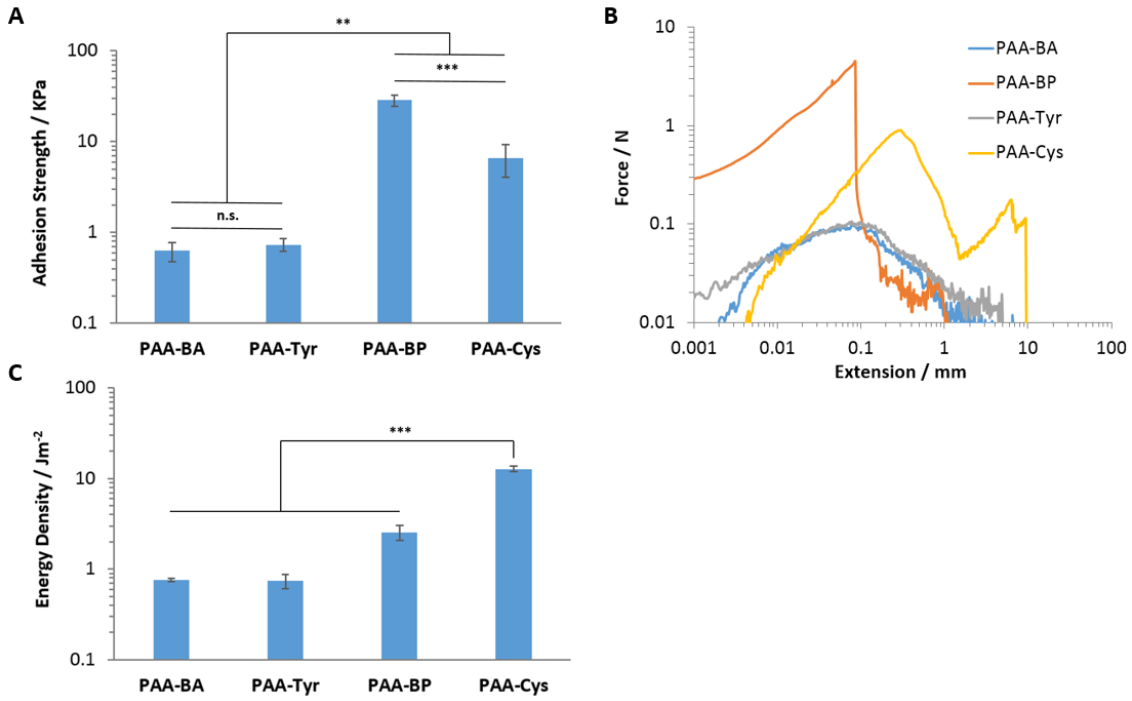


**Figure 5.16.** Tensile bond tests for adhesion of hydrogels to porcine keratinized gingiva. (A) Adhesion strength of gels (maximum tensile force (N)/contact area ($m^2$)). (B) Force-extension for gels at a constant extension speed of 2.5 mm/min. (C) Energy density for gels (detachment work (J)/contact area ($m^2$)). Error bars show standard errors for repeats across samples (sample size $n \geq 3$). **, $p \leq 0.01$. ***, $p \leq 0.001$. n.s., non-significant.

For PAA-BP gels, failure for epicardium tests was adhesive at the glass interface and for tests on the gingiva failure was at the tissue interface (see Figure 5.15C and Figure 5.17D for tests on the epicardium and gingiva, respectively). Similarly to tests on SAMs, PAA-BP gels failed in a brittle manner with minimal extension of the gels occurring before failure at the tissue or glass interface (Figure 5.14B and Figure 5.16B). Accordingly, high adhesion strengths were measured (28.7 KPa for the gingiva; Figure 5.16A) with a

comparatively small value for the energy density being recorded (2.6 $Jm^{-2}$ for the gingiva; Figure 5.16C).

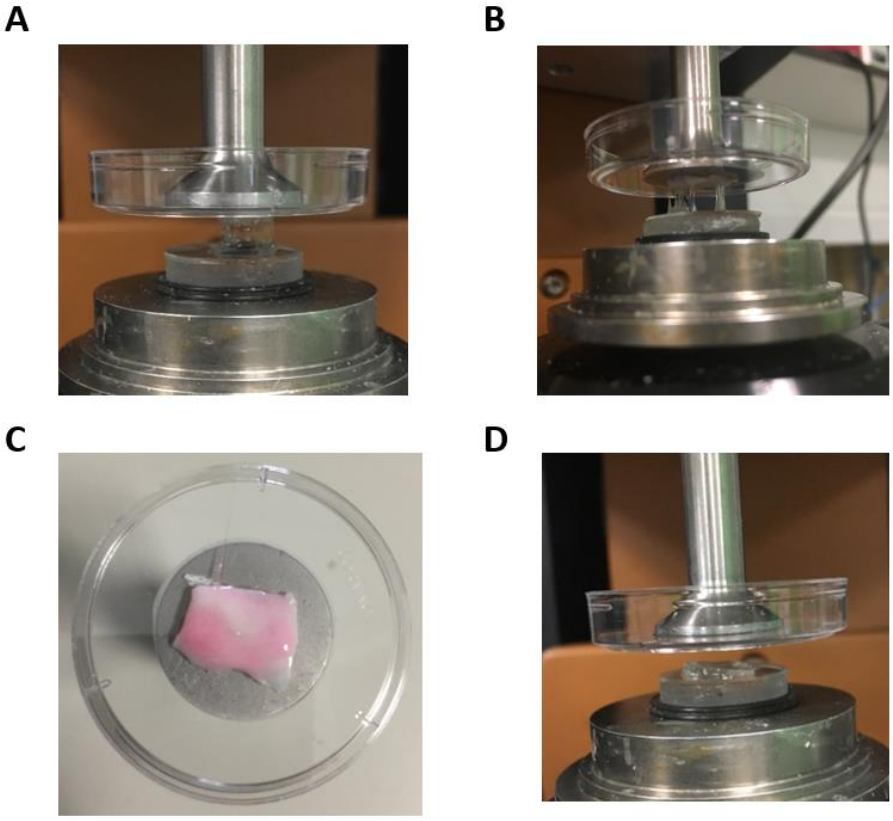


**Figure 5.17.** Images from tensile bond tests of gels to porcine keratinized gingiva. (A) Significant deformation observed for PAA-BA gel during testing. (B) Significant deformation observed for PAA-Cys gel during testing with the formation of long fibres between tissue and glass. (C) Partial deposition of PAA-Tyr gel on gingiva surface following cohesive failure of gel. The gel can be seen to maintain near-complete wetting of the tissue surface. (D) Complete deposition of PAA-BP gel on glass surface following adhesive failure of gel at tissue interface.

For lap shear experiments, testing could only be done on gels which displayed an appropriate mechanical strength, due to the vertical loading of samples in the testing apparatus. As such, testing was only carried out on the two UV-curable gels. Similarly to the tensile bond tests, PAA-BP and PAA-Cys gels displayed distinct modes of failure from

one another, with PAA-BP gels displaying a more brittle mode of failure (Figure 5.18C) and PAA-Cys gels a more elastic one (Figure 5.18D).

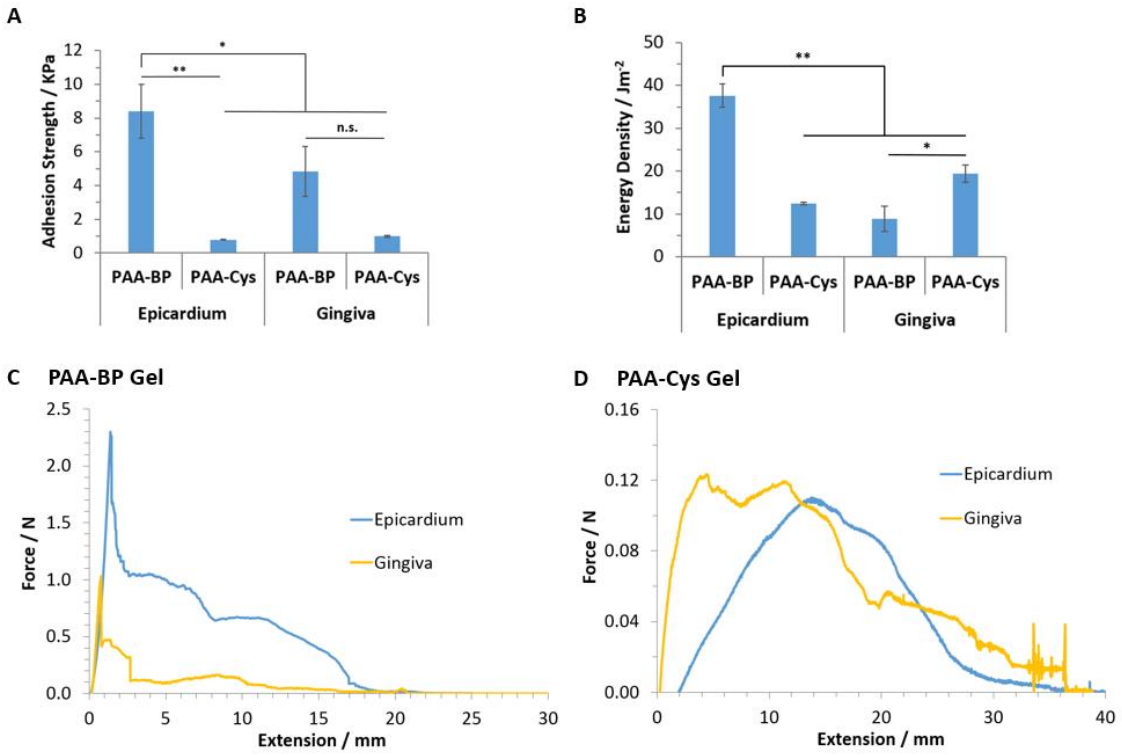


**Figure 5.18.** Lap shear tests for adhesion of PAA-BP and PAA-Cys hydrogels to porcine epicardium and keratinized gingiva at a constant extension speed of 10 mm/min. (A) Adhesion strength of gels (maximum tensile force (N)/contact area ($m^2$)). (B) Energy density for gels (detachment work (J)/contact area ($m^2$)). (C) Force-extension curves for PAA-BP gels. (D) Force-extension curves for PAA-Cys gels. Error bars show standard errors for repeats across samples (sample size $n \geq 3$). *, $p \leq 0.05$. **, $p \leq 0.01$. n.s., non-significant.

Figure 5.19 shows images taken during shear testing of PAA-BP gels. Failure of PAA-BP gels, for tests on the epicardium, was adhesive at the glass interface (Figure 5.19A/B). For tests on the gingiva, failure was adhesive again and this occurred at either the glass or tissue interface, or a combination of the two (Figure 5.19C/D). These modes of failure are similar to those observed in the tensile bond tests and they suggest that PAA-BP gels are adhering to the epicardium with greater strength than to the gingiva. It is proposed

that this results partly from the greater compliance and the greater ability of epicardium samples to retain water than the gingiva. This would lead to a greater infiltration of the polymer into the epicardium surface prior to UV initiation, and, subsequently, an enhanced adhesion strength to this tissue.

In addition, differences in tissue adhesion are likely a result of variations in surface biochemistry between tissues. The strong adhesion of PAA-BP gels to the epicardium suggests epicardial adhesion is occurring as a result of strong chemical bonding via radical thiyls. In comparison to these results, colloidal probe AFM experiments in Chapter 4 also indicated significantly stronger interactions of PAA to the epicardium, compared with the gingiva (Figure 4.16). Due to the relatively low functionalisation levels of our polymers studied (< 20% in all cases; Table 5.2), the non-specific adhesion of PAA to tissues may impact on the overall adhesion behaviour observed, although this would be insufficient to promote adhesion alone, without covalent bonding. Colloidal probe AFM experiments also highlighted the strong influence of the cell glycocalyx on non-specific adhesion (Figure 4.13 and Figure 4.14), perhaps indicating that the glycocalyx is more developed within the epicardium than the keratinized gingiva. Indeed, Servais *et al.* performed uniaxial tensile adhesion tests between pectin/CMC formulations and the mesothelium of several different tissues, demonstrating the significant reduction in adhesion forces following treatment with enzymes that are known to disrupt the glycocalyx layer (such as neuraminidase). As such, they indicate the role of the glyococalyx in adhesion at length scales similar to the ones that we have studied.[257]

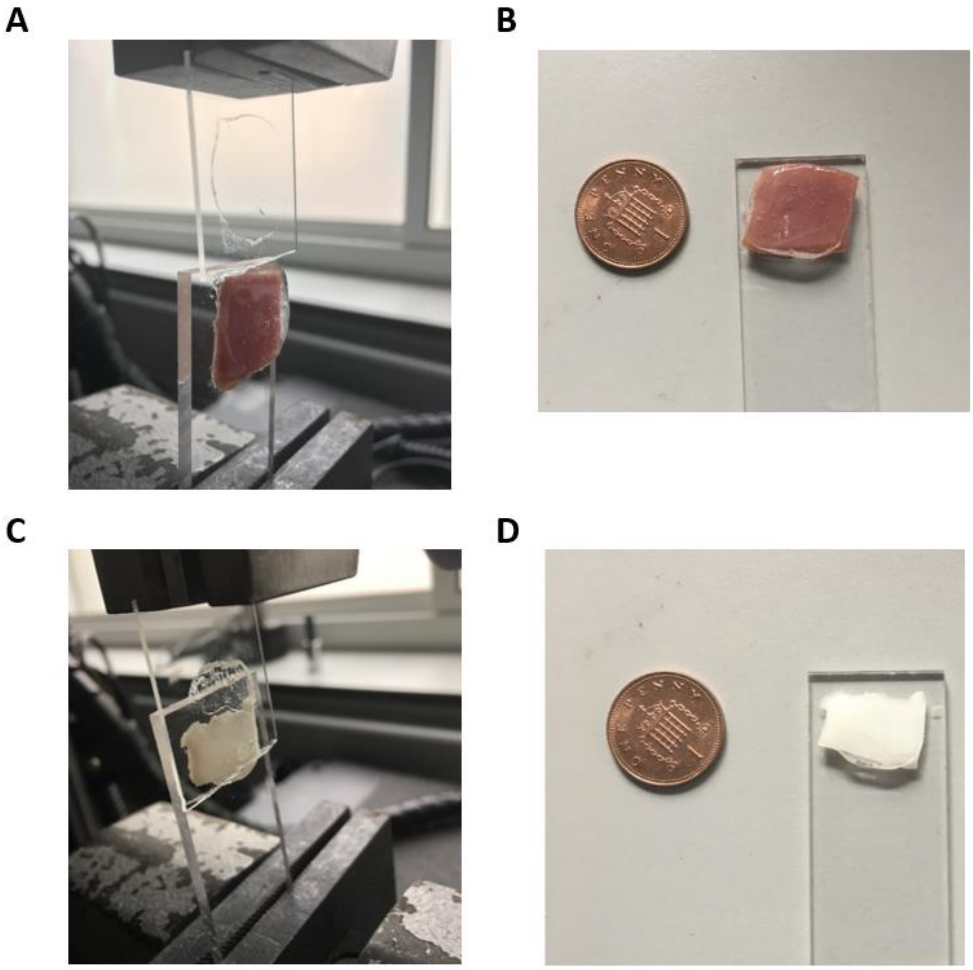


**Figure 5.19.** Images from lap shear adhesion tests for PAA-BP hydrogels to porcine epicardium and keratinized gingiva. (A) Failure for tests on the epicardium was adhesive at the glass interface. (B) Complete deposition of PAA-BP gel on epicardium surface following failure of gel at glass interface. (C) Failure for tests on the gingiva was adhesive and occurred in some instance at the glass interfaces and at other times at the tissue interface. In the image shown failure is at the tissue interface. (D) Complete deposition of PAA-BP gel on gingival surface following failure of gel at glass interface.

For PAA-Cys gels, failure was adhesive and occurred at the tissue interface for tests on both the epicardium and gingiva. Figure 5.20 shows images taken form the shear testing of PAA-Cys gels. The significant elasticity of PAA-Cys gels can be observed, with long fibres bridging the gap between the substrates during testing (Figure 5.20B/C). Similarly to results from the tensile bond tests, the adhesion strength of PAA-Cys gels to each tissue type was significantly lower than that of PAA-BP gels (Figure 5.18A). When looking

at the data for energy density, this difference is then reduced (and even inverted in the case of the gingiva; Figure 5.18B), as a result of the elasticity of PAA-Cys gels during testing.

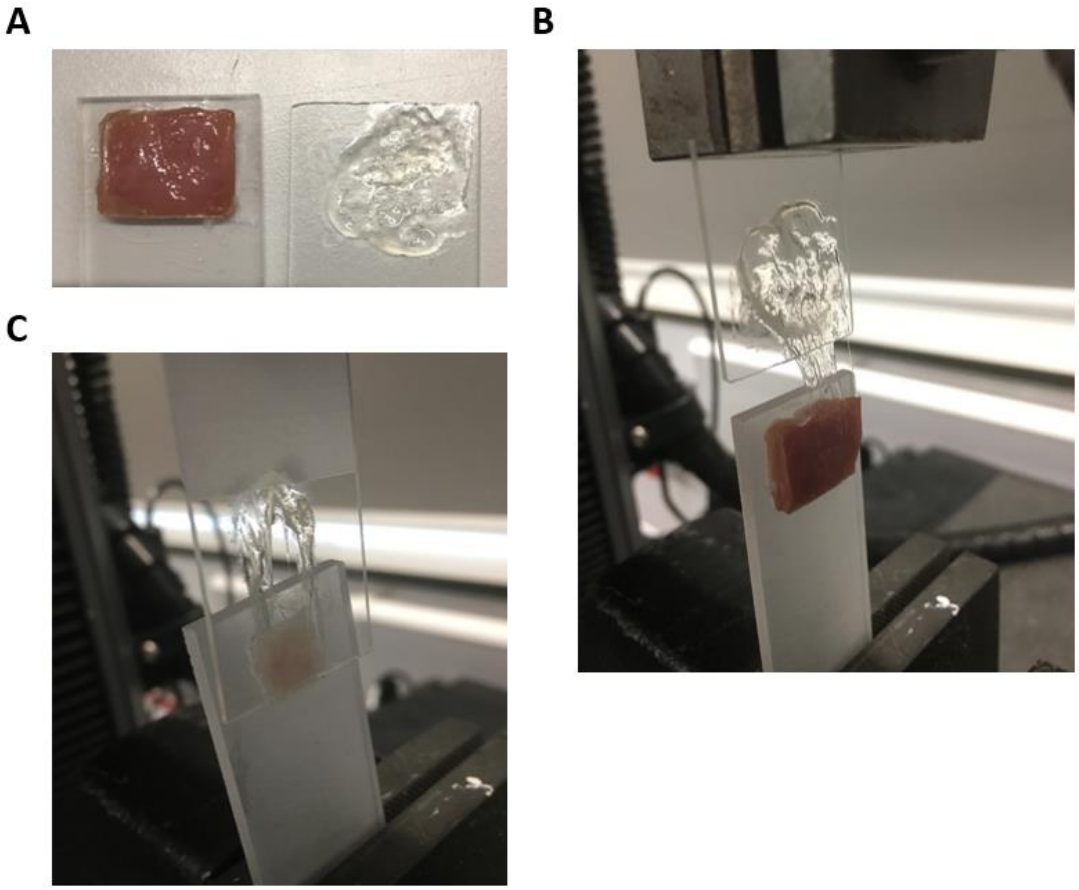


**Figure 5.20.** Images from lap shear adhesion tests for PAA-Cys hydrogels to porcine epicardium and keratinized gingiva. (A) Failure for tests on the epicardium was adhesive at the tissue interface. (B) High elasticity was seen for PAA-Cys hydrogels with long fibres forming between epicardium samples and glass substrate during testing. (C) Failure for tests on the gingiva was adhesive and occurred in some instance at the glass interfaces and at other times at the tissue interface. Large extension of the PAA-Cys gels was observed during testing.

For tensile bond and lap shear tests, the thicknesses of tissue samples used are not insignificant in comparison to gel thicknesses, and as such the tissues' mechanical properties will have an affect on the force values that are recorded. Furthermore, the

significantly different mechanical properties observed for epicardium and gingiva tissue samples (see Figure 4.5) are likely to influence the adhesion profiles observed for our gels. Evidence for the greater compliance of the epicardium, and the effect that this has on the results obtained, can be found when analysing force-extension profiles. Extension lengths at which the maximum force values are recorded, are much greater for the epicardium compared with the gingiva (Figure 5.14B, Figure 5.16B and Figure 5.18C/D), indicating the influence of tissue deformation on the data obtained.

From these results, hydrogel/soft tissue adhesion is clearly a result of several different factors; these include the tissue mechanics, bulk mechanics of the gels, weak non-specific adhesion forces, and strong covalent bonding. Even though the complex interplay of these different factors regulates adhesion, overall conclusions can still be drawn from these results. For example, from nanoindentation experiments the epicardium is softer than the gingiva, yet displays stronger bonding from lap shear results. This clearly indicates the strengthening of these interfaces with gels, particularly in the case of PAA-BP. In addition, gels with stronger mechanical properties, such as PAA-BP and PAA-Cys, clearly showed stronger bonding with tissues, perhaps also accentuated by their ability to strongly bond via radical thiyls.

## 5.4 Summary

The gelation dynamics and mechanical properties were investigated for a variety of different PAA hydrogels (all at a polymer concentration of 15% (w/v)), via oscillatory rheometry. In addition, the adhesion of the different gels, to SAMs and soft tissue samples, was quantified via tensile bond and lap shear tests. In the adhesion studies the adhesion strength and energy density were characterised; these represent the maximum force and total work required to separate the two slides per unit area, respectively.

PAA gels functionalised with tyramine showed slow curing under visible light in the presence of eosin Y. From rheology experiments, these gels showed overall weak mechanical properties but demonstrated behaviour and structural rigidity consistent with that of chemically crosslinked gels. PAA-Tyr gels have a promising potential for use within biomedical applications due to their visible light-mediated crosslinking strategy and the associated benefits of this. Adhesion studies to hydroxyl and methacrylate SAMs, through tensile bond tests, indicated no difference in the adhesion profiles of gels to either substrate. This was a result observed for all four gels tested and suggests that the adhesion profiles are dominated by the bulk mechanical properties of the gel rather than their interaction to the underlying substrate. Accordingly, even though PAA-Tyr gels showed good bonding to tissue surfaces, their overall adhesion strength was limited by their weak mechanical properties. With regards to these gels, future experiments should aim for higher functionalisation levels, and should investigate the use of a co-initiator and/or co-monomer in order to further accelerate radical generation and resulting functional group conversion.

PAA gels functionalised with boronic acid showed crosslinking when mannan was added in solution. Experiments confirmed that this crosslinking was a result of interactions between boronic acid and the polysaccharide. Rheology results for mannan-crosslinked gels indicated strong viscoelastic properties in comparison to the other chemically crosslinked systems. During adhesion tests PAA-BA gels demonstrated excellent elasticity and toughness, displaying adhesion strengths similar to, or greater than, those of PAA-Tyr gels, despite their lower mechanical properties. These properties are thought to result partly from the transient network of these gels, where crosslinks are able to break and reform during mechanical disruption.

Next, thiyl bonded gels were studied. Alkene-functionalised PAA revealed rapid and significant crosslinking under UV light through thiol-ene chemistry. These gels demonstrated increases in storage moduli of several orders of magnitude upon crosslinking, and revealed an elastic profile typical of a strong covalently crosslinked gel. Thiol-functionalised PAA gels revealed crosslinking under UV light through the interactions between neighbouring thiols. These gels showed initially high modulus values, prior to UV treatment, indicating significant crosslinking by air oxidation alone.

Adhesion studies indicate that PAA-BP and PAA-Cys gels have different modes of failure. PAA-BP displays brittle failure from surfaces, characterised by an initial strong detachment force to surfaces, followed by a rapid failure and detachment. PAA-Cys, on the other hand, demonstrates a more elastic profile of failure; these gels typically display a moderate initial adhesion strength before a very gradual detachment from surfaces, with long fibres forming between opposing substrates. Failure for PAA-BP was typically from the glass substrate, rather than the tissue, indicating that good bonding is occurring between the tissue surface and the gel. It is suggested that the elasticity of PAA-Cys gels

helps them to maintain conformal contact with the tissue surface; this, alongside the enhanced stretchability of these gels, enables the generation of the large energy densities observed.

These adhesion studies, alongside those from colloidal probe AFM experiments in Chapter 4, highlight the influence of tissue biochemistry on adhesive interactions. The strong adhesion of PAA-BP and PAA-Cys gels to tissues, particularly the epicardium, suggests chemical bonding via radical thiyls is a dominant mechanism. Furthermore, it is suggested that non-specific interactions, such as those between PAA and the glycocalyx of cell surfaces, play a role in adhesion. Combining these adhesion studies together, hydrogel/soft tissue adhesion is clearly a result of the interplay of several different factors; these include the tissue mechanics and bulk mechanics of the gels, as well as interactions occurring as a result of non-specific adhesion forces and covalent bonding.

# CHAPTER 6

## Conclusions and Future Directions

This thesis presents the chemical design and characterisation of PAA-based biomaterials for soft tissue adhesion. Through comparing the chemical design of these materials with their adhesive properties at both the nano and macroscale, we hope to inspire rational design of a novel generation of bioadhesives. This chapter will bring together some of the key findings of this work with a discussion on some of the future directions that could be pursued.

PAA was functionalised with a variety of different moieties, including an alkene, boronic acid, hydroxyl and thiol-end group. Funtionalisation was obtained through either Steglich esterification, DMTMM-mediated conjugation, or conjugation to bromoalkanes via nucleophilic substitution. Functionalisation via DMTMM proved to be an effective alternative to EDC/NHS for amine conjugation. In addition, functionalisation with bromoalkanes proved to be a very simple method for conjugation of PAA to a wide range of moieties. One of the purposes of this work was to enable the synthesis of materials that can form gels through crosslinks via physical or chemical bonds. As such, high functionalisation levels are required in order to form materials with sufficiently high crosslinking and corresponding mechanical properties. Functionalisations via DMTMM were limited to less than 5%, typically as a result of the lack of solubility of different reaction components or by the gelation of the final product during the polymer purification steps. Accordingly, a future direction of this work would be to further investigate alternative methods for amine conjugation, such as EDC/NHS, with the aim of obtaining higher functionalisation levels. With these increases in functionalisation levels improvements in the mechanical and adhesive properties of these gels would be expected.

Thiol-ene reactions were also investigated for alkene-functionalised PAA, both as a means of further functionalising polymers and also as a way of chemically crosslinking gels. As such, the effect of pH on reaction efficiencies was an important parameter to study. It was identified that thiol-ene reactions are restricted to more acidic conditions in the case of functionalised PAA, with the greatest efficiencies typically occurring at pH 5. It was proposed that this arises from the high density of negatively charged carboxylates along the PAA backbone, which may result in a local pH higher than expected.

In order to study the non-specific interactions between our polymeric biomaterials and soft tissues, colloidal probe-based atomic force microscopy (AFM) was used, requiring the production of polymer brushes. Well-defined brushes of PAA with controlled thickness and high grafting densities were produced on both planar and spherical substrates. Attempts were also made to functionalise PAA brushes with bromotoluene-boronic acid; however, this was with limited success. It is thought that brush degrafting was occurring through a mechanism of solvent-induced stretching, facilitated by the high temperatures required for functionalisation, the solvents used, or the high concentrations of base. Consequently, it is suggested that for functionalisation of PAA brushes, future work should investigate methods other than conjugation via bromoalkanes. As an example, methods such as DMTMM or EDC/NHS-mediated ligation may be more effective due to the lower temperatures and milder conditions required.

To gain a better understanding of the relationship between polymer chemistry and nanoscale adhesion mechanisms, the adhesion of three types of polymer brushes to cells and tissues was studied: Poly(acrylic acid) (PAA), poly(dimethylaminoethyl methacrylate) (PDMAEMA) and poly(olgioethylene glycol methacrylate) (POEGMA),

which were selected due to their distinct physico-chemical properties (anionic, cationic and neutral hydrophilic polymers, respectively). The adhesion of these brushes to a range of model monolayers, with a range of chemistries, was also investigated. These experiments revealed the complexity of weak polyelectrolyte brushes, with adhesion arising from combinations of electrostatic, Van der Waals interactions and hydrogen bonding. In comparison to the other polymers studied, experiments revealed the particularly strong adhesion of PAA brushes to a wide range of surface chemistries, including to model cell monolayers that were studied (epithelial cell sheets).

The impact of the cell glycocalyx on adhesion was investigated via enzymatic treatment of primary keratinocytes with heparinise III and neuraminidase, both of which are known to disrupt the glycocalyx layer. The adhesion of both PDMAEMA and PAA to these cells was found to reduce significantly upon treatment, particularly in the case of PAA brushes, indicating the importance of the glycocalyx in regulating non-specific adhesion between polymers and cells. Adhesion studies of brushes to tissues (gingival epithelium and epicardium), revealed the influence of the tissues' mechanical properties on adhesion as a result of the conformal contact of soft tissues to soft matter interfaces. The stiffness of tissues was characterised through AFM-based nanoindentation.

From the results for the study of adhesion at the nanoscale, the prediction of interactions between polymer brushes and even relatively simple interfaces, such as SAMs, proved to be incredibly complex. Accordingly, in the study of brush adhesion to cells and tissues relatively elaborate models, such as molecular dynamics simulations based on atomistic and coarse grain models, will be required to capture the complex nature of polymer brush-interactions with biological samples. These models should attempt to consider factors such as the brush morphology within different solutions, the

interaction of brushes with molecules that may be in solution, the mechanical properties of the surface to which the brush is adhering, and the contribution of non-specific interactions to polymeric adhesion.

The adhesion of four different PAA-based hydrogels to soft tissues was also studied. Macroscale adhesion tests, including tensile bond and lap shear tests, where used. The polymer-gelation systems used presented different types of chemical and physical crosslinks and crosslinking mechanisms. Two of these gels were formed through UV initiation, one gel used visible light-mediated crosslinking, and the final gel utilised physical crosslinking through the interaction between boronic acid moieties and the polysaccharide mannan. The interactions of these gels with different SAMs (hydroxyl and methacrylate) highlighted the importance of the bulk mechanical properties of the gel on adhesion strength to the underlying substrate. These bulk mechanical properties, as well as the gelation dynamics, were studied via oscillatory shear rheology.

PAA gels functionalised with tyramine and cured under visible light in the presence of eosin Y showed slow curing and overall weak mechanical properties. Accordingly, the adhesion strength of these gels to soft tissues was weak, as limited by the poor mechanical properties of the gel. These gels had a relatively low functionalisation level (1.9%) and as such it is suggested that future studies should aim to focus on alternative functionalisation methods to obtain higher levels. Furthermore, future studies could investigate the use of a co-initiator and/or co-monomer system in order to further accelerate radical generation and resulting functional group conversion.

Rheological characterisation of PAA gels, functionalised with boronic acid and crosslinked with mannan, revealed viscoelastic properties typical of a physical gel. During adhesion tests these gels demonstrated good elasticity and toughness, displaying

adhesion strengths similar to or greater than those of PAA-Tyramine gels, despite their lower mechanical properties. An interesting extension of this work would be to investigate the effect of higher concentrations of mannan on the bulk mechanical and adhesive properties of these gels, as only one concentration was investigated. In addition, future experiments could investigate the effect of different polysaccharides on the crosslinking strength of these gels.

Alkene-functionalised PAA revealed rapid and significant crosslinking under UV light through thiol-ene chemistry. These gels demonstrated a rheological profile typical of a strong covalently crosslinked gel. Thiol-functionalised PAA gels revealed crosslinking under UV light through the interactions between neighbouring thiols. Prior to UV treatment these gels showed initially high modulus values indicating significant crosslinking by air oxidation alone. Both these thiyl crosslinked gels demonstrated strong mechanical properties and strong adhesion to tissue samples, perhaps indicating that bonding via radical thiyls is a dominant mechanism in adhesion to these tissues. These adhesion studies, alongside those from AFM adhesion experiments, highlight the influence of tissue biochemistry on adhesion. Non-specific interactions, such as those between PAA and the glycocalyx of cell surfaces, are expected to contribute to the overall adhesion strength of gels. Our adhesion studies point to the need for an improved understanding and characterisation of the surface chemistry of tissues, to which biomaterials bonding is required. As an example, very little data was found on the structure and morphology of the glycocalyx in epithelial layers. Without this data it is difficult to predict the non-specific (and covalent) interactions occurring between tissues and polymers, and so these can only be inferred indirectly.

Another factor that was found to strongly influence adhesion both at the nanoscale and macroscale, was the mechanical properties of the tissues to which brushes and polymeric biomaterials were bonded. The keratinized gingiva and epicardium tissue samples were found to have significantly different mechanical properties, thereby strongly influencing the adhesion observed to both. An interesting extension of these adhesion studies would be to look at the adhesion of polymeric materials to a wider variety of tissue samples, particularly those with similar mechanical properties. Through these studies, the influence of tissue biochemistry on adhesion could be better inferred.

These studies clearly indicate that soft tissue adhesion is a complex process, involving non-specific interactions and covalent bonding, which are further regulated by the mechanical properties of the bulk biomaterial, the soft tissue and their interface. In order to further progress these studies there is a need for an in-depth characterisation of the surface chemistry of a variety of tissues types, in combination with adhesion studies to each. Through this multi-faceted approach, the effect of tissue biochemistry on polymer adhesion can be better inferred, enabling a more advanced understanding of the chemistry of adhesive interactions. Furthermore, studies of polymer brush adhesion at the nanoscale reveal the complexity of interactions between even relatively simple interfaces. Accordingly, to capture the complex nature of polymer brush-interactions with biological samples such as cell and tissues, relatively elaborate models will be required.

# References


1. Mehdizadeh, M. & Yang, J. Design Strategies and Applications of Tissue Bioadhesives. *Macromol. Biosci.* **13,** 271–288 (2013).

2. Palacio, M. L. B. & Bhushan, B. Bioadhesion: a review of concepts and applications. *Philos. Trans. R. Soc. A Math. Phys. Eng. Sci.* **370,** 2321–2347 (2012).

3. Ghobril, C. & Grinstaff, M. W. The chemistry and engineering of polymeric hydrogel adhesives for wound closure: a tutorial. *Chem. Soc. Rev.* **44,** 1820–1835 (2015).

4. Annabi, N. *et al.* Surgical materials: Current challenges and nano-enabled solutions. *Nano Today* **9,** 574–589 (2014).

5. Bressan, E. *et al.* Biopolymers for Hard and Soft Engineered Tissues: Application in Odontoiatric and Plastic Surgery Field. *Polymers (Basel).* **3,** 509–526 (2011).

6. Venugopal, J. R. *et al.* Biomaterial strategies for alleviation of myocardial infarction. *J. R. Soc. Interface* **9,** 1–19 (2012).

7. Bhagat, V. & Becker, M. L. Degradable Adhesives for Surgery and Tissue Engineering. *Biomacromolecules* **18,** 3009–3039 (2017).

8. Tiwari, S., Patil, R. & Bahadur, P. Polysaccharide Based Scaffolds for Soft Tissue Engineering Applications. *Polymers (Basel).* **11,** 1 (2018).

9. Samprasit, W. *et al.* Mucoadhesive electrospun chitosan-based nanofibre mats for dental caries prevention. *Carbohydr. Polym.* **117,** 933–940 (2015).

10. Tsibouklis, J., Middleton, A. M., Patel, N. & Pratten, J. Toward mucoadhesive hydrogel formulations for the management of xerostomia: The physicochemical, Biological, and Pharmacological Considerations. *J. Biomed. Mater. Res. - Part A* **101,** 3327–3338 (2013).

11. Markman, J. L., Rekechenetskiy, A., Holler, E. & Ljubimova, J. Y. Nanomedicine therapeutic approaches to overcome cancer drug resistance. *Adv. Drug Deliv. Rev.* **65,** 1866–1879 (2013).

12. Kanamala, M., Wilson, W. R., Yang, M., Palmer, B. D. & Wu, Z. Mechanisms and biomaterials in pH-responsive tumour targeted drug delivery: A review. *Biomaterials* **85,** 152–167 (2016).

13. Dinh, T. N., Hou, S., Park, S., Shalek, B. A. & Jeong, K. J. Gelatin Hydrogel Combined with Polydopamine Coating to Enhance Tissue Integration of Medical Implants. *ACS Biomater. Sci. Eng.* **4,** 3471–3477 (2018).

14. Berg, J. M., Tymoczko, J. L. & Stryer, L. Biochemistry. *W H Free.* **New York.,** 320–323 (2002).

15. Wong, J., Chilkoti, A. & Moy, V. T. Direct force measurements of the streptavidin – biotin interaction. *Biomol. Eng.* **16,** 45–55 (1999).

16. Beer, P., Gale, P. & Smith, D. Supramolecular Chemistry. *Oxford Chemistry Primers* at <https://global.oup.com/academic/product/supramolecular-chemistry-9780198504474?cc=gb&lang=en&>

17. Gelbart, W. M. Van Der Waals Forces: A handbook for Biologists, Chemists, Engineers, and Physicists. *Phys. Today* **59,** 52–52 (2006).

18. Meyer, E. E., Rosenberg, K. J. & Israelachvili, J. Recent progress in understanding hydrophobic interactions. *Proc. Natl. Acad. Sci. U. S. A.* **103,** 15739–15746 (2006).

19. Rahmany, M. B. & Van Dyke, M. Biomimetic approaches to modulate cellular adhesion in biomaterials: A review. *Acta Biomater.* **9,** 5431–7 (2013).

20. Zhu, J. & Marchant, R. E. Design properties of hydrogel tissue-engineering scaffolds. *Expert Rev. Med. Devices* **8,** 607–626 (2011).

21. Gupta, B., Plummer, C., Bisson, I., Frey, P. & Hilborn, J. Plasma-induced graft polymerization of acrylic acid onto poly(ethylene terephthalate) films: Characterization and human smooth muscle cell growth on grafted films. *Biomaterials* **23,** 863–871 (2002).

22. El-Sherbiny, I. M. & Yacoub, M. H. Hydrogel scaffolds for tissue engineering: Progress and challenges. *Glob. Cardiol. Sci. Pract.* **2013,** 38 (2013).

23. WICHTERLE, O. & LÍM, D. Hydrophilic Gels for Biological Use. *Nature* **185,** 117–118 (1960).

24. Nho, Y., Park, J. & Lim, Y. Preparation of Poly(acrylic acid) Hydrogel by Radiation Crosslinking and Its Application for Mucoadhesives. *Polymers (Basel).* **6,** 890–898 (2014).

25. Andrews, G. P., Laverty, T. P. & Jones, D. S. Mucoadhesive polymeric platforms for controlled drug delivery. *Eur. J. Pharm. Biopharm.* **71,** 505–518 (2009).

26. Salamat-Miller, N., Chittchang, M. & Johnston, T. P. The use of mucoadhesive polymers in buccal drug delivery. *Adv. Drug Deliv. Rev.* **57,** 1666–1691 (2005).

27. Zhu, W., Chuah, Y. J. & Wang, D. Bioadhesives for internal medical applications: A review. *Acta Biomater.* **74,** 1–16 (2018).

28. Annabi, N. *et al.* Engineering a highly elastic human protein–based sealant for surgical applications. *Sci. Transl. Med.* **9,** eaai7466 (2017).

29. Li, J. *et al.* Tough adhesives for diverse wet surfaces. *Science (80-. ).* **357,** 378–381 (2017).

30. Li, Z. & Guan, J. Hydrogels for cardiac tissue engineering. *Polymers (Basel).* **3,** 740–761 (2011).

31. Giraud, M.-N. *et al.* Hydrogel-based Engineered Skeletal Muscle Grafts Normalize Heart Function Early After Myocardial Infarction. *Artif. Organs* **32,** 692–700 (2008).

32. El-Sherbiny, I. & Yacoub, M. Hydrogel scaffolds for tissue engineering: Progress and challenges. *Glob. Cardiol. Sci. Pract.* **2013,** 316–42 (2013).

33. Cruise, G. M. *et al.* In vitro and in vivo performance of porcine islets encapsulated in interfacially photopolymerized poly(ethylene glycol) diacrylate membranes. *Cell Transplant.* **8,** 293–306 (1999).

34. Hill-West, J. L., Chowdhury, S. M., Slepian, M. J. & Hubbell, J. a. Inhibition of thrombosis and intimal thickening by in situ photopolymerization of thin hydrogel barriers. *Proc. Natl. Acad. Sci.* **91,** 5967–5971 (1994).

35. Levenberg, S. *et al.* Differentiation of human embryonic stem cells on three-dimensional polymer scaffolds. *Proc Natl Acad Sci U S A* **100,** 12741–12746 (2003).

36. Yin, M.-J. *et al.* Rapid 3D Patterning of Poly(acrylic acid) Ionic Hydrogel for Miniature pH Sensors. *Adv. Mater.* **28,** 1394–1399 (2016).

37. Elliott, J. E., Macdonald, M., Nie, J. & Bowman, C. N. Structure and swelling of poly(acrylic acid) hydrogels: effect of pH, ionic strength, and dilution on the crosslinked polymer structure. *Polymer (Guildf).* **45,** 1503–1510 (2004).

38. Huang, Y., Yu, H. & Xiao, C. pH-sensitive cationic guar gum/poly (acrylic acid) polyelectrolyte hydrogels: Swelling and in vitro drug release. *Carbohydr. Polym.* **69,** 774–783 (2007).

39. Dubolazov, A. V, Nurkeeva, Z. S., Mun, G. a & Khutoryanskiy, V. V. Design of mucoadhesive polymeric films based on blends of poly(acrylic acid) and (hydroxypropyl)cellulose. *Biomacromolecules* **7,** 1637–43 (2006).

40. Bromberg, L., Temchenko, M., Alakhov, V. & Hatton, T. A. Bioadhesive properties and rheology of polyether-modified poly(acrylic acid) hydrogels. *Int. J. Pharm.* **282,** 45–60 (2004).

41. De Giglio, E., Cometa, S., Cioffi, N., Torsi, L. & Sabbatini, L. Analytical investigations of poly(acrylic acid) coatings electrodeposited on titanium-based implants: A versatile approach to biocompatibility enhancement. *Anal. Bioanal. Chem.* **389,** 2055–2063 (2007).

42. Lee, W., Lee, T. G. & Koh, W. G. Grafting of Poly(acrylic acid) on the Poly(ethylene glycol) Hydrogel Using Surface-initiated Photopolymerization for Covalent Immobilization of Collagen. *J. Ind. Eng. Chem.* **13,** 1195–1200 (2007).

43. Nho, Y.-C., Park, J.-S. & Lim, Y.-M. Preparation of Poly(acrylic acid) Hydrogel by Radiation Crosslinking and Its Application for Mucoadhesives. *Polymers (Basel).* **6,** 890–898 (2014).

44. Squier, C. a & Kremer, M. J. Biology of oral mucosa and esophagus. *J. Natl. Cancer Inst. Monogr.* **52242,** 7–15 (2001).

45. Derrien, M. *et al.* Mucin-bacterial interactions in the human oral cavity and digestive tract. *Gut Microbes* **1,** 254–268 (2010).

46. Park, H. & Robinson, J. R. Mechanisms of Mucoadhesion of Poly(acrylic Acid)

Hydrogels. *Pharm. Res. An Off. J. Am. Assoc. Pharm. Sci.* **4,** 457–464 (1987).

47. Yang, S. Y. *et al.* A bio-inspired swellable microneedle adhesive for mechanical interlocking with tissue. *Nat. Commun.* **4,** 1702 (2013).

48. Vote, B. J. & Elder, M. J. Cyanoacrylate glue for corneal perforations: A description of a surgical technique and a review of the literature. *Clin. Exp. Ophthalmol.* **28,** 437–442 (2000).

49. Yang, J., Bai, R., Chen, B. & Suo, Z. Hydrogel Adhesion: A Supramolecular Synergy of Chemistry, Topology, and Mechanics. *Adv. Funct. Mater.* **1901693,** 1901693 (2019).

50. Chen, Q. Z. *et al.* Characterisation of a soft elastomer poly(glycerol sebacate) designed to match the mechanical properties of myocardial tissue. *Biomaterials* **29,** 47–57 (2008).

51. Ma, P. X. Biomimetic materials for tissue engineering. *Adv. Drug Deliv. Rev.* **60,** 184–198 (2008).

52. University of Michigan, Histology and Virtual Microscopy Learning Resources. *University of Michigan Health System, Learning Resource Centre* at <http://histology.med.umich.edu/>

53. Pratt, R. Stratified Squamous Epithelium (Keratinized). *AnatomyOne* at <http://www.anatomyone.com/a/stratified-squamous-epithelium-keratinized/>

54. Gail, J. & Tortora, G. *Anatomy and Physiology From Science to Life, 3rd Edition*. *Wiley* (John Wiley & Sons, 2013). at <http://eu.wiley.com/WileyCDA/WileyTitle/productCd-EHEP002147.html>

55. Eurell, J., Frappier, B. & Dellmann, H.-D. *Dellmann's Textbook of Veterinary Histology*. (Wiley, 2006). at <https://books.google.com/books?id=FnS4uiOlRT0C&pgis=1>

56. Freshney, R. & Freshney, M. *Culture of Epithelial Cells*. (Wiley, 2004). at <https://books.google.com/books?id=KqKNxeWlU6MC&pgis=1>

57. Marieb, E., Mitchell, S. & Smith, L. *Human Anatomy Laboratory Manual with Cat Dissections, 7th Edition*. (Pearson, 2014).

58. Oral Mucosa - Pocket Dentistry. *Pocket Dentistry* (2015). at <http://pocketdentistry.com/9-oral-mucosa/>

59. Ovaere, P., Lippens, S., Vandenabeele, P. & Declercq, W. The emerging roles of serine protease cascades in the epidermis. *Trends Biochem. Sci.* **34,** 453–63 (2009).

60. Dawson, D. V. *et al.* Organization, barrier function and antimicrobial lipids of the oral mucosa. *Int. J. Cosmet. Sci.* **35,** 220–223 (2013).

61. Turabelidze, A. *et al.* Intrinsic Differences between Oral and Skin Keratinocytes. *PLoS One* **9,** e101480 (2014).

62. Ganjare, A., Bagul, N., Kathariya, R. & Oberoi, J. 'Cell junctions of oral mucosa'- in a nutshell. *QScience Connect* **2015,** 7 (2015).

63. Larjava, H., Koivisto, L., Hakkinen, L. & Heino, J. Epithelial Integrins with Special Reference to Oral Epithelia. *J. Dent. Res.* **90,** 1367–1376 (2011).

64. Boks, M. A. *et al.* The Human Glycoprotein Salivary Agglutinin Inhibits the Interaction of DC-SIGN and Langerin with Oral Micro-Organisms. *J. Innate Immun.* (2016). doi:10.1159/000443016

65. Rodriguez, E. R. & Tan, C. D. Structure and Anatomy of the Human Pericardium. *Prog. Cardiovasc. Dis.* **59,** 327–340 (2017).

66. Cao, J. & Poss, K. D. The epicardium as a hub for heart regeneration. *Nat. Rev. Cardiol.* **15,** 631–647 (2018).

67. Wang, C., Yan, Q., Liu, H. B., Zhou, X. H. & Xiao, S. J. Different EDC/NHS activation mechanisms between PAA and PMAA brushes and the following amidation reactions. *Langmuir* **27,** 12058–12068 (2011).

68. Carbodiimide Crosslinker Chemistry. *ThermoFisher Scientific* at <https://www.thermofisher.com/uk/en/home/life-science/protein-biology/protein-biology-learning-center/protein-biology-resource-library/pierce-protein-methods/carbodiimide-crosslinker-chemistry.html>

69. Conde, J. *et al.* Revisiting 30 years of biofunctionalization and surface chemistry of inorganic nanoparticles for nanomedicine. *Front. Chem.* **2,** 48 (2014).

70. Levy, T., Déjugnat, C. & Sukhorukov, G. B. Polymer Microcapsules with Carbohydrate-Sensitive Properties. *Adv. Funct. Mater.* **18,** 1586–1594 (2008).

71. Sato, T., Aoyagi, T., Ebara, M. & Auzély-Velty, R. Catechol-modified hyaluronic acid: in situ-forming hydrogels by auto-oxidation of catechol or photo-oxidation using visible light. *Polym. Bull.* (2017). doi:10.1007/s00289-017-1937-y

72. Loebel, C., D'Este, M., Alini, M., Zenobi-Wong, M. & Eglin, D. Precise tailoring of tyramine-based hyaluronan hydrogel properties using DMTMM conjugation. *Carbohydr. Polym.* **115,** 325–333 (2015).

73. Loebel, C., Broguiere, N., Alini, M., Zenobi-Wong, M. & Eglin, D. Microfabrication of Photo-Cross-Linked Hyaluronan Hydrogels by Single- and Two-Photon Tyramine Oxidation. *Biomacromolecules* **16,** 2624–2630 (2015).

74. D'Este, M., Eglin, D. & Alini, M. A systematic analysis of DMTMM vs EDC/NHS for ligation of amines to Hyaluronan in water. *Carbohydr. Polym.* **108,** 239–246 (2014).

75. Kunishima, M. *et al.* 4-(4,6-dimethoxy-1,3,5-triazin-2-yl)-4-methyl-morpholinium chloride: an efficient condensing agent leading to the formation of amides and esters. *Tetrahedron* **55,** 13159–13170 (1999).

76. Raw, S. A. An improved process for the synthesis of DMTMM-based coupling reagents. *Tetrahedron Lett.* **50,** 946–948 (2009).

77. Thompson, K. & Michielsen, S. Novel synthesis of N-substituted polyacrylamides: Derivatization of poly(acrylic acid) with amines using a triazine-based condensing reagent. *J. Polym. Sci. Part A Polym. Chem.* **44,** 126–136 (2006).

78. Pelet, J. M. & Putnam, D. An in-depth analysis of polymer-analogous conjugation using DMTMM. *Bioconjug. Chem.* **22,** 329–337 (2011).

79. Iwasawa, T., Wash, P., Gibson, C. & Rebek, J. Reaction of an introverted carboxylic acid with carbodiimide. *Tetrahedron* **63,** 6506–6511 (2007).

80. Radau, G. Suppression of Formation of N,N'-Dicyclohexylurea Derivatives During DCC-Activation of Proline-Containing Dipeptides. *Monatshefte für Chemie - Chem. Mon.* **134,** 1033–1036 (2003).

81. Luo, Y., Ran, Q., Wu, S. & Shen, J. Synthesis and characterization of a poly(acrylic acid)-graft-methoxy poly(ethylene oxide) comblike copolymer. *J. Appl. Polym. Sci.* **109,** 3286–3291 (2008).

82. O'Boyle, N. M. *et al.* Synthesis and evaluation of antiproliferative microtubule-destabilising combretastatin A-4 piperazine conjugates. *Org. Biomol. Chem.* **17,** 6184–6200 (2019).

83. Northrop, B. H. & Coffey, R. N. Thiol-ene click chemistry: Computational and kinetic analysis of the influence of alkene functionality. *J. Am. Chem. Soc.* **134,** 13804–13817 (2012).

84. Hoyle, C. & Bowman, C. N. Thiol–Ene Click Chemistry. *Angew. Chemie Int. Ed.* **49,** 1540–1573 (2010).

85. Tan, K. Y., Ramstedt, M., Colak, B., Huck, W. T. S. & Gautrot, J. E. Study of thiol–ene chemistry on polymer brushes and application to surface patterning and protein adsorption. *Polym. Chem.* **7,** 979–990 (2016).

86. Costa, P., Gautrot, J. E. & Connelly, J. T. Directing cell migration using micropatterned and dynamically adhesive polymer brushes. *Acta Biomater.* **10,** 2415–2422 (2014).

87. Kade, M. J., Burke, D. J. & Hawker, C. J. The power of thiol-ene chemistry. *J. Polym. Sci. Part A Polym. Chem.* **48,** 743–750 (2010).

88. Colak, B., Da Silva, J. C. S., Soares, T. A. & Gautrot, J. E. Impact of the Molecular Environment on Thiol-Ene Coupling for Biofunctionalization and Conjugation. *Bioconjug. Chem.* **27,** 2111–2123 (2016).

89. Chen, J. J., Struk, K. N. & Brennan, A. B. Surface modification of silicate glass using 3-(mercaptopropyl) trimethoxysilane for thiol-ene polymerization. *Langmuir* **27,** 13754–13761 (2011).

90. Ettehadi Gargari, J., Sid Kalal, H., Niknafs, D. & Khanchi, A. Synthesis of silica/PAA NPs via combining RAFT polymerization and thiol-ene click reaction and postpolymerization modifications with arsenazo (III). *Polym. Adv. Technol.* **29,** 2806–2815 (2018).

91. DeForest, C. A., Polizzotti, B. D. & Anseth, K. S. Sequential click reactions for synthesizing and patterning three-dimensional cell microenvironments. *Nat. Mater.* **8,** 659–664 (2009).

92. Ionin, B. I. & Ershov, B. A. *NMR Spectroscopy in Organic Chemistry*. *NMR Spectroscopy in Organic Chemistry* (1995). doi:10.1007/978-1-4684-1785-2

93. Dais, P. & Spyros, A. *Nuclear Magnetic Resonance*. *Chemical Analysis of Food: Techniques and Applications* (Elsevier, 2012). doi:10.1016/B978-0-12-384862-8.00004-2

94. Harrell, M. L. & Bergbreiter, D. E. Using 1 H NMR Spectra of Polymers and Polymer Products To Illustrate Concepts in Organic Chemistry. *J. Chem. Educ.* **94,** 1668–1673 (2017).

95. Atta-ur-Rahman, M. I. C. *Applications of NMR Spectroscopy: Volume 2*. *Bentham Science Publishers* (2015).

96. Kleinberg, R. L. & Jackson, J. A. An introduction to the history of NMR well logging. *Concepts Magn. Reson.* **13,** 340–342 (2001).

97. Drioli, E. & Giorno, L. *Comprehensive Membrane Science and Engineering*. (Elsevier Science, 2010).

98. Zhu, H. & Nyström, M. Cleaning results characterized by flux, streaming potential and FTIR measurements. in *Colloids and Surfaces A: Physicochemical and Engineering Aspects* **138,** 309–321 (1998).

99. Maruyama, T. *et al.* FT-IR analysis of BSA fouled on ultrafiltration and microfiltration membranes. *J. Memb. Sci.* **192,** 201–207 (2001).

100. Megone, W., Roohpour, N. & Gautrot, J. E. Impact of surface adhesion and sample heterogeneity on the multiscale mechanical characterisation of soft biomaterials. *Sci. Rep.* **8,** 1–10 (2018).

101. Davis, K. a. & Matyjaszewski, K. Atom transfer radical polymerization of tert-butyl acrylate and preparation of block copolymers. *Macromolecules* **33,** 4039–4047 (2000).

102. Lego, B., Skene, W. G. & Giasson, S. Swelling Study of Responsive Polyelectrolyte

Brushes Grafted from Mica Substrates: Effect of pH, Salt, and Grafting Density. *Macromolecules* **43,** 4384–4393 (2010).

103. Faniran, J. A. & Shurvell, H. F. Infrared spectra of phenylboronic acid (normal and deuterated) and diphenyl phenylboronate. *Can. J. Chem.* **46,** 2089–2095 (1968).

104. Wang, Y. M. *et al.* Poly(acrylic acid) brushes pattern as a 3D functional biosensor surface for microchips. *Appl. Surf. Sci.* **266,** 313–318 (2013).

105. Tavakkoli Yaraki, M. *et al.* Synthesis and optical properties of cysteamine-capped ZnS quantum dots for aflatoxin quantification. *J. Alloys Compd.* **690,** 749–758 (2017).

106. Loebel, C., D'Este, M., Alini, M., Zenobi-Wong, M. & Eglin, D. Precise tailoring of tyramine-based hyaluronan hydrogel properties using DMTMM conjugation. *Carbohydr. Polym.* **115,** 325–333 (2015).

107. Shu, X. Z., Liu, Y., Palumbo, F. & Prestwich, G. D. Disulfide-crosslinked hyaluronan-gelatin hydrogel films: A covalent mimic of the extracellular matrix for in vitro cell growth. *Biomaterials* **24,** 3825–3834 (2003).

108. Shu, X. Z., Liu, Y., Luo, Y., Roberts, M. C. & Prestwich, G. D. Disulfide cross-linked hyaluronan hydrogels. *Biomacromolecules* **3,** 1304–1311 (2002).

109. Grabowska, B. & Holtzer, M. Structural examination of the cross-linking reaction mechanism of polyacrylate binding agents. *Arch. Metall. Mater.* **54,** 427–437 (2009).

110. Huang, R. *et al.* In situ synthesis of protein-resistant poly(oligo(ethylene glycol)methacrylate) films in capillary for protein separation. *RSC Adv.* **4,** 4883–4888 (2014).

111. Dai, J. *et al.* High-Capacity Binding of Proteins by Poly(Acrylic Acid) Brushes and Their Derivatives. *Langmuir* **22,** 4274–4281 (2006).

112. Cullen, S. P., Liu, X., Mandel, I. C., Himpsel, F. J. & Gopalan, P. Polymeric Brushes as Functional Templates for Immobilizing Ribonuclease A: Study of Binding Kinetics and Activity. *Langmuir* **24,** 913–920 (2008).

113. Cullen, S. P., Mandel, I. C. & Gopalan, P. Surface-anchored Poly(2-vinyl-4,4-

dimethyl azlactone) brushes as templates for Enzyme immobilization. *Langmuir* **24,** 13701–13709 (2008).

114. Ren, X., Wu, Y., Cheng, Y., Ma, H. & Wei, S. Fibronectin and bone morphogenetic protein-2-decorated poly(OEGMA-r-HEMA) brushes promote osseointegration of titanium surfaces. *Langmuir* **27,** 12069–12073 (2011).

115. Yu, Q. *et al.* Protein adsorption and cell adhesion/detachment behavior on dual-responsive silicon surfaces modified with poly(N-isopropylacrylamide)-block-polystyrene copolymer. *Langmuir* **26,** 8582–8588 (2010).

116. Qian, H. & He, L. Surface-initiated activators generated by electron transfer for atom transfer radical polymerization in detection of DNA point mutation. *Anal. Chem.* **81,** 4536–4542 (2009).

117. Nguyen, A. T., Baggerman, J., Paulusse, J. M. J., Zuilhof, H. & Van Rijn, C. J. M. Bioconjugation of protein-repellent zwitterionic polymer brushes grafted from silicon nitride. *Langmuir* **28,** 604–610 (2012).

118. Hu, W., Liu, Y., Lu, Z. & Li, C. M. Poly[oligo(ethylene glycol) methacrylate-co-glycidyl methacrylate] Brush Substrate for Sensitive Surface Plasmon Resonance Imaging Protein Arrays. *Adv. Funct. Mater.* **20,** 3497–3503 (2010).

119. Rodriguez-Emmenegger, C., Janel, S., de los Santos Pereira, A., Bruns, M. & Lafont, F. Quantifying bacterial adhesion on antifouling polymer brushes via single-cell force spectroscopy. *Polym. Chem.* **6,** 5740–5751 (2015).

120. Park, Y. S., Ito, Y. & Imanishi, Y. pH-Controlled Gating of a Porous Glass Filter by Surface Grafting of Polyelectrolyte Brushes. *Chem. Mater.* **9,** 2755 (1997).

121. Wittemann, a., Haupt, B. & Ballauff, M. Adsorption of proteins on spherical polyelectrolyte brushes in aqueous solution. *Phys. Chem. Chem. Phys.* **5,** 1671–1677 (2003).

122. Chen, H. & Hsieh, Y.-L. Enzyme immobilization on ultrafine cellulose fibers via poly(acrylic acid) electrolyte grafts. *Biotechnol. Bioeng.* **90,** 405–13 (2005).

123. Chiang, E. N., Dong, R., Ober, C. K. & Baird, B. a. Cellular Responses to Patterned Poly(acrylic acid) Brushes. *Langmuir* **27,** 7016–7023 (2011).

124. Bisson, I. *et al.* Acrylic acid grafting and collagen immobilization on poly(ethylene terephthalate) surfaces for adherence and growth of human bladder smooth muscle cells. *Biomaterials* **23,** 3149–58 (2002).

125. Li, D., Sheng, X. & Zhao, B. Environmentally Responsive 'Hairy' Nanoparticles: Mixed Homopolymer Brushes on Silica Nanoparticles Synthesized by Living Radical Polymerization Techniques. *J. Am. Chem. Soc.* **127,** 6248–6256 (2005).

126. Wu, T. *et al.* Behavior of surface-anchored poly(acrylic acid) brushes with grafting density gradients on solid substrates: 1. Experiment. *Macromolecules* **40,** 8756–8764 (2007).

127. Krishnamoorthy, M., Hakobyan, S., Ramstedt, M. & Gautrot, J. E. Surface-Initiated Polymer Brushes in the Biomedical Field: Applications in Membrane Science, Biosensing, Cell Culture, Regenerative Medicine and Antibacterial Coatings. *Chem. Rev.* **114,** 10976–11026 (2014).

128. Barbey, R. *et al.* Polymer Brushes via Surface-Initiated Controlled Radical Polymerization: Synthesis, Characterization, Properties, and Applications. *Chem. Rev.* **109,** 5437–5527 (2009).

129. *Polymer Brushes*. **1,** (Wiley, 2004).

130. Wu, L., Glebe, U. & Böker, A. Surface-initiated controlled radical polymerizations from silica nanoparticles, gold nanocrystals, and bionanoparticles. *Polym. Chem.* **6,** 5143–5184 (2015).

131. Zoppe, J. O. *et al.* Surface-Initiated Controlled Radical Polymerization: State-of-the-Art, Opportunities, and Challenges in Surface and Interface Engineering with Polymer Brushes. *Chem. Rev.* **117,** 1105–1318 (2017).

132. Treat, N. D., Ayres, N., Boyes, S. G. & Brittain, W. J. A facile route to poly(acrylic acid) brushes using atom transfer radical polymerization. *Macromolecules* **39,** 26–29 (2006).

133. Tsarevsky, N. V., Braunecker, W. A. & Matyjaszewski, K. Electron transfer reactions relevant to atom transfer radical polymerization. *J. Organomet. Chem.* **692,** 3212–3222 (2007).

134. Braunecker, W. A., Tsarevsky, N. V., Gennaro, A. & Matyjaszewski, K. Thermodynamic components of the atom transfer radical polymerization equilibrium: Quantifying solvent effects. *Macromolecules* **42,** 6348–6360 (2009).

135. Kizhakkedathu, J. N. & Brooks, D. E. Synthesis of poly(N,N-dimethylacrylamide) brushes from charged polymeric surfaces by aqueous ATRP: Effect of surface initiator concentration. *Macromolecules* **36,** 591–598 (2003).

136. Cui, Y. *et al.* Synthesis of thermosensitive PNIPAM-co-MBAA nanotubes by atom transfer radical polymerization within a porous membrane. *Macromol. Rapid Commun.* **26,** 1552–1556 (2005).

137. Wu, T., Efimenko, K. & Genzer, J. Preparing high-density polymer brushes by mechanically assisted polymer assembly. *Macromolecules* **34,** 684–686 (2001).

138. Coessens, V., Pintauer, T. & Matyjaszewski, K. Functional polymers by atom transfer radical polymerization. *Prog. Polym. Sci.* **26,** 337–377 (2001).

139. Dong, R., Krishnan, S., Baird, B. a., Lindau, M. & Ober, C. K. Patterned biofunctional poly(acrylic acid) brushes on silicon surfaces. *Biomacromolecules* **8,** 3082–3092 (2007).

140. Rodriguez-Emmenegger, C., Janel, S., de los Santos Pereira, A., Bruns, M. & Lafont, F. Quantifying bacterial adhesion on antifouling polymer brushes via single-cell force spectroscopy. *Polym. Chem.* **6,** 5740–5751 (2015).

141. Czeslik, C. *et al.* Salt-induced protein resistance of polyelectrolyte brushes studied using fluorescence correlation spectroscopy and neutron reflectometry. *Phys. Chem. Chem. Phys.* **6,** 5557–5563 (2004).

142. Hollmann, O. & Czeslik, C. Characterization of a planar poly(acrylic acid) brush as a materials coating for controlled protein immobilization. *Langmuir* **22,** 3300–3305 (2006).

143. Czeslik, C., Jackler, G., Steitz, R. & von Grünberg, H.-H. Protein Binding to Like-Charged Polyelectrolyte Brushes by Counterion Evaporation. *J. Phys. Chem. B* **108,** 13395–13402 (2004).

144. Brown, A. A., Khan, N. S., Steinbock, L. & Huck, W. T. S. Synthesis of oligo(ethylene

glycol) methacrylate polymer brushes. *Eur. Polym. J.* **41,** 1757–1765 (2005).

145. Jonas, A. M., Glinel, K., Oren, R., Nysten, B. & Huck, W. T. S. Thermo-Responsive Polymer Brushes with Tunable Collapse Temperatures in the Physiological Range. *Macromolecules* **40,** 4403–4405 (2007).

146. An, Y., Li, D., Roohpour, N., Gautrot, J. E. & Barber, A. H. Failure mechanisms in denture adhesives. *Dent. Mater.* 1–9 (2016). doi:10.1016/j.dental.2016.01.007

147. Lego, B., François, M., Skene, W. G. & Giasson, S. Polymer Brush Covalently Attached to OH-Functionalized Mica Surface via Surface-Initiated ATRP: Control of Grafting Density and Polymer Chain Length. *Langmuir* **25,** 5313–5321 (2009).

148. Husseman, M. *et al.* Controlled Synthesis of Polymer Brushes by 'Living' Free Radical Polymerization Techniques. *Macromolecules* **32,** 1424–1431 (1999).

149. Magenau, A. J. D., Kwak, Y., Schröder, K. & Matyjaszewski, K. Highly Active Bipyridine-Based Ligands for Atom Transfer Radical Polymerization. *ACS Macro Lett.* **1,** 508–512 (2012).

150. Ma, Q. & Wooley, K. L. The preparation of t-butyl acrylate, methyl acrylate, and styrene block copolymers by atom transfer radical polymerization: Precursors to amphiphilic and hydrophilic block copolymers and conversion to complex nanostructured materials. *J. Polym. Sci. Part A Polym. Chem.* **38,** 4805–4820 (2000).

151. Nap, R., Gong, P. & Szleifer, I. Weak polyelectrolytes tethered to surfaces: Effect of geometry, acid–base equilibrium and electrical permittivity. *J. Polym. Sci. Part B Polym. Phys.* **44,** 2638–2662 (2006).

152. Israels, R., Leermakers, F. a. M. & Fleer, G. J. On the Theory of Grafted Weak Polyacids. *Macromolecules* **27,** 3087–3093 (1994).

153. Gong, P., Wu, T., Genzer, J. & Szleifer, I. Behavior of Surface-Anchored Poly(acrylic acid) Brushes with Grafting Density Gradients on Solid Substrates: 2. Theory. *Macromolecules* **40,** 8765–8773 (2007).

154. Hehmeyer, O. J., Arya, G., Panagiotopoulos, A. Z. & Szleifer, I. Monte Carlo simulation and molecular theory of tethered polyelectrolytes. *J. Chem. Phys.* **126,**

244902 (2007).

155. Jenkins, F. & White, H. in *Fundamentals of Optics* 474–496 (McGraw-Hill Primis Custom Publishing, 2001).

156. Tsarevsky, N. V & Matyjaszewski, K. 'Green' atom transfer radical polymerization: from process design to preparation of well-defined environmentally friendly polymeric materials. *Chem. Rev.* **107,** 2270–2299 (2007).

157. Xie, Y. *et al.* Synthesis of highly porous poly(tert-butyl acrylate)-b-polysulfone-b-poly(tert-butyl acrylate) asymmetric membranes. *Polym. Chem.* **7,** 3076–3089 (2016).

158. Louette, P., Bodino, F. & Pireaux, J.-J. Poly(acrylic acid) (PAA) XPS Reference Core Level and Energy Loss Spectra. *Surf. Sci. Spectra* **12,** 22–26 (2005).

159. Currie, E. P. K., Sieval, A. B., Fleer, G. J. & Stuart, M. A. C. Polyacrylic acid brushes: Surface pressure and salt-induced swelling. *Langmuir* **16,** 8324–8333 (2000).

160. Willott, J. D. *et al.* Critical salt effects in the swelling behavior of a weak polybasic brush. *Langmuir* **30,** 1827–1836 (2014).

161. Krishnamoorthy, M. *et al.* Solution Conformation of Polymer Brushes Determines Their Interactions with DNA and Transfection Efficiency. *Biomacromolecules* **18,** 4121–4132 (2017).

162. Borozenko, O. *et al.* Monitoring in real-time the degrafting of covalently attached fluorescent polymer brushes grafted to silica substrates-effects of pH and salt. *Macromolecules* **44,** 8177–8184 (2011).

163. Menzel, M. *et al.* Entropic death of nonpatterned and nanopatterned polyelectrolyte brushes. *J. Polym. Sci. Part A Polym. Chem.* **57,** 1283–1295 (2019).

164. Melzak, K. A., Yu, K., Bo, D., Kizhakkedathu, J. N. & Toca-Herrera, J. L. Chain Length and Grafting Density Dependent Enhancement in the Hydrolysis of Ester-Linked Polymer Brushes. *Langmuir* **31,** 6463–6470 (2015).

165. Ataman, N. C. & Klok, H. A. Degrafting of Poly(poly(ethylene glycol) methacrylate) Brushes from Planar and Spherical Silicon Substrates. *Macromolecules* **49,** 9035–9047 (2016).

166. Galvin, C. J., Bain, E. D., Henke, A. & Genzer, J. Instability of Surface-Grafted Weak Polyacid Brushes on Flat Substrates. *Macromolecules* **48,** 5677–5687 (2015).

167. Suk, J. S., Xu, Q., Kim, N., Hanes, J. & Ensign, L. M. PEGylation as a strategy for improving nanoparticle-based drug and gene delivery. *Adv. Drug Deliv. Rev.* **99,** 28–51 (2016).

168. Sanjuan, S., Perrin, P., Pantoustier, N. & Tran, Y. Synthesis and swelling behavior of pH-responsive polybase brushes. *Langmuir* **23,** 5769–5778 (2007).

169. Synatschke, C. V., Schallon, A., Jérôme, V., Freitag, R. & Müller, A. H. E. Influence of polymer architecture and molecular weight of poly(2-(dimethylamino)ethyl methacrylate) polycations on transfection efficiency and cell viability in gene delivery. *Biomacromolecules* **12,** 4247–4255 (2011).

170. Li, D., Sharili, A. S., Connelly, J. & Gautrot, J. E. Highly Stable RNA Capture by Dense Cationic Polymer Brushes for the Design of Cytocompatible, Serum-Stable SiRNA Delivery Vectors. *Biomacromolecules* **19,** 606–615 (2018).

171. Hucknall, A., Rangarajan, S. & Chilkoti, A. In pursuit of zero: Polymer brushes that resist the adsorption of proteins. *Adv. Mater.* **21,** 2441–2446 (2009).

172. Swar, S. *et al.* Effective poly(ethylene glycol) methyl ether grafting technique onto Nylon 6 surface to achieve resistance against pathogenic bacteria Staphylococcus aureus and Pseudomonas aeruginosa. *J. Mater. Sci.* **53,** 14104–14120 (2018).

173. Heuberger, M., Drobek, T. & Spencer, N. D. Interaction forces and morphology of a protein-resistant poly(ethylene glycol) layer. *Biophys. J.* **88,** 495–504 (2005).

174. Boettiger, D. & Wehrle-Haller, B. Integrin and glycocalyx mediated contributions to cell adhesion identified by single cell force spectroscopy. *J. Phys. Condens. Matter* **22,** 194101 (2010).

175. Rho, J. Y., Roy, M. E., Tsui, T. Y. & Pharr, G. M. Elastic properties of microstructural components of human bone tissue as measured by nanoindentation. *J. Biomed. Mater. Res.* **45,** 48–54 (1999).

176. Bembey, A. K., Oyen, M. L., Bushby, A. J. & Boyde, A. Viscoelastic properties of bone as a function of hydration state determined by nanoindentation. in

*Philosophical Magazine* **86,** 5691–5703 (2006).

177. Oliver, W. C. & Pharr, G. M. An improved technique for determining hardness and elastic modulus using load and displacement sensing indentation experiments. *J. Mater. Res.* **7,** 1564–1583 (1992).

178. Oliver, W. C. & Pharr, G. M. Measurement of hardness and elastic modulus by instrumented indentation: Advances in understanding and refinements to methodology. *J. Mater. Res.* **19,** 3–20 (2004).

179. Sneddon, I. N. The relation between load and penetration in the axisymmetric boussinesq problem for a punch of arbitrary profile. *Int. J. Eng. Sci.* **3,** 47–57 (1965).

180. Chen, J. & Lu, G. Finite element modelling of nanoindentation based methods for mechanical properties of cells. *J. Biomech.* **45,** 2810–2816 (2012).

181. Chen, J. Nanobiomechanics of living cells: A review. *Interface Focus* **4,** (2014).

182. Qian, L. & Zhao, H. Nanoindentation of soft biological materials. *Micromachines* **9,** (2018).

183. Oyen, M. L. & Cook, R. F. A practical guide for analysis of nanoindentation data. *J. Mech. Behav. Biomed. Mater.* **2,** 396–407 (2009).

184. Sherratt, M. J. *et al.* Fibrillin-rich microfibrils of the extracellular matrix: Ultrastructure and assembly. *Micron* **32,** 185–200 (2001).

185. Akhtar, R., Sherratt, M. J., Cruickshank, J. K. & Derby, B. Characterizing the elastic properties of tissues. *Mater. Today* **14,** 96–105 (2011).

186. Cross, S. E., Jin, Y. S., Rao, J. & Gimzewski, J. K. Nanomechanical analysis of cells from cancer patients. *Nat. Nanotechnol.* **2,** 780–783 (2007).

187. Kuznetsova, T. G., Starodubtseva, M. N., Yegorenkov, N. I., Chizhik, S. A. & Zhdanov, R. I. Atomic force microscopy probing of cell elasticity. *Micron* **38,** 824–833 (2007).

188. Andreu, I. *et al.* Heterogeneous micromechanical properties of the extracellular matrix in healthy and infarcted hearts. *Acta Biomater.* **10,** 3235–3242 (2014).

189. Berry, M. F. Mesenchymal stem cell injection after myocardial infarction improves myocardial compliance. *AJP Hear. Circ. Physiol.* **290,** H2196–H2203 (2006).

190. Kossivas, F., Cao, L., Michaelides, M., Kyprianou, A. & Constantinides, C. Regional elastic modulus measurements of the ex-vivo murine heart using atomic force microscopy. *Int. J. Nanotechnol.* **10,** 1064–1077 (2013).

191. Mathur, A. B., Collinsworth, A. M., Reichert, W. M., Kraus, W. E. & Truskey, G. A. Endothelial, cardiac muscle and skeletal muscle exhibit different viscous and elastic properties as determined by atomic force microscopy. *J. Biomech.* **34,** 1545–1553 (2001).

192. Soufivand, a. a., Navidbakhsh, M. & Soleimani, M. Is it appropriate to apply Hertz model to describe cardiac myocytes' mechanical properties by atomic force microscopy nanoindentation? *Micro Nano Lett.* **9,** 153–156 (2014).

193. Lieber, S. C. *et al.* Aging increases stiffness of cardiac myocytes measured by atomic force microscopy nanoindentation. *Am. J. Physiol. Heart Circ. Physiol.* **287,** H645–H651 (2004).

194. Jacot, J. G., Martin, J. C. & Hunt, D. L. Mechanobiology of cardiomyocyte development. *J. Biomech.* **43,** 93–98 (2010).

195. Lieber, S. C. *et al.* Measurement of the Transverse Apparent Elastic Modulus in Mammalian Cardiac Myocytes. in *Advances in Bioengineering* **2003,** 117–118 (ASME, 2003).

196. Ahmad, R., Abu-Hassan, M. I., Li, Q. & Swain, M. V. Three dimensional quantification of mandibular bone remodeling using standard tessellation language registration based superimposition. *Clin. Oral Implants Res.* **24,** 1273–1279 (2013).

197. Chen, J., Ahmad, R., Li, W., Swain, M. & Li, Q. Biomechanics of oral mucosa. *J. R. Soc. Interface* **12,** 20150325 (2015).

198. Tomlin, H. R. & Wilson, H. J. The measurement of thickness and hardness of oral soft tissues. *Br. Dent. J.* **124,** 22–27 (1968).

199. INOUE, K., ARIKAWA, H., FUJII, K., SHINOHARA, N. & KAWAHATA, N. Viscoelastic

properties of Oral Soft Tissue. *Dent. Mater. J.* **4,** 47–53,121 (1985).

200. Kydd, W. L. & Mandley, J. The stiffness of palatal mucoperiosteum. *J. Prosthet. Dent.* **18,** 116–121 (1967).

201. Goktas, S., Dmytryk, J. J. & McFetridge, P. S. Biomechanical Behavior of Oral Soft Tissues. *J. Periodontol.* **82,** 1178–1186 (2011).

202. McKee, C. T., Last, J. a, Russell, P. & Murphy, C. J. Indentation Versus Tensile Measurements of Young's Modulus for Soft Biological Tissues. *Tissue Eng. Part B Rev.* **17,** 155–164 (2011).

203. D'Sa, D. J., Chan, H.-K. & Chrzanowski, W. Attachment of micro- and nano-particles on tipless cantilevers for colloidal probe microscopy. *J. Colloid Interface Sci.* **426,** 190–198 (2014).

204. Butt, H.-J., Cappella, B. & Kappl, M. Force measurements with the atomic force microscope: Technique, interpretation and applications. *Surf. Sci. Rep.* **59,** 1–152 (2005).

205. Kappl, M. & Butt, H. J. The colloidal probe technique and its application to adhesion force measurements. *Part. Part. Syst. Charact.* **19,** 129–143 (2002).

206. Rodriguez-Emmenegger, C. *et al.* Polymer brushes showing non-fouling in blood plasma challenge the currently accepted design of protein resistant surfaces. *Macromol. Rapid Commun.* **32,** 952–957 (2011).

207. Hackett, A. J. *et al.* Conductive surfaces with dynamic switching in response to temperature and salt. *J. Mater. Chem. B* **3,** 9285–9294 (2015).

208. Tan, K. Y., Gautrot, J. E. & Huck, W. T. S. Formation of Pickering Emulsions Using Ion-Specific Responsive Colloids †. *Langmuir* **27,** 1251–1259 (2011).

209. Santos, D. E. S., Li, D., Ramstedt, M., Gautrot, J. E. & Soares, T. A. Conformational Dynamics and Responsiveness of Weak and Strong Polyelectrolyte Brushes: Atomistic Simulations of Poly(dimethyl aminoethyl methacrylate) and Poly(2-(methacryloyloxy)ethyl trimethylammonium chloride). *Langmuir* **35,** 5037–5049 (2019).

210. Rzhepishevska, O. *et al.* The surface charge of anti-bacterial coatings alters

motility and biofilm architecture. *Biomater. Sci.* **1,** 589–602 (2013).

211. Schön, P. *et al.* Probing biofouling resistant polymer brush surfaces by atomic force microscopy based force spectroscopy. *Colloids Surfaces B Biointerfaces* **102,** 923–930 (2013).

212. Inoue, Y., Nakanishi, T. & Ishihara, K. Elastic repulsion from polymer brush layers exhibiting high protein repellency. *Langmuir* **29,** 10752–10758 (2013).

213. Inoue, Y., Nakanishi, T. & Ishihara, K. Adhesion force of proteins against hydrophilic polymer brush surfaces. *React. Funct. Polym.* **71,** 350–355 (2011).

214. Bhairamadgi, N. S., Pujari, S. P., Van Rijn, C. J. M. & Zuilhof, H. Adhesion and friction properties of fluoropolymer brushes: On the tribological inertness of fluorine. *Langmuir* **30,** 12532–12540 (2014).

215. Yu, Y., Kieviet, B. D., Kutnyanszky, E., Vancso, G. J. & De Beer, S. Cosolvency-induced switching of the adhesion between Poly(methyl methacrylate) brushes. *ACS Macro Lett.* **4,** 75–79 (2015).

216. Elmahdy, M. M., Drechsler, A., Bittrich, E., Uhlmann, P. & Stamm, M. Interactions between silica particles and poly(2-vinylpyridine) brushes in aqueous solutions of monovalent and multivalent salts. *Colloid Polym. Sci.* **292,** 1999–2012 (2014).

217. Gautrot, J. E. *et al.* Solution Conformation of Polymer Brushes Determines Their Interactions with DNA and Transfection Efficiency. *Biomacromolecules* **18,** 4121–4132 (2017).

218. Tan, K. Y. *et al.* Decoupling geometrical and chemical cues directing epidermal stem cell fate on polymer brush-based cell micro-patterns. *Integr. Biol. (Camb).* **5,** 899–910 (2013).

219. Qu, F., Li, D., Ma, X., Chen, F. & Gautrot, J. E. A Kinetic Model of Oligonucleotide-Brush Interactions for the Rational Design of Gene Delivery Vectors. *Biomacromolecules* **20,** 2218–2229 (2019).

220. Sader, J. E., Larson, I., Mulvaney, P. & White, L. R. Method for the calibration of atomic force microscope cantilevers. *Rev. Sci. Instrum.* **66,** 3789–3798 (1995).

221. Heim, L. O., Rodrigues, T. S. & Bonaccurso, E. Direct thermal noise calibration of

colloidal probe cantilevers. *Colloids Surfaces A Physicochem. Eng. Asp.* **443,** 377–383 (2014).

222. Hang, F. *et al.* In situ tensile testing of nanofibers by combining atomic force microscopy and scanning electron microscopy. *Nanotechnology* **22,** 365708 (2011).

223. Ohnemus, U. *et al.* An ex-vivo oral mucosa infection model for the evaluation of the topical activity of antifungal agents. *Mycoses* **51,** 21–29 (2008).

224. von Werne, T. & Patten, T. E. Preparation of Structurally Well-Defined Polymer−Nanoparticle Hybrids with Controlled/Living Radical Polymerizations. *J. Am. Chem. Soc.* **121,** 7409–7410 (1999).

225. Hinterwirth, H. *et al.* Quantifying thiol ligand density of self-assembled monolayers on gold nanoparticles by inductively coupled plasma-mass spectrometry. *ACS Nano* **7,** 1129–1136 (2013).

226. Ma, H., Hyun, J., Stiller, P. & Chilkoti, A. 'Non-Fouling' Oligo(ethylene glycol)-Functionalized Polymer Brushes Synthesized by Surface-Initiated Atom Transfer Radical Polymerization. *Adv. Mater.* **16,** 338–341 (2004).

227. Gautrot, J. E. *et al.* Exploiting the superior protein resistance of polymer brushes to control single cell adhesion and polarisation at the micron scale. *Biomaterials* **31,** 5030–5041 (2010).

228. Drechsler, A. *et al.* Interaction forces between microsized silica particles and weak polyelectrolyte brushes at varying pH and salt concentration. *Langmuir* **26,** 6400–6410 (2010).

229. Burke, S. E. & Barrett, C. J. Acid-base equilibria of weak polyelectrolytes in multilayer thin films. *Langmuir* **19,** 3297–3303 (2003).

230. Liu, G. *et al.* Insight into the origin of the thermosensitivity of poly[2-(dimethylamino) ethyl methacrylate]. *ChemPhysChem* **8,** 2254–2259 (2007).

231. Nagy, L. N. *et al.* Preparation, purification, and characterization of aminopropyl-functionalized silica sol. *J. Colloid Interface Sci.* **390,** 34–40 (2012).

232. Wu, Z., Xiang, H., Kim, T., Chun, M. S. & Lee, K. Surface properties of

submicrometer silica spheres modified with aminopropyltriethoxysilane and phenyltriethoxysilane. *J. Colloid Interface Sci.* **304,** 119–124 (2006).

233. Vaidya, S., Thaplyal, P. & Ganguli, A. Enhanced functionalization of Mn2O3@SiO2 core-shell nanostructures. *Nanoscale Res. Lett.* **6,** 169 (2011).

234. Ansar, S., Chakraborty, S. & Kitchens, C. pH-Responsive Mercaptoundecanoic Acid Functionalized Gold Nanoparticles and Applications in Catalysis. *Nanomaterials* **8,** 339 (2018).

235. Elmahdy, M. M., Drechsler, A., Bittrich, E., Uhlmann, P. & Stamm, M. Interactions between silica particles and poly(2-vinylpyridine) brushes in aqueous solutions of monovalent and multivalent salts. *Colloid Polym. Sci.* **292,** 1999–2012 (2014).

236. Stamm, M., Kremer, F., Synytska, A., Uhlmann, P. & Drechsler, A. Tuning the Adhesion of Silica Microparticles to a Poly(2-vinyl pyridine) Brush: An AFM Force Measurement Study. *Langmuir* **28,** 15555–15565 (2012).

237. De Vos, W. M., Leermakers, F. A. M., De Keizer, A., Stuart, M. A. C. & Kleijn, J. M. Field theoretical analysis of driving forces for the uptake of proteins by like-charged polyelectrolyte brushes: Effects of charge regulation and patchiness. *Langmuir* **26,** 249–259 (2010).

238. Schlierf, M., Ramakrishnan, S., Keller, A., Krainer, G. & Grundmeier, G. Cation-Induced Stabilization and Denaturation of DNA Origami Nanostructures in Urea and Guanidinium Chloride. *Small* **13,** 1702100 (2017).

239. Urbic, T. Ions increase strength of hydrogen bond in water. *Chem. Phys. Lett.* **610–611,** 159–162 (2014).

240. OBrien, J. T. & Williams, E. R. Effects of ions on hydrogen-bonding water networks in large aqueous nanodrops. *J. Am. Chem. Soc.* **134,** 10228–10236 (2012).

241. Yang, Y. & Cui, Q. Interactions between phosphate and water in solution: A natural bond orbital based analysis in a QM/MM framework. *J. Phys. Chem. B* **111,** 3999–4002 (2007).

242. Thatcher, G. R. J., Cameron, D. R., Nagelkerke, R. & Schmitke, J. Selective hydrogen bonding as a mechanism for differentiation of sulfate and phosphate at

biomolecular receptor sites. *J. Chem. Soc. Chem. Commun.* 386 (1992). doi:10.1039/c39920000386

243. Raftari, M., Zhang, Z. J., Carter, S. R., Leggett, G. J. & Geoghegan, M. Nanoscale Contact Mechanics between Two Grafted Polyelectrolyte Surfaces. *Macromolecules* **48,** 6272–6279 (2015).

244. Sakata, S., Inoue, Y. & Ishihara, K. Molecular Interaction Forces Generated during Protein Adsorption to Well-Defined Polymer Brush Surfaces. *Langmuir* **31,** 3108–3114 (2015).

245. Synytska, A. *et al.* Biocompatible polymeric materials with switchable adhesion properties. *Soft Matter* **6,** 5907–5914 (2010).

246. Friedsam, C., Bécares, A. D. C., Jonas, U., Seitz, M. & Gaub, H. E. Adsorption of polyacrylic acid on self-assembled monolayers investigated by single-molecule force spectroscopy. *New J. Phys.* **6,** 9–9 (2004).

247. Friedsam, C., Seitz, M. & Gaub, H. E. Investigation of polyelectrolyte desorption by single molecule force spectroscopy. *J. Phys. Condens. Matter* **16,** S2369–S2382 (2004).

248. Godawat, R., Jamadagni, S. N. & Garde, S. Characterizing hydrophobicity of interfaces by using cavity formation, solute binding, and water correlations. *Proc. Natl. Acad. Sci.* **106,** 15119–15124 (2009).

249. Levine, Z. A. *et al.* Surface force measurements and simulations of mussel-derived peptide adhesives on wet organic surfaces. *Proc. Natl. Acad. Sci.* **113,** 4332–4337 (2016).

250. Watt, F. M. & Green, H. Stratification and terminal differentiation of cultured epidermal cells. *Nature* **295,** 434–436 (1982).

251. Majewski, A. P. *et al.* PDMAEMA-grafted core-shell-corona particles for nonviral gene delivery and magnetic cell separation. *Biomacromolecules* **14,** 3081–3090 (2013).

252. Agarwal, S., Zhang, Y., Maji, S. & Greiner, A. PDMAEMA based gene delivery materials. *Mater. Today* **15,** 388–393 (2012).

253. Tan, K. Y. *et al.* Decoupling geometrical and chemical cues directing epidermal stem cell fate on polymer brush-based cell micro-patterns. *Integr. Biol. (United Kingdom)* **5,** 899–910 (2013).

254. Weinbaum, S., Tarbell, J. M. & Damiano, E. R. The Structure and Function of the Endothelial Glycocalyx Layer. *Annu. Rev. Biomed. Eng.* **9,** 121–167 (2007).

255. Owens, D. W., Brunton, V. G., Parkinson, E. K. & Frame, M. C. E-cadherin at the cell periphery is a determinant of keratinocyte differentiation in vitro. *Biochem. Biophys. Res. Commun.* **269,** 369–376 (2000).

256. Singh, A. *et al.* Glomerular Endothelial Glycocalyx Constitutes a Barrier to Protein Permeability. *J. Am. Soc. Nephrol.* **18,** 2885–2893 (2007).

257. Servais, A. B. *et al.* Structural Heteropolysaccharide Adhesion to the Glycocalyx of Visceral Mesothelium. *Tissue Eng. Part A* **24,** 199–206 (2018).

258. Araña, M. *et al.* Epicardial delivery of collagen patches with adipose-derived stem cells in rat and minipig models of chronic myocardial infarction. *Biomaterials* **35,** 143–151 (2014).

259. Tano, N. *et al.* Epicardial placement of mesenchymal stromal cell-sheets for the treatment of ischemic cardiomyopathy; In vivo proof-of-concept study. *Mol. Ther.* **22,** 1864–1871 (2014).

260. Ohtsuka, A., Yamana, S. & Murakami, T. Localization of membrane-associated sialomucin on the free surface of mesothelial cells of the pleura, pericardium, and peritoneum. *Histochem. Cell Biol.* **107,** 441–447 (1997).

261. COLLAN, Y. & RAESTE, A.-M. Electron microscopy of exfoliated cells of human oral mucosa. *Eur. J. Oral Sci.* **86,** 374–385 (1978).

262. Nguyen, V., Ndoye, A. & Hall, L. Programmed cell death of keratinocytes culminates in apoptotic secretion of a humectant upon secretagogue action of acetylcholine. *J. Cell Sci.* **114,** 1189–1204 (2001).

263. Wolff, K. & Schreiner, E. An electron microscopic study on the extraneous coat of keratinocytes and the intercellular space of the epidermis. *J. Invest. Dermatol.* **51,** 418–430 (1968).

264. Collins, L. M. C. & Dawes, C. The Surface Area of the Adult Human Mouth and Thickness of the Salivary Film Covering the Teeth and Oral Mucosa. *J. Dent. Res.* **66,** 1300–1302 (1987).

265. Sengupta, A. *et al.* Distribution of MUC1 in the normal human oral cavity is localized to the ducts of minor salivary glands. *Arch. Oral Biol.* **46,** 529–538 (2001).

266. Vitkov, L., Krautgartner, W. D., Hannig, M. & Fuchs, K. Fimbria-mediated bacterial adhesion to human oral epithelium. *FEMS Microbiol. Lett.* **202,** 25–30 (2001).

267. Chevalier, M., Sakarovitch, C., Precheur, I., Lamure, J. & Pouyssegur-Rougier, V. Antiseptic mouthwashes could worsen xerostomia in patients taking polypharmacy. *Acta Odontol. Scand.* **73,** 267–273 (2015).

268. Zhao, X., Huebsch, N., Mooney, D. J. & Suo, Z. Stress-relaxation behavior in gels with ionic and covalent crosslinks. in *Journal of Applied Physics* **107,** (2010).

269. Lee, K. Y. *et al.* Controlling mechanical and swelling properties of alginate hydrogels independently by cross-linker type and cross-linking density. *Macromolecules* **33,** 4291–4294 (2000).

270. Sun, J.-Y. *et al.* Highly stretchable and tough hydrogels. *Nature* **489,** 133–136 (2012).

271. Gramlich, W. M., Kim, I. L. & Burdick, J. A. Synthesis and orthogonal photopatterning of hyaluronic acid hydrogels with thiol-norbornene chemistry. *Biomaterials* **34,** 9803–9811 (2013).

272. Shih, H. & Lin, C. C. Cross-linking and degradation of step-growth hydrogels formed by thiol-ene photoclick chemistry. *Biomacromolecules* **13,** 2003–2012 (2012).

273. Colak, B., Di Cio, S. & Gautrot, J. E. Biofunctionalized Patterned Polymer Brushes via Thiol-Ene Coupling for the Control of Cell Adhesion and the Formation of Cell Arrays. *Biomacromolecules* **19,** 1445–1455 (2018).

274. Noshadi, I. *et al.* In vitro and in vivo analysis of visible light crosslinkable gelatin methacryloyl (GelMA) hydrogels. *Biomater. Sci.* **5,** 2093–2105 (2017).

275. Han, S. & Chien-Chi, L. Visible-Light-Mediated Thiol-Ene Hydrogelation Using

Eosin-Y as the Only Photoinitiator. *Macromol. Rapid Commun.* **34,** 269–273 (2013).

276. Fedorovich, N. E. *et al.* The effect of photopolymerization on stem cells embedded in hydrogels. *Biomaterials* **30,** 344–353 (2009).

277. Guan, Y. & Zhang, Y. Boronic acid-containing hydrogels: synthesis and their applications. *Chem. Soc. Rev.* **42,** 8106 (2013).

278. Wu, X. *et al.* Selective sensing of saccharides using simple boronic acids and their aggregates. *Chem. Soc. Rev.* **42,** 8032–48 (2013).

279. Xu, Z., Deng, P., Tang, S. & Li, J. Fluorescent boronic acid terminated polymer grafted silica particles synthesized via click chemistry for affinity separation of saccharides. *Mater. Sci. Eng. C* **40,** 228–234 (2014).

280. Heleg-Shabtai, V., Aizen, R., Orbach, R., Aleman-Garcia, M. A. & Willner, I. Gossypol-cross-linked boronic acid-modified Hydrogels: A functional matrix for the controlled release of an anticancer drug. *Langmuir* **31,** 2237–2242 (2015).

281. Deng, C. C., Brooks, W. L. A., Abboud, K. A. & Sumerlin, B. S. Boronic acid-based hydrogels undergo self-healing at neutral and acidic pH. *ACS Macro Lett.* **4,** 220–224 (2015).

282. Oyen, M. L. Mechanical characterisation of hydrogel materials. *Int. Mater. Rev.* **59,** 44–59 (2014).

283. Ahearne, M., Yang, Y. & Liu, K. Mechanical Characterisation of Hydrogels for Tissue Engineering Applications. *Tissue Eng.* **4,** 1–16 (2008).

284. Kanayama, N. & Kitano, H. Interfacial recognition of sugars by boronic acid-carrying self-assembled monolayer. *Langmuir* **16,** 577–583 (2000).

285. Jay, J. I., Langheinrich, K., Hanson, M. C., Mahalingam, A. & Kiser, P. F. Unequal stoichiometry between crosslinking moieties affects the properties of transient networks formed by dynamic covalent crosslinks. *Soft Matter* **7,** 5826–5835 (2011).

286. He, L., Fullenkamp, D. E., Rivera, J. G. & Messersmith, P. B. PH responsive self-healing hydrogels formed by boronate-catechol complexation. *Chem. Commun.*

**47,** 7497–7499 (2011).

287. Henderson, K. J., Zhou, T. C., Otim, K. J. & Shull, K. R. Ionically cross-linked triblock copolymer hydrogels with high strength. *Macromolecules* **43,** 6193–6201 (2010).

288. Webber, R. E., Creton, C., Brown, H. R. & Gong, J. P. Large strain hysteresis and mullins effect of tough double-network hydrogels. *Macromolecules* **40,** 2919–2927 (2007).

289. Yu, Q. M., Tanaka, Y., Furukawa, H., Kurokawa, T. & Gong, J. P. Direct observation of damage zone around crack tips in double-network gels. *Macromolecules* **42,** 3852–3855 (2009).

290. Hoang Thi, T. T., Lee, Y., Ryu, S. B., Sung, H. & Park, K. D. Oxidized cyclodextrin-functionalized injectable gelatin hydrogels as a new platform for tissue-adhesive hydrophobic drug delivery. *RSC Adv.* **7,** 34053–34062 (2017).

291. Chung, H. & Grubbs, R. H. Rapidly Cross-Linkable DOPA Containing Terpolymer Adhesives and PEG-Based Cross-Linkers for Biomedical Applications. (2012). doi:10.1021/ma3017986

292. Young, E. *et al.* Rapidly light-activated surgical protein glue inspired by mussel adhesion and insect structural crosslinking. *Biomaterials* **67,** 11–19 (2015).